College of
ENGINEERING
VILLANOVA
UNIVERSITY

Center for Advanced Communications

Villanova University

FINAL REPORT

(10/1/2001 – 3/31/2007)

CLASSIFICATION AND DISCRIMINATION OF SOURCES WITH TIME-VARYING FREQUENCY AND SPATIAL SPECTRA

Submitted to

Office of Naval Research

Grant No. N00014-98-1-0176

Principal Investigator

Moeness G. Amin

Contributors

Prof. Moeness Amin
Prof. Yimin Zhang
Dr. Genyuan Wang
Mr. Baha Obeidat
Mr. Pawan Setlur
Mr. Habib Estephan

April 2007

20070503425

Table of Contents

Executive Summary

Classification and Discrimination of Sources
with Time-Varying Frequency and Spatial Spectra

ONR Grant No. N00014-98-1-0176

Moeness Amin (PI)

This final report presents the results of the research performed under ONR grant number N00014-98-1-0176 over the period of October 1st, 2001 to March 31st, 2007. The research team working on this project consists of Prof. Moeness Amin (PI), Prof. Yimin Zhang (Research Professor), Dr. Genyuan Wang (Postdoctoral Fellow), Mr. Baha Obeidat, Mr. Pawan Setlur (Graduate Student), and Mr. Habib Estephan (Graduate Student). We have also collaborated with Dr. Thayananthan Thayaparan (Defense Research and Development, Canada), Dr. Gordon Frazer (DSTO, Australia), Prof. Ahmad Hoorfar (Villanova University), and Prof. Kehu Yang (Xidian University, China).

The research efforts over the life of this grant have evolved around 1) Concurrent Operation of Two Over-the-Horizon Radars, 2) Spatial Polarimetric Time-Frequency Distributions for Moving Target Tracking, 3) Imaging Through Unknown Walls Using Different Standoff Distances, 4) Autofocusing of Through-the-Wall Radar Imagery under Unknown Wall Characteristics, 5) Blind Source Separation in the Time-Frequency Domain Based on Multiple Hypothesis Testing, 6) Estimation of FM Parameters using a Time-Frequency Hough Transform. Below, we address each of the above contributions. Each one of the above contributions forms a chapter of this report. Each chapter has its own Abstract, Introduction, Conclusion, and References. It also has its own equation and figure numbers.

1. Concurrent Operation of Two Over-the-Horizon Radars

Over-the-horizon radar (OTHR) systems perform wide-area surveillance at long range well beyond the limit of the horizon of conventional line-of-sight (LOS) radars. With a single OTHR, information about the target range and Doppler frequency in the slant range direction can be obtained. However, such information does not uniquely determine the movement of the targets. To respond to the needs for advanced wide-area surveillance, we have proposed a concurrent operation of two OTHR systems. The use of two OTHRs, positioned at different locations, not only extends the coverage for enhanced surveillance, but also offers higher-dimensional information of a moving target. By exploiting the reflective and refractive nature of high-frequency (HF) radiowave propagation through the ionosphere or the conducting sea surface, over-the-horizon radar (OTHR) systems perform wide-area surveillance at long range well beyond the limit of the horizon of conventional line-of-sight (LOS) radars. Improved characterizations of the targets can be achieved by using multiple OTHRs operating simultaneously as compared to a single OTHR operating alone. We have considered concurrent operations of two OTHR systems that occupy the same frequency band with different chirp waveforms. The objective is to respond to the advanced wide-area surveillance needs without reducing the wave repetitive frequency. For this purpose, a new cross-radar interference cancelation technique is developed and its effectiveness is verified through both analytical and simulation results.

2. Spatial Polarimetric Time-Frequency Distributions for Moving Target Tracking

We have introduced the spatial polarimetric time-frequency distributions (SPTFDs) as a platform for processing polarized nonstationary signals incident on multiple dual-polarized double-feed antennas.

i

Based on this platform, we have developed the polarimetric time-frequency MUSIC (PTF-MUSIC) methods for direction-of-arrival (DOA) estimation of nonstationary sources with distinct polarization characteristics, and have examined the feasibility of the PTF-MUSIC methods for tracking moving sources with time-varying polarization characteristics. We have demonstrated the significance of polarization diversity in challenging direction finding problems, where the sources are closely spaced, and discuss important issues relevant to utilization of polarization diversity. The SPTFD has the capability of incorporating both the instantaneous polarization information and time-frequency signatures of the different sources in the field of view. The incorporation of specific time-frequency points or regions, where one or more signals reside, enhances signal-to-noise ratio (SNR) and allows source discrimination and source elimination. This, in turn, leads to DOA performance improvement and reductions in the required number of array sensors. The PTF-MUSIC significantly outperforms the existing time-frequency MUSIC, polarimetric MUSIC and conventional MUSIC direction finding techniques.

3. Imaging Through Unknown Walls Using Different Standoff Distances

Through-the-Wall Radar Imaging (TWRI) is an emerging technology that addresses a number of civilian problems and has a dual-use with obvious military applications as well. TWRI is a complex and difficult problem that requires cross-disciplinary research. There are many challenges facing Through-the-Wall Radar Imaging system development, namely, the system should be reliable, portable, light weight, small-size, and have both short acquisition time and set-up time. It is important for the system performance to be robust to ambiguities and inaccuracies in wall parameters and to the presence of non-uniform walls, multiple walls, and operator motion. Ultimately, the system should have high range and cross range resolutions, which are application specific. Finally, the TWRI system must be able to detect and classify motions in a populated scene and in the presence of heavy clutter, which may include interior back and side walls, water pipes, electrical cords, and various types of furniture items.. In through-the-wall imaging, errors in wall parameters cause targets to be imaged away from their true positions. The displacement in target locations depends on the accuracy of the estimates of the wall parameters as well as the target position relative to the antenna array. A technique using two or more standoff distances of the imaging system from the wall is proposed for application under wall parameter ambiguities. Two different imaging schemes can then be applied to correct for errors in wall characteristics. The first scheme relies on forming target displacement trajectories, each corresponding to a different standoff distance, and assuming different values of wall thickness and dielectric constant. The target position is then determined as the trajectories cross-over point. In the second scheme, an image sequence is generated. Each specific image in this sequence is obtained by summing those corresponding to different standoff distances, but with the same assumed wall parameters. An imaging focusing metric can then be adopted to determine the target position. We have analyzed the above two schemes, and provides extensive simulation examples demonstrating their effectiveness.

4. Autofocusing of Through-the-Wall Radar Imagery under Unknown Wall Characteristics

The quality and reliability of through-the-wall radar imagery is governed, among other things, by the knowledge of the wall characteristics. Ambiguities in wall characteristics smear and blur the image, and also shift the imaged target positions. An autofocusing technique, based on higher order statistics, is presented which corrects for errors under unknown walls. Simulation results show that the proposed technique provides high-quality focused images with target locations in close proximity to true target positions. The non-convex multi-modal nature of the autofocussing cost function may occasionally force the algorithm to converge to a small local solution or could prevent it from convergence at all. The viability of the image quality optimization may be improved by enhancing the optimization algorithm to effectively tackle the multiplicity of local solutions. However, this investigation was beyond the scope of our work. We, therefore, have assumed that the algorithm initializations lead to a local or global solution or the system operator guides the tuning of the wall parameters to optimize the image quality metric. We have analyzed the target image intensity under far-field conditions and assume the wall parameter error values to be small. Our analysis shows that exact as well as incorrect assumed wall characteristics,

defined by wall thickness and dielectric constant, can lead to focused images with imaged target positions in close proximity to true target locations.

5. Blind Source Separation in the Time-Frequency Domain Using Multiple Hypothesis Testing

The problem of blind source separation (BSS) involves recovery of a number of unobserved signals from their observed mixtures. In certain applications, such as radar, the signals of interest are typically wideband, but instantaneously narrowband in nature. A good example is FM signals. These nonstationary signals, which exhibit a significant variation in spectral content over the observation interval, may be processed using techniques that exploit the nonstationary signal properties, in particular the instantaneous frequency, to obtain improved performance over more general methods. We have considered a time-frequency (t-f) based approach for blind separation of nonstationary signals. In particular, we have proposed a time-frequency 'point selection' algorithm based on multiple hypothesis testing, which allows automatic selection of auto- or cross-source locations in the time-frequency plane. The selected t-f points are then used via a joint diagonalization and off-diagonalization algorithm to perform source separation. The proposed algorithm is developed assuming deterministic signals with additive white complex Gaussian noise.

6. Estimation of FM Parameters using a Time-Frequency Hough Transform

We have considered the estimation of the phase parameters of mono- or multicomponent FM signals from noisy observations. A number of approaches exist for estimating the signal instantaneous frequency, given particular phase models such as the polynomial phase transform (PPT), also known as the higher-order ambiguity function (HAF), generalized product and integrated forms of the HAF, the Wigner-Hough transform (WHT), and a generalized time-frequency Hough transform. The WHT is of particular interest for linear FM signals, as it offers optimal detection and asymptotically efficient estimation, with an improved SNR performance threshold over other methods such as the PPT. It also provides significant suppression of cross-terms in the multicomponent case. An estimator for the phase parameters of mono- and multicomponent FM signals, with both good numerical properties and statistical performance has been proposed. The proposed approach is based on the Hough transform of the pseudo Wigner-Ville time-frequency distribution (PWVD). It is shown that the numerical properties of the estimator can be improved by varying the PWVD window length. The effect of the window time extent on the statistical performance of the estimator is delineated. Experimental data was used for validation of the statistical properties.

List of Publications

(Publications listed in bold font make up the different chapters of this report)

Journal Papers

[1]   W. Mu, M. G. Amin, and Y. Zhang, "Bilinear signal synthesis in array processing," IEEE Transactions on Signal Processing, vol. 51, no. 1, pp. 90-100, January 2003.

[2]   Y. Zhang, M. G. Amin, and G. J. Frazer, "High-resolution time-frequency distributions for maneuvering target detection in over-the-horizon radars," IEE Proceedings on Radar, Sonar and Navigation, vol. 150, no.4, pp. 299-304, Aug. 2003.

[3]   G. Wang, X.-G. Xia, B. T. Root, V. C. Chen, Y. Zhang, and M. G. Amin, "Maneuvering target detection in over-the-horizon radar by using adaptive clutter rejection and adaptive chirplet transform," IEE Proceedings on Radar, Sonar and Navigation, vol. 150, no. 4, pp. 292-298, Aug. 2003.

[4]   F. Ahmad, G. J. Frazer, S. A. Kassam, and M. G. Amin, "Design and implementation of near-field, wideband synthetic aperture beamformers," IEEE Transactions on Aerospace and Electronic Systems, vol. 40, no. 1, pp 206-221, January 2004.

[5]   M. G. Amin and Y. Zhang, "Bilinear signal synthesis using polarization diversity," IEEE Signal Processing Letters, vol. 11, no. 3, pp 338-340, March 2004.

[6]   A. Belouchrani, K. Abed-Meraim, M. G. Amin, and A.M. Zoubir, "Blind separation of non-stationary sources," IEEE Signal Processing Letters, July 2004.

[7]   F. Ahmad, M. G. Amin, S. A. Kassam, "Synthetic aperture beamformer for imaging through a dielectric wall," IEEE Transactions on Aerospace and Electronic Systems, January 2005.

[8]   Y. Zhang, K. Yang, and M. G. Amin, "Subband array implementations for space-time adaptive processing," EURASIP Journal on Applied Signal Processing, vol. 2005, no. 1, pp. 99-111, Jan. 2005.

[9]   G. Wang, M. G. Amin, and Y. Zhang, "A new approach for target locations in the presence of wall ambiguity," IEEE Transactions on Aerospace and Electronic Systems, January 2006.

[10]   **Y. Zhang, B. Obeidat, and M. G. Amin, "Spatial polarimetric time-frequency distributions for direction-of-arrival estimations," IEEE Transactions on Signal Processing, April 2006.**

[11] Y. Zhang and M. Amin, "Blind separation of nonstationary sources based on spatial time-frequency distributions," EURASIP Journal on Applied Signal Processing, vol. 2006, article ID 64785, 13 pages, 2006.

[12] **G. Wang and M. Amin, "Imaging through unknown walls using different standoff distances," IEEE Transactions on Signal Processing, October 2006.**

[13] F. Ahmad and M. Amin, "A noncoherent approach to through-the-wall radar imaging," IEEE Transactions on Aerospace and Electronic Systems, October 2006.

[14] **Y. Zhang, G. J. Frazer, and M. G. Amin, "Concurrent operation of two over-the-horizon radars," IEEE Journal of Selected Topics in Signal Processing, special issue on Adaptive Waveform Design for Agile Sensing and Communication, in press.**

[15] **F. Ahmad, M. G. Amin, G. Mandapati, "Autofocusing of through-the-wall radar imagery under unknown wall characteristics," IEEE Transactions on Aerospace Electronics Systems, in press.**

[16] **L. Cirillo, A. Zoubir and M. Amin, "Blind Source Separation in the Time-Frequency Domain Based on Multiple Hypothesis Testing," submitted to IEEE Transactions on Signal Processing.**

[17] **L. Cirillo, A. Zoubir and M. Amin, "Estimation of FM Parameters using a Time-Frequency Hough Transform," submitted to IEEE Transactions on Signal Processing.**

Book Chapters

[18] M. G. Amin and Y. Zhang, "Interference suppression in spread spectrum communication systems," in J. G. Proakis (ed.), The Wiley Encyclopedia of Telecommunications, New York, NY: John Wiley, 2002.

[19] M. G. Amin and Y. Zhang, "Spatial time-frequency distributions and their applications," in B. Boashash (ed.), Time-Frequency Signal Analysis and Processing, Oxford, UK: Elsevier, 2003.

[20] M. G. Amin, Y. Zhang, G. J. Frazer, and A. R. Lindsey, "Spatial time-frequency distributions: Theory and applications," in L. Debnath (ed.), Wavelets and Signal Processing, Boston, MA: Birkhauser, 2003.

[21] Y. Zhang, M. G. Amin, and B. Obeidat, "Polarimetric array processing for nonstationary signals," in S.Chandran (ed.), Adaptive Antenna Arrays: Trends and Applications, Berlin, Germany: Springer-Verlag, 2004.

[22] Y. Zhang, B. Obeidat, and M. G. Amin, "Polorimetric time-frequency MUSIC for direction finding of moving sources with time-varying polarizations," in S. Chandran (ed.), Advances in Direction-of-Arrival Estimation, Boston, MA: Artech House, 2006.

Conference Publications

[23] G. J. Frazer and M. G. Amin, "Characterization of near-field scattering using quadratic sensor-angle distributions," Proceedings of the IEEE International Conference on Acoustics, Speech and Signal Processing, Orlando, FL, May 2002.

[24] G. J. Frazer and M. G. Amin, "Characterization Of Near-Field Scattering Using A Multiple Weighted Summed Beamformer," Proceedings of SPIE 2002, Advanced Signal Processing Algorithms, Architectures and Implementations XII, Seattle, WA, July 2002.

[25] A. Hassanien, A. B. Gershman, and M. G. Amin, "Time-frequency ESPRIT for direction-of arrival estimation of chirp signals," IEEE Sensor Array and Multichannel Signal Processing Workshop, Rosslyn, VA, Aug. 2002.

[26] Y. Zhang, M. G. Amin, and G. J. Frazer, "A new approach to FM jammer suppression for digital communications", Proceedings of the IEEE Sensor Array and Multichannel Signal Processing Workshop, Rosslyn, VA, Aug. 2002.

[27] G. J. Frazer and M. G. Amin, "Near-field scatter measurements using quadratic sensor-angle distributions", in Proceedings of the Second IEEE Sensor and Multichannel Signal Processing Workshop, Washington, DC, Aug. 2002.

[28] Y. Zhang, M. G. Amin, and H. Ge, "Nonstationary interference suppression in DS/SS communications using space-time oblique projection techniques," IEEE International Symposium on Signal Processing and Information Technology, Marrakech, Morocco, December 2002.

[29] Y. Zhang, M. G. Amin, and A. R. Lindsey, "Improved blind separations of nonstationary sources based on spatial time-frequency distributions," Fourth International Symposium on Independent Component Analysis and Blind Signal Processing, Nara, Japan, April 2003.

[30] Y. Zhang, M. Amin, and G. Frazer, "High Resolution Time-Frequency Distribution for Maneuvering Target Detection in Over-The-Horizon Radars," IEEE International Conference on Acoustics, Speech and Signal Processing, Hong Kong, China, April 2003.

[31] L. Cirillo, A. Zoubir, and M. Amin, "Auto-Term Detection Using Time-Frequency Array Processing," IEEE International Conference on Acoustics, Speech and Signal Processing, Hong Kong, China, April 2003.

[32] F. Ahmad, G. Frazer, S. Kassam, and M. Amin, "A New Approach for Near-Field Wideband Synthetic Aperture Beamforming," IEEE International Conference on Acoustics, Speech and Signal Processing, Hong Kong, China, April 2003.

[33] G. Wang, X. Xia, B. Root, V. Chen, M. Amin, and Y. Zhang, "Maneuvering Target Detection In Over-The-Horizon Radar By Using Adaptive Chirplet Transform," IEEE International Conference on Acoustics, Speech and Signal Processing, Hong Kong, China, April 2003.

[34] Y. Zhang, M. G. Amin, and B. Obeidat, "Spatial polarimetric time-frequency distributions and applications to direction-of-arrival estimation," SPIE Annual Meeting, San Diego, CA, Aug. 2003.

[35] Y. Zhang, B. A. Obeidat, and M. G. Amin, "Polarimetric time-frequency MUSIC in coherent signal environment," IEEE Workshop on Statistical Signal Processing, St. Louis, MO, Sept. 2003.

[36] B. A. Obeidat, Y. Zhang, and M. G. Amin, "Polarimetric time-frequency ESPRIT," Proceedings of the 37th Asilomar Conference on Signals, Systems, and Computers, Pacific Grove, CA, Nov., 2003.

[37] Y. Zhang and M. Amin, "Spatial And Polarization Correlations In Nonstationary Array Processing," Proceedings of the IEEE International Conference on Acoustics, Speech, and Signal Processing, Montreal, Canada, May 2004.

[38] B. Obeidat, Y. Zhang, and M. Amin, "Range And Doa Estimation Of Polarized Near-Field Signals Using Fourth-Order Statistics," Proceedings of the IEEE International Conference on Acoustics, Speech, and Signal Processing, Montreal, Canada, May 2004.

[39] Y. Zhang and M. G. Amin, "Spatial and polarization correlations in array processing," Proceedings of the IEEE Sensor Array and Multichannel Signal Processing Workshop, Barcelona, Spain, July 2004.

[40] Y. Zhang, M. G. Amin, and G. J. Frazer, "Simultaneous operation of two over-the-horizon radars," Proceedings of the SPIE Annual Conference, Denver, CO, Aug. 2004.

[41] G. Wang, Y. Zhang, and M. G. Amin, "Cooperation diversity using differential distributed space-time codes," Proceedings of the The Joint Conference of Asia-Pacific Conference on Communications and International Symposium on Multi-Dimensional Mobile Communications, Beijing, China, Aug. 2004.

[42] B. A. Obeidat, Y. Zhang, and M. G. Amin, "DOA and polarization estimation for wideband sources," Proceedings of the Annual Asilomar Conference on Signals, Systems, and Computers, Pacific Grove, CA, Nov. 2004.

[43] Y. Zhang, B. A. Obeidat, and M. G. Amin, "Nonstationary array processing for sources with time-varying polarizations," Proceedings of the Annual Asilomar Conference on Signals, Systems, and Computers, Pacific Grove, CA, Nov. 2004.

[44] M. G. Amin, "A noncoherent radar system approach for through-the-wall imaging," Proceedings of the SPIE Defense & Security Symposium, Conference on Sensors, and Command, Control, Communications, and Intelligence (C3I), Orlando, FL, March 2005.

[45] L. Cirillo, A. Zoubir and M. G. Amin, "Direction finding of nonstationary signals using a time-frequency hough transform," Proceedings of the IEEE International Conference on Acoustics, Speech, and Signal Processing, Philadelphia, PA, March 2005.

[46] B. Obeidat, Y. Zhang, and M. G. Amin, "Nonstationary array processing for tracking moving targets with time-varying polarizations," Proceedings of the IEEE International Conference on Acoustics, Speech, and Signal Processing, Philadelphia, PA, March 2005.

[47] F. Ahmad, M. Amin, and S. Kassam, " A beamforming approach to stepped-frequency synthetic aperture through-wall radar imaging," Proceedings of the IEEE Workshop on Computational Advances in Multi-Sensor Adaptive Processing, Puerto Vallarta , Mexico, December 2005.

[48] F. Ahmad and M. Amin "A Noncoherent Approach to Radar Localization through Unknown Walls" Proceedings of the 2006 IEEE RADAR Conference,Verona, NY, April 2006.

[49] H. Estephan, F. Ahmad, M. Amin, "An Interactive Software for Real-Time Simulation of Through-the-Wall Imaging Radar," Proceedings of the IEEE International Conference on Acoustics, Speech, and Signal Processing, Toulouse, France, May 2006.

[50] L. Cirillo, A. Zoubir, M. Amin, "Estimation of FM Parameters using a Time-Frequency Hough Transform," Proceedings of the IEEE International Conference on Acoustics, Speech, and Signal Processing, Toulouse, France, May 2006

[51] S. Aviyente, F. Ahmad, and M. Amin, "Information theoretic measures for through-the-wall surveillance," Proceedings of the IEEE Workshop on Sensor Array and Multi-channel Processing, Waltham, MA, July 2006.

[52] F. Ahmad, M. Amin, P. Sutler, and P. Zemany, "Moving target localization for indoor imaging using dual frequency cw radars," Proceedings of the IEEE Workshop on Sensor Array and Multi-channel Processing, Waltham, MA, July 2006.

[53] F. Ahmad and M. Amin, "Analyses of autofocusing schemes for indoor imaging with unknown walls," Proceedings of the IEEE Workshop on Sensor Array and Multi-channel Processing, Waltham, MA, July 2006.

[54] F. Ahmad, M.G. Amin, "Through-the-Wall Radar Imaging Experiments," Proceedings of the IEEE Workshop on Signal Processing Applications for Public Security and Forensics, Washington, D.C., April 2007.

[55] S. Aviyente, F. Ahmad, M.G. Amin, "Information theoretic measures for change detection in urban sensing applications, Proceedings of the IEEE Workshop on Signal Processing Applications for Public Security and Forensics, Washington, D.C., April 2007.

[56] F. Ahmad, M. G. Amin, "High-resolution imaging using capon beamformers for urban sensing applications," Proceedings of the IEEE International Conference on Acoustics, Speech, and Signal Processing, Honolulu, HI, April 2007.

[57] P. Setlur, M. G. Amin, F. Ahmad, "Cramer-Rao bounds for range and motion parameter estimations using dual frequency radars," Proceedings of the IEEE International Conference on Acoustics, Speech, and Signal Processing, Honolulu, HI, April 2007.

[58] L. Cirillo, A. Zoubir, and M. Amin, "Estimation of near-field parameters using spatial time-frequency distributions," Proceedings of the IEEE International Conference on Acoustics, Speech, and Signal Processing, Honolulu, HI, April 2007.

[59] P. Setlur, M. G. Amin, F. Ahmad, "A Frequency Diverse Doppler Radar for Range-to-Motion Estimation in Urban Sensing Applications," Proceedings of the 2007 International Waveform Diversity and Design Conference, Pisa, Italy, June 2007.

Chapter 1

Concurrent Operation of Two
Over-the-Horizon Radars

Abstract

By exploiting the reflective and refractive nature of high-frequency (HF) radiowave propagation through the ionosphere or the conducting sea surface, over-the-horizon radar (OTHR) systems perform wide-area surveillance at long range well beyond the limit of the horizon of conventional line-of-sight (LOS) radars. Improved characterizations of the targets can be achieved by using multiple OTHRs operating simultaneously as compared to a single OTHR operating alone. In this chapter, we consider concurrent operations of two OTHR systems that occupy the same frequency band with different chirp waveforms. The objective is to respond to the advanced wide-area surveillance needs without reducing the wave repetitive frequency. For this purpose, a new cross-radar interference cancelation technique is developed and its effectiveness is verified through both analytical and simulation results.

I. Introduction

Over-the-horizon radar (OTHR) systems perform wide-area surveillance at long range well beyond the limit of the horizon of conventional line-of-sight (LOS) radars [1]–[3]. It can track aircraft more than 3000 km away and over millions of square kilometers of open ocean [4]. Further, OTHR permits more accurate landfalls of Hurricane landfall, with more complete information about the size, shape, and extent of the interface between storm and ambient airflow. In coastal wave forecasts, OTHR can characterize the wave field in the open ocean from which coastal forecasts are derived, so as early evacuations of coastal areas.

With a single OTHR, information about the target range and Doppler frequency in the slant range direction can be obtained. However, such information does not uniquely determine the movement of the targets. To respond to the needs for advanced wide-area surveillance, we propose in this chapter a concurrent operation of two OTHR systems. The use of two OTHRs, positioned at different locations, not only extends the coverage for enhanced surveillance, but also offers higher-dimensional information of a moving target. This information is key in achieving improved target classification and predictions of ballistic destinations. Fig. 1 illustrates such a scenario. When only radar A is operational, the range and Doppler information is estimated in terms of (Tx A – target – Rx A). With radar B added to the operation, information about the following combinations can also be obtained: (Tx B – target – Rx B, Tx A – target – Rx B, Tx B – target – Rx A). In a single-radar setting, the movement of a target in the direction orthogonal to the slant path between radar A and the target can only be detected when the target passes through different cross-range bins. In a dual-radar system, on the other hand, Doppler frequencies related to the aforementioned four slant path combinations can be detected when radar B is also employed as the transmitter or/and receiver.

A key limitation of HF radar is the trade-off between the selection of an appropriate operating frequency and the demand for radar waveform bandwidth that is commensurate with the radar range resolution requirements. While the operation band of OTHR systems is nominally 3–30 MHz, the effective operating frequency bandwidth available to a particular radar at any given time is further limited due to propagation constraints. The
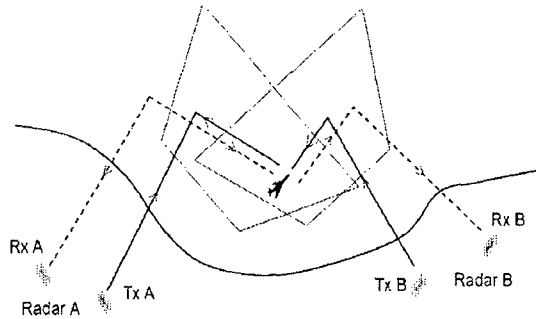
Fig. 1. Illustration of concurrent operation of multiple OTHRs.

problem described above is further compounded when a network of two or more radars is in use. Present operation of multiple OTHR systems requires the reduction of wave repetition frequency (WRF) or the division of the waveform bandwidth. These conditions can be relaxed if effective mitigation of cross-radar interference can be achieved [5]. In this case, the same frequency band can be concurrently occupied by two OTHR systems with different waveforms, leaving both the WRF and bandwidth uncompromised.

In this chapter, we consider linear frequency modulated (LFM) waveforms with different frequency sweeping orientations. In general, modern OTHRs use LFM pulses (for monostatic radar designs) or linear frequency-modulated continuous-wave (FM/CW) waveforms for bistatic designs (typical of the larger skywave radar cases). While discrete coded waveforms are used in some radar systems, they are not the preferred signal mode of operation in OTHR [5]. LFM (indeed almost any waveform with continuous and differentiable phase law) is simpler to generate at a desired level of fidelity than discrete waveforms.

Various signal processing methods have been considered for the suppression of impulsive and transient interference signals for enhanced OTHR performance (see for example [6]–[10]). However, to our knowledge, signal detection and cross-radar interference mitigation in a dual-radar OTHR system was not considered until [5]. This chapter develops a new cross-radar interference cancelation approach which is similar but more robust compared to the approach in [5]. It is important to note that the OTHR problem addressed here is quite different from the multistatic adaptive radar reception and pulse compression methods developed for other types of radar and synthetic aperture radar (SAR) systems

3

which apply beamforming for spatial processing [11], [12]. In OTHR systems, beamforming is performed primarily for the selection of cross-range bins and thus the spatial selectivity may not be further utilized at subsequent signal processing.

The rest part of this chapter is organized as follows. Section II introduces the signal model based on reference [13] for single-radar operation. This model is extended in Section III to dual-radar operation scenarios, and the effect of cross-radar interference is discussed [5]. Section IV considers the suppression of cross-radar interference, and a new cross-radar interference cancelation method is developed. The performance of dual-radar systems as well as the cross-radar interference mitigation is analyzed in Section V. Simulation results using measured clutter data and synthesized target signals are provided in Section VI.

II. Signal Model

In this section, we review the signal model based on reference [13] for the radar applications where the frequency band of interest is solely occupied by a single OTHR system. An OTHR typically employs FM/CW signals consisting of a coherent series of chirps to determine the target time-delay (slant range) and Doppler information [14]. Each waveform is an LFM, or chirp, signal of the form

$$
v_p(t) = \begin{cases} \exp(j\pi B f_r t^2), & 0 \leq t < T_r \\ 0, & \text{otherwise}, \end{cases} \tag{1}
$$

where T_r and $f_r = 1/T_r$ are respectively the waveform repetition interval (WRI) and WRF, and B is the bandwidth of the chirp. The transmitted radar signal, $u(t)$, for the lth revisit consists of a series of M LFM waveforms, i.e.,

$$
u(t) = \alpha_0 \exp(j\omega_0 t) \sum_{m=0}^{M-1} v_p(t - mT_r - t_l), \tag{2}
$$

where α_0 is a complex scaler representing the transmitted signal amplitude and phase, $\omega_0 = 2\pi f$ is the radar operating frequency, and t_l is the time of the lth revisit. For M transmitted waveforms, the signal duration, called the coherent integration time (CIT), is $T_c = MT_r$. In this chapter, we only consider one revisit and, therefore, the index of l is omitted thereafter, and $t_l = 0$ is assumed.

4

The received signal corresponding to a target s can be expressed as

$$u_s(t) = \tilde{\alpha}_s \exp\left[j(\omega_0 + \omega_s)\left(t - \frac{p_s}{c}\right)\right] \sum_{m=0}^{M-1} v_p\left(t - \frac{d_s}{c} - mT_r\right)$$
$$+ \eta(t), \tag{3}$$

where $\tilde{\alpha}_s$ represents the radar return amplitude and phase, p_s is the phase path length corresponding to the phase delay, c is the speed of light, ω_s is the Doppler frequency shift, d_s is the two-way slant (group) range, and $\eta(t)$ represents additive noise. Note that, while the distances from target s to the radar transmitter and receiver are different, this difference is negligible and only its effect in the phase is considered.

In the process of dechirpping, the received signal is mixed with a delayed version of the transmitted signal, i.e.,

$$w(t) = u_s(t)u^*(t - T_0) \tag{4}$$

where superscript * denotes complex conjugate, and delay T_0 specifies the minimum delay or start range of the dwell illumination region (DIR). Passing $w(t)$ through a low pass filter (LPF), which eliminates ω_0 and $2\omega_0$ components and only retains the baseband component, results in the dechirped signal, $q(t)$, given by

$$q(t) = \alpha_s \exp(j\omega_s t)\sum_{m=0}^{M-1}\exp\left[-j(2\pi B f_r)\left(\frac{d_s}{c} - T_0\right)(t - mT_r)\right]$$
$$+ \xi(t), \tag{5}$$

where the constant phase and amplitude terms are lumped into α_s and where $\xi(t)$ is the low pass filtered noise.

Let $t' = t - mT_r$. The waveform is sampled at time intervals $t' = nT_s$, giving the discrete signal $q[m,n] = q_m(nT_s)$ as

$$q[m,n] = \alpha_s \exp(j\omega_s mT_r)\exp\left\{j\left[\omega_s - 2\pi B f_r\left(\frac{d_s}{c} - T_0\right)\right]nT_s\right\}$$
$$+ \xi_{m,n}, \tag{6}$$

which is the product of two complex sinusoids in pulse index m and sample index n, combined with the additive noise $\xi_{m,n}$. The phase changes over n within one pulse provide

5

slant range information while the phase changes over m from pulse to pulse give Doppler information.

A two-dimensional (2-D) discrete Fourier transform (DFT) of $q[m, n]$ over the two variables m and n gives a complex range-Doppler surface, $Q[m', n']$. The N-point DFT over n within one pulse gives the slant range distribution indexed by n', whereas the M-point DFT over m across waveforms gives the Doppler frequency distribution indexed by m'. The slant range bin width of $Q[m', n']$ is equal to $\Delta d = c/(2B)$, whereas the Doppler bin width is equal to $\Delta \omega = 2\pi/T_c = 2\pi/(MT_r)$. The maximum unambiguous Doppler frequency is $f_{\max} = 1/(2T_r)$.

To reduce slant range and Doppler sidelobes in $Q[m', n']$, slant range window W_n is applied to $q[m, n]$ over n and Doppler window W_m is applied to $q[m, n]$ over m before performing the respective DFTs. With the slant range and Doppler windowing, the complex range-Doppler surface can be written as

$$
\begin{aligned}
Q[m', n'] = \alpha_s \mathrm{DFT}_M & \left[W_m \exp(j\omega_s m T_r) \right] \\
& \cdot \mathrm{DFT}_N \left[W_n \exp\left\{ j \left[\omega_s - 2\pi B f_r \left(\frac{d_s}{c} - T_0 \right) \right] n T_s \right\} \right] \\
& + \xi_{m', n'},
\end{aligned}
\tag{7}
$$

where $\xi_{m', n'}$ is additive noise in the complex range-Doppler domain.

III. Dual-Radar Operation

Now we consider a concurrent operation of two radars which are widely separated. Each radar transmits its own LFM waveform with the same WRF. The two radars are assumed to have carrier frequency alignment and the difference between their ionospheric propagation conditions is not considered. We use the following prototype waveforms of the two radars (the subscripts 1 and 2 represent radars A and B, respectively)

$$
v_{p,1}(t) = v_p(t) = \begin{cases} \exp(j\pi B f_r t^2), & 0 \le t < T_r \\ 0, & \text{otherwise} \end{cases}
\tag{8}
$$

and

$$
v_{p,2}(t) = v_p^*(t) = \begin{cases} \exp(-j\pi B f_r t^2), & 0 \le t < T_r \\ 0, & \text{otherwise.} \end{cases}
\tag{9}
$$

6

Then, the transmitted radar signals become

$$u_i(t) = \alpha_{0,i} \exp(j\omega_0 t) \sum_{m=0}^{M-1} v_{p,i}(t - mT_r), \quad i = 1, 2. \tag{10}$$

The received signal from a target s at radar k $(k = 1, 2)$ corresponding to the signal transmitted from both radar transmitters is expressed as

$$u_{s,k}(t) = \sum_{i=1}^{2} \tilde{\alpha}_{s,i,k} \exp\left[j(\omega_0 + \omega_{s,i,k}) \left(t - \frac{p_{s,i,k}}{c} \right) \right]$$
$$\cdot \sum_{m=0}^{M-1} v_{p,i} \left(t - \frac{d_{s,i,k}}{c} - mT_r \right) + \eta_k(t), \tag{11}$$

where $\tilde{\alpha}_{s,i,k}$, $p_{s,i,k}$, and $d_{s,i,k}$ represent the respective magnitude and phase, phase path delay, and two-way slant range for target s with signal transmitted from radar i and received by radar k, and $\omega_{s,i,k}$ is the Doppler frequency shift corresponding to transmit radar i and receive radar k. In addition, $\eta_k(t)$ denotes the additive noise.

Without loss of generality, consider the receive signal at radar A, i.e., $k = 1$. Then, the received signal can be expressed in the following three terms

$$u_{s,1}(t) = u_{s,1,1}(t) + u_{s,2,1}(t) + \eta_1(t), \tag{12}$$

where the first two terms respectively represent the contributions of radar A and radar B. The received signal is then processed using reception modes matched to both radar A and radar B.

At the reception mode matched to radar A, the following equation is used to dechirp the signal,

$$w_1(t) = u_{s,1}(t)u_1^*(t - T_0) = u_{s,1,1}(t)u_1^*(t - T_0)$$
$$+ u_{s,2,1}(t)u_1^*(t - T_0) + \eta_1(t)u_1^*(t - T_0). \tag{13}$$

The first term of the right-hand side is the auto-correlated term of radar A and is identical to (4) corresponding to the single-radar mode. Therefore, the result of the LPF output, using the new notations defined for the dual-radar scenario, is expressed as

$$q_{1,1}(t) = \alpha_{s,1,1} \exp(j\omega_{s,1,1}t)$$
$$\cdot \sum_{m=0}^{M-1} \exp\left[-j2\pi B f_r \left(\frac{d_{s,1,1}}{c} - T_0 \right) t' \right]. \tag{14}$$

7

where $t' = t - mT_r$. The second term is the cross-radar interference term, and its LPF output is expressed as

$$
\begin{aligned}
q_{2,1}(t) &= u_{s,2,1}(t)u_1^*(t - T_0) \\
&= \tilde{\alpha}_{s,2,1} \exp\left[j(\omega_0 + \omega_{s,2,1})\left(t - \frac{p_{s,2,1}}{c}\right)\right] \\
&\quad \cdot \sum_{m=0}^{M-1} v_{p,2}\left(t' - \frac{d_{s,2,1}}{c}\right) \\
&\quad \cdot \alpha_{0,2}^* \exp(-j\omega_0 t)\sum_{m=0}^{M-1} v_{p,1}^*(t' - T_0) \\
&= \tilde{\alpha}_{s,2,1}\alpha_{0,2}^* \exp\left[-j\omega_0\frac{\phi_{s,2,1}}{c} + j\omega_{s,2,1}\left(t - \frac{p_{s,2,1}}{c}\right)\right] \\
&\quad \cdot \sum_{m=0}^{M-1} \exp\left\{-j\pi B f_r\left[\left(t' - \frac{d_{s,2,1}}{c}\right)^2 + (t' - T_0)^2\right]\right\} \\
&= \alpha_{s,2,1}\exp(j\omega_{s,2,1}t) \\
&\quad \cdot \sum_{m=0}^{M-1} \exp\left\{-j2\pi B f_r\left[(t')^2 - \left(\frac{d_{s,2,1}}{c} + T_0\right)t'\right]\right\},
\end{aligned}
\tag{15}
$$

where $\alpha_{s,2,1}$ includes the constant phase and amplitudes terms. Similar to the single-radar case, we sample the signal $q_{1,1}(t)$ and $q_{1,2}(t)$ at $t' = nT_s$, and the results are denoted as $q_{1,1}[m,n]$ and $q_{2,1}[m,n]$, respectively. Then, the 2-D DFT results of $q_{1,1}[m,n]$ and $q_{2,1}[m,n]$ are expressed, respectively, as

$$
\begin{aligned}
Q_{1,1}[m',n'] &= \alpha_{s,1,1}\mathrm{DFT}_M[W_m \exp(j\omega_{s,1,1}mT_r)] \\
&\quad \cdot \mathrm{DFT}_N\left\{W_n \exp\left[j\left(\omega_{s,1,1} - 2\pi B f_r\left(\frac{d_{s,1,1}}{c} - T_0\right)\right)nT_s\right]\right\}
\end{aligned}
\tag{16}
$$

and

$$
\begin{aligned}
Q_{2,1}[m',n'] &= \alpha_{s,2,1}\mathrm{DFT}_M[W_m \exp(j\omega_{s,2,1}mT_r)] \\
&\quad \cdot \mathrm{DFT}_N\left\{W_n \exp\left[-j2\pi B f_r(nT_s)^2 \right.\right. \\
&\qquad \left.\left. +j\left(\omega_{s,2,1} + 2\pi B f_r\left(\frac{d_{s,2,1}}{c} + T_0\right)\right)nT_s\right]\right\}.
\end{aligned}
\tag{17}
$$

Both components, in addition to the noise, contribute to the complex range-Doppler surface. The signal transmitted from radar A is the auto-radar response at the radar A

8

reception mode and is localized in both range and Doppler domains. On the other hand, the cross-radar interference only maintains the Doppler information with respect to slow time T_r. In this case, its range-domain response is a chirp signal with respect to the fast time T_s and the chirp rate is twice that of the transmitted signal. That is, the cross-radar interference keeps the Doppler information whereas the range profile information is lost.

Combining $Q_{1,1}[m', n']$ and $Q_{2,1}[m', n']$ as well as noise results in

$$Q_1[m', n'] = Q_{1,1}[m', n'] + Q_{1,1}[m', n'] + \xi_1[m', n']. \tag{18}$$

In addition to the ordinary operation mode matched to radar A's waveform, radar A can also process the received data using radar B's waveform for dechirping. Due to symmetry, the complex range-Doppler surfaces corresponding to the Radar B reception mode can be readily written as

$$\tilde{Q}_1[m', n'] = \tilde{Q}_{1,1}[m', n'] + \tilde{Q}_{2,1}[m', n'] + \tilde{\xi}_1[m', n'], \tag{19}$$

where

$$\tilde{Q}_{1,1}[m', n'] = \alpha_{s,1,1} \mathrm{DFT}_M[W_m \exp(j\omega_{s,1,1} m T_r)]$$
$$\cdot \mathrm{DFT}_N \left\{ W_n \exp \left[j2\pi B f_r (nT_s)^2 \right. \right.$$
$$\left. \left. + j \left(\omega_{s,1,1} - 2\pi B f_r \left(\frac{d_{s,1,1}}{c} + T_0 \right) \right) nT_s \right] \right\}, \tag{20}$$

and

$$\tilde{Q}_{2,1}[m', n'] = \alpha_{s,2,1} \mathrm{DFT}_M[W_m \exp(j\omega_{s,2,1} m T_r)]$$
$$\cdot \mathrm{DFT}_N \left\{ W_n \exp \left[j \left(\omega_{s,2,1} + 2\pi B f_r \left(\frac{d_{s,2,1}}{c} - T_0 \right) \right) nT_s \right] \right\}. \tag{21}$$

In this case, the signal transmitted from radar B is the auto-radar response and is localized in both range and Doppler domains. The signal transmitted from radar A becomes cross-radar interference which is localized only in the Doppler domain.

IV. Cross-Radar Interference Cancelation

As demonstrated in the previous discussion, when both radars are operational, a target will return both radar signals, resulting in a received signal with the desirable signal superimposed a cross-radar interference. In this section, we consider the cancelation of such interference.

9

A. Technical Challenges

The interference cancelation process resembles that in the multiuser CDMA communications where dispersive channels are involved [15]–[17]. In the underlying scenario, the chirp signal waveforms act as the spreading codes. However, there are significant differences between the problem at hand and the multiuser CDMA problems. These differences, which prevent the multiuser detection methods to be directly applicable to cross-radar interference cancelation, are summarized below.

(1) The primary purpose of a CDMA communication system is to deliver information over a multiuser channel. The system is usually designed such that the channels are quasi-stationary, i.e., the channel variation over a certain period is negligible. Therefore, interference cancelation as well as the information detection can be performed within each symbol or over the coherent time of the channels. Usually, processing of a longer period improves the performance, at the expense of higher computational costs. Channel coding is also commonly used to provide additional protection against channel distortion. In the OTHR problems, the information of interest is included in the characteristics of the time-varying channels (clutter and target), whereas the transmit waveform itself does not bear any information. As a result, problems may arise in suppressing cross-radar interference in both single- or multi-waveform period approaches. Processing interference cancelation individually for each waveform may differently alter the phase information and result in wrong Doppler information or Doppler aliasing. On the other hand, joint processing over multiple waveforms requires separate considerations of the clutter and target echo signals because their phase variations due to the Doppler effect differ from each other.

(2) In CDMA multiuser detection problems, the aim is to sufficiently reduce the multiuser interference for correct information detection. In the underlying OTHR applications, the signal-to-clutter ratio is very low and a moderate level of interference cancelation is not necessarily sufficient to improve the visibility of the echo signals from moving targets.

(3) In CDMA systems, there is redundancy in the signal bandwidth for each user due to spectrum spreading, and the channel order is often limited. Therefore, orthogonal or quasi-orthogonal waveform design for different users is possible. OTHR radar systems, on the other hand, are design to fully utilize the time-frequency resource to obtain the

information in the joint range-Doppler domain, and the target may appear in any range cell. As a result, orthogonal waveform design over the entire range cells is impractical. As we discussed in Section I, LFM waveforms are often preferred in OTHR systems. Thus, the reduction of the auto- and cross-correlation between the signals for different users and corresponding to different time lags is limited.

The first two issues can be resolved by converting the slow time into the Doppler frequency domain. In doing so, weak signals corresponding to moving targets are separated from strong stationary clutter, which is typically concentrated in low frequencies. In the frequency domain, as we discussed above, the time-varying channels corresponding to moving targets become stationary Doppler. In addition, in the Doppler frequency bins where a moving target is positioned, the target signals often have a higher power than that of clutter, making the target detection possible.

For the third issue, we take advantage of the sparseness of the target signals and consider iterative interference cancelation in this chapter. The detailed techniques are presented in the next subsection.

B. Interference Cancelation

For convenience of representation and matrix operation, we rewrite (16) as

$$
\begin{aligned}
Q_{1,1}[m', n'] \\
= \alpha_{s,1,1} \left(\mathbf{f}_{m'} \mathbf{W}_M \mathbf{F}_M^* \epsilon_{l_{a,1,1}} \right) \cdot \left(\mathbf{f}_{n'} \mathbf{W}_N \cdot \mathrm{diag}(\mathbf{v}_1^*) \cdot \mathbf{V}_1^* e_{l_{b,1,1}} \right) \\
= \alpha_{s,1,1} \left(\mathbf{f}_{m'} \mathbf{W}_M \mathbf{F}_M^* \epsilon_{l_{a,1,1}} \right) \cdot \left(\mathbf{f}_{n'} \cdot \mathrm{diag}(\mathbf{v}_1^*) \cdot \mathbf{W}_N \mathbf{V}_1^* e_{l_{b,1,1}} \right),
\end{aligned}
\tag{22}
$$

where $\mathbf{F}_M$ (or $\mathbf{F}_N$) denotes the $M \times M$ (or $N \times N$) Fourier transform matrix, $\mathbf{f}_{m'}$ (or $\mathbf{f}_{n'}$) denotes the m'th (or n'th) row of $\mathbf{F}_M$ (or $\mathbf{F}_N$), $\mathbf{W}_M$ (or $\mathbf{W}_N$) is an $M \times M$ (or $N \times N$) diagonal matrix with proper window coefficients as its diagonal elements, $\mathrm{diag}(\mathbf{v}_1)$ is a diagonal matrix with

$$
\mathbf{v}_1 = [v_{p,i}[0], \ v_{p,i}[1], \cdots, \ v_{p,i}[N-1]]
\tag{23}
$$

as its diagonal elements, where $v_{p,i}[n] = v_{p,i}(nT_s)$. In addition,

$$\mathbf{V}_i = \begin{bmatrix} v_{p,i}[0] & v_{p,i}[1] & \cdots & v_{p,i}[N-2] & v_{p,i}[N-1] \\ v_{p,i}[N-1] & v_{p,i}[0] & \cdots & v_{p,i}[N-3] & v_{p,i}[N-2] \\ \cdots & \cdots & \cdots & \cdots & \cdots \\ v_{p,i}[1] & v_{p,i}[2] & \cdots & v_{p,i}[N-1] & v_{p,i}[0] \end{bmatrix},$$

$$i = 1, 2, \tag{24}$$

and ϵ_l and $\mathbf{e}_l$ are, respectively, $M \times 1$ and $2N \times 1$ vectors with all zeros except a unit value at the lth element. For a target whose Doppler radian frequency with respect to radar A is $\omega_{s,1,1}$ and its range is $d_{s,1,1}$, we have

$$l_{a,1,1} = \frac{M}{2\pi}\omega_{s,1,1}T_r + 1, \tag{25}$$

and

$$l_{b,1,1} = Nf_r\left(\frac{d_{s,1,1}}{c} - T_0\right) - \frac{N\omega_{s,1,1}}{2\pi B} + 1. \tag{26}$$

Typically, the contribution of $\omega_{s,1,1}$ to the short-time frequency shift is negligible, and $l_{b,1,1}$ is primarily determined by the range $d_{s,1,1}$ relative to the reference time T_0.

Stacking $Q_{1,1}[m', n']$ for the N range cells $n' = 0, ..., N-1$, we obtain

$$\mathbf{q}_{1,1}[m'] = \begin{bmatrix} Q_{1,1}[m', 0] + Q_{2,1}[m', 0] \\ \cdots \\ Q_{1,1}[m', N-1] + Q_{2,1}[m', N-1] \end{bmatrix}$$

$$= \alpha_{s,1,1}\left(\mathbf{f}_{m'}\mathbf{W}_M\mathbf{F}_M^*\epsilon_{l_{a,1,1}}\right) \cdot \left(\mathbf{F}_N \cdot \text{diag}(\mathbf{v}_1^*) \cdot \mathbf{W}_N\mathbf{V}_1\mathbf{e}_{l_{b,1,1}}\right). \tag{27}$$

Note that, in practice, the received signal is often oversampled (i.e., $N > BT_r$) to achieve an enhanced range resolution. In this case, the N frequency bins of $\mathbf{F}_N$ are chosen to span the signal bandwidth $[-B/2, B/2]$, rather than the entire viewable bandwidth $[-1/2T_s, 1/2T_s]$. Thus, we can rewrite the above expression as

$$\mathbf{q}_{1,1}[m'] = \alpha_{s,1,1}\left(\mathbf{f}_{m'}\mathbf{W}_M\mathbf{F}_M^*\epsilon_{l_{a,1,1}}\right) \cdot \left(\mathbf{V}_1^H\mathbf{W}_N\mathbf{V}_1\mathbf{e}_{l_{b,1,1}}\right). \tag{28}$$

Note that, while we used the same notation $\mathbf{q}_{1,1}[m']$ in both (27) and (28), the results in these two equations differ in their phase. Nevertheless, for simplicity, no distinctions are made between the two variables, as only their respective amplitudes affect target detection.

In general, $l_{a,1,1}$ and $l_{b,1,1}$ do not necessarily take integer values, resulting in smeared representations over multiple neighboring range bins. Furthermore, in practice, clutter arises due to a collection of reflection and scattering from earth or ocean surfaces. When multiple targets exist, the reflected signal may arrive through a single or multiple paths. Therefore, we generalize the two vectors $\epsilon_{l_{a,1,1}}$ and $\mathbf{e}_{l_{b,1,1}}$ into arbitrary $M \times 1$ vector $\mathbf{h}_{a,1,1}$ and $N \times 1$ vector $\mathbf{h}_{b,1,1}$, respectively, to represent the collective contributions from targets and clutters. Similarly, we denote $\mathbf{h}_{a,2,1}$ and $\mathbf{h}_{b,2,1}$ as the contribution corresponding to signal transmitted from radar B. Notice that the clutter energy is highly localized in very low Doppler frequencies and cannot be resolved in the range domain, whereas the target energy typically positions away from the zero Doppler frequencies and is localized in range.

Rewriting (28) by using $\mathbf{h}_{a,1,1}$ and $\mathbf{h}_{b,1,1}$, and deriving $\mathbf{q}_{2,1}[m']$, $\tilde{\mathbf{q}}_{1,2}[m']$, and $\tilde{\mathbf{q}}_{2,2}[m']$ corresponding to (17), (20), and (21), respectively, we have

$$\mathbf{q}_{1,1}[m'] = \alpha_{s,1,1} \left(\mathbf{f}_m \mathbf{W}_M \mathbf{F}_M^* \mathbf{h}_{a,1,1} \right) \cdot \left(\mathbf{V}_1^H \mathbf{W}_N \mathbf{V}_1 \mathbf{h}_{b,1,1} \right), \tag{29}$$

$$\mathbf{q}_{2,1}[m'] = \alpha_{s,2,1} \left(\mathbf{f}_m \mathbf{W}_M \mathbf{F}_M^* \mathbf{h}_{a,2,1} \right) \cdot \left(\mathbf{V}_1^H \mathbf{W}_N \mathbf{V}_2 \mathbf{h}_{b,2,1} \right), \tag{30}$$

$$\tilde{\mathbf{q}}_{1,1}[m'] = \alpha_{s,1,1} \left(\mathbf{f}_m \mathbf{W}_M \mathbf{F}_M^* \mathbf{h}_{a,1,1} \right) \cdot \left(\mathbf{V}_2^H \mathbf{W}_N \mathbf{V}_1 \mathbf{h}_{b,1,1} \right), \tag{31}$$

$$\tilde{\mathbf{q}}_{2,1}[m'] = \alpha_{s,2,1} \left(\mathbf{f}_m \mathbf{W}_M \mathbf{F}_M^* \mathbf{e}_{l_{a,2,1}} \right) \cdot \left(\mathbf{V}_2^H \mathbf{W}_N \mathbf{V}_2 \mathbf{h}_{b,2,1} \right). \tag{32}$$

Therefore, at the m'th Doppler frequency bin, these vectors can be combined to form a $2N \times 1$ vector, expressed as

$$\begin{aligned}
\mathbf{q}_1[m'] &= \begin{bmatrix} \mathbf{q}_{1,1}[m'] + \mathbf{q}_{2,1}[m'] \\ \tilde{\mathbf{q}}_{1,1}[m'] + \tilde{\mathbf{q}}_{2,1}[m'] \end{bmatrix} \\
&= \begin{bmatrix} \mathbf{V}_1^H \\ \mathbf{V}_2^H \end{bmatrix} \mathbf{W}_N \begin{bmatrix} \mathbf{V}_1 & \mathbf{V}_2 \end{bmatrix} \begin{bmatrix} \mathbf{h}_{b,1,1} \alpha_{s,1,1} \mathbf{f}_m \mathbf{W}_M \bar{\mathbf{F}}_M \mathbf{h}_{a,1,1} \\ \mathbf{h}_{b,2,1} \alpha_{s,2,1} \mathbf{f}_m \mathbf{W}_M \bar{\mathbf{F}}_M \mathbf{h}_{a,2,1} \end{bmatrix} \\
&\stackrel{\text{def}}{=} \begin{bmatrix} \mathbf{V}_1^H \\ \mathbf{V}_2^H \end{bmatrix} \mathbf{W}_N \begin{bmatrix} \mathbf{V}_1 & \mathbf{V}_2 \end{bmatrix} \begin{bmatrix} \tilde{\mathbf{h}}_{b,1,1}[m'] \\ \tilde{\mathbf{h}}_{b,2,1}[m'] \end{bmatrix}.
\end{aligned} \tag{33}$$

The upper N elements of $\mathbf{q}_1[m']$ represents the auto-radar responses in the range-Doppler domain, whereas the lower N elements denotes the cross-radar interference. In the above equation, $\alpha_{s,1,1} \mathbf{f}_m \mathbf{W}_M \mathbf{F}_M^* \mathbf{h}_{a,1,1}$ and $\alpha_{s,2,1} \mathbf{f}_m \mathbf{W}_M \mathbf{F}_M^* \mathbf{h}_{a,2,1}$ are two complex scalars representing the overall strength in Doppler frequency bin m'. They are multiplied by vectors

$\mathbf{h}_{b,l,1}$ and $\mathbf{h}_{b,2,1}$, respectively, to form a vector $\tilde{\mathbf{h}}_{b,1} = [\tilde{\mathbf{h}}_{b,l,1}^T[m'], \tilde{\mathbf{h}}_{b,2,1}^T[m']]^T$ of $2N$ unknown (dependent) elements depicting the contribution from targets and scatterers in the N range cells, corresponding to the signals transmitted from radar A (auto-radar reception mode) and radar B (cross-radar reception mode). Our goal in this section is to eliminate the cross-radar interference without compromising the auto-radar responses. The return signals due to radar A and radar B cannot be directly separated because matrix $\mathbf{V} = [\mathbf{V}_1, \mathbf{V}_2]$ involved in the above expression is a wide matrix. In other words, although we have $2N$ observations ($\mathbf{q}_1[m']$ obtained using both radar A and radar B reception modes) and the aforementioned $2N$ unknowns, the problem cannot be directly solved as the observation vector is rank deficient.

Below, we employ iterative interference cancelation method to take advantage of the fact that the signals of interest which arise from moving targets are typically sparse in range. We first compute the $2N \times 2N$ matrix

$$\tilde{\mathbf{Q}}_1 = \mathbf{V}^H \mathbf{W}_N \mathbf{V} \mathbf{I}_{2N} = \mathbf{V}^H \mathbf{W}_N \mathbf{V}, \tag{34}$$

i.e., a collection of the response of $\mathbf{q}_1$ corresponding to all $2N$ possible impulse values of $\tilde{\mathbf{h}}_{b,1,1}$ or $\tilde{\mathbf{h}}_{b,2,1}$ being $\mathbf{e}_i, i = 1, \cdots, 2N$, where $\mathbf{I}_{2N}$ is the $2N \times 2N$ identity matrix. Note that the above result is independent of m'. Also, we compute $\mathbf{q}_1[m']$ based on (33) for $m' = 0, \cdots, M - 1$.

For each frequency bin index m', the following steps are performed in each iteration. The concept behind the iterative cross-radar interference cancellation is similar to the CLEAN techniques [18]–[20].

(1) Find the maximum value $q_{1,\max}^{(l)}[m'] = [\mathbf{q}_1^{(l)}[m']]_{n'^*}$, where n'^* is the position of the maximum value. We use $^{(l)}$ to identify the lth iteration and define $\mathbf{q}_1^{(1)}[m'] \overset{\text{def}}{=} \mathbf{q}_1[m']$. Thus, it can be considered that there is a point source at the n'^*th range cell.

(2) Compute the cross-radar interference-free Doppler-range response corresponding to the point source at the n'^*th range cell as

$$\hat{\mathbf{q}}_1^{(l)}[m'] = \begin{cases} \tilde{\mathbf{q}}_1^{(A)}[n'^*] \cdot \tilde{\mathbf{q}}_1^H[n'^*] \cdot \mathbf{q}_1[m']/|\tilde{\mathbf{q}}_1[n'^*]|^2, \\ \qquad\qquad 0 \leq n'^* \leq N - 1, \\ \tilde{\mathbf{q}}_1^{(B)}[n'^*] \cdot \tilde{\mathbf{q}}_1^H[n'^*] \cdot \mathbf{q}_1[m']/|\tilde{\mathbf{q}}_1[n'^*]|^2, \\ \qquad\qquad N \leq n'^* \leq 2N - 1, \end{cases} \tag{35}$$

14

where

$$\tilde{\mathbf{q}}_1[n'^*] = \tilde{\mathbf{Q}}_1 \mathbf{e}_{n'^*} = \mathbf{V}^H \mathbf{W}_N \mathbf{V} \mathbf{e}_{n'^*} \tag{36}$$

is the n'^*th column of $\tilde{\mathbf{Q}}_1$, $\tilde{\mathbf{q}}_1^{(A)}[n'^*]$ (or $\tilde{\mathbf{q}}_1^{(B)}[n'^*]$) equals to $\mathbf{q}_1[n'^*]$ with the second N elements (or the first N element) set to zero.

(3) Remove the cross-radar interference-contaminated Doppler-range response corresponding to the point source at the n'^*th range cell from the residual response by updating the residual response as

$$\mathbf{q}_1^{(l+1)}[m'] = \mathbf{q}_1^{(l)}[m'] - \tilde{\mathbf{q}}_1[n'^*]\tilde{\mathbf{q}}_1^H[n'^*]\mathbf{q}_1^{(l)}[m']/|\tilde{\mathbf{q}}_1[n'^*]|^2. \tag{37}$$

The number of iterations can be either prefixed or adaptively determined by the level of the peak residual energy. The signal waveform after L iterations of cross-radar interference mitigation is obtained as $\mathbf{q}_1^{(L+1)}[m'] + \sum_{l=1}^{L} \hat{\mathbf{q}}_1^{(l)}[m']$.

V. Performance Analysis

To analysis the performance of the dual-radar system as well as the effectiveness of cross-radar interference reduction, we consider a frequency bin m' at which a point target is positioned corresponding to the waveform of radar A and thus generate cross-radar interference when it is received to match the waveform of radar B. Due to the symmetry, only the performance at radar A is considered. We assume that a target is located at the kth range cell and its return signal due to radar A's transmitted waveforms falls at the m'th Doppler frequency bin.

We start with (33) and express the channel model as

$$\tilde{\mathbf{h}}_{b,1} = \alpha\, \mathbf{e}_k + \mathbf{z}_1, \tag{38}$$

where $\alpha \mathbf{e}_k$ represents a localized target in the kth range cell, and $\mathbf{z}_1 = [\mathbf{z}_{1,1}^T, \mathbf{z}_{2,1}^T]^T$ is the external noise vector. Note that index m' is omitted in this section for the simplicity of expression, because only frequency bin m' is considered in this section. The internal thermal noise is typically of much less impact compared to clutter and its contribution is neglected in the analysis. We are most interested in the Doppler frequencies that are not very low, thus it is justified to assume that the elements of $\mathbf{z}_1$ are independent and

15

identically distributed (i.i.d.) complex Gaussian random variables with zero mean and joint variance matrix $\sigma_z^2 \mathbf{I}_{2N}$. Note that σ_z^2 depends on Doppler bin index m'.

Without loss of generality, we assume that $\mathbf{v}_i$ is normalized to have a unit norm, i.e., $|\mathbf{v}_i|^2 = \mathbf{v}_i^H \mathbf{v}_i = 1$ for $i = 1, 2$. As each elements of $\mathbf{v}_i$ is of constant magnitude, we have $[\mathbf{v}_i]_k^*[\mathbf{v}_i]_k = 1/N$. For the convenience of understanding to the performance, some numerical results are provided for the radar system setting illustrated in Table 1. From these parameters, the number of sweeps is $M = T_c f_r = 256$ and the number of range cells is $N = f_s/f_r = 400$.

TABLE I

RADAR SYSTEM PARAMETERS

Parameter	Value	(Unit)
Carrier frequency (f)	13.957	MHz
Signal bandwidth (B)	8	KHz
Waveform repetition frequency (f_r)	50	Hz
Sampling frequency (f_s)	20	KHz
Coherent integration time (T_c)	5.12	sec

A. Single Radar Operation

As the baseline, we first consider the situation where only a single radar (i.e., radar A) is operated. In this case, the received signal is expressed as

$$\tilde{\mathbf{h}}_{b,1}^{(A)} = \alpha \, \mathbf{e}_k^{(A)} + \mathbf{z}_{1,1}, \tag{39}$$

where $\tilde{\mathbf{h}}_{b,1}^{(A)}$ denotes an $N \times 1$ vector consisting of the first N elements of $\tilde{\mathbf{h}}_{b,1}$ and, similarly, $\mathbf{e}_k^{(A)}$ denotes an $N \times 1$ vector consisting of the first N elements of $\mathbf{e}_k$. In this case, we obtain

$$\mathbf{q}_1 = \mathbf{q}_{1,1} = \mathbf{V}_1^H \mathbf{W}_N \mathbf{V}_1 \tilde{\mathbf{h}}_{b,1}^{(A)} = \mathbf{V}_1^H \mathbf{W}_N \mathbf{V}_1 [\alpha \, \mathbf{e}_k^{(A)} + \mathbf{z}_{1,1}]. \tag{40}$$

For range cells that are separated from the kth range cell by more than the mainlobe width, the effect of target signal is small, particularly when a proper window is used. Thus, we only consider the signal component at the lth range cell which is expressed as

$$[\mathbf{q}_1^{(s)}]_l = \alpha [\mathbf{e}_k^{(A)}]^T \mathbf{V}_1^H \mathbf{W}_N \mathbf{V}_1 \mathbf{e}_k^{(A)} = \alpha A_W, \tag{41}$$

16

where $A_W = (1/N) \sum_{i=1}^{N} \text{diag}[\mathbf{W}_N]$ is the average value of the window coefficients of $\mathbf{W}_N$. The noise component in (40) is

$$\mathbf{q}_1^{(z)} = \mathbf{V}_1^H \mathbf{W}_N \mathbf{V}_1 \mathbf{z}_{1,1}, \tag{42}$$

which has a zero mean and covariance matrix

$$\begin{aligned}
\text{var}[\mathbf{q}_1^{(z)}] &= E\left[\mathbf{V}_1^H \mathbf{W}_N \mathbf{V}_1 \mathbf{z}_{1,1} \mathbf{z}_{1,1}^H \mathbf{V}_1^H \mathbf{W}_N \mathbf{V}_1\right] \\
&= \sigma_z^2 \left[\mathbf{V}_1^H \mathbf{W}_N \mathbf{V}_1 \mathbf{V}_1^H \mathbf{W}_N \mathbf{V}_1\right],
\end{aligned} \tag{43}$$

where $E[\cdot]$ denotes statistical expectation. The n'th diagonal elements of the above covariance matrix, denoted as $[\text{var}[\mathbf{q}_1^{(z)}]]_{n',n'} = \sigma_z^2 \left[\mathbf{V}_1^H \mathbf{W}_N \mathbf{V}_1 \mathbf{V}_1^H \mathbf{W}_N \mathbf{V}_1\right]_{n',n'} = \gamma \sigma_z^2$, represents the noise auto-variance at each range cell whose values depends on the sampling rate, signal bandwidth, and the selected window.

Therefore, the signal-to-noise ratio (SNR), evaluated at the range-Doppler result $\mathbf{q}_1$, is obtained as

$$\text{SNR}_{\text{single}} = \frac{|\alpha|^2 A_W^2}{\gamma \sigma_z^2}. \tag{44}$$

For the parameters listed in Table 1, the auto-variance $\gamma \sigma_z^2$ is about $2.5 \sigma_z^2$ (without window) and $0.94 \sigma_z^2$ (with Hanning window), yielding SNR values of $(\text{SNR}_0 - 4)$ dB or $(\text{SNR}_0 - 5.7)$ dB, respectively, without and with the window, where $\text{SNR}_0 = 10 \log_{10}(|\alpha|^2/\sigma_z^2)$ dB.

B. Dual-Radar Operation

Now we consider the situation where two radars concurrently transmit signals. For simplicity and without loss of generality, we assume that only the signal transmitted from radar A generate target return at the m'th Doppler frequency bin. Due to the linearity of radar system response, it is straightforward to extend the results to multiple targets or the situation where the return signals arisen from both radar A and radar B have the same Doppler frequency.

In the assumed situation, we have

$$\mathbf{q}_1 = \mathbf{V}^H \mathbf{W}_N \mathbf{V} \tilde{\mathbf{h}}_{b,1} = \mathbf{V}^H \mathbf{W}_N \mathbf{V}[\alpha \, \mathbf{e}_k + \mathbf{z}_1]. \tag{45}$$

It is obvious that the signal component $[\mathbf{q}_1^{(s)}]_l$ remains the same as (41). The noise vector

$$\mathbf{q}_1^{(z)} = \mathbf{V}^H \mathbf{W}_N \mathbf{V} \mathbf{z}_1 = \mathbf{V}^H \mathbf{W}_N \mathbf{V}_1 \mathbf{z}_{1,1} + \mathbf{V}^H \mathbf{W}_N \mathbf{V}_2 \mathbf{z}_{2,1} \tag{46}$$

has a zero mean, and its covariance matrix is obtained as

$$\begin{aligned}
\text{var}[\mathbf{q}_1^{(z)}] &= E\left[\mathbf{V}^H \mathbf{W}_N \mathbf{V} \mathbf{z}_1 \mathbf{z}_1^H \mathbf{V}^H \mathbf{W}_N \mathbf{V}\right] \\
&\quad + \sigma_z^2 \left[\mathbf{V}^H \mathbf{W}_N (\mathbf{V}_1 \mathbf{V}_1^H + \mathbf{V}_2 \mathbf{V}_2^H) \mathbf{W}_N \mathbf{V}\right] \\
&= 2\sigma_z^2 \left[\mathbf{V}^H \mathbf{W}_N \mathbf{V}_1 \mathbf{V}_1^H \mathbf{W}_N \mathbf{V}\right].
\end{aligned} \tag{47}$$

That is, a 3 dB clutter enhancement is introduced because of the dual radar operations. As a result, the SNR becomes

$$\text{SNR}_{\text{dual}} = \frac{|\alpha|^2 A_W^2}{2\gamma \sigma_z^2}. \tag{48}$$

In addition, the concurrent use of two radars causes cross-radar interference. When radar A processes the received signal with radar B mode, the cross-radar interference becomes

$$\mathbf{q}_1^{(i)} = \mathbf{L}^{(B)} \mathbf{q}_1^{(s)} = \alpha\, \mathbf{V}_2^H \mathbf{W}_N \mathbf{V} \mathbf{e}_k = \alpha\, \mathbf{V}_2^H \mathbf{W}_N \mathbf{V}_1 \mathbf{e}_k^{(A)}, \tag{49}$$

where $\mathbf{L}^{(B)} = [\mathbf{O}_N, \mathbf{I}_N]$ with $\mathbf{O}_N$ denoting the $N \times N$ zero matrix. As we discussed earlier, the cross-radar interference spans the entire range cells, and its power averaged over the N range cells is obtained as

$$\frac{1}{N}[\mathbf{q}_1^{(i)}]^H \mathbf{q}_1^{(i)} = \frac{|\alpha|^2}{N} \mathbf{e}_k^{(A)} \mathbf{V}_1^H \mathbf{W}_N \mathbf{V}_2 \mathbf{V}_2^H \mathbf{W}_N \mathbf{V}_1 \mathbf{e}_k^{(A)} = \frac{\gamma |\alpha|^2}{N}. \tag{50}$$

Therefore, the resulting average signal-to-interference ratio (SIR) is

$$\text{SIR}_{\text{dual}} = \frac{N A_W^2}{\gamma}, \tag{51}$$

which, for the parameters given in Table 1, is about 22 dB without a window or 20.3 dB with the Hanning window.

C. Performance of Interference Cancelation

Consider one iteration of the interference cancelation process. We obtain the final result as the sum of two components, $\hat{\mathbf{q}}_1^{(1)}$ and $\mathbf{q}_1^{(2)}$, expressed as

$$
\begin{aligned}
\hat{\mathbf{q}}_1^{(1)} + \mathbf{q}_1^{(2)} &= \mathbf{q}_1 - \tilde{\mathbf{q}}_1[k] \cdot \tilde{\mathbf{q}}_1^H[k] \cdot \mathbf{q}_1 / |\tilde{\mathbf{q}}_1[k]|^2 \\
&\quad + \tilde{\mathbf{q}}_1^{(A)}[k] \cdot \tilde{\mathbf{q}}_1^H[k] \cdot \mathbf{q}_1 / |\tilde{\mathbf{q}}_1[k]|^2 \\
&= \mathbf{q}_1 - \tilde{\mathbf{q}}_1^{(B)}[k] \cdot \tilde{\mathbf{q}}_1^H[k] \cdot \mathbf{q}_1 / |\tilde{\mathbf{q}}_1[k]|^2.
\end{aligned}
\tag{52}
$$

Evidently, the interference cancelation process does not change the result corresponding to the radar A mode, thus the SNR in the auto-radar reception mode remains unchanged, i.e.,

$$
\mathrm{SNR}_{\mathrm{cancel}} = \frac{|\alpha|^2 A_W^2}{2\gamma\sigma_z^2}.
\tag{53}
$$

On the other hand, we can show that the cross-radar interference due to the target return is totally eliminated. At the cross-radar reception mode, we have

$$
\begin{aligned}
&\mathbf{L}^{(B)}[\hat{\mathbf{q}}_1^{(1)} + \mathbf{q}_1^{(2)}]^{(s)} \\
&= \mathbf{L}^{(B)}\mathbf{q}_1^{(s)} - \mathbf{L}^{(B)}\tilde{\mathbf{q}}_1^{(B)}[k] \cdot \tilde{\mathbf{q}}_1^H[k] \cdot \alpha \mathbf{V}^H \mathbf{W}_N \mathbf{V}\, \mathbf{e}_k / |\tilde{\mathbf{q}}_1[k]|^2 \\
&= \alpha \mathbf{V}_2^H \mathbf{W}_N \mathbf{V} \mathbf{e}_k - \frac{\alpha \mathbf{V}_2^H \mathbf{W}_N \mathbf{V} \mathbf{e}_k \mathbf{e}_k^H \mathbf{V}^H \mathbf{W}_N \mathbf{V} \mathbf{V}^H \mathbf{W}_N \mathbf{V} \mathbf{e}_k}{\mathbf{e}_k^H \mathbf{V}^H \mathbf{W}_N \mathbf{V} \mathbf{V}^H \mathbf{W}_N \mathbf{V} \mathbf{e}_k} \\
&= 0.
\end{aligned}
\tag{54}
$$

The residual undesired signal components after cross-radar interference cancelation are made up of the original noise and the residual error due to the erroneous estimation of $\mathbf{q}_1$ at the kth range cell. They are given by

$$
\begin{aligned}
&\mathbf{q}_{1,\mathrm{cancel}}^{(z)} \\
&= \mathbf{L}^{(B)}[\hat{\mathbf{q}}_1^{(1)} + \mathbf{q}_1^{(2)}]^{(z)} \\
&= \mathbf{L}^{(B)}\mathbf{q}_1^{(z)} - \mathbf{L}^{(B)}\tilde{\mathbf{q}}_1^{(B)}[k] \cdot \tilde{\mathbf{q}}_1^H[k] \cdot \mathbf{V}^H \mathbf{W}_N \mathbf{V} \mathbf{z}_1 / |\tilde{\mathbf{q}}_1[k]|^2 \\
&= \mathbf{L}^{(B)}\mathbf{V}^H \mathbf{W}_N \mathbf{V} \mathbf{z}_1 - \frac{\mathbf{V}_2^H \mathbf{W}_N \mathbf{V} \mathbf{e}_k \mathbf{e}_k^H \mathbf{V}^H \mathbf{W}_N \mathbf{V} \mathbf{V}^H \mathbf{W}_N \mathbf{V} \mathbf{z}_1}{\mathbf{e}_k^H \mathbf{V}^H \mathbf{W}_N \mathbf{V} \mathbf{V}^H \mathbf{W}_N \mathbf{V} \mathbf{e}_k} \\
&= \mathbf{L}^{(B)}\mathbf{V}^H \mathbf{W}_N \mathbf{V} \mathbf{z}_1 - \frac{1}{2\gamma}\mathbf{V}_2^H \mathbf{W}_N \mathbf{V} \mathbf{e}_k \mathbf{e}_k^H [\mathbf{V}^H \mathbf{W}_N \mathbf{V}]^2 \mathbf{z}_1,
\end{aligned}
\tag{55}
$$

where $\mathbf{A}^2 = \mathbf{AA}$. Consider the fact that the noise variance before the interference cancelation is the same for both radar reception modes and over all range cells. The operation in the second term of the above equation is a projection of random noise components to a structured vector of unit norm. The power of this term (i.e., the residual error) is much smaller than that of the first term at the right-hand side (i.e., the original noise). That is, the additional noise introduced by the cross-radar interference cancelation process is insignificant. For example, for the parameters provided in Table 1, the average power difference between these two terms is 17.6 dB, and the difference becomes about 19 dB when a Hanning window is applied.

In practice, there is no need to distinguish the two terms in the above equation. We can express the output signal-to-interference-plus-noise ratio (SINR) at the cross-radar reception mode as

$$\text{SINR}_{\text{cancel}} = \frac{|\alpha|^2 A_W^2}{\text{var}[\mathbf{q}_{1,\text{cancel}}^{(z)}]} \approx \frac{|\alpha|^2 A_W^2}{2\gamma\sigma_z^2}. \tag{56}$$

We point out that the actual level of residual error may be higher due to several reasons, primarily the incomplete cancelation of cross-range interference when the target return energy at the auto-radar reception mode is smeared or distributed in the range-Doppler domain.

VI. Simulation Results

We have conducted simulations using measured clutter data. A synthetic test target has been injected into the received time series to provide a reference for the assessment of the performance in target SNR depending on processing options. Key parameters of the radar system are shown in Table 1, where the data consists of a 256-sweep duration. The Doppler frequency corresponding to the Tx A – target – Rx A path is 10 Hz, and that corresponding to the Tx B – target – Rx A path is 14 Hz. The propagation delay of both paths relative to the reference time is 8 ms. For the convenience of visualizing the effect of cross-radar interference and assessing the effectiveness of interference cancelation, the strength of the synthesized target is set to be relatively high. The SNR and SIR results are assessed for the Tx A – target – Rx A path at the 10 Hz Doppler frequency bin. Background noise power is obtained when no target returns are injected.

When the two radar systems concurrently transmit, the time-frequency signature is the superposition of the results of the two radar systems, as depicted in Fig. 2(a) using short-time Fourier transform (STFT), where appropriate windows are applied. Figs. 2(b) and (c) are the corresponding range-Doppler maps with the receiver matching the signal transmitted from radar A and radar B, respectively. It is evident that cross-radar interference maintains the Doppler frequency information whereas the fast-time (range) information is missing and the cross-radar interference spreads over the entire fast-time width (range). As a result, it is seen that, while cross-radar interference exists, the range and Doppler of the target can be clearly identified in this case. The average SNR (the ratio between the signal power and the average noise power over all range cells) is 36.7 dB, and the SNR evaluated at the target range cell is 40.3 dB. The SIR is 20.2 dB, which is very close to the analytic result.

Figure 3 shows the range-Doppler maps as a result of five iterations of cross-radar interference cancelation. In this plot, the average SNR and the cell SNR in the auto-radar reception mode remain at the same values of 36.7 dB and 40.3 dB, respectively. In the cross-radar reception mode, the average SINR is also 36.7 dB, and the average power of the residual error due to cross-radar interference is 7.5 dB lower than that of the original noise. This confirms that substantial interference mitigation has been achieved without compromising the target signal.

VII. Conclusion

We have considered a concurrent operation of two OTHR systems for improved estimation of target maneuvering. A new method for cross-radar interference mitigation was developed and its performance was analyzed. The usefulness of the proposed method was demonstrated by using measured clutter data and a synthetic test target. It was shown that applying cross-radar interference cancelation techniques, such as those presented in this chapter, can substantially suppress cross-radar interference without compromising the auto-radar responses, leading to enhanced target detection and characterization.

References

[1] J. M. Headrick and M. I. Skolnik, "Over-the-horizon radar in the HF band," *Proc. IEEE*, vol. 62, pp. 664–673, 1974.

[2] L. F. McNamara, *The Ionosphere, Communications, Surveillance, and Direction Finding*, Melnourne, FL: Krieger Publishing, 1991.

[3] G. D. McNeal, "The high-frequency environment at the ROTHR Amchitka radar site," *Radio Science*, vol. 30, pp. 739–746, May–June 1995.

[4] T. M. Georges, J. A. Harlan, "New horizons for over-the-horizon radar?" *IEEE Antennas and Propagation Magazine*, vo. 36, no. 4, pp. 14–24, Aug. 1994.

[5] Y. Zhang, G. J. Frazer, and M. G. Amin, "Simultaneous operation of two over-the-horizon radars," *Proc. SPIE, Advanced Signal Processing Algorithms, Architectures, and Implementations XIV*, pp. 313–324, Denver, CO, Aug. 2004.

[6] J. R. Barnum and E. E. Simpson, "Over-the-horizon radar sensitivity enhancement by impulse noise excision," in *Proc. IEEE Nat. Radar Conf.*, pp. 252–256, 1997.

[7] M. Turley, "Impulse noise rejection in HF radar using a linear prediction technique," in *Proc. IEEE Int. Conf. Radar*, pp. 358–362, 2003.

[8] G. Wang, X.-G. Xia, B. T. Root, V. C. Chen, Y. Zhang, and M. G. Amin, "Manoeuvring target detection in over-the-horizon radar using adaptive clutter rejection and adaptive chirplet transform," *IEE Prof. Radar, Sonar and Navigation*, vol. 150, no. 4, pp. 292–298, Aug. 2003.

[9] Y. Zhang, M. G. Amin, and G. J. Frazer, "High-resolution time-frequency distributions for manoeuvring target detection in over-the-horizon radars," *IEE Prof. Radar, Sonar and Navigation*, vol. 150, no. 4, pp. 299–304, Aug. 2003.

[10] X. Guo, H. Sun, and T. S. Yeo, "Transient interference excision in over-the-horizon radar using adaptive time-frequency analysis," *IEEE Trans. Geoscience and Remote Sensing*, vol. 43, no. 4, pp. 722–725, April 2005.

[11] D. Cerutti-Maori and J.H.G. Ender, "Performance analysis of multistatic configurations for spaceborne GMTI based on the auxiliary beam approach," *IEE Proc. Radar, Sonar and Navigation*, vol. 153, no. 2, pp. 96–103, April 2006.

[12] S.D. Blunt and K. Gerlach, "Multistatic adaptive pulse compression," *IEEE Trans. Aerospace and Electronic System*, vol. 42, no. 3, pp. 891–902, July 2006.

[13] J. Krolik, "Target localization and track association for over-the-horizon radar with a statistical ionospheric model," Tech. Rep. submitted to ONR, July 1999.

[14] D. E. Barrick, "FM/CW radar signals and digital processing," Tech. Rep. ERL283-WPL26, National Oceanic and Atmospheric Administration, July 1973.

[15] U. Madhow and M. Honig, "MMSE interference suppression for direct-sequence spread spectrum CDMA," *IEEE Trans. Commun.*, vol. 42, pp. 3178–3188, Dec. 1994.

[16] S. Verdu, *Multiuser Detection*. Cambridge, UK: Cambridge Univ. Press, 1998.

[17] X. Wang and H. V. Poor, "Space-time multiuser detection in multipath CDMA channels," *IEEE Trans. Signal Processing*, vol. 47, no. 9, pp. 2356–2374, Sept. 1999.

[18] J. Hogbom, "Aperture synthesis with a nonregular distribution of interferometer baselines," *Astrophys. J. Suppl. Ser.*, vol. 15, pp. 417-426, 1974.

[19] U. J. Schartz, "Mathematical-statistical description of the iterative beam removing technique," *Astron. Astrophys.*, vol. 65, pp. 345-356, 1978.

[20] Y. I. Abramovich, "A recursive method for the resolution of wideband signals with substantially different intensities," *Radio Eng. Electron. Phys.*, vol. 23, no. 8, pp. 66–70, 1978.
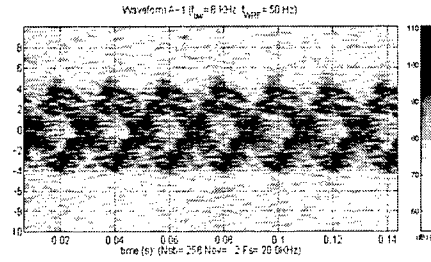
(a)Time-frequency signature of the received signal
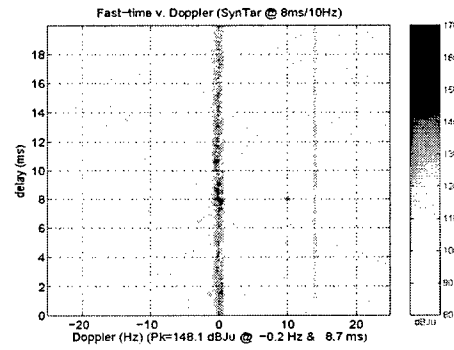
(b)Range-Doppler map matched to radar A's waveform
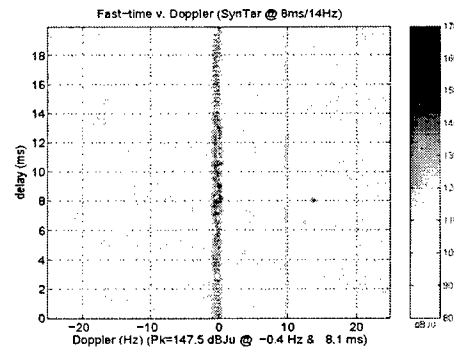
(c)Range-Doppler map matched to radar B' waveform

Fig. 2. Dual radar operation results without interference cancelation.
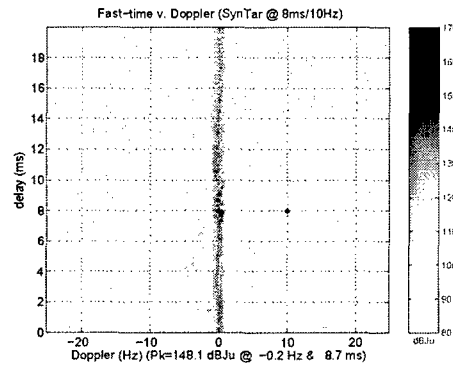
(a)Matched to radar A's waveform
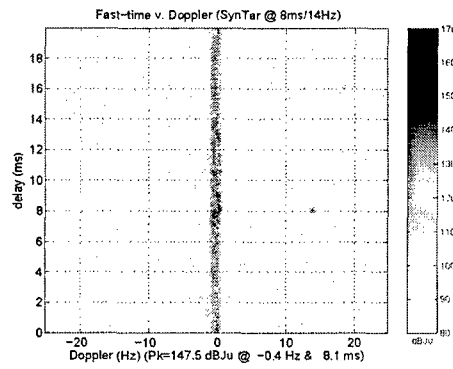
(b)Matched to radar B's waveform

Fig. 3. Range-Doppler maps with interference cancelation.

Chapter 2

Spatial Polarimetric Time-Frequency Distributions for Direction-of-Arrival Estimations

Abstract

Time-frequency distributions (TFDs) are traditionally applied to a single antenna receiver with a single polarization. Recently, spatial time-frequency distributions (STFDs) have been developed for receivers with multiple single-polarized antennas, and successfully applied for direction-of-arrival (DOA) estimation of nonstationary signals. In this chapter, we consider dual-polarized antenna arrays and extend the STFD to utilize the source polarization properties. The spatial polarimetric time-frequency distributions (SPTFDs) are introduced as a platform for processing polarized nonstationary signals which are received by an array of dual-polarized double-feed antennas. The chapter deals with narrowband far-field point sources that lie in the plane of the receiver array. The source signals are decomposed into two orthogonal polarization components, such as vertical and horizontal. The ability to incorporate signal polarization empowers the STFDs with an additional degree of freedom, leading to improved signal and noise subspace estimates for direction-finding. The polarimetric time-frequency MUSIC (PTF-MUSIC) method for DOA estimation based on the SPTFD platform is developed and shown to outperform the time-frequency, polarimetric, and conventional MUSIC techniques, when applied separately.

I. Introduction

Time-frequency distributions (TFDs) have been used for nonstationary signal analysis and synthesis in various areas, including speech, biomedicine, automotive industry, and machine monitoring [1], [2]. Over the past few years, the spatial dimension has been incorporated, along with the time and frequency variables, into quadratic and higher-order TFDs, and led to the introduction of spatial time-frequency distributions (STFDs) for nonstationary array signal processing [3], [4]. The relationship between the TFDs of the sensor data and the TFDs of the individual source waveforms is defined by the steering, or the mixing, matrix, and was found to be similar to that encountered in the traditional covariance matrix approach to array processing. This similarity has allowed subspace-based estimation methods to utilize the source instantaneous frequency for direction-finding. It has been shown that the MUSIC [5] and ESPRIT [6] techniques based on STFDs outperform their counterparts based on data covariance matrices, when applied for direction-of-arrival (DOA) estimation of sources of nonstationary temporal characteristics [4], [7], [8], [9].

Polarization and polarization diversities, on the other hand, are commonly used in wireless and satellite communications as well as various types of radar systems [10], [11]. Antenna and target polarization properties are widely employed in remote sensing and synthetic aperture radar (SAR) applications [12], [13], [14]. Airborne and spaceborne platforms as well as meteorological radars include polarization information [15], [16]. Additionally, polarization plays an effective role for target identification in the presence of clutter [17], [18], and has also been incorporated in antenna arrays to improve signal parameter estimation, including DOA and time-of-arrival (TOA) [19], [20], [21], [22], [23], [24].

The two important areas of time-frequency (t-f) signal representations and polarimetric signal processing have not been integrated or considered within the same platform, despite the extensive research work separately performed under each area. In this chapter, we introduce the spatial polarimetric time-frequency distributions (SPTFDs) for double-feed dual-polarized arrays, where the source time-frequency and polarization signatures are concurrently utilized. The advantages of the proposed SPTFD platform are demonstrated using narrowband farfield point-like emitters that lie in the plane of the receiver array. The signal polarization information empowers the STFDs with an additional degree of freedom, leading to improved spatial resolution and source discrimination.

27

The SPTFD is used to define the polarimetric time-frequency MUSIC (PTF-MUSIC) algorithm, which is formulated based on the source combined t-f and polarization properties are applied for DOA estimation of polarized nonstationary signals. The PTF-MUSIC technique is shown to outperform the MUSIC techniques that only incorporate either the t-f or the polarimetric source characteristics. The application to an ESPRIT-like method is introduced separately in [25].

This chapter is organized as follows. Section II discusses the signal model and briefly reviews TFDs and STFDs. Section III considers dual-polarized antenna arrays and introduces the concept of spatial polarimetric time-frequency distributions (SPTFDs). The PTF-MUSIC algorithm is proposed in Section IV. Sections V and VI, respectively, consider the issues of spatio-polarimetric correlations and DOA estimations of signals with time-varying polarization characteristics. Spatial and polarization averaging methods for coherent signal decorrelation are investigated in Section VII. Computer simulations, demonstrating the effectiveness of the proposed methods, are provided in Section VIII.

Throughout this chapter, lower case bold and capital bold letters (e.g., $\mathbf{a}$ and $\mathbf{A}$) are used to represent vectors and matrices, respectively. Moreover, $E[\cdot]$ denotes expectation operation, $(\cdot)^*$ denotes complex conjugate, $(\cdot)^T$ denotes transpose, and $(\cdot)^H$ denotes conjugate transpose (Hermitian). We use $(\cdot)^{[i]}$ to denote polarization i, $(\cdot)^{(k)}$ to denote the kth subarray. In addition, $\|\cdot\|$ denotes the vector norm, $\otimes$ denotes Kronecker product operator, and $\odot$ denotes Hadamard product operator.

II. Signal Model

A. Time-Frequency Distributions

The Cohen's class of TFDs of a signal $x(t)$ is defined as [1]

$$D_{xx}(t,f) = \iint \varphi(t-u,\tau)x(u+\frac{\tau}{2})x^*(u-\frac{\tau}{2})e^{-j2\pi f\tau}dud\tau, \tag{1}$$

where t and f represent the time and frequency indexes, respectively and $j = \sqrt{-1}$. The kernel $\varphi(t,\tau)$ uniquely defines the TFD and is a function of the time and lag variables. In this chapter, all the integrals are from $-\infty$ to ∞.

The cross-term TFD of two signals $x_k(t)$ and $x_l(t)$ is defined by

$$D_{x_k x_l}(t,f) = \iint \varphi(t-u,\tau)x_k(u+\frac{\tau}{2})x_l^*(u-\frac{\tau}{2})e^{-j2\pi f\tau}dud\tau. \tag{2}$$

B. Spatial Time-Frequency Distributions

The STFDs have already been developed for single-polarized antenna arrays [4], [7]. Consider a narrowband direction-finding problem where the signal bandwidth is small relative to its carrier frequency. We note that the wideband array processing for nonstationary signals, which has been examined in [26] and [27], is outside the scope of the proposed approach. The following linear data model is assumed,

$$\mathbf{x}(t) = \mathbf{y}(t) + \mathbf{n}(t) = \mathbf{A}\mathbf{s}(t) + \mathbf{n}(t), \tag{3}$$

where the $m \times n$ matrix $\mathbf{A} = [\mathbf{a}_1, \mathbf{a}_2, \ldots, \mathbf{a}_n]$ is the mixing matrix that holds the spatial information. The number of array elements is m, whereas n represents the number of signals incident on the array. In the above equation, $\mathbf{A} = \mathbf{A}(\mathbf{\Phi}) = [\mathbf{a}(\phi_1), \mathbf{a}(\phi_2), \ldots, \mathbf{a}(\phi_n)]$, where $\mathbf{\Phi} = [\phi_1, \phi_2, \ldots, \phi_n]$ and $\mathbf{a}(\phi_k)$ is the spatial signature for source k. Each element of the $n \times 1$ vector $\mathbf{s}(t) = [s_1(t) \quad s_2(t) \quad \ldots \quad s_n(t)]^T$ is a mono-component signal. Due to the mixing at each sensor, the elements of the $m \times 1$ sensor data vector $\mathbf{x}(t)$ become multi-component signals. $\mathbf{n}(t)$ is an $m \times 1$ additive noise vector, which consists of independent zero-mean, white and Gaussian distributed processes.

The STFD of a data vector $\mathbf{x}(t)$ is expressed as [3]

$$\mathbf{D_{xx}}(t, f) = \iint \varphi(t - u, \tau)\mathbf{x}(u + \frac{\tau}{2})\mathbf{x}^H(u - \frac{\tau}{2})e^{-j2\pi f\tau} du d\tau, \tag{4}$$

where the (k, l)th element of $\mathbf{D_{xx}}(t, f)$ is given by Eq. (2) for $k, l = 1, 2, \ldots, m$. The noise-free STFD is obtained by substituting Eq. (3) in Eq. (4),

$$\mathbf{D_{xx}}(t, f) = \mathbf{A}(\mathbf{\Phi})\mathbf{D_{ss}}(t, f)\mathbf{A}^H(\mathbf{\Phi}), \tag{5}$$

where $\mathbf{D_{ss}}(t, f)$ is the TFD matrix of $\mathbf{s}(t)$ which consists of auto- and cross-source TFDs. With the presence of the noise, which is uncorrelated with the signals, the expected value $\mathbf{D_{xx}}(t, f)$ yields

$$E[\mathbf{D_{xx}}(t, f)] = \mathbf{A}(\mathbf{\Phi})E[\mathbf{D_{ss}}(t, f)]\mathbf{A}^H(\mathbf{\Phi}) + \sigma^2\mathbf{I}. \tag{6}$$

In the above equation, σ^2 is the noise power, $\mathbf{I}$ is the identity matrix, and $E[\cdot]$ denotes the statistical expectation operator.

Equation (6) is similar to the commonly used formula in narrowband array processing problems, relating the source covariance matrix to the sensor spatial covariance matrix. Here, the covariance matrices are replaced by the source and sensor TFD matrices. The two subspaces

29

spanned by the principle eigenvectors of $\mathbf{D_{xx}}(t, f)$ and the columns of $\mathbf{A}(\mathbf{\Phi})$ are, therefore, identical. The STFD matrix can be constructed from the t-f points with highly localized signal energy, thus allowing the corresponding signal and noise subspace estimates to be more robust to noise than their counterparts obtained using the data covariance matrix, $\mathbf{R_{xx}} = E[\mathbf{x}(t)\mathbf{x}^H(t)]$ [4], [8], [9]. Further, the source discriminations, provided through the flexibility of selecting t-f points or regions, permit DOA estimations to be performed for only individual or subgroup of sources. In this respect, the number of impinging sources can exceed the number of array sensors. The above attractive properties allow key problems in various array processing applications to be addressed and solved using a new formulation (6), which is more tuned to nonstationary signal environments.

III. Spatial Polarimetric Time-Frequency Distributions

A. Polarimetric Modeling

For a transverse electromagnetic (TEM) wave incident on the array, shown in Fig. 1, the electric field can be described as

$$
\begin{aligned}
\vec{E}(t) \quad &= E_\theta(t)\hat{\theta} + E_\phi(t)\hat{\phi} \\
&= [E_\theta(t)\cos(\theta)\cos(\phi) - E_\phi(t)\sin(\phi)]\hat{x} \\
&\quad + [E_\theta(t)\cos(\theta)\sin(\phi) + E_\phi(t)\cos(\phi)]\,\hat{y} + E_\theta(t)\sin(\theta)\hat{z},
\end{aligned} \tag{7}
$$

where $\hat{\phi}$ and $\hat{\theta}$ are, respectively, the spherical unit vectors along the azimuth and elevation angles ϕ and θ, viewed from the source. The unit vectors $\hat{x}$, $\hat{y}$ and $\hat{z}$ are defined along the x, y, and z directions, respectively. For simplicity and without loss of generality, it is assumed that the source signal is in the x-y plane, whereas the array is located in the y-z plane. Accordingly, $\theta = 90$ degrees, $\hat{\theta} = -\hat{z}$, and

$$
\vec{E}(t) = -E_\phi(t)\sin(\phi)\hat{x} + E_\phi(t)\cos(\phi)\hat{y} + E_\theta(t)\hat{z}. \tag{8}
$$

We denote $s(t)$ as the source magnitude measured at the receiver reference sensor, with polarization angle $\gamma \in [0, \frac{\pi}{2}]$, and polarization phase difference $\eta \in (-\pi, \pi]$. The source horizontal and vertical polarization components, $s^{[v]}(t)$ and $s^{[h]}(t)$, can then be expressed in terms of the respective spherical fields, $E_\theta(t)$ and $E_\phi(t)$, as

$$
E_\theta(t) = s^{[v]}(t) = s(t)\cos(\gamma), \tag{9}
$$

$$E_\phi(t) = s^{[h]}(t) = s(t)\sin(\gamma)e^{j\eta}. \tag{10}$$

A signal is referred to as linearly polarized if $\eta = 0$ or $\eta = 180$ degrees. Substituting Eqs. (9) and (10) in Eq. (8) results in

$$\vec{E}(t) = s(t)[-\cos(\gamma)\sin(\phi)\hat{x} + \cos(\phi)\sin(\gamma)e^{j\eta}\hat{y} + \cos(\gamma)\hat{z}]. \tag{11}$$

Now we consider that n signals impinge on the array, consisting of m dual-polarized antennas. The vertical and horizontal components of the kth source are expressed as

$$
\begin{aligned}
s_k^{[v]}(t) &= s_k(t)\cos(\gamma_k) \triangleq c_{k1}s_k(t) \\
s_k^{[h]}(t) &= s_k(t)\sin(\gamma_k)e^{j\eta_k} \triangleq c_{k2}s_k(t),
\end{aligned} \tag{12}
$$

where the parameters $c_{k1} = \cos(\gamma_k)$ and $c_{k2} = \sin(\gamma_k)e^{j\eta_k}$ denote the vertical and horizontal polarization coefficients. The corresponding signal received at the lth dual-polarized antenna, with vertical and horizontal antennas located in the $\hat{z}$ and $\hat{y}$ directions, is expressed as

$$\underline{y}_l(t) = [y_l^{[v]}(t),\ y_l^{[h]}(t)]^T = \sum_{k=1}^{n}[a_{kl}^{[v]}\vec{E}_k \cdot \hat{z},\ a_{kl}^{[h]}\vec{E}_k \cdot \hat{y}]^T = \sum_{k=1}^{n}[a_{kl}^{[v]}s_k^{[v]}(t),\ a_{kl}^{[h]}s_k^{[h]}(t)\cos(\phi_k)]^T, \tag{13}$$

where "$\cdot$" represents the dot product, $\vec{E}_k$ is the electric field vector corresponding to the kth source, and $a_{kl}^{[v]}$ and $a_{kl}^{[h]}$, respectively, are the lth elements of the vertically and horizontally polarized array vectors, $\mathbf{a}^{[v]}(\phi_k)$ and $\mathbf{a}^{[h]}(\phi_k)$. It is assumed that the array has been calibrated and both $\mathbf{a}^{[v]}(\phi)$ and $\mathbf{a}^{[h]}(\phi)$ are known and normalized such that $||\mathbf{a}^{[v]}(\phi)||^2 = ||\mathbf{a}^{[h]}(\phi)||^2 = m$. It is noted that the $\cos(\phi_k)$ term in the horizontally polarized array manifold can be absorbed in the array calibration over the region of interest and, therefore, removed from further consideration. Then, the above equation is simplified as

$$\underline{y}_l(t) = [a_{kl}^{[v]}s_k^{[v]}(t),\ a_{kl}^{[h]}s_k^{[h]}(t)]^T = s_k(t)\left(\begin{bmatrix} a_{kl}^{[v]} & a_{kl}^{[h]} \end{bmatrix}^T \odot \begin{bmatrix} c_{k1} & c_{k2} \end{bmatrix}^T\right) \triangleq s_k(t)\mathbf{a}_{kl} \odot \mathbf{c}_k, \tag{14}$$

where the vector $\mathbf{c}_k = [c_{k1}, c_{k2}]^T = [\cos(\gamma_k), \sin(\gamma_k)e^{j\eta_k}]$ represents the polarization signature of the kth source.

B. Polarimetric Time-Frequency Distributions

For a dual-polarized sensor, k, we define the self- and cross-polarized TFDs, respectively, as

$$D_{x_k^{[i]}x_k^{[i]}}(t,f) = \iint \varphi(t-u,\tau)x_k^{[i]}(u+\frac{\tau}{2})(x_k^{[i]}(u-\frac{\tau}{2}))^* e^{-j2\pi f\tau}\,du\,d\tau \tag{15}$$

31

and

$$D_{x_k^{[i]}x_k^{[j]}}(t, f) = \iint \varphi(t - u, \tau)x_k^{[i]}(u + \frac{\tau}{2})(x_k^{[j]}(u - \frac{\tau}{2}))^* e^{-j2\pi f\tau} du d\tau, \tag{16}$$

where the superscripts i and j denote either v or h. The self- and cross-polarized TFDs constitute the 2×2 polarimetric TFD (PTFD) matrix,

$$\mathbf{D}_{\underline{x}_k\underline{x}_k}(t, f) = \iint \varphi(t - u, \tau)\underline{x}_k(u + \frac{\tau}{2})\underline{x}_k^H(u - \frac{\tau}{2})e^{-j2\pi f\tau} du d\tau. \tag{17}$$

The diagonal entries of $\mathbf{D}_{\underline{x}_k\underline{x}_k}(t, f)$ are the self-polarized TFDs, $D_{x_k^{[i]}x_k^{[i]}}(t, f)$, whereas the off-diagonal elements are the cross-polarized terms $D_{x_k^{[i]}x_k^{[j]}}(t, f)$, $i \neq j$.

C. Spatial Polarimetric Time-Frequency Distributions

Equations (13)–(17) correspond to the case of a single dual-polarization sensor. With an m-sensor array, the data vector, for each polarization i, $i = v$ or h, is expressed as,

$$\mathbf{x}^{[i]}(t) = [x_1^{[i]}(t), x_2^{[i]}(t), \ldots, x_m^{[i]}(t)]^T = \mathbf{y}^{[i]}(t) + \mathbf{n}^{[i]}(t) = \mathbf{A}^{[i]}(\mathbf{\Phi})\mathbf{s}^{[i]}(t) + \mathbf{n}^{[i]}(t). \tag{18}$$

The generalization of single-sensor polarimetric time-frequency distributions to a multi-sensor receiver is obtained using Eq. (18). Instead of the scalar variable TFD of Eq. (15), we define the self-polarized STFD matrix of vector $\mathbf{x}^{[i]}(t)$ for polarization i as

$$\mathbf{D}_{\mathbf{x}^{[i]}\mathbf{x}^{[i]}}(t, f) = \iint \varphi(t - u, \tau)\mathbf{x}^{[i]}(u + \frac{\tau}{2})(\mathbf{x}^{[i]}(u - \frac{\tau}{2}))^H e^{-j2\pi f\tau} du d\tau, \tag{19}$$

which, in the noise-free environment, can be expressed as

$$\mathbf{D}_{\mathbf{x}^{[i]}\mathbf{x}^{[i]}}(t, f) = \mathbf{A}^{[i]}(\mathbf{\Phi})\mathbf{D}_{\mathbf{s}^{[i]}\mathbf{s}^{[i]}}(t, f)\left(\mathbf{A}^{[i]}(\mathbf{\Phi})\right)^H. \tag{20}$$

In a similar manner, the cross-polarization STFD matrix between the data vectors with two different polarizations i and j can be expressed as,

$$\mathbf{D}_{\mathbf{x}^{[i]}\mathbf{x}^{[j]}}(t, f) = \iint \varphi(t - u, \tau)\mathbf{x}^{[i]}(u + \frac{\tau}{2})\left(\mathbf{x}^{[j]}(u - \frac{\tau}{2})\right)^H e^{-j2\pi f\tau} du d\tau, \tag{21}$$

which becomes

$$\mathbf{D}_{\mathbf{x}^{[i]}\mathbf{x}^{[j]}}(t, f) = \mathbf{A}^{[i]}(\mathbf{\Phi})\mathbf{D}_{\mathbf{s}^{[i]}\mathbf{s}^{[j]}}(t, f)\left(\mathbf{A}^{[j]}(\mathbf{\Phi})\right)^H \tag{22}$$

when the noise is ignored.

Based on Eq. (18), the following extended data vector can be constructed for both polarizations,

$$
\begin{aligned}
\mathbf{x}(t) &= \begin{bmatrix} \mathbf{x}^{[v]}(t) \\ \mathbf{x}^{[h]}(t) \end{bmatrix} = \begin{bmatrix} \mathbf{A}^{[v]}(\boldsymbol{\Phi}) & 0 \\ 0 & \mathbf{A}^{[h]}(\boldsymbol{\Phi}) \end{bmatrix} \begin{bmatrix} \mathbf{s}^{[v]}(t) \\ \mathbf{s}^{[h]}(t) \end{bmatrix} + \begin{bmatrix} \mathbf{n}^{[v]}(t) \\ \mathbf{n}^{[h]}(t) \end{bmatrix} \\
&= \begin{bmatrix} \mathbf{A}^{[v]}(\boldsymbol{\Phi}) & 0 \\ 0 & \mathbf{A}^{[h]}(\boldsymbol{\Phi}) \end{bmatrix} \begin{bmatrix} \mathbf{Q}^{[v]} \\ \mathbf{Q}^{[h]} \end{bmatrix} \mathbf{s}(t) + \begin{bmatrix} \mathbf{n}^{[v]}(t) \\ \mathbf{n}^{[h]}(t) \end{bmatrix} \\
&= \mathbf{B}(\boldsymbol{\Phi})\mathbf{Q}\mathbf{s}(t) + \mathbf{n}(t),
\end{aligned}
\tag{23}
$$

where

$$
\mathbf{B}(\boldsymbol{\Phi}) = \begin{bmatrix} \mathbf{A}^{[v]}(\boldsymbol{\Phi}) & 0 \\ 0 & \mathbf{A}^{[h]}(\boldsymbol{\Phi}) \end{bmatrix}
\tag{24}
$$

is block-diagonal, and

$$
\mathbf{Q} = \begin{bmatrix} \mathbf{Q}^{[v]} \\ \mathbf{Q}^{[h]} \end{bmatrix}
\tag{25}
$$

is the polarization signature vector of the sources, where

$$
\mathbf{q}^{[v]} = [\cos(\gamma_1), \ldots, \cos(\gamma_n)]^T, \quad \mathbf{Q}^{[v]} = \mathrm{diag}(\mathbf{q}^{[v]}),
\tag{26}
$$

$$
\mathbf{q}^{[h]} = [\sin(\gamma_1)e^{j\eta_1}, \ldots, \sin(\gamma_n)e^{j\eta_n}]^T, \quad \mathbf{Q}^{[h]} = \mathrm{diag}(\mathbf{q}^{[h]}).
\tag{27}
$$

Accordingly,

$$
\mathbf{B}(\boldsymbol{\Phi})\mathbf{Q} = \begin{bmatrix} \mathbf{a}^{[v]}(\phi_1)\cos(\gamma_1) & \cdots & \mathbf{a}^{[v]}(\phi_n)\cos(\gamma_n) \\ \mathbf{a}^{[h]}(\phi_1)\sin(\gamma_1)e^{j\eta_1} & \cdots & \mathbf{a}^{[h]}(\phi_n)\sin(\gamma_n)e^{j\eta_n} \end{bmatrix} = \begin{bmatrix} \tilde{\mathbf{a}}(\phi_1) & \cdots & \tilde{\mathbf{a}}(\phi_n) \end{bmatrix}.
\tag{28}
$$

The above matrix can be viewed as the extended mixing matrix, with $\mathbf{a}(\tilde{\phi}_k)$ representing the joint spatial-polarimetric signature of signal k. The extended spatial polarization signature vector for the kth source is

$$
\tilde{\mathbf{a}}(\phi_k) = \begin{bmatrix} \mathbf{a}^{[v]}(\phi_k)\cos(\gamma_k) \\ \mathbf{a}^{[h]}(\phi_k)\sin(\gamma_k)e^{j\eta_k} \end{bmatrix}.
\tag{29}
$$

It is clear that the dual-polarization array, compared to single-polarization case, doubles the vector space dimensionality.

It is now possible to combine the polarimetric, spatial, and t-f properties of the source signals incident on the receiver array. The STFD of the dual-polarization data vector, $\mathbf{x}(t)$, can be written as

$$
\mathbf{D}_{\mathbf{xx}}(t, f) = \iint \varphi(t - u, \tau)\mathbf{x}(u + \frac{\tau}{2})\mathbf{x}^H(u - \frac{\tau}{2})e^{-j2\pi f\tau}\,du\,d\tau.
\tag{30}
$$

$\mathbf{D_{xx}}(t, f)$, formulated in Eq. (30), is referred to as the spatial polarimetric time-frequency distribution (SPTFD) matrix. This distribution, or matrix, serves as a general framework within which typical problems in array processing, including direction-finding, can be addressed, as shown in the next section.

When the effect of noise is ignored, the SPTFD matrix is related to the source TFD matrix by

$$\mathbf{D_{xx}}(t, f) = \mathbf{B}(\mathbf{\Phi})\mathbf{Q}\mathbf{D_{ss}}(t, f)\mathbf{Q}^H\mathbf{B}^H(\mathbf{\Phi}). \tag{31}$$

IV. Polarimetric Time-Frequency MUSIC

Time-frequency MUSIC (TF-MUSIC) has been recently introduced to improve spatial resolution of sources with clear t-f signatures [7]. The proposed PTF-MUSIC is an important generalization of the TF-MUSIC for dealing with polarized signals and polarized arrays. It is based on the search for the minimum values of the orthogonal projection of the array vector, defined in the joint spatial and polarimetric domains, on the noise subspace obtained from the SPTFD matrix over selected t-f regions.

Consider the following spatial signature matrix

$$\mathbf{F}(\phi) = \frac{1}{\sqrt{m}} \begin{bmatrix} \mathbf{a}^{[v]}(\phi) & \mathbf{0} \\ \mathbf{0} & \mathbf{a}^{[h]}(\phi) \end{bmatrix} \tag{32}$$

corresponding to DOA ϕ. Since $||\mathbf{a}^{[i]}(\phi)||^2 = m$, $\mathbf{F}^H(\phi)\mathbf{F}(\phi)$ is the 2×2 identity matrix.

To search in the joint spatial and polarimetric domains, we define the following spatio-polarimetric search vector

$$\mathbf{f}(\phi, \mathbf{c}) = \frac{\mathbf{F}(\phi)\mathbf{c}}{||\mathbf{F}(\phi)\mathbf{c}||} = \mathbf{F}(\phi)\mathbf{c}, \tag{33}$$

where the vector $\mathbf{c} = [c_1 \ c_2]^T$ is a unit norm vector with unknown polarization coefficients. In Eq. (33), we have used the fact that $||\mathbf{F}(\phi)\mathbf{c}|| = [\mathbf{c}^H\mathbf{F}^H(\phi)\mathbf{F}(\phi)\mathbf{c}]^{\frac{1}{2}} = (\mathbf{c}^H\mathbf{c})^{\frac{1}{2}} = 1$.

The PTF-MUSIC spectrum is given by the following function,

$$P(\phi) = [\min_{\mathbf{c}} \mathbf{f}^H(\phi, \mathbf{c})\mathbf{U}_n\mathbf{U}_n^H\mathbf{f}(\phi, \mathbf{c})]^{-1} = [\min_{\mathbf{c}} \mathbf{c}^H\mathbf{F}^H(\phi)\mathbf{U}_n\mathbf{U}_n^H\mathbf{F}(\phi)\mathbf{c}]^{-1}, \tag{34}$$

where $\mathbf{U}_n$ is the noise subspace obtained from the SPTFD matrix in Eq. (30) using selected t-f points. For t-f based DOA estimation methods, t-f averaging and joint block-diagonalization are two known techniques that can be used to integrate the different STFD or SPTFD matrices

constructed at multiple t-f points [4], [7], [30]. The selection of those points from high energy concentration regions pertaining to all or some of the sources enhances the SNR and allows the t-f based MUSIC algorithms to be more robust to noise [4] compared to its conventional MUSIC counterpart.

In Eq. (34), the term in brackets is minimized by finding the minimum eigenvalue of the 2×2 matrix $\mathbf{F}^H(\phi)\mathbf{U}_n\mathbf{U}_n^H\mathbf{F}(\phi)$. Thus, a computationally expensive search in the polarization domain is avoided by performing a simple eigen-decomposition on a 2×2 matrix. As a result, the PTF-MUSIC spectrum can be expressed as

$$P(\phi) = \lambda_{\min}^{-1}[\mathbf{F}^H(\phi)\mathbf{U}_n\mathbf{U}_n^H\mathbf{F}(\phi)], \tag{35}$$

where $\lambda_{\min}[\cdot]$ denotes the minimum eigenvalue operator. The DOAs of the sources are estimated as the locations of the highest peaks in the PTF-MUSIC spectrum. For each angle ϕ_k corresponding to the n signal arrivals, $k = 1, 2, \ldots, n$, the polarization parameters of the respective source signal can be estimated from

$$\hat{\mathbf{c}}(\phi_k) = \mathbf{v}_{\min}[\mathbf{F}^H(\phi_k)\mathbf{U}_n\mathbf{U}_n^H\mathbf{F}(\phi_k)], \tag{36}$$

where $\mathbf{v}_{\min}[\cdot]$ is the eigenvector corresponding to the minimum eigenvalue $\lambda_{\min}[\cdot]$.

V. Spatio-Polarimetric Correlations

The spatial resolution capability of an array highly depends on the correlation between the propagation signatures of the source arrivals [4], [31]. This is determined by the normalized inner product of the respective array manifold vectors. In the underlying problem, in which both the spatial and polarimetric dimensions are involved, the joint spatio-polarimetric correlation coefficient between sources l and k is defined using the extended array manifold $\tilde{\mathbf{a}}(\phi)$, i.e.,

$$\begin{aligned} \beta_{l,k} &= \frac{1}{m}\tilde{\mathbf{a}}^H(\phi_k)\tilde{\mathbf{a}}(\phi_l) = \frac{1}{m}\left(c_{k1}^*c_{l1}\left(\mathbf{a}^{[v]}(\phi_k)\right)^H\mathbf{a}^{[v]}(\phi_l) + c_{k2}^*c_{l2}\left(\mathbf{a}^{[h]}(\phi_k)\right)^H\mathbf{a}^{[h]}(\phi_l)\right) \\ &= c_{k1}^*c_{l1}\beta_{l,k}^{[v]} + c_{k2}^*c_{l2}\beta_{l,k}^{[h]}, \end{aligned} \tag{37}$$

where $\beta_{l,k}^{[i]} = \frac{1}{m}\left(\mathbf{a}^{[i]}(\phi_k)\right)^H\mathbf{a}^{[i]}(\phi_l)$ is the spatial correlation coefficient between sources l and k for polarization i, with $i = v$ or h.

An interesting case arises when the vertically and horizontally polarized array manifolds are identical, i.e., $\mathbf{a}^{[v]}(\phi) = \mathbf{a}^{[h]}(\phi)$. In this case, $\beta_{l,k}^{[v]} = \beta_{l,k}^{[h]}$, and the joint spatio-polarimetric

35

correlation coefficient becomes the product of the individual spatial and polarimetric correlations, that is,

$$\beta_{l,k} = \beta_{l,k}^{[v]} \rho_{l,k} \tag{38}$$

with

$$\rho_{l,k} = \mathbf{c}_k^H \mathbf{c}_l = \cos(\gamma_l) \cos(\gamma_k) e^{j(\eta_l - \eta_k)} + \sin(\gamma_l) \sin(\gamma_k) \tag{39}$$

representing the polarimetric correlation coefficient. In particular, for linear polarizations, $\eta_l = \eta_k = 0$, and Eq. (39) reduces to

$$\rho_{l,k} = \cos(\gamma_l - \gamma_k). \tag{40}$$

Since $|\rho_{l,k}| \leq 1$, with the equality holds only when the two sources have identical polarization states, the spatio-polarization correlation coefficient is always smaller than that of the individual spatial correlation coefficient. The reduction in the correlation value due to polarization diversity, through the introduction of $\rho_{l,m}$, translates to improved source distinctions. As such, two sources that could be difficult to resolve using the single-polarized spatial array manifold $\mathbf{a}^{[v]}(\phi)$ or $\mathbf{a}^{[h]}(\phi)$ can be easily separated using the extended spatio-polarized array manifold, defined by $\tilde{\mathbf{a}}(\phi)$. This improvement is more evident in the case when the source spatial correlation is high, but the respective polarimetric correlation is low.

VI. Sources with Time-Varying Polarizations

In this section, we consider the performance of DOA estimation when the source signals have time-varying polarization signatures. Time-varying polarizations are often observed when active or passive sources move or change orientations [32]. The performance of polarimetric MUSIC and PTF-MUSIC techniques are discussed and compared. For simplicity, we consider in this section the noise-free environment.

A. Polarimetric MUSIC

Given the time-varying nature of the source signal polarizations, the covariance matrix of the received signal vector is

$$\mathbf{R_{xx}} = E\left[\mathbf{x}(t)\mathbf{x}^H(t)\right] = E\left\{ \begin{bmatrix} \mathbf{A}^{[v]}(\mathbf{\Phi})(\mathbf{q}^{[v]}(t) \odot \mathbf{s}(t)) \\ \mathbf{A}^{[h]}(\mathbf{\Phi})(\mathbf{q}^{[h]}(t) \odot \mathbf{s}(t)) \end{bmatrix} \begin{bmatrix} \mathbf{A}^{[v]}(\mathbf{\Phi})(\mathbf{q}^{[v]}(t) \odot \mathbf{s}(t)) \\ \mathbf{A}^{[h]}(\mathbf{\Phi})(\mathbf{q}^{[h]}(t) \odot \mathbf{s}(t)) \end{bmatrix}^H \right\}. \tag{41}$$

We replace the expectation operator by time-averages. Then,

$$
\begin{aligned}
\mathbf{R_{xx}} &= \mathbf{B}(\mathbf{\Phi}) \begin{bmatrix} \overline{\mathbf{q}^{[v]}(t)(\mathbf{q}^{[v]}(t))^H} \odot \hat{\mathbf{R}}_{ss} & \overline{\mathbf{q}^{[v]}(t)(\mathbf{q}^{[h]}(t))^H} \odot \hat{\mathbf{R}}_{ss} \\ \overline{\mathbf{q}^{[h]}(t)(\mathbf{q}^{[v]}(t))^H} \odot \hat{\mathbf{R}}_{ss} & \overline{\mathbf{q}^{[h]}(t)(\mathbf{q}^{[h]}(t))^H} \odot \hat{\mathbf{R}}_{ss} \end{bmatrix} \mathbf{B}^H(\mathbf{\Phi}) \\
&= \mathbf{B}(\mathbf{\Phi}) \left\{ \begin{bmatrix} \overline{\mathbf{q}^{[v]}(t)(\mathbf{q}^{[v]}(t))^H} & \overline{\mathbf{q}^{[v]}(t)(\mathbf{q}^{[h]}(t))^H} \\ \overline{\mathbf{q}^{[h]}(t)(\mathbf{q}^{[v]}(t))^H} & \overline{\mathbf{q}^{[h]}(t)(\mathbf{q}^{[h]}(t))^H} \end{bmatrix} \odot \begin{bmatrix} \hat{\mathbf{R}}_{ss} & \hat{\mathbf{R}}_{ss} \\ \hat{\mathbf{R}}_{ss} & \hat{\mathbf{R}}_{ss} \end{bmatrix} \right\} \mathbf{B}^H(\mathbf{\Phi}), \quad (42)
\end{aligned}
$$

where $\overline{(\cdot)}$ denotes the average and $\hat{\mathbf{R}}_{ss}$ is the time-average estimate of the source covariance matrix. The time-varying source signal polarization vectors are defined, similarly to Eqs. (26) and (27), as

$$
\mathbf{q}^{[v]}(t) = [\cos(\gamma_1(t)), \ldots, \cos(\gamma_n(t))]^T, \tag{43}
$$

$$
\mathbf{q}^{[h]}(t) = [\sin(\gamma_1(t))e^{j\eta_1(t)}, \ldots, \sin(\gamma_n(t))e^{j\eta_n(t)}]^T. \tag{44}
$$

If the source signal polarizations assume constant values, i.e., $\mathbf{q}^{[v]}(t) = \mathbf{q}^{[v]}$ and $\mathbf{q}^{[h]}(t) = \mathbf{q}^{[h]}$, then the noise-free received signal covariance matrix becomes

$$
\mathbf{R'_{xx}} = \mathbf{B}(\mathbf{\Phi}) \left(\begin{bmatrix} \mathbf{q}^{[v]}(\mathbf{q}^{[v]})^H & \mathbf{q}^{[v]}(\mathbf{q}^{[h]})^H \\ \mathbf{q}^{[h]}(\mathbf{q}^{[v]})^H & \mathbf{q}^{[h]}(\mathbf{q}^{[h]})^H \end{bmatrix} \odot \begin{bmatrix} \mathbf{R}_{ss} & \mathbf{R}_{ss} \\ \mathbf{R}_{ss} & \mathbf{R}_{ss} \end{bmatrix} \right) \mathbf{B}^H(\mathbf{\Phi}). \tag{45}
$$

The effect of the signal time-varying polarization on the covariance matrix is evident from Eqs. (42) and (45). The two cases of time-varying and time-invariant polarizations will lead to the same performance if their corresponding covariance matrices are identical. Consider, for example, a covariance matrix due to two source signals. The first signal has a linearly time-varying polarization over the observation period from 0 to 90 degrees, whereas the second signal's linear polarization varies from 90 to 0 degrees over the same period. This case is equivalent to both sources assuming fixed, time-invariant polarization of $\gamma = 45$ degrees, and thereby, the source polarization diversity cannot be utilized in DOA estimation using polarimetric MUSIC.

To achieve polarization diversity in the above case, the data covariance matrix in Eq. (42) should be constructed from the moving average of the received data vector, instead of averaging over the entire data record. However, using few samples compromises the precision and robustness of direction estimation.

B. PTF-MUSIC

In the presence of time-varying polarized sources, the auto- and cross-polarized SPTFD, defined in Eqs. (19) and (21), respectively, can be expressed as

$$
\begin{aligned}
&\mathbf{D}_{\mathbf{x}^{[i]}\mathbf{x}^{[j]}}(t, f) \\
&= \iint \varphi(t - u, \tau)\mathbf{x}^{[i]}(u + \frac{\tau}{2})(\mathbf{x}^{[j]}(u - \frac{\tau}{2}))^H e^{-j2\pi f\tau} du d\tau \\
&= \mathbf{A}^{[i]}(\boldsymbol{\Phi}) \left[\iint \varphi(t - u, \tau) \left(\mathbf{q}^{[i]}(u + \frac{\tau}{2})(\mathbf{q}^{[j]}(u - \frac{\tau}{2}))^H \right) \right. \\
&\quad \left. \odot \left(\mathbf{s}(u + \frac{\tau}{2})\mathbf{s}^H(u - \frac{\tau}{2}) \right) e^{-j2\pi f\tau} du d\tau \right] \left(\mathbf{A}^{[j]}(\boldsymbol{\Phi}) \right)^H \\
&= \mathbf{A}^{[i]}(\boldsymbol{\Phi}) \left[\iint \varphi(t - u, \tau)\mathbf{G}^{[ij]}(u, \tau) \odot \mathbf{K}(u, \tau)e^{-j2\pi f\tau} du d\tau \right] \left(\mathbf{A}^{[j]}(\boldsymbol{\Phi}) \right)^H \\
&= \mathbf{A}^{[i]}(\boldsymbol{\Phi})\mathbf{D}_{\mathbf{s}^{[i]}\mathbf{s}^{[j]}}(t, f) \left(\mathbf{A}^{[j]}(\boldsymbol{\Phi}) \right)^H,
\end{aligned}
\tag{46}
$$

where $\mathbf{G}^{[ij]}(t, \tau) = \mathbf{q}^{[i]}(t + \frac{\tau}{2})(\mathbf{q}^{[j]}(t - \frac{\tau}{2}))^H$, and $\mathbf{K}(t, \tau) = \mathbf{s}(t + \frac{\tau}{2})\mathbf{s}^H(t - \frac{\tau}{2})$. We assume that the frequency and the polarization signatures of the sources change almost linearly within the temporal span of the t-f kernel. Then, using the first-order Taylor-series expansion, the polarization-dependent terms can be approximated as $\gamma_k(t + \frac{\tau}{2}) = \gamma_k(t) + \frac{\tau}{2}\dot{\gamma}_k(t)$, where $\dot{\gamma}_k(t) = \frac{d}{dt}\gamma_k(t)$. The autoterms of the source polarization information, which reside on the diagonals of $\mathbf{G}^{[vv]}(t, \tau), \mathbf{G}^{[vh]}(t, \tau), \mathbf{G}^{[hv]}(t, \tau)$ and $\mathbf{G}^{[hh]}(t, \tau)$, are given by

$$
[\mathbf{G}^{[vv]}(t, \tau)]_{kk} = \frac{1}{2} [\cos(2\gamma_k(t)) + \cos(\tau\dot{\gamma}_k(t))] \tag{47}
$$

$$
\left[\mathbf{G}^{[vh]}(t, \tau)\right]_{kk} = \frac{1}{2} [\sin(2\gamma_k(t)) - \sin(\tau\dot{\gamma}_k(t))] \tag{48}
$$

$$
\left[\mathbf{G}^{[hv]}(t, \tau)\right]_{kk} = \frac{1}{2} [\sin(2\gamma_k(t)) + \sin(\tau\dot{\gamma}_k(t))] \tag{49}
$$

$$
\left[\mathbf{G}^{[hh]}(t, \tau)\right]_{kk} = \frac{1}{2} [-\cos(2\gamma_k(t)) + \cos(\tau\dot{\gamma}_k(t))], \tag{50}
$$

respectively. For symmetric t-f kernels, $\varphi(t, \tau)$, the second sinusoidal terms in Eqs. (48) and (49) assume zero values in the TFD. Therefore, $\mathbf{D}_{\mathbf{s}^{[i]}\mathbf{s}^{[j]}}(t, f)$ can be expressed at the autoterm points as

$$
D_{s_k^{[v]}s_k^{[v]}}(t, f) = \frac{1}{2}\cos(2\gamma_k(t))D_{s_k s_k}(t, f) + c_{kk}(t, f) \tag{51}
$$

$$
D_{s_k^{[h]}s_k^{[h]}}(t, f) = -\frac{1}{2}\cos(2\gamma_k(t))D_{s_k s_k}(t, f) + c_{kk}(t, f) \tag{52}
$$

$$
D_{s_k^{[v]}s_k^{[h]}}(t, f) = D_{s_k^{[h]}s_k^{[v]}}(t, f) = \frac{1}{2}\sin(2\gamma_k(t))D_{s_k s_k}(t, f) \tag{53}
$$

with

$$c_{kk}(t,f) = \frac{1}{2} \iint \cos(\tau \dot{\gamma}_k(t)) \varphi(t-u,\tau) \, [\mathbf{K}(t,\tau)]_{kk} \, e^{-j2\pi f\tau} du d\tau. \tag{54}$$

When different sources are uncorrelated, their time-frequency signatures have no significant overlap. If the t-f points located in the autoterm region of the kth source are used in constructing the SPTFD matrix, then

$$\mathbf{D_{xx}}(t,f) = \begin{bmatrix} \mathbf{a}^{[v]}(\phi_k) & 0 \\ 0 & \mathbf{a}^{[h]}(\phi_k) \end{bmatrix} \mathbf{M}_k \begin{bmatrix} \mathbf{a}^{[v]}(\phi_k) & 0 \\ 0 & \mathbf{a}^{[h]}(\phi_k) \end{bmatrix}^H, \tag{55}$$

where

$$\mathbf{M}_k = \frac{1}{2} D_{s_k s_k}(t,f) \begin{bmatrix} \cos(2\gamma_k(t)) & \sin(2\gamma_k(t)) \\ \sin(2\gamma_k(t)) & -\cos(2\gamma_k(t)) \end{bmatrix} + \begin{bmatrix} c_{kk}(t,f) & 0 \\ 0 & c_{kk}(t,f) \end{bmatrix}.$$

In the new structure of the SPTFD matrix of Eq. (55), the source time-varying polarization has the effect of loading the diagonal elements with $c_{kk}(t,f)$ and, as such, alters the eigenvalues of the above 2×2 matrix. However, the eigenvector of $\mathbf{M}_k$ remain unchanged. The new eigenvalues are $\lambda_{1,2} = c_{kk}(t,f) \pm \frac{1}{2} D_{s_k s_k}(t,f)$. The signal polarization signature, i.e., the eigenvector corresponding to the maximum eigenvalue, is $\mathbf{v}_{k,\max} = \begin{bmatrix} \cos(\gamma_k(t)) & \sin(\gamma_k(t)) \end{bmatrix}^T$. Therefore, in the context of PTF-MUSIC, the instantaneous polarization characteristics can be utilized for source discriminations.

VII. Subarray and Polarimetric Averaging

In coherent signal environments, spatial smoothing [28] and polarization averaging [29] methods are commonly applied in the MUSIC algorithms to restore the rank of the source matrix, prior to signal and noise subspace estimations. While spatial smoothing has a drawback of reducing the array aperture, polarization averaging eliminates pertinent source polarization information. In a combined spatial and polarization averaging approach, signal polarizations can be used to limit the reduction in array aperture. This, in turn, increases the number of coherent sources that can be resolved by the array over the case where only spatial averaging is performed.

In this section, the above methods are considered for the PTF-MUSIC for estimating DOAs of coherent sources in the context of TFDs, using dual-polarized double-feed arrays. For subarray averaging, uniform linear arrays (ULAs) are assumed with identical array manifolds for both polarizations, i.e. $\mathbf{a}^{[v]}(\phi) = \mathbf{a}^{[h]}(\phi) = \mathbf{a}(\phi)$. For polarization averaging, only the latter assumption (identical manifolds for both polarizations) is required.

39

A. Subarray Averaging

Subarray averaging involves dividing the m dual-polarized antenna array into p overlapping subarrays of $m_1 = m - p + 1$ antennas, and averaging the respective p subarray SPTFD matrices. Define $\mathbf{A}_1(\boldsymbol{\Phi})$ as the new $m_1 \times n$ steering matrix for the first subarray which consists of the first m_1 rows of matrix $\mathbf{A}(\boldsymbol{\Phi}) = \mathbf{A}^{[v]}(\boldsymbol{\Phi}) = \mathbf{A}^{[h]}(\boldsymbol{\Phi})$. The data vector at the kth subarray is expressed as

$$\mathbf{x}^{(k)}(t) = \begin{bmatrix} \mathbf{x}^{(k)[v]}(t) \\ \mathbf{x}^{(k)[h]}(t) \end{bmatrix} = \mathbf{B}_1^{(k)}(\boldsymbol{\Phi}) \begin{bmatrix} \mathbf{s}^{[v]}(t) \\ \mathbf{s}^{[h]}(t) \end{bmatrix} + \begin{bmatrix} \mathbf{n}^{(k)[v]}(t) \\ \mathbf{n}^{(k)[h]}(t) \end{bmatrix}, k = 1, 2, \ldots, m_1, \tag{56}$$

where $\mathbf{n}^{(k)[i]}(t)$ is the noise vector at the subarray for polarization i, $i = v$ or h,

$$\mathbf{B}_1^{(k)}(\boldsymbol{\Phi}) = \begin{bmatrix} \mathbf{A}_1(\boldsymbol{\Phi})\boldsymbol{\Lambda}^{k-1}(\boldsymbol{\Phi}) & \mathbf{0} \\ \mathbf{0} & \mathbf{A}_1(\boldsymbol{\Phi})\boldsymbol{\Lambda}^{k-1}(\boldsymbol{\Phi}) \end{bmatrix}, \tag{57}$$

$$\boldsymbol{\Lambda}(\boldsymbol{\Phi}) = \text{diag}\left[e^{-j2\pi \frac{d}{\lambda} \sin(\phi_1)}, \cdots, e^{-j2\pi \frac{d}{\lambda} \sin(\phi_n)} \right]. \tag{58}$$

where d denotes the sensor interelement spacing and λ denotes the source wavelength. Denoting $\mathbf{D}_{\mathbf{xx}}^{(k)}(t, f)$ as the SPTFD matrix corresponding to $\mathbf{x}^{(k)}(t)$ of the kth subarray, the spatially smoothed SPTFD matrix is defined by averaging $\mathbf{D}_{\mathbf{xx}}^{(k)}(t, f)$ over the p subarrays, i.e.,

$$\mathbf{D}_{\mathbf{xx}SA}(t, f) = \frac{1}{p} \sum_{k=1}^{p} \mathbf{D}_{\mathbf{xx}}^{(k)}(t, f). \tag{59}$$

The averaged SPTFD matrix can be written as the augmentation of four spatially-smoothed auto- and cross-polarized SPTFD matrices, expressed as

$$\mathbf{D}_{\mathbf{xx}SA}(t, f) = \begin{bmatrix} \mathbf{D}_{\mathbf{xx}SA}^{[vv]}(t, f) & \mathbf{D}_{\mathbf{xx}SA}^{[vh]}(t, f) \\ \mathbf{D}_{\mathbf{xx}SA}^{[hv]}(t, f) & \mathbf{D}_{\mathbf{xx}SA}^{[hh]}(t, f) \end{bmatrix}. \tag{60}$$

The (k, l)-th element of $\mathbf{D}_{\mathbf{xx}SA}^{[ij]}(t, f)$, $i, j = v, h$, with $k, l = 1, 2, \ldots, m_1$, of the auto- ($i = j$) and cross-polarized ($i \neq j$) matrices in the above equation can be described as

$$\begin{aligned} D_{x_k x_l SA}^{[ij]}(t, f) &= \frac{1}{p} \sum_{r=1}^{p} D_{x_{k+r-1} x_{l+r-1}}^{[ij]}(t, f) \\ &= \frac{1}{p} \sum_{r=1}^{p} \left(\sum_{b=1}^{n} \sum_{c=1}^{n} a_{b, k+r-1} \left(a_{c, l+r-1} \right)^* D_{s_b s_c}^{[ij]}(t, f) \right) \\ &= \sum_{b=1}^{n} \sum_{c=1}^{n} \left(\frac{1}{p} \sum_{r=1}^{p} a_{b, k+r-1} \left(a_{c, l+r-1} \right)^* \right) D_{s_b s_c}^{[ij]}(t, f) \\ &= \sum_{b=1}^{n} \sum_{c=1}^{n} \left(\frac{1}{p} \breve{\mathbf{a}}_{c,k}^{H} \breve{\mathbf{a}}_{b,l} \right) D_{s_b s_c}^{[ij]}(t, f) = \sum_{b=1}^{n} \sum_{c=1}^{n} \breve{\beta}_{b,c,k,l} D_{s_b s_c}^{[ij]}(t, f), \end{aligned} \tag{61}$$

where $\breve{\mathbf{a}}_{b,l} = [e^{-j2\pi(l-1)\frac{d}{\lambda}\sin(\theta_b)}, e^{-j2\pi l\frac{d}{\lambda}\sin(\theta_b)}, \cdots, e^{-j2\pi(l+p-2)\frac{d}{\lambda}\sin(\theta_b)}]^T$ is the steering vector of a subgroup of p sensors for which the received signals are averaged, and $\breve{\beta}_{b,c,k,l} = \breve{\mathbf{a}}_{c,k}^H \breve{\mathbf{a}}_{b,l}/p$ is the spatial correlation between signals b and c defined in the p-sensor group. It is easy to show that $|\breve{\beta}_{b,b,k,l}| = 1$ for any b, whereas $|\breve{\beta}_{b,c,k,l}| < 1$ for $b \neq c$. Different values of k and l affect the phase of $|\breve{\beta}_{b,c,k,l}|$ but not its magnitude. Therefore, averaging the TFDs of the received data across the p array sensors reduces the interactions between source signals, whereas the source autoterms remain unchanged. This in turn reduces the off-diagonal elements of the source TFD matrix $\mathbf{D}_{ss}(t,f)$ and leads to matrix rank restoration.

B. Polarimetric Averaging

Similar to subarray averaging, polarimetric averaging aims at combating the rank deficiency of the source SPTFD matrix, $\mathbf{D}_{ss}(t,f)$, provided that the sources have different polarization states. The polarimetric averaged SPTFD matrix is defined as

$$\mathbf{D}_{\mathbf{xx}PA}(t,f) = \frac{1}{2}\left[\mathbf{D}_{\mathbf{x}^{[v]}\mathbf{x}^{[v]}}(t,f) + \mathbf{D}_{\mathbf{x}^{[h]}\mathbf{x}^{[h]}}(t,f)\right]. \tag{62}$$

As with subarray averaging, polarization averaging also reduces source signal crossterms depending on the polarization correlation between them, as was shown in [33].

C. Combined Spatial and Polarimetric Averaging

Polarization averaging can also be used in conjunction with subarray averaging. Denote $\mathbf{D}_{\mathbf{x}^{[v]}\mathbf{x}^{[v]}}^{(k)}(t,f)$ and $\mathbf{D}_{\mathbf{x}^{[h]}\mathbf{x}^{[h]}}^{(k)}(t,f)$ as the STFDs corresponding to $\mathbf{x}^{(k)[v]}(t)$ and $\mathbf{x}^{(k)[h]}(t)$, respectively. Then, the combined subarray and polarization averaged SPTFD matrix becomes

$$\mathbf{D}_{\mathbf{xx}SPA}(t,f) = \frac{1}{2p}\sum_{k=1}^{p}\left[\mathbf{D}_{\mathbf{x}^{[v]}\mathbf{x}^{[v]}}^{(k)}(t,f) + \mathbf{D}_{\mathbf{x}^{[h]}\mathbf{x}^{[h]}}^{(k)}(t,f)\right]. \tag{63}$$

It is implicit in Eqs. (59)–(63) that whether it is polarization and/or subarray averaging, source decorrelation is performed for each t-f point. Once the rank deficiency in the SPTFD matrices corresponding to multiple t-f points is restored, one can estimate the DOAs through PTF-MUSIC (for subarray averaging) or TF-MUSIC (for polarimetric or combined spatial and polarimetric averaging since the polarimetric information is lost in the process of averaging).

D. Decorrelation Requirements

Consider that n_0 sources are selected in the t-f domain, out of which a maximum number of n_c sources are coherent with each other. It is well-known that to decorrelate n_c coherent sources

using spatial averaging, the minimum number of subarrays must be $p \geq n_c$. In addition, the condition $m_1 > n_0$ is required so that the DOAs of all n_0 sources can be identified. However, when polarization averaging is used in addition to subarray averaging, only half the number of subarrays is needed, i.e. $p \geq \lceil n_c/2 \rceil$, given that the polarization states of the coherent sources are not identical. Accordingly, to decorrelate two coherent sources with different polarization states, polarization averaging alone will suffice. To decorrelate four coherent sources with different polarization states, polarization averaging accompanied with two subarays will then be required. The proof of the reduction of the number of subarrays in the presence of polarization averaging was provided in [29] for non-time-frequency based methods. The extension to the t-f based methods is rather straightforward, and achieved by substituting the covariance matrix with a STFD or SPTFD matrix [34].

E. Remarks

From the above discussion, the following remarks are in order.

1. Polarization averaging does not require a ULA, a condition that has to be satisfied in subarray averaging. However, the dual-polarized sensors must be identically polarized and both polarizations have the identical array manifolds.

2. Polarization averaging is beneficial for matrix rank restoration only when the coherent sources have different polarization states. Polarization averaging sacrifices the polarization information and, therefore, signal polarization parameters can not be estimated.

3. In some cases, polarization averaging must be utilized along with subarray averaging. For example, when three sources impinge on a five-sensors ULA, while polarization averaging combined with two subarrays can resolve the source DOAs, subarray averaging alone would fail.

VIII. Simulations

A. Uncorrelated Source Scenarios

We consider two sources (sources 1 and 2) with chirp waveforms in the presence of an undesired sinusoidal signal (source 3) which impinge on a ULA of four ($m = 4$) dual-polarized cross-dipoles with half-wavelength interelement spacing. The vertical and horizontal array manifolds are set to be equal. Table 1 shows the sources' respective normalized starting and end frequencies, DOAs (measured from the the broadside), and the two polarization parameters, γ and η. All signals have the same signal power (SNR=13dB). The task is to find the DOAs of the chirp signals.

The data length is 256 samples and the length of the rectangular window used in the pseudo Wigner-Ville distribution (PWVD) is 65 samples.

As proposed in [35], averaging the sensor TFDs across the array mitigates the source crossterms and, as such, enhances the source t-f signatures. The PWVDs averaged over the four sensors are shown in Figs. 2(a) and 2(b), respectively, for the vertical and horizontal polarizations. Because the sources are closely spaced, crossterm mitigation through array averaging is limited. To further suppress the crossterms, we utilize both the spatial and polarimetric dimensions. Fig. 2(c) shows the PWVD averaged over the four sensors as well as both polarizations. In this case, since source 1 and source 2 have orthogonal polarizations, the crossterms between the two chirp signals are completely suppressed, revealing the source instantaneous frequencies and the true chirp signatures. The t-f points along these signatures can, subsequently, be considered for STFD and SPTFD matrix constructions.

The PTF-MUSIC spectrum is computed and the results are compared with the conventional MUSIC, polarimetric MUSIC, and TF-MUSIC. The MUSIC spectra for three independent trials are shown in Fig. 3. For the conventional and TF-MUSIC, only the vertical polarization components are used. For the TF- and the PTF-MUSIC, 192 t-f points were selected along the signatures of each of the two chirp signals meanwhile the sinusoidal signal is eliminated from consideration. The TF-MUSIC benefits from fewer sources and increased SNR, whereas the polarimetric MUSIC utilizes the distinction in the source polarization properties. Both attributes are enjoyed by the PTF-MUSIC. It is evident that only the proposed PTF-MUSIC accurately estimates the DOAs of the two chirp sources.

Figure 4 shows the root mean square error (RMSE) performance of estimated DOA for the four MUSIC methods. The results are obtained using 50 independent trials for each value of SNR and averaged over all the selected sources. The RMSE performance of the conventional MUSIC with twice the number of sensors (i.e., 8 sensors) is also included for comparison. It is seen that the PTF-MUSIC outperforms all other methods. The PTF-MUSIC enjoys about 5dB gain over the polarimetric MUSIC due to the source selection/discrimination capability and the localization of the source signal energy.

B. Coherent Source Scenarios

In the second set of simulations, we consider a ULA of five ($m = 5$) dual-polarized cross-dipoles with half-wavelength interelement spacing. Three sources are considered. The first two sources

(sources 1 and 2) are coherent and of identical chirp signatures, whereas the third one is an undesired sinusoidal signal (source 3). Table II shows the signal parameters. All signals have the same signal power (SNR=10dB). The data length is 256 samples. The PWVD averaged over the five dual-polarized sensors is shown in Fig. 5.

1. Polarimetric Averaging

Polarimetric averaging of the STFD matrices of the data samples across the vertical and the horizontal polarizations can successfully decorrelate coherent sources. Fig. 6 shows the spectra of the conventional MUSIC and TF-MUSIC, respectively, over three independent trials, where polarimetric averaging was employed on the five vertical and five horizontal antennas. For the TF-MUSIC method, only the two coherent sources (i.e., sources 1 and 2) are selected. It is evident that both methods show a clear spectrum peak for source 1 as a result of successful decorrelation of the two coherent sources. However, only the TF-MUSIC shows an exemplary performance for both sources due to the source selection capability.

2. Subarray and Polarization Averaging

In this simulation, polarimetric averaging is performed combined with spatial smoothing. The spectra of the MUSIC and the TF-MUSIC techniques utilizing the combined polarization and subarray averaging are shown in Fig. 7. In this case, the number of subarrays is 2. For comparison, we plotted in Fig. 8 the spectra using the conventional MUSIC method, applied to 10 vertically-polarized antenna array. Due to the close spatial separation between sources 2 and 3, the performance of all non-time-frequency based methods is not satisfactory. Only the TF-MUSIC spectrum, which drops the third signal from consideration, shows sharp and less biased peaks at the DOAs of the two coherent sources.

C. Sources with Time-Varying Polarization

Two chirp signals impinge upon a uniform linear array (ULA) of five cross-polarized (horizontal and vertical) dual-feed sensors. The parameters of the two chirp signals are listed in Table III. Fig. 9 shows the PWVD of two chirp signals. The interelement spacing of the sensors is half a wavelength. The array responses in both horizontal and vertical polarizations are identical. The SNR is 5dB. The source signals' polarization angles $\gamma_1(t)$ and $\gamma_2(t)$ change linearly in the observation period of 512 samples and are shown in Fig. 10. The length of the rectangular window used in the PWVD is 65 samples.

44

We compare the spectra of polarimetric MUSIC and PTF-MUSIC algorithms, where the sources have time-dependent polarizations. When all data samples are used to construct the covariance matrix, polarimetric MUSIC estimation fails to resolve the two sources as both sources appear to have the same polarization (see Fig. 11(a)). This is due to the fact that the two sources have the same second-order moment of the polarization signature over the observation period and, therefore, the covariance matrix based polarimetric MUSIC method cannot distinguish their instantaneous polarization differences.

To take advantage of the time-varying polarizations, therefore, we use 95 snapshots in constructing the covariance matrix for the polarimetric MUSIC in a moving averaging scheme, whereas 95 consecutive t-f points are used for the PTF-MUSIC. Figures 11(b) and (c) show the performance of the polarimetric MUSIC and PTF-MUSIC in tracking the DOA, as the source signal polarization changes. Both methods performance degrades when the polarization distinctions among the two source signal decrease. This is evident in the estimation in the middle region of the two figures. However, the performance of the PTF-MUSIC is superior to that of the polarimetric MUSIC when the sources have a time-varying polarization.

IX. Conclusion

A platform to deal with diversely polarized sources emitting nonstationary signals with clear time-frequency (t-f) signatures has been introduced. This platform, which is termed *Spatial polarimetric time-frequency distributions (SPTFDs)*, utilizes the polarimetric, spatial, and temporal signatures of signals impinging on an array of sensors. Each sensor is of double-feed, dual-polarized antennas. The SPTFD incorporates the time-frequency distributions (TFD) of the received data across the polarization and spatial variables. It allows the discrimination of sources based on their respective direction-of-arrival as well as their polarization and t-f signal characteristics. The use of TFD reveals the source time-varying frequency natures, and as such, permits the consideration of those t-f points of high signal energy concentrations. The eigen-decomposition of SPTFDs constructed from a portion of, or the entire, t-f signatures of all or a subset of the incoming signals is used to define the polarimetric time-frequency MUSIC (PTF-MUSIC) algorithm. This algorithm is show to outperform other existing MUSIC methods, including conventional MUSIC, time-frequency MUSIC, and polarimetric MUSIC. For coherent signal environments, the ability to collect the data from the horizontal and vertical polarized antenna arrays, separately, provides the flexibility to trade off subarray and polarization averag-

45

ing for source matrix rank restoration, and as such, can be used to limit the reduction in array aperture necessary for source decorrelations. The chapter considered the application of TFDs to sources with a time-varying polarization in the context of array processing. It has been shown that the difference in the instantaneous polarizations of the sources can be uniquely utilized by the proposed approach to maintain polarization diversity, specifically, in the cases when the source polarizations have similar span of polarization angles over the observation period.

References

[1] L. Cohen, "Time-frequency distributions — a review," *Proc. IEEE*, vol. 77, no. 7, pp. 941–981, July 1989.

[2] S. Qian and D. Chen, *Joint Time-Frequency Analysis — Methods and Applications*, Englewood Cliffs, NJ: Prentice Hall, 1996.

[3] A. Belouchrani and M. G. Amin, "Blind source separation based on time-frequency signal representations," *IEEE Trans. Signal Processing*, vol. 46, no. 11, pp. 2888–2897, Nov. 1998.

[4] Y. Zhang, W. Mu, and M. G. Amin, "Subspace analysis of spatial time-frequency distribution matrices," *IEEE Trans. Signal Processing*, vol. 49, no. 4, pp. 747–759, April 2001.

[5] R. O. Schmidt, "Multiple emitter location and signal parameter estimation," *IEEE Trans. Antennas Propagat.*, vol. 34, no. 3, pp. 276–280, March 1986.

[6] R. Roy and T. Kailath, "ESPRIT-estimation of signal parameters via rotational invariance techniques," *IEEE Trans. Acoust., Speech, Signal Processing*, vol. 37, pp. 984–995, July 1989.

[7] A. Belouchrani and M. G. Amin, "Time-frequency MUSIC," *IEEE Signal Processing Letters*, vol. 6, pp. 109–110, May 1999.

[8] Y. Zhang, W. Mu, and M. G. Amin, "Time-frequency maximum likelihood methods for direction finding," *J. Franklin Inst.*, vol. 337, no. 4, pp. 483–497, July 2000.

[9] M. G. Amin and Y. Zhang, "Direction finding based on spatial time-frequency distribution matrices," *Digital Signal Processing*, vol. 10, no. 4, pp. 325–339, Oct. 2000.

[10] W. C. Y. Lee and Y. S. Yeh, "Polarization diversity for mobile radio," *IEEE Trans. Commun.*, vol. COM-20, pp. 912–923, May 1972.

[11] D. Giuli, "Polarization diversity in radars," *Proc. IEEE*, vol. 74, no. 2, pp. 245–269, Feb. 1986.

[12] A. I. Kozlov, L. P. Ligthart, and A. I. Logvin, *Mathematical and Physical Modelling of Microwave Scattering and Polarimetric Remote Sensing*, London, U.K.: Kluwer Academic, 2001.

[13] D. J. McLaughlin, Y. Wu, W. G. Stevens, X. Zhang, M. J. Sowa, and B. Weijers, "Fully polarimetric bistatic radar scattering behavior of forested hills," *IEEE Trans. Antennas Propagat.*, vol. 50, no. 2, pp. 101–110, Feb. 2002.

[14] F. Sadjadi, "Improved target classification using optimum polarimetric SAR signatures," *IEEE Trans. Aerosp. Electron. Syst.*, vol. 38, no. 1, pp. 38–49, Jan. 2002.

[15] A. L. Pazmany, R. E. McIntosh, R. D. Kelly, and G. Vali, "An airborne 95 GHz dual-polarized radar for cloud studies," *IEEE Trans. Geoscience and Remote Sensing*, vol. 32, no. 4, pp. 731–739, July 1994.

[16] S. H. Yueh, W. J. Wilson, and S. Dinardo, "Polarimetric radar remote sensing of ocean surface wind," *IEEE Trans. Geoscience and Remote Sensing*, vol. 40, no. 4, pp. 793–800, April 2002.

[17] G. A. Ioannidids and D. E. Hammers, "Optimum antenna polarizations for target discrimination in clutter," *IEEE Trans. Antennas Propagat.*, vol. AP-27, pp. 357–363, 1979.

[18] D. A. Garren, A. C. Odom, M. K. Osborn, J. S. Goldstein, S. U. Pillai, and J. R. Guerci, "Full-polarization matched-illumination for target detection and identifica-tion," *IEEE Trans. Aerosp. Electron. Syst.*, vol. 38, no. 3, pp. 824–837, July 2002.

[19] E. R. Ferrara and T. M. Parks, "Direction finding with an array of antennas having diverse polarizations," *IEEE Trans. Antennas Propagat.*, vol. 31, pp. 231–236, March 1983.

[20] J. Li and R. J. Compton, "Angle and polarization estimation using ESPRIT with a polarization sensitive array," *IEEE Trans. Antennas Propagat.*, vol. 39, pp. 1376–1383, Sept. 1991.

[21] D. Rahamim, R. Shavit, and J. Tabrikian, "Coherent Source Localization Using Vector Sensor Arrays," *IEEE ICASSP*, Hong Kong, Hong Kong, May 2003.

[22] Q. Cheng and Y. Hua, "Performance Analysis of the MUSIC and PENCIL-MUSIC Algorithms for Diversely Polarized Array," *IEEE Trans. Signal Processing*, vol. 42, no. 11, pp. 3150–3165, Nov. 1994.

[23] K. T. Wong and M. D. Zoltowski, "Self-Initiating MUSIC Direction Finding and Polarization Estimation in Spatio-Polarizational Beamspace," *IEEE Trans. on Antennas Propagat.*, vol. 48, no. 9, pp. 1235–1245, Sept. 2000.

[24] K. T. Wong, L. Li, and M. D. Zoltowski, "Root-MUSIC-based direction-finding and polarization estimation using diversely polarized possibly collocated antennas," *IEEE Antennas Wireless Propagat. Letters*, vol. 3, no. 8, pp. 129–132, 2004.

[25] B. A. Obeidat, Y. Zhang, and M. G. Amin, "Polarimetric time-frequency ESPRIT," *Ann. Asilomar Conf. Signals, Sys., and Comput.*, Pacific Grove, CA, Nov. 2003.

[26] A. B. Gershman and M. G. Amin, "Wideband direction-of-arrival estimation of multiple chirp signals using spatial time-frequency distributions," *IEEE Signal Processing Letters*, vol. 7, no. 6, June 2000.

[27] N. Ma and J. T. Goh, "DOA estimation for broadband chirp signals," *IEEE ICASSP*, Montreal, Canada, May 2004.

[28] T. Shan, M. Wax and T. Kailath, "On Spatial Smoothing for Direction-of-arrival Estimation of Coherent Signals," *IEEE Trans. Acoust., Speech, Signal Processing*, vol. ASSP-33, pp. 806–811, Aug. 1985.

[29] H. Yamada, K. Onishi and Y. Yamaguchi, "Polarimetric superresolution technique for 2-D radar target imaging," *SPIE Proc.*, vol. 3120, pp. 317–326, 1997.

[30] A. Belouchrani, M. G. Amin, and K. Abed-Meraim, "Direction finding in correlated noise fields based on joint block-diagonalization of spatio-temporal correlation matrices," *IEEE Signal Processing Letters*, vol. 4, no. 9, pp. 266–268, Sept. 1997.

[31] P. Stoica and A. Nehorai, "MUSIC, maximum likelihood and Cramer-Rao bound," *IEEE Trans. Acoust., Speech, and Sig. Proc.*, vol. 37, no. 5, pp. 720–741, May 1989.

[32] Y. Zhang and M. G. Amin, "Joint Doppler and polarization characterization of moving targets," *IEEE AP-S Int. Symp. and USNC/URSI National Radio Science Meeting*, Monterey, CA, June 2004.

[33] M. G. Amin and Y. Zhang, "Bilinear signal synthesis using polarization diversity," *IEEE Signal Processing Letters*, vol. 11, no. 3, pp. 338–340, March 2004.

[34] B. A. Obeidat, *Polarimetric Array Processing for Nonstationary Signals*, M.Sc. Thesis, Villanova Univ., 2004.

[35] W. Mu, M. G. Amin, and Y. Zhang, "Bilinear signal synthesis in array processing," *IEEE Trans. Signal Processing*, vol. 51, pp. 90-100, Jan. 2003.

TABLE I

SIGNAL PARAMETERS (UNCORRELATED SOURCE SCENARIO)

	start freq.	end freq.	DOA (deg.)	γ (deg.)	η (deg.)
source 1	0.20	0.40	−3	45	0
source 2	0.22	0.42	3	45	180
source 3	0.10	0.10	9	20	0

TABLE II

SIGNAL PARAMETERS (COHERENT SOURCE SCENARIO)

	start freq.	end freq.	DOA (deg.)	γ (deg.)	η (deg.)
source 1	0.20	0.50	−6	35	5
source 2	0.20	0.50	6	45	170
source 3	0.10	0.10	12	25	−90

TABLE III

SIGNAL PARAMETERS (TIME-VARYING POLARIZATION SCENARIO)

	start freq.	end freq.	DOA (deg.)	γ (deg.)	η (deg.)
source 1	0.10	0.30	4	0 to 90	0
source 2	0.20	0.40	12	90 to 0	0
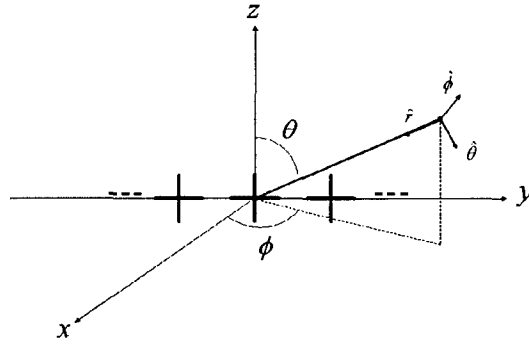
Fig. 1. Dual-polarized array.
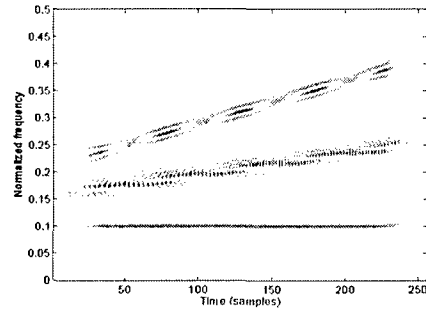
(a) PWVD averaged over the vertically-polarized array sensors.
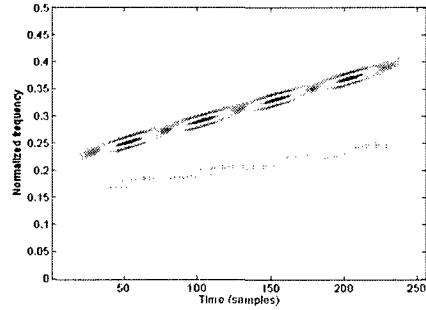
(b) PWVD averaged over the horizontally-polarized array sensors.
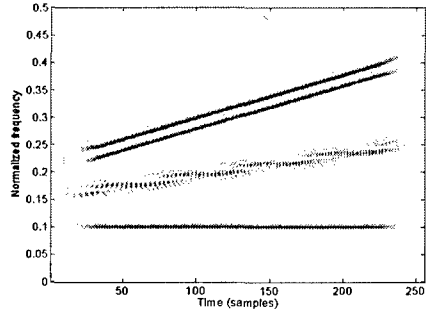
(c) PWVD averaged over array sensors and polarizations.

Fig. 2. Averaged PWVD results.

50

(a) Conventional MUSIC   (b) Polarimetric MUSIC

(c) TF-MUSIC   (d) PTF-MUSIC
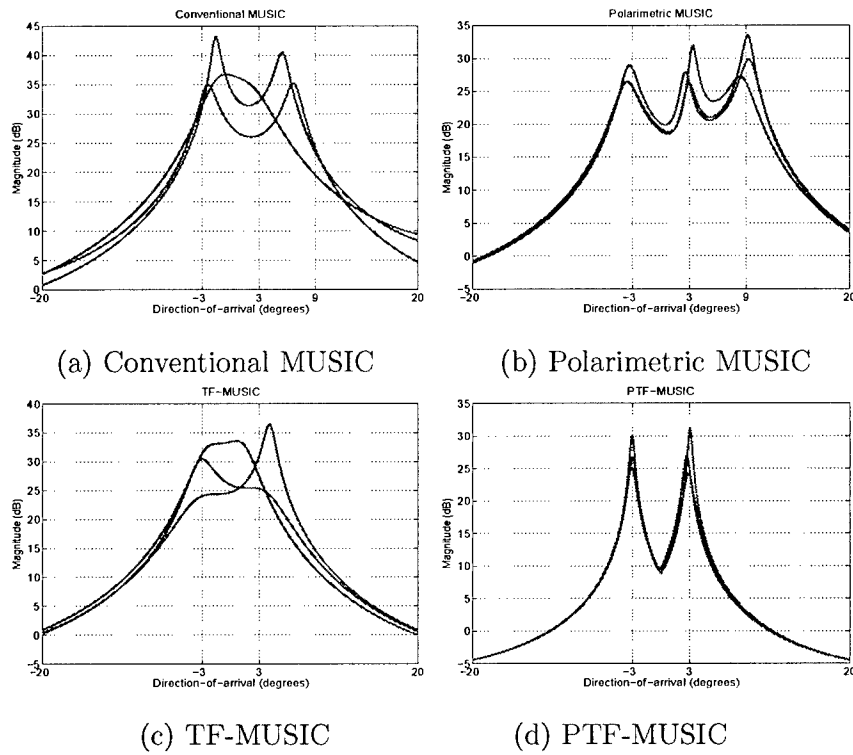
Fig. 3. Comparison of MUSIC spectra.
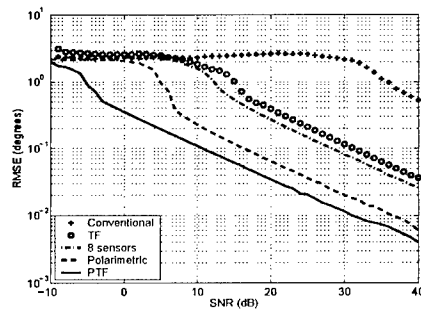
Fig. 4. RMSE performance of the MUSIC methods.
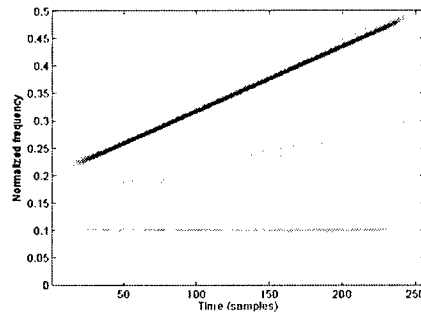
Fig. 5. PWVD averaged over all array sensors and polarizations.

51

(a) Conventional MUSIC   (b) TF-MUSIC (2 signals chosen)
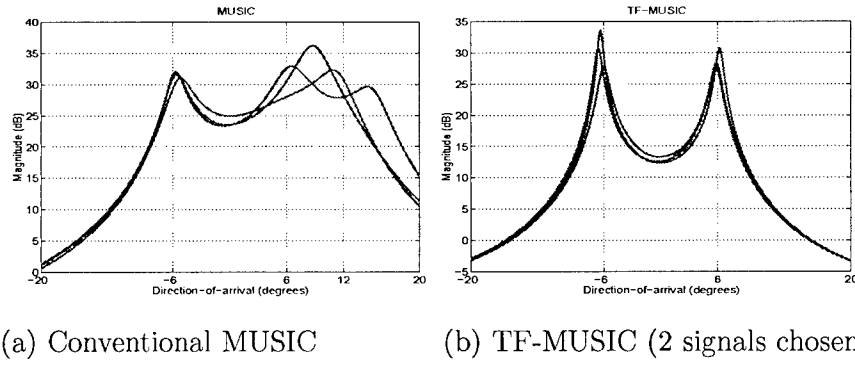
Fig. 6. Conventional MUSIC and TF-MUSIC spectra with polarization averaging.

(a) MUSIC   (b) TF-MUSIC (2 signals chosen)
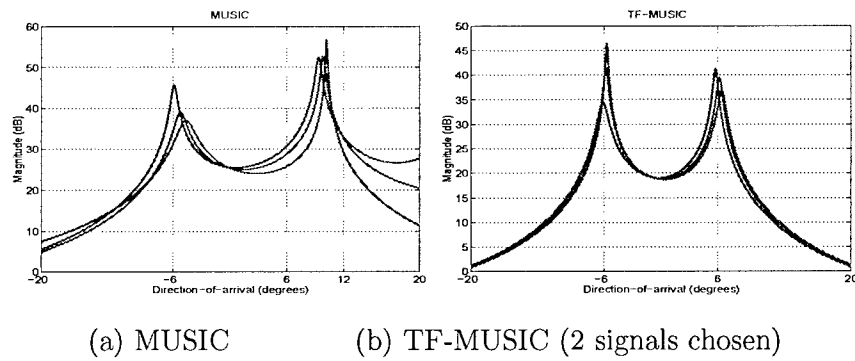
Fig. 7. Conventional and TF-MUSIC spectra with spatial smoothing and polarization averaging.
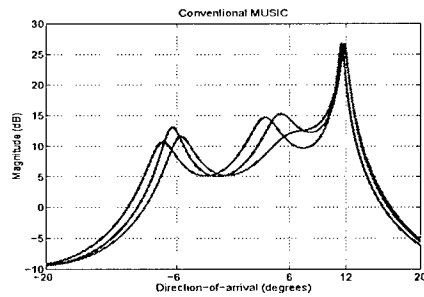
Fig. 8. 10-sensor conventional MUSIC with spatial smoothing.
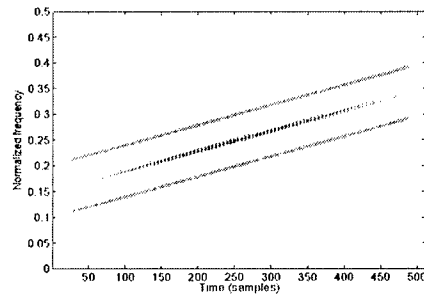
Fig. 9. PWVD of two chirp signals arriving at the reference sensor.

52
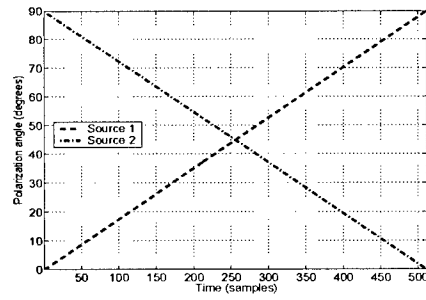
Fig. 10. Time-varying polarization signatures of the sources.
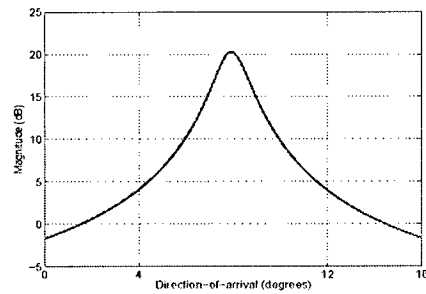
(a) Polarimetric MUSIC spectra based on the entire data
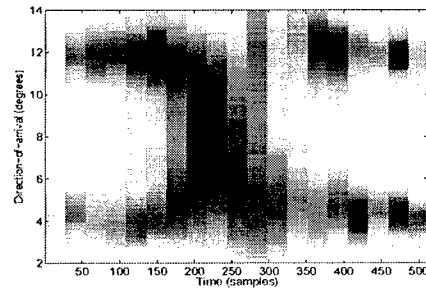
(b) Polarimetric MUSIC tracking
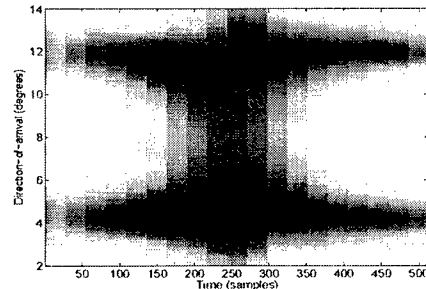
(c) PTF-MUSIC tracking

Fig. 11. MUSIC spectra in time-varying polarization scenario.

53

Chapter 3

Imaging Through Unknown Walls Using Different Standoff Distances

Abstract

In through-the-wall imaging, errors in wall parameters cause targets to be imaged away from their true positions. The displacement in target locations depends on the accuracy of the estimates of the wall parameters as well as the target position relative to the antenna array. A technique using two or more standoff distances of the imaging system from the wall is proposed for application under wall parameter ambiguities. Two different imaging schemes can then be applied to correct for errors in wall characteristics. The first scheme relies on forming target displacement trajectories, each corresponding to a different standoff distance, and assuming different values of wall thickness and dielectric constant. The target position is then determined as the trajectories cross-over point. In the second scheme, an image sequence is generated. Each specific image in this sequence is obtained by summing those corresponding to different standoff distances, but with the same assumed wall parameters. An imaging focusing metric can then be adopted to determine the target position. The chapter analyzes the above two schemes, and provides extensive simulation examples demonstrating their effectiveness.

1 INTRODUCTION

Through-the-Wall Radar Imaging (TWRI) is an emerging technology that addresses a number of civilian problems and has a dual-use with obvious military applications as well. TWRI is a complex and difficult problem that requires cross-disciplinary research. Fundamentally, it is a hybrid between two main areas, statistical signal, radar, and array processing, on one hand, and antennas and electromagnetics, on the other. There are many challenges facing Through-the-Wall Radar Imaging system development, namely, the system should be reliable, portable, light weight, small-size, and have both short acquisition time and set-up time. It is important for the system performance to be robust to ambiguities and inaccuracies in wall parameters and to the presence of non-uniform walls, multiple walls, and operator motion. Ultimately, the system should have high range and cross range resolutions, which are application specific. Finally, the TWRI system must be able to detect and classify motions in a populated scene and in the presence of heavy clutter, which may include interior back and side walls, water pipes, electrical cords, and various types of furniture items.

There are two different approaches to through-the-wall Radar imaging. The first approach is coherent imaging that requires wideband beamforming to be applied, using transmitter and receiver antenna arrays [1-11]. The other is the non-coherent approach that involves several, more simplified and stand-alone radar units. In this case, imaging is performed based on the trilateration technique [12-17]. In this chapter, we focus on the coherent imaging approach. There are several studies on the coherent TWRI to detect stationary and moving target behind the walls with known wall characteristics, such as dielectric constant [1-11]. In practical situations, however, the wall parameters are not exactly known. The errors in wall parameters impact the imaged target position as well as the target spread and intensity profile. A TWRI technique that provides correct target location without the knowledge of the wall parameters was proposed in [18]. The technique in [18] requires data to be acquired using at least two different array placement positions against the wall. At each position, imaging is performed for different assumed values of wall parameters. The displacements in target position due to incorrect wall parameter values form a

trajectory, which traces the highest peak of the target image as its shifts. The trajectories for different array positions, or structures, are shown to intersect at the true target position. The application of the scheme proposed in [18], however, may be limited in practice. Safety reasons may prohibit the system operator from reaching the wall.

Inspired by the work in [18], we introduce in this chapter two new approaches for imaging of point targets under wall parameter ambiguities. In both schemes, imaging is performed at least at two standoff distances. At each standoff distance, the array may be arbitrarily placed. These generalized schemes include the approach in [18] as a special case, where the array is only placed against the wall. In the first proposed approach, for each standoff distance, several images are obtained using different assumed wall characteristics. The extent of the shift of the target image from its true position depends on the error between the assumed and exact wall parameters. The target displacement trajectory is then constructed by connecting the peak values of its images. The intersection of the trajectories corresponding to different standoff distances indicates the target position.

The above approach is effective at short distances from the wall. We note that, unlike the approach in

[18] in which the imaging system only moves parallel to the wall, different standoff distances from the wall can generate images with significantly different angle resolutions. The image of a target from a long standoff distance occupies several image pixels in both angle and range, especially for targets with large incident angle. To overcome image dispersion, we propose a second approach in which we use the effects of both target displacement and blurriness. A composite image sequence is generated with different wall parameters using two or more standoff distances. Each specific element in the image sequence is obtained, for given wall parameter values, by summing the images generated at the two array positions. Since targets are imaged in their true positions with least blurriness when correct wall parameters are used, an image focusing metric may be applied to determine the image corresponding to proper wall thickness and dielectric constant. In this chapter, we use the Entropy measure [19, 20] and show its effectiveness in locating the target behind unknown walls.

The organization of the chapter is as follows. We provide in Section 2 the fundamental equations of wideband through-the-wall radar imaging from a standoff distance. The effect of wall parameter ambiguities on target displacement is discussed in Section 3. In Section 4, a target location estimation approach using of two or more standoff distances is presented. In Section 5, we propose a general implementation of TWRI and target location estimation using two or more array positions at long standoff distances. The conclusion is provided in Section 6.

2   WIDEBAND BEAMFORMING

The wideband beamforming for imaging through the wall has been presented in [9,18], for the antennas placed against the wall. Below, we discuss the general case for arbitrary standoff distance. An *M*-element transmit and an *N*-element receive system is used for imaging. The region to be imaged is located along the positive z-axis. The *m*-th transmitter, located at $\mathbf{x}_{t_m} = (x_{t_m}, z_{t_m})$, illuminates the scene with the wideband signal $s(t)$. The reflection by any target located in the region being imaged is collected at the *n*-th receiver located at $\mathbf{x}_{r_n} = (x_{r_n}, z_{r_n})$. For a single point target located at $\mathbf{x}_p = (x_p, z_p)$, the output of the *n*-th receiver is given by

$$y_{mn}(\mathbf{x}_p) = a(\mathbf{x}_p)s(t - \tau_{p,mn}), \qquad (1)$$

where $a(\mathbf{x}_p)$ is the complex reflectivity of the point target. The propagation delay, $\tau_{p,mn}$, encountered by the signal as it travels from the *m*-th transmitter to the target located at $\mathbf{x}_p$, and back to the *n*-th receiver, is given by

$$\tau_{p,mn} = \frac{r_{m,p} + r_{n,p}}{c} + \frac{l_{m,p} + l_{n,p}}{v} \qquad (2)$$

where c and v are the propagation speeds in the air and in the wall respectively. The variables $r_{m,p}$ and $r_{n,p}$ ($l_{m,p}$ and $l_{n,p}$), respectively, represent the traveling distances of the wave in the air (wall) from the *m*-th transmitter to the target p and from the target to the *n*-th receiver. These parameters are depicted in Fig.1.

The region of interest is divided into a finite number of pixels in range and angle. The complex composite signal corresponding to the image of the pixel located at $\mathbf{x}_q$ (at range R_q in the direction θ_q) is obtained by applying time delays and weights to the data at the N receivers, and summing the results. The block diagram of the imaging system is shown in Fig. 2. For a single target case, the system output is given by [9]

$$b_q(t) = \sum_{m=1}^{M} \sum_{n=1}^{N} w_{t_m} w_{r_n} a(\mathbf{x}_p) s(t - \tau_{p,mn} + \tau_{q,mn})$$ (3)

where w_{r_n} and w_{t_m} are the weights applied to the output of the n-th receiver and the component signal obtained using m-the transmitter. The focusing delay $\tau_{q,mn}$ is applied to the output of the n-th receiver when the transmitter is at the m-th location. This delay, which is given by

$$\tau_{q,mn} = \frac{r_{m,q} + r_{n,q}}{c} + \frac{l_{m,q} + l_{n,q}}{v},$$ (4)

synchronizes the arrivals at different receive locations for the same pixel, and as such allows coherent imaging. The complex amplitude image value for the pixel located at $\mathbf{x}_q$ is obtained by passing the signal $O_q(t)$ through a filter $h(t) = s^*(-t)$, which is matched to the transmitted pulse, and sampling the output of the filter at time $t = 0$,

$$I(\mathbf{x}_q) = (b_q(t) * h(t))|_{t=0} .$$ (5)

The process described by Eqs. (3-5) is performed for all pixels in the region of interest to generate the composite image of the scene. The general case of multiple targets can be obtained by superposition of target reflections.

3   TARGET IMAGE DISPLACEMENT

Errors in wall thickness and dielectric constant impact the traveling time both inside and outside the wall, and subsequently, lead to errors in the applied focusing delays for coherent imaging, given by equation (4). Using estimates, denoted by "~", rather than true values of the wall parameters, equation (4) changes to

$$\widetilde{\tau}_{q,mn} = \frac{\widetilde{r}_{m,q} + \widetilde{r}_{n,q}}{c} + \frac{\widetilde{l}_{m,q} + \widetilde{l}_{n,q}}{\widetilde{v}}, \tag{6}$$

where $\widetilde{v} = \dfrac{c}{\sqrt{\varepsilon_e}}$ is the estimated propagation speed through the wall. Due to errors in propagation speed,

$\widetilde{\tau}_{q,mn} \neq \tau_{q,mn}$. A shift in target position due to focusing delay errors will require $\widetilde{\tau}_{q,mn} = \tau_{p,mn}, \forall m, n$,

i.e., a new set of focusing delays in the presence of wall errors must equal the target propagation delays,

given by Eq. (2).

3.1 The Effect of Wall Thickness Errors

If the assumed wall thickness is $d_e = d + \Delta d$, and the dielectric constant is known, then the

focusing delay for the target at the p-th image pixel from the m-th transmit antenna to the n-th receive

antenna is

$$\widetilde{\tau}_{p,mn,d} = \tau_{p,mn} + \Delta \tau_{p,mn,d} \tag{7}$$

Eq. (3), with $q=p$, can be rewritten as

$$\tau_{p,mn} = \frac{h}{c \cos(\varphi_{t_m,p})} + \frac{h}{c \cos(\varphi_{r_n,p})} + \frac{\sqrt{\varepsilon} d}{c \cos(\theta_{t_m,p})} + \frac{\sqrt{\varepsilon} d}{c \cos(\theta_{r_n,p})}, \tag{8}$$

where $h = h_1 + h_2 = z_p - z_{t_m} - d$. The parameters h_1, h_2 are, as shown in Fig. 1, the distances of the wall

to the transmit antenna and the target, respectively. The change in focusing delay due to the error Δd is

$$\Delta \tau_{p,mn,d} = \frac{\Delta d}{c} \left(\frac{\sin(\varphi_{t_m,p} - \theta_{t_m,p})}{\sin(\theta_{t_m,p})} + \frac{\sin(\varphi_{r_n,p} - \theta_{r_n,p})}{\sin(\theta_{r_n,p})} \right). \tag{9}$$

The derivation of Eq. (9) is given in Appendix A. It is clear from the above equation that the change in

the focusing delay is a linear function of Δd and is a nonlinear function of the incident angles. This

shows that the change in the focusing delay is generally antenna-dependent. If dielectric constant $\varepsilon > 1$,

then $\varphi_{t_m,p} > \theta_{t_m,p}$ and $\varphi_{r_n,p} > \theta_{r_n,p}$. It follows from Eq. (9) that if the wall thickness is over estimated,

i.e., $\Delta d > 0$, then $\Delta\tau_{p,mn,d} > 0$. That is, if d_e is greater than the true value d, the applied focusing delays are longer than those required to coherently combine the signal returns for a target at pixel p, i.e., $\tilde{\tau}_{p,mn} > \tau_{p,mn}$. Now, consider a pixel q that is closer to the wall than p, with $\tau_{q,mn} < \tau_{p,mn}$. To image pixel q, where is no target, under the assumption of wall thickness, $d_e > d$, the applied focusing delays are typically greater than those required if there were no wall errors. In this case, $\tilde{\tau}_{q,mn} > \tau_{q,mn}$. The above two time delay inequalities suggest that there could be a pixel q where $\tilde{\tau}_{q,mn} \approx \tau_{p,mn}$, rendering a displacement of the target from location p to location q. We note that a pure shift in the target position requires $\tilde{\tau}_{q,mn} = \tau_{p,mn}$, for all values of m and n, otherwise a shift is accompanied with blurriness. The above argument is illustrated in Fig. 4, in which we consider three targets at different positions behind the wall located at $(3, 30^0)$, $(3, -30^0)$, $(5, 0^0)$. The transmit and receive arrays are symmetric about their center point, and are placed against the wall. The transmit array consists of four antennas with inter-element spacing of 0.6 meter. The receive array consists of eight antennas with inter-element spacing 0.075 meter, which is half wavelength of signal with 2GHz carrier frequency. Both the transmit and receive arrays are located along the x-axis at positions listed in Table 1. The wall thickness is $d = 0.4$ meter and the dielectric constant is $\varepsilon = 9$, representing a concrete wall. The carrier frequency is 2 GHz and the pulse bandwidth is 1 GHz[1]. The dielectric constant is assumed known, i.e., $\varepsilon_e = \varepsilon$, but the wall thickness is unknown and assumed as $d_e = 0.1, 0.2, 0.3, 0.4, 0.5, 0.6$ m. The images corresponding to different pairs of wall parameters (ε, d_e) are generated using Eq. (3) and are superimposed. Fig. 4 shows that the targets are clearly shifted away from their true positions. If $\Delta d = d_e - d > 0$, then the target images move toward the array and vise versa. Below, we analyze the effect of the wall thickness errors on target displacement in angle, for an arbitrary standoff distance.

---

[1] These signal parameters are typically used in the underlying applications [9,21].

3.1.1 Shift of Target in the Image Due to Wall Thickness Error

The m-th transmit antenna is located at (x_{t_m}, z_{t_m}), as shown in Fig.1. In this case, the traveling time, $\tau_{p,m}$, between the m-th transmit antenna to the target p, *located at (*x_p, z_p*)*, is expressed as

$$\tau_{p,m} = \frac{z_p - z_{t_m} - d}{c \cos(\varphi_{t_m,p})} + \frac{\sqrt{\varepsilon}d}{c \cos(\theta_{t_m,p})} . \tag{10}$$

Assume that under the wall error $\Delta d = d_e - d$, the target, whose true position is p at (x_p, z_p), appears at point q at (x_q, z_q). Denote $\Delta x_{pq} = x_q - x_p$ and $\Delta z_{pq} = z_q - z_p$. The relationship between Δx_{pq} and Δz_{pq} is shown in Fig. 5. For small value of Δd, the estimated time delay from the m-th antenna to point q is expressed as

$$\tilde{\tau}_{q,m} = \tau_{p,m} + \Delta \tau_{pq,m} , \tag{11}$$

$$\Delta \tau_{pq,m} = \frac{\partial \tau_{p,m}}{\partial d} \Delta d + \frac{\partial \tau_{p,m}}{\partial x_q} \Delta x_{pq} + \frac{\partial \tau_{p,m}}{\partial z_q} \Delta z_{pq} = \frac{\Delta d \sin(\varphi_{t_m,p} - \theta_{t_m,p})}{c \sin(\theta_{t_m,p})} + \frac{\Delta x_{pq} \sin(\varphi_{t_m,p})}{c} + \frac{\Delta z_{pq} \cos(\varphi_{t_m,p})}{c} . \tag{12}$$

Note that $\dfrac{\partial \tau_{p,m}}{\partial d} \triangleq \dfrac{\sin(\varphi_{t_m,p} - \theta_{t_m,p})}{c \sin(\theta_{t_m,p})}$, obtained from (A.9), has considered the subsequent changes of the incident angles due to the change in d. For the array antenna to synthesize an image at position q of a target physically present at location p, the difference between $\tilde{\tau}_{q,m}$ and $\tau_{p,m}$ should ideally be zero for all M antennas. To simplify the problem, we consider small array apertures, and assume the following two conditions to be satisfied at the center of the array (it is not necessary that there physically exists an antenna at the center of the array). First, the time delay $\tilde{\tau}_{q,0}$, where the subscript "0" denotes the center of the array, should be equal to $\tau_{p,0}$,

$$\Delta \tau_{pq,0} = 0 . \tag{13}$$

Second, the above time difference is invariant with the position of target p, i.e.,

$$\partial \Delta \tau_{pq,0} / \partial \varphi_{t_0,p} = 0.$$ (14)

From Eq. (12),

$$\Delta \tau_{pq,0} = \frac{\Delta d}{c} \left[\sqrt{\varepsilon} \cos(\theta_{t_0,p}) - \cos(\varphi_{t_0,p}) \right] + \frac{\Delta x_{pq} \sin(\varphi_{t_0,p})}{c} + \frac{\Delta z_{pq} \cos(\varphi_{t_0,p})}{c},$$ (15)

where $\theta_{t_0,p}$ and $\varphi_{t_0,p}$ are respectively, the incident and refraction angles in the wall and the air, related to the path from the center of the transmit array to the target p. Accordingly,

$$\frac{\partial \Delta \tau_{pq,0}}{\partial \varphi_{t_0,p}} = \frac{\Delta d}{c} \left(-\frac{\sin(\theta_{t_0,p})\cos(\varphi_{t_0,p})}{\cos(\theta_{t_0,p})} + \sin(\varphi_{t_0,p}) \right) + \frac{\Delta x_{pq}\cos(\varphi_{t_0,p})}{c} - \frac{\Delta z_{pq}\sin(\varphi_{t_0,p})}{c}.$$ (16)

From (13) and (15),

$$\frac{\Delta d}{c} \left[\sqrt{\varepsilon} \cos(\theta_{t_0,p}) - \cos(\varphi_{t_0,p}) \right] \sin(\varphi_{t_0,p}) + \frac{\Delta x_{pq}\sin^2(\varphi_{t_0,p})}{c} + \frac{\Delta z_{pq}\cos(\varphi_{t_0,p})\sin(\varphi_{t_0,p})}{c} = 0.$$ (17)

From (14) and (16), we obtain

$$\frac{\Delta d}{c} \left(-\frac{\sin(\theta_{t_0,p})\cos^2(\varphi_{t_0,p})}{\cos(\theta_{t_0,p})} + \sin(\varphi_{t_0,p})\cos(\varphi_{t_0,p}) \right) + \frac{\Delta x_{pq}\cos^2(\varphi_{t_0,p})}{c} - \frac{\Delta z_{pq}\sin(\varphi_{t_0,p})\cos(\varphi_{t_0,p})}{c} = 0.$$ (18)

Adding (17) to (18),

$$\Delta x_{pq} = -\Delta d \left(\sqrt{\varepsilon} \cos(\theta_{t_0,p})\sin(\varphi_{t_0,p}) - \frac{\sin(\theta_{t_0,p})\cos^2(\varphi_{t_0,p})}{\cos(\theta_{t_0,p})} \right) = -\Delta d \tan(\theta_{t_0,p})(\varepsilon - 1).$$ (19)

Similarly, we can obtain

$$\Delta z_{pq} = -\Delta d \left(\frac{\cos(\varphi_{t_0,p})}{\cos(\theta_{t_0,p})} \sqrt{\varepsilon} - 1 \right).$$ (20)

From (19) and (20),

$$\frac{\Delta x_{pq}}{\Delta z_{pq}} = \frac{(\varepsilon - 1)\sin(\theta_{t_0,p})}{\cos(\varphi_{t_0,p})\sqrt{\varepsilon} - \cos(\theta_{t_0,p})}.$$ (21)

Now, define the function

$$f(\theta) = \frac{\sin(\theta)}{\cos(\varphi)\sqrt{\varepsilon} - \cos(\theta)} \tag{22}$$

with $\frac{\sin(\varphi)}{\sin(\theta)} = \sqrt{\varepsilon}, 0 \le \theta, \varphi < \frac{\pi}{2}$. Therefore,

$$f'(\theta) = \frac{\cos(\theta)\left(\sqrt{\varepsilon}\cos(\varphi) - \cos(\theta)\right) - \sin\theta\left(\sqrt{\varepsilon}\cos'(\varphi) + \sin(\theta)\right)}{\left(\cos(\varphi)\sqrt{\varepsilon} - \cos(\theta)\right)^2}, \tag{23}$$

where

$$\cos'(\varphi) = \frac{d\left(\sqrt{1 - \varepsilon\sin^2(\theta)}\right)}{d\theta} = -\frac{\varepsilon\sin(\theta)\cos(\theta)}{\cos(\varphi)}. \tag{24}$$

From (23) and (24),

$$f'(\theta) = \frac{\sqrt{\varepsilon}\cos(\theta) - \cos(\varphi)}{\left(\cos(\varphi)\sqrt{\varepsilon} - \cos(\theta)\right)^2 \cos(\varphi)} > 0. \tag{25}$$

The above equation remains valid when the two way traveling time (from transmitter to target and from target to receiver) is considered. When incorporating the effect of both arrays, the shift of the image is given by

$$\Delta x_{pq} = -\Delta d(\varepsilon - 1)[\tan(\theta_{t_0,p}) + \tan(\theta_{r_0,p})] \tag{26}$$

$$\Delta z_{pq} = -\Delta d\left(\frac{\cos(\varphi_{t_0,p})}{\cos(\theta_{t_0,p})}\sqrt{\varepsilon} + \frac{\cos(\varphi_{r_0,p})}{\cos(\theta_{r_0,p})}\sqrt{\varepsilon} - 2\right) \tag{27}$$

where $\theta_{r_0,p}$ and $\varphi_{r_0,p}$ are respectively, the incident and refraction angles in the wall and in the air, related to the path from target p to the center of the receive array.

3.2 The Effect of Dielectric Constant Errors

Similar to the wall thickness error, errors in the dielectric constant also impact the imaging quality. However, closed form expressions similar to (26, 27) are difficult to obtain due to nonlinearity of the relationship involving dielectric constant errors. If the estimated, or assumed, dielectric constant is $\varepsilon_e = \varepsilon + \Delta\varepsilon$, with known wall thickness, then the corresponding focusing delay for the pixel p becomes

63

$$\tilde{\tau}_{p,mn,\varepsilon} = \tau_{p,mn} + \Delta\tau_{p,mn,\varepsilon} \tag{28}$$

where

$$\Delta\tau_{p,mn,\varepsilon} = \frac{d\Delta\varepsilon}{2\sqrt{\varepsilon}c}\left(\frac{1}{\cos(\theta_{t_m,p})} + \frac{1}{\cos(\theta_{r_n,p})}\right). \tag{29}$$

The derivation of Eq.(29) is given in Appendix B. It is clear that $\Delta\tau_{p,mn,\varepsilon} > 0$ for $\Delta\varepsilon > 0$. Similar to the

case of $d_e > d$, discussed in Section 3.1, for $\varepsilon_e > \varepsilon$, the target at location p may be displaced to some

pixel q closer to the wall. For illustration, we consider the same wall characteristics and the same three

targets as in Section 3.1. In this case, however, we assume knowledge of the true wall thickness,

$d_e = d$, but we use different values of the wall dielectric constant,

$\varepsilon_e = 3.24, 4.48, 6.25, 9, 12.25, 14.44, 17.64$. The images corresponding to different pairs of wall

parameters are superimposed in Fig. 6, which shows clear displacement of the targets.

4 TARGET LOCATION ESTIMATION USING TWO DISPLACEMENT TRAJECTORIES

Consider two standoff distances of the antenna arrays with array centers at $(x_1, -z_1), (x_2, -z_2)$,

respectively, with $z_1 < z_2$. The analysis in Section 3 also applies to this general system placement.

(I) *For target located at* (x_p, z_p) *and* $x_1 = x_2 = x_p$. Let $\theta_{1,p}$, $\theta_{2,p}$ denote the incident angle

relative to the array center, for standoff distance z_1 and z_2, respectively. For the target located at

(x_p, z_p), $\theta_{1,p} = \theta_{2,p} = 0$. Equations (19) and (20) state that target p is imaged away from its true

position in the z-direction if a wall thickness error is introduced. The above argument is verified by the

simulation results in Fig. 7. In this simulation, three targets, located at $(3\sin(30^0), 3\cos(30^0))$,

$(-3\sin(30^0), 3\cos(30^0))$, and $(0,5)$ are imaged from two standoff distances of the radar system, at $(0,0)$m

and $(0,-3)$m. Dielectric constant $\varepsilon = 9$, and different assumed wall thicknesses,

$\Delta d = -0.3, -0.2, -0.1, 0, 0.1, 0.2, 0.3$ m are used. Fig. 7 shows that the image of the target at (0,5) shifts in

range with different assumed wall thickness, but assumes the same position for the two standoff distances.

(II) *For target located at* (x_p, z_p), *with* $\theta_{1,p}, > \theta_{2,p} > 0$. Since $\theta_{1,p}, > \theta_{2,p} > 0$, then according

to Eq. (25), the target imaged from the first standoff distance has a different angular shift compared to its

image from the second standoff distance. Accordingly, images of the target generated at different standoff

distances separate under errors in the wall thickness. The target is, however, imaged at its true position

when the true wall thickness is used. Although, for $\Delta d > 0$, both target images with different standoff

distances shift towards the array, the image of the first standoff distance with larger incident angle $\theta_{1,p}$

moves closer to the array than that of the second standoff distance with smaller $\theta_{2,p}$. This is verified by

the simulation in Fig. 7. The peaks of the images in Fig. 7 are marked as "." and "*" in Fig. 8, for the two

standoff distances. Figs.(7, 8) demonstrate that the image shift trajectories of the target

($3\sin(30^0), 3\cos(30^0)$) cross at its true position. As depicted in the same figures, the above argument also

applies to the other non-center target. Similar behavior of target images and trajectories is exhibited for

the case in which the dielectric constant is assumed.

We consider next the general case, where both the wall thickness and dielectric constant are

unknown. The two system standoff distances at (0,0) and (0,-3) is used to image three targets located at

($4.5\sin(18^0), 4.5\cos(18^0)$) m, ($4.5\sin(-18^0), \cos(-18^0)$) m, and (0,5.5) m. The wall parameters are

$d = 0.4$ m, $\varepsilon = 9$. The simulation result is presented in Fig. 9 with assumed dielectric

constant $\varepsilon_e = 12.25 \neq \varepsilon$, and seven assumed wall thickness values $d_e = 0.1, 0.2, 0.3, 0.4, 0.5, 0.6, 0.7$ m. The

figure shows that the image trajectories from the two standoff distances of each side target intersect

approximately at the true wall thickness value.

5   AN ALTERNATIVE IMAGING APPROACH

The analysis in the previous section shows that the intersection of the target image trajectories for

two standoff distances provides good estimates of the wall parameters, yielding correct target locations.

The trajectory is formed by tracing the target image peaks. This approach works well for smaller stand-off distances. However, there are potential problems in adopting this approach for longer standoff distances. As argued below, a target may be represented by multiple peaks.

5.1 Problem in tracking image peaks

It is important to note that in order to find the intersection of the target displacement trajectories with two different standoff distances, the coordinate systems must not be changed for different array positions. For each standoff distance, the imaged region is divided into small image pixels with the same range and angle coordinate system. Suppose the center of the imaging system at one standoff distance is chosen as the origin of the coordinate system. Using the same coordinates, the images obtained at a longer standoff distance will have a lower angle resolution. Furthermore, the pixels in the same range cell corresponding to one standoff distance may not have the same time delay to the center of array when imaged from another standoff distance. Therefore, a target, especially one with a long distance from antenna array, might be imaged in several image pixels that extend over several angle and range cells. This argument is verified by the simulation result in Fig. 10. We consider five targets located at $(7,30^0)$, $(7,18^0)$, $(7,0^0)$, $(7,-18^0)$, $(7,-30^0)$. The exact values of wall thickness and dielectric constant are 0.4m and 9, respectively. The transmit and receive antenna arrays have the structure depicted in the Table1, with standoff distance 8m.

Theoretically, the peak position of target image is in the center of the target image. However, the image is obtained by the discrete sampling of image pixels in range and angle. Therefore, the sample points might not be exactly in the center of the target image. Tracing the target shifts of low resolution images could cause problems for the target location estimation schemes that incorporate target trajectory intersections.

5.2 New approach for imaging using different array placements

From the analysis in Section 4, the target images generated from different standoff distances coincide or highly overlap at the target true position, when the true wall parameters are used. When an incorrect wall thickness is applied, the target is imaged in different positions from the two standoff distances, i.e., it will appear separated in a superimposed image. Therefore, one approach to estimate the true position of a target, is to form the composite images with different assumed wall thickness values, and find the wall characteristics at which the images of the target from different standoff distances are mostly overlapping. The latter can be accomplished using a focusing or sharpness metric. In the following, we give a pseudo code of the proposed target location estimation algorithm with known dielectric constant, ε.

(1) Generate a sequence of images $A_{d_{e1}}, A_{d_{e2}}, \cdots, A_{d_{eK}}$, for a given array standoff distance and using ε. These images correspond to the assumed wall thickness values $d_{e_1}, d_{e_2}, \cdots, d_{eK}$.

(2) Repeat step 1 and generate another sequence of images $B_{d_{e1}}, B_{d_{e2}}, \cdots, B_{d_{eK}}$, for another standoff distance.

(3) Generate a composed image $I_{d_{e1}}, I_{d_{e2}}, \cdots, I_{d_{eK}}$ from $A_{d_{e1}}, A_{d_{e2}}, \cdots, A_{d_{eK}}$ and $B_{d_{e1}}, B_{d_{e2}}, \cdots, B_{d_{eK}}$, with $I_{d_{ek}} = A_{d_{ek}} + B_{d_{ek}}, k = 1, \ldots, K$. $I_{d_{e1}}, I_{d_{e2}}, \cdots, I_{d_{eK}}$ is a new and composite image sequence over the assumed wall thickness variable.

(4) Find the optimum wall thickness d_{ek_0} at which the applied focusing criterion assumes the largest or the smallest value for the image sequence $I_{d_{e1}}, I_{d_{e2}}, \cdots, I_{d_{eK}}$. If multiple answers exist, then select the one which is more physically acceptable.

(5) A more accurate estimate of the wall thickness can be obtained if more images $A_{d_{e1}}, A_{d_{e2}}, \cdots, A_{d_{eK}}$ and $B_{d_{e1}}, B_{d_{e2}}, \cdots, B_{d_{eK}}$ are generated and added around the initial estimate, d_{ek_0}.

(6) Use the wall parameter (ε, d_{ek_0}) to generate the final image.

There are different criteria that can be used in Step 4 to measure the image focusing levels. One of the most commonly used focusing criterion is the Minimum Entropy [19,20]. For each composite target image $I_{d_{ei}}$ in the target image sequence $I_{d_{e1}}, I_{d_{e2}}, \cdots, I_{d_{eK}}$, we calculate the entropy $E(d_{ei})$ of $I_{d_{ei}}$, as

$$E(d_{ei}) = -\sum_{l=1}^{L}\sum_{j=1}^{J} p_{l,j}(d_{ei})\log(p_{l,j}(d_{ei})), \qquad p_{l,j}(d_{ei}) = \left|x_{d_{ei}}(l,j)\right|^2. \qquad (30)$$

where $p_{l,j}(d_{ei})$ is the square of the pixel value $x_{d_{ei}}(l,j)$, L and J are the range and cross range sizes of image $I_{d_{ei}}$ respectively. The parameter $\hat{d}_e$, corresponding to the smallest value of $E(d_{ei})$, is taken as the estimate of the wall thickness. The motivation of using the minimum entropy of the composite image to measure the degree of overlapping of images $A_{d_{ei}}$ and $B_{d_{ei}}$ is that the more $A_{d_{ei}}$ and $B_{d_{ei}}$ overlap, the larger the change in the image pixel values. The above criterion is typically applied in SAR, ISAR motion compensation and auto-focus [19,20]. We note that there are other equally effective criteria [22-25] that can also be used in equation (30).

For illustration, consider the original transmit and receive antenna structures of Table 1. The imaging system is positioned at $(-3,-4)$ m and $(1,-8)$ m, respectively. We consider three targets behind the wall, located at $(0,7)$ m, $(7\sin(30^0), 7\cos(30^0))$ m, and $(-7\sin(30^0), 7\cos(30^0))$ m. The true wall parameters are $d = 0.4$ m, $\varepsilon = 9$. In the simulation, the dielectric constant is known. For each array placement, the wall thickness values $d_e = 0.1, 0.15, 0.2, 0.25, 0.30, 35, 0.4, 0.45, 0.55, 0.6, 65, 0.7$ m are assumed. Superimposed images from the two standoff distances are shown in Fig.11 (a), and the corresponding peaks of the images are shown in Fig.11 (b). Fig.11 (b) shows that, due to large target image dispersions over neighboring pixels, the target trajectories cannot be properly formed. Therefore, we resort to using a focusing metric to solve the problem. The Entropy of the composite image in Fig.11 (a) is computed and plotted with the solid line in Fig. 11 (c) with respect to the assumed wall thickness. It

shows a minimum value at $d_e = d = 0.4$m. The above algorithm can also be applied to estimate the dielectric constant when the wall thickness is unknown.

In the next example, we examine the sensitivity of the proposed techniques to the imaging system placements. Fig. 12 shows a simulation result for the targets of Fig.11, but the two standoff positions (0, -4)m and (0,-8)m are used instead of (-3, -4)m and (1,-8)m in Fig. 11. Fig.12 shows the target images with different assumed wall thickness. The incident angles from the standoff positions in Fig. 12 are smaller than those in Fig.11, causing the images to overlap, while they are separated in Fig.11. The Entropy of the composite images for Fig.12 (a) is plotted with the ".-" line in Fig.11 (c). It does not reach a minimum at the true value d=0.4m of wall thickness. Similar behavior is observed when the system is shifted parallel to the wall without changing the standoff distance.

5.3 Imaging with Both Parameters Unknown

Now, we consider the case in which both the wall thickness and the dielectric constant are unknown. We first assume a value of one of the two parameters, say the dielectric constant, ε_e. Then, we proceed with the same steps used in Section 5.2, where the dielectric constant is known. That is, we generate a sequence of images using different assumed values of the wall thickness. The trajectories of target displacements with different standoff distances cross at some assumed wall thickness d_{ε_e}. Notice that the estimated d_{ek_0} in this case depends on the assumed dielectric constant, ε_e. Therefore, the pair (ε_e, d_{ek_0}) employed to generate the final image is not unique.

Consider the two standoff positions of the imaging system, and the true wall parameters to be the same as those in Fig.11. We assume the wall dielectric constant to be $\varepsilon_e = 12.25$. For each one of the array position, the wall thickness values $d_e = 0.1, 0.15, 0.2, 0.25, 0.30, 35, 0.4, 0.45, 0.55, 0.6, 65, 0.7$ m are assumed. Superimposed images from the two standoff distances are generated and the corresponding peaks of the images are shown in Fig.13 (a). Similar to Fig. 11 (b), the target trajectories cannot be properly formed by tracing the highest peaks of the images and the intersection points are not clear.

69

Therefore, we resort to using a focusing metric to solve the problem. The entropy of composite image for each wall pair is computed and plotted in Fig.13 (b) with respect to the assumed wall thickness. The entropy assumes a minimum value at $d_e = 0.35$m, which differs from the true wall thickness value. However, the wall parameter pair $(d_e, \varepsilon_e) = (0.35, 12.25) \neq (d, \varepsilon)$ yields correct target positions for both standoff distances. This is because the effects of the errors in both d and ε are canceled out, leading to the correct set of delays required to coherently combine the waveform returns from the target positions. The imaging results for 4 m and 8m standoff distances are shown in Figs.14 (a) and 14 (b), respectively.

6 CONCLUSIONS

"Seeing" through the wall using radio frequencies is an emerging technology that is currently sought out by both the commercial and government sectors. For logistical and safety reasons, imaging is preferably performed at a standoff distance from the external wall. This requirement, combined with the fact that wall characteristics may be unknown, presents a challenge in producing accurate and reliable images. In this chapter, we proposed a wideband beamforming-based technique that allows the system operator to perform imaging with wall parameter ambiguities and from a standoff distance. The approach depends on the assumption that imaging can be obtained at two or multiple standoff distances. We focused on point targets and assume single uniform walls. The approach traces the images as they shift in position for different assumed wall thickness and dielectric constant. The target image trajectories for two standoff distances intersect. The wall parameters corresponding to the intersection point are used to provide the target positions. The chapter presented an alternative approach which is useful at long standoff distances and incorporates both the shift and blurriness effects of the target when using incorrect wall parameters. The Entropy was applied to the composite images from two standoff distances to determine the target position with least blurriness. Several simulation examples were presented which demonstrated the effectiveness of the proposed approach. This chapter has only dealt with two-dimensional imaging using one-dimensional array. The applicability of the proposed techniques to 3-D imaging is expected to hold, but should be separately analyzed and verified.

Appendix A

For simplicity, we only consider the traveling time from a transmit antenna to the target. As shown in Fig. 5, without errors in the wall thickness estimation,

$$x_{p,m} = x_p - x_{tm} = d \tan(\theta_{t_m,p}) + h \tan(\varphi_{t_m,p}),$$
(A.1)

where $h = h_1 - h_2 = z_p - z_{t_m} - d$. We consider the traveling time when there is an error $\Delta d = d_e - d$ in the estimated wall thickness. When d changes to $d + \Delta d$ (and subsequently h changes to $h - \Delta d$) and $\varphi_{t_m,p}$ changes to $\varphi_{t_m,p} + \Delta\varphi_{t_m,p}$ (and subsequently $\theta_{t_m,p}$ changes to $\theta_{t_m,p} + \Delta\theta_{t_m,p}$), the change in $x_{p,m}$ can be approximated by

$$\Delta x_{p,m} = \frac{\partial x_{p,m}}{\partial d} \Delta d + \frac{\partial x_{p,m}}{\partial h} \Delta h + \frac{\partial x_{p,m}}{\partial \theta_{t_m,p}} \Delta\theta_{t_m,p} + \frac{\partial x_{p,m}}{\partial \varphi_{t_m,p}} \Delta\varphi_{t_m,p}$$

$$= \tan(\theta_{t_m,p})\Delta d + \tan(\varphi_{t_m,p})\Delta h + d\cos^{-2}(\theta_{t_m,p})\Delta\theta_{t_m,p} + h\cos^{-2}(\varphi_{t_m,p})\Delta\varphi_{t_m,p}.$$
(A.2)

For the path to pass through the true target position, $\Delta x_{p,m} = 0$. That is,

$$\Delta d \tan(\theta_{t_m,p}) + \Delta h \tan(\varphi_{t_m,p}) + d\cos^{-2}(\theta_{t_m,p})\Delta\theta_{t_m,p} + h\cos^{-2}(\varphi_{t_m,p})\Delta\varphi_{t_m,p} = 0.$$
(A.3)

From the Snell's law, $\sin(\varphi_{t_m,p}) = \sqrt{\varepsilon}\sin(\theta_{t_m,p})$, we can deduce the approximation

$$\Delta\theta_{t_m,p} = \Delta\varphi_{t_m,p} \frac{\cos(\varphi_{t_m,p})}{\sqrt{\varepsilon}\cos(\theta_{t_m,p})}.$$
(A.4)

Substituting (A.4) in (A.3) yields

$$\Delta d \tan(\theta_{t_m,p}) + \Delta h \tan(\varphi_{t_m,p}) + \frac{d}{\sqrt{\varepsilon}}\cos^{-3}(\theta_{t_m,p})\cos(\varphi_{t_m,p})\Delta\varphi_{t_m,p} + h\cos^{-2}(\varphi_{t_m,p})\Delta\varphi_{t_m,p} = 0.$$
(A.5)

Since $\Delta h = -\Delta d$, then

$$\Delta\varphi_{t_m,p} = \frac{\Delta d[\tan(\varphi_{t_m,p}) - \tan(\theta_{t_m,p})]}{\dfrac{d}{\sqrt{\varepsilon}}\dfrac{\cos(\varphi_{t_m,p})}{\cos^3(\theta_{t_m,p})} + \dfrac{h}{\cos^2(\varphi_{t_m,p})}}.$$
(A.6)

(A.6) shows the necessary shift of the incident angles for the path traveling from the m-th antenna to the point p when the wall thickness error is taken into account. On the other hand, the total travel time from the m-th antenna to the target position p is given by

$$\tau_{p,m} = \frac{1}{c} \left(\frac{\sqrt{\varepsilon} d}{\cos(\theta_{t_m,p})} + \frac{h}{\cos(\varphi_{t_m,p})} \right). \tag{A.7}$$

Therefore, the additional travel time due to Δd and $\Delta \varphi_{t_m,p}$ can be expressed using first-order approximation as

$$
\begin{aligned}
\Delta \tau_{p,m} &= \frac{\partial \tau_{p,m}}{\partial d} \Delta d + \frac{\partial \tau_{p,m}}{\partial \theta_{t_m,p}} \Delta \theta_{t_m,p} + \frac{\partial \tau_{p,m}}{\partial \varphi_{t_m,p}} \Delta \varphi_{t_m,p} \\
&= \frac{\partial \tau_{p,m}}{\partial d} \Delta d + \Delta \varphi_{t_m,p} \left(\frac{\partial \tau_{p,m}}{\partial \theta_{t_m,p}} \frac{\cos(\varphi_{t_m,p})}{\sqrt{\varepsilon} \cos(\theta_{t_m,p})} + \frac{\partial \tau_{p,m}}{\partial \varphi_{t_m,p}} \right) \\
&= \frac{\Delta d}{c} \left(\frac{\sqrt{\varepsilon}}{\cos(\theta_{t_m,p})} - \frac{1}{\cos(\varphi_{t_m,p})} \right) + \frac{\Delta \varphi_{t_m,p}}{c} \left(\frac{d \cos(\varphi_{t_m,p})}{\cos^2(\theta_{t_m,p})} \tan(\theta_{t_m,p}) + \frac{h}{\cos(\varphi_{t_m,p})} \tan(\varphi_{t_m,p}) \right) \\
&= \frac{\Delta d}{c} \left(\frac{\sqrt{\varepsilon}}{\cos(\theta_{t_m,p})} - \frac{1}{\cos(\varphi_{t_m,p})} \right) + \frac{\Delta d}{c} [\tan(\varphi_{t_m,p}) - \tan(\theta_{t_m,p})] \sin(\varphi_{t_m,p}) \\
&= \frac{\Delta d}{c} [\sqrt{\varepsilon} \cos(\theta_{t_m,p}) - \cos(\varphi_{t_m,p})] = \frac{\Delta d}{c} \frac{\sin(\varphi_{t_m,p} - \theta_{t_m,p})}{\sin(\theta_{t_m,p})}.
\end{aligned}
\tag{A.8}
$$

Appendix B

We consider the situation where there is an error in the estimated value of the dielectric constant of the wall material, $\Delta \varepsilon = \varepsilon_e - \varepsilon$. The incident angles are adjusted so that the new path links the m-th antenna and the target point, p. From (A.1), we obtain the following first-order approximation,

$$\Delta x_{p,m} = \frac{\partial x_{p,m}}{\partial \theta_{t_m,p}} \Delta \theta_{t_m,p} + \frac{\partial x_{p,m}}{\partial \varphi_{t_m,p}} \Delta \varphi_{t_m,p} = \frac{\Delta \theta_{t_m,p} d}{\cos^2(\theta_{t_m,p})} + \frac{\Delta \varphi_{t_m,p} d}{\cos^2(\varphi_{t_m,p})}. \tag{B.1}$$

For the path to pass through the true target position, $\Delta x_{p,m} = 0$. That is,

$$\frac{\Delta\theta_{t_m,p}d}{\cos^2(\theta_{t_m,p})} + \frac{\Delta\varphi_{t_m,p}d}{\cos^2(\varphi_{t_m,p})} = 0. \tag{B.2}$$

From (A.9), the additional time due to the error $\Delta\varepsilon$ becomes

$$\Delta\tau_{p,m} = \frac{\partial\tau_{p,m}}{\partial\varepsilon}\Delta\varepsilon + \frac{\partial\tau_{p,m}}{\partial\theta_{t_m,p}}\Delta\theta_{t_m,p} + \frac{\partial\tau_{p,m}}{\partial\phi_{p,m}}\Delta\varphi_{t_m,p}$$

$$= \frac{1}{c}\left(\frac{\Delta\varepsilon}{2\sqrt{\varepsilon}}\frac{d}{\cos(\theta_{t_m,p})} + \frac{\sqrt{\varepsilon}d\sin(\theta_{t_m,p})}{\cos^2(\theta_{t_m,p})}\Delta\theta_{t_m,p} + \frac{h\sin(\varphi_{t_m,p})}{\cos^2(\varphi_{t_m,p})}\Delta\varphi_{t_m,p}\right) = \frac{\Delta\varepsilon}{2c\sqrt{\varepsilon}}\frac{d}{\cos(\theta_{t_m,p})}.$$

$$\tag{B.3}$$

REFERENCES

[1]   D. D. Ferris Jr. and N. C. Currie, "A survey of current technologies for through-the-wall surveillance (TWS)", *Proc. SPIE*, vol. 3577, pp. 62-72, *Sensors, C3I, Infor. and Training Techn. for Law Enforcement*, Boston, MA, Nov. 1998.

[2]   S. Nag, H. Fluhler, and M. Barnes, "Preliminary Interferometric Images of Moving Targets obtained using a Time-Modulated Ultra-Wide Band Through-Wall Penetration Radar", *Proc. IEEE Radar Conference*, pp. 64-69, Atlanta, GA, May 2001.

[3]   N. C. Wild and al," Ultrasonic through-the wall surveillance system", *Proc. SPIE*, vol. 4232, pp. 167-176, *Enabling Techn. for Law Enforcement and Security*, Boston, MA, Nov. 2000.

[4]   E. F. Greneker, "RADAR flashlight for through-the-wall detection of humans", *Proc. SPIE*, Vol. 3375, pp. 280-285, *Targets and Backgrounds: Characterization and Representation IV*, Orlando, FL, April 1998. .

[5]   J. D. Black, "Motion and Ranging Sensor through-the-wall surveillance system", *Proc. SPIE*, Vol. 4708, pp. 114-121, *Sensors and C3I Technologies for Homeland Defense and Law Enforcement*, Orlando, FL, *April 2002.*

[6]   A. R. Hunt, "Stepped-frequency CW radar for concealed weapon detection and through-the-wall surveillance", *Proc. SPIE*, Vol. 4708, pp. 99-105, *Sensors and C3I Technologies for Homeland Defense and Law Enforcement*, Orlando, FL, *April 2002.*

[7]   S. Nag, et. Al., "An Ultra-wideband through-the-wall Radar for detecting the motion of people in real time", *Proc. SPIE*, Vol. 4744, pp. 48-57, *Radar Sensor Technology and Data Visualization*, Orlando, FL , April 2002.

[8]   D. G. Falconer, R. W. Ficklin, K. G. Konolige, "Detection, location, and identification of building occupants using a robot-mounted through-wall radar", *Proc. SPIE*, Vol. 4037, pp. 72-81, *Battlefield Biomedical Technology II*, Orlando, FL, April 2000.

[9]   F. Ahmad, M. G. Amin, and S. A. Kassam, "Synthetic aperture beamformer for imaging through a dielectric wall," *IEEE Trans. on AES*, Vol. 41, No. 1, pp. 271-283, Jan. 2005.

[10]   W. Choi, and T. Sarkar, "Echo cancellation using a homomorphic deconvolution," *IEEE AP-S International Symposium and USNC/URSI National Radio Science Meeting*, Monterey, CA, June 2004.

[11]   A. R. Hunt, "Image formation through walls using a distributed radar sensor network," *IEEE AP-S International Symposium and USNC/URSI National Radio Science Meeting*, Monterey, CA, June 2004.

[12]   P. Withington, H. Fluhler, and S. Nag, "Enhancing homeland security with advanced UWB sensors," *IEEE Microwave Magazine*, Vol. 4, No.3, pp.51-58, Sept. 2003.

[13]   C. Chen, K. Yao, and R. E. Hudson, "Source Localization and Beamforming", *IEEE Signal Processing Magazine*, pp. 30-39, May 2002.

[14]   V. Murino, C. Regazzoni, A. Trucco, G. Vernazza, "A Noncoherent correlation technique and focused beamforming for ultrasonic underwater imaging: A comparative analysis", *IEEE Trans. Ultrason., Ferroelec., Freq. Contr.*, Vol. 41, No. 5, pp. 621-630, Sept. 1994.

[15]   D. G. Falconer, K. N. Steadman, and D. G. Watters, "Through-the wall differential radar", *Proc. SPIE*, Vol. 2938, pp. 147-151, *Enabling Technologies for Law Enforcement*, Boston, MA, Nov. 1996.

[16]   D. E. Manolakis, "Efficient Solution and Performance Analysis of 3-D Position Estimation by Trilateration", *IEEE Trans. AES*, Vol. 32, No. 4, pp. 1239-1248, Oct. 1996.

[17]   F. Ahmad, M. G. Amin, "A Noncoherent Radar System Approach for Through-The-Wall Imaging," Proc. SPIE, Vol. 5778, *Sensor, and Command, Control, Communications, and Intelligence Technologies for Homeland Security and Homeland Defense IV*, Bellingham, WA, March-April 2005.

[18]   G. Wang, and M. G. Amin, "A new approach for target locations in the presence of wall ambiguities," *IEEE Symposium on Signal Processing and Information Technology (ISSPIT'04)*, Rome, Italy, Dec. 2004.

[19]   G. Wang and Z. Bao, "The minimum entropy criterion of range alignment in ISAR motion compensation," *International Radar Conference Radar'97* , pp.236-239, Edinburgh, UK, October 1997.

[20]   M. Soumekh, "Auto-focusing of wide-bandwidth and wide-beamwidth SAR imagery," *International Conference on Image Processing* (ICIP'05) Genova, September 2005.

[21]   A. Safaai-Jazi, S. Riad, A. Muqaibel, and A. Bayram, "Ultra-wideband propagation measurements and channel modeling," *DARPA technical report*, available at http://www.darpa.mil/ato/programs/netex/models.pdf

[22] L. Ta-Hsin, and L. Ke-Shin, "Deblurring two-tone images by a joint estimation approach using higher-order statistics" *Proceedings of the IEEE Signal Processing Workshop on Higher-Order Statistics,* Banff, Canada 1997.

[23] L. Alparone, F. Argenti, B. Aiazzi, and S. Baronti, "Multiresolution approaches to adaptive speckle reduction in synthetic aperture radar images" *2003 International Conference on Image Processing,* vol.1, Barcelona, Spain, 2003.

[24] S. Fortune, M. Hayes and P. Gough "Statistical Autofocus of Synthetic Aperture Sonar Images using Image Contrast Optimization", *OCEANS 2001, Vol.1, IEEE,* Honolulu, HI.

[25] G. Mandapati and M. Amin, "Blurness and focusing-defocusing for through the wall radar imaging with wall ambiguities," *IEEE Symposium on Signal Processing and Information Technology, ISSPIT'04,* Rome, Italy, Dec. 2004.
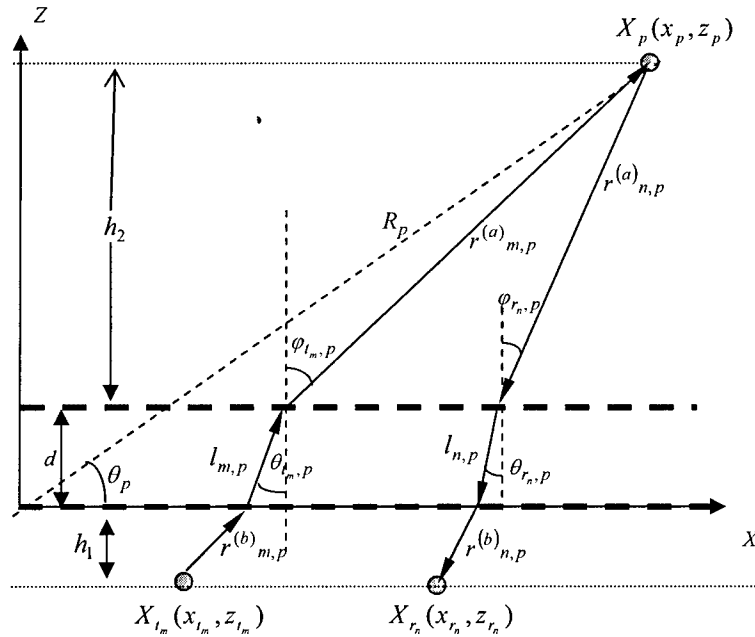
Figure 1: Geometry for computing the distances on transmit and receive
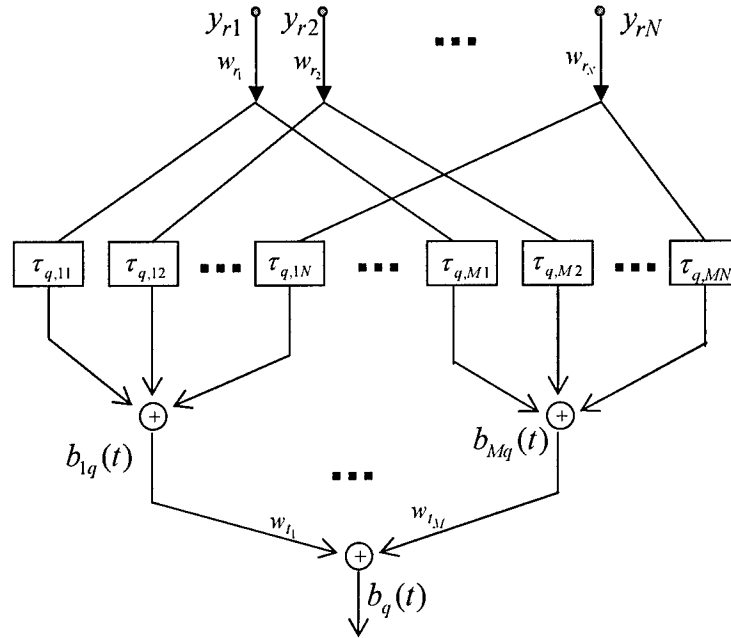
Figure 2: Block diagram of the post-data acquisition beamformer

Element #	1	2	3	4	5	6	7	8
Transmit (m)	-0.9	-0.3	0.3	0.9				
Receive (m)	-0.2625	-0.1875	-0.1125	-0.0375	0.0375	0.1125	0.1875	0.2625

Table 1: Transmit and Receive array locations

(a)

(b)
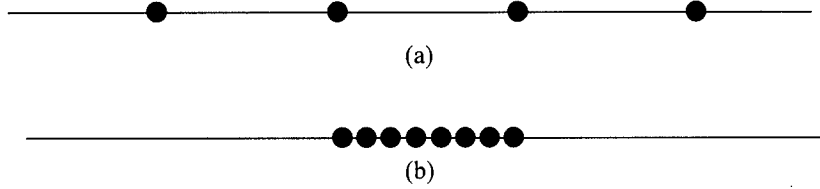
Figure 3. (a) Transmit array   (b) Receive array

76
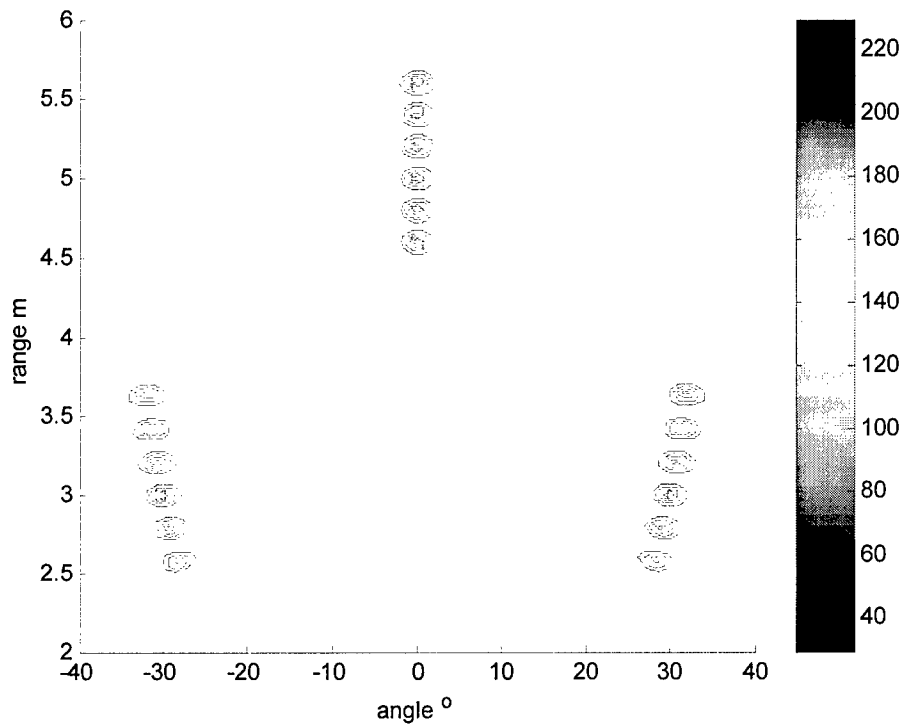
Figure 4. Shifts in images for different assumed wall thickness values
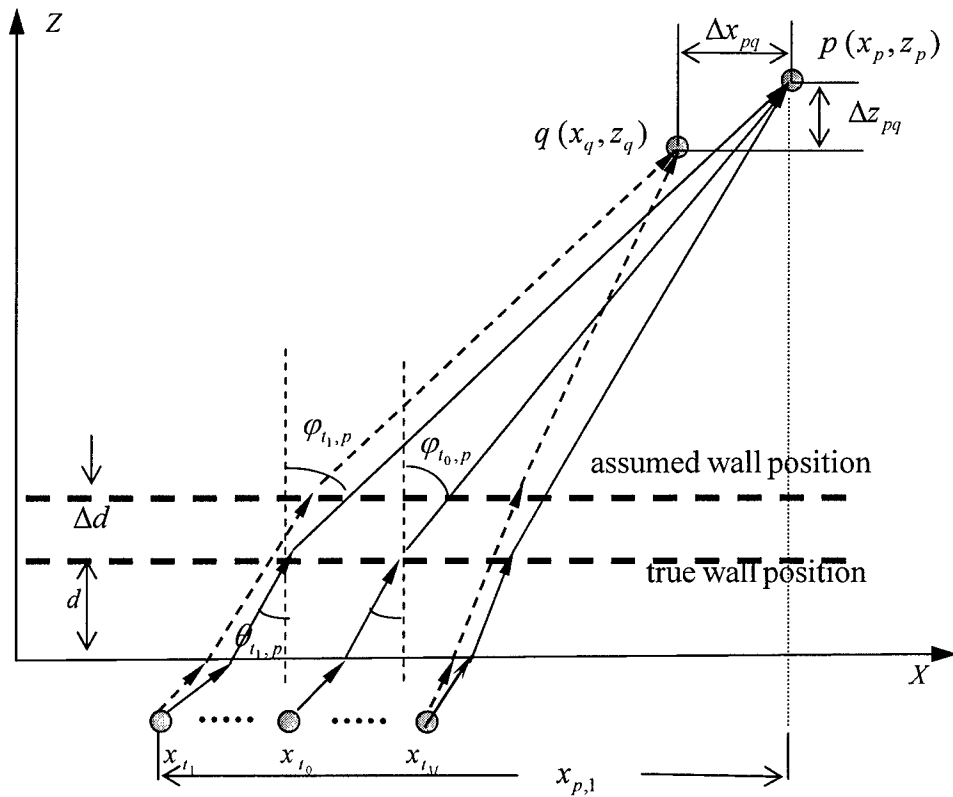
Figure 5. Geometry for computing the imaged position q corresponding to target p.
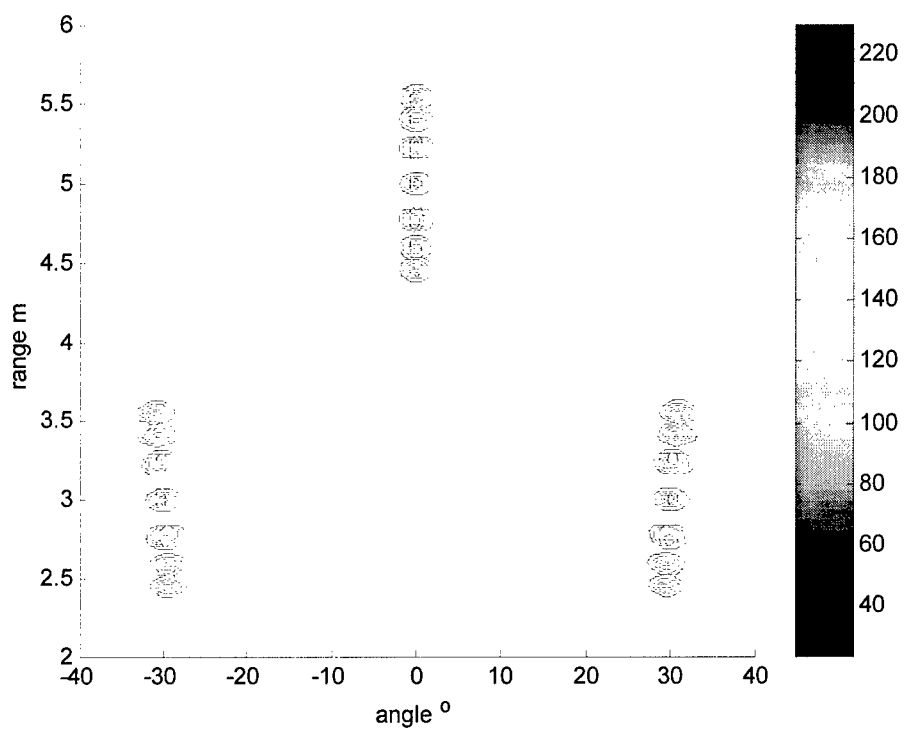
Figure 6. Shifts in images for different assumed dielectric constant values
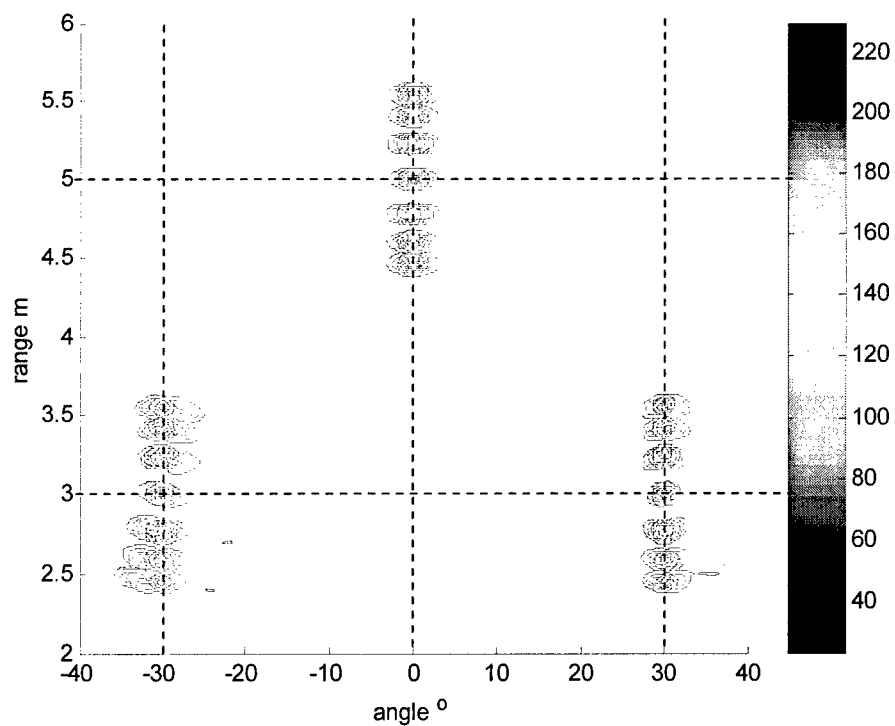
Figure 7. Image results with two different standoff distances
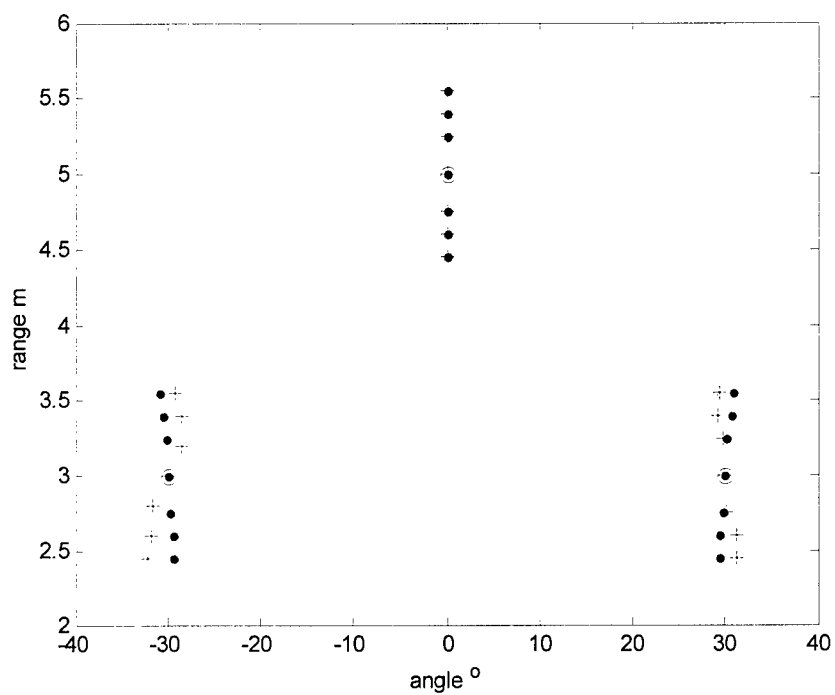
Figure 8. Peaks of the images in Fig.7
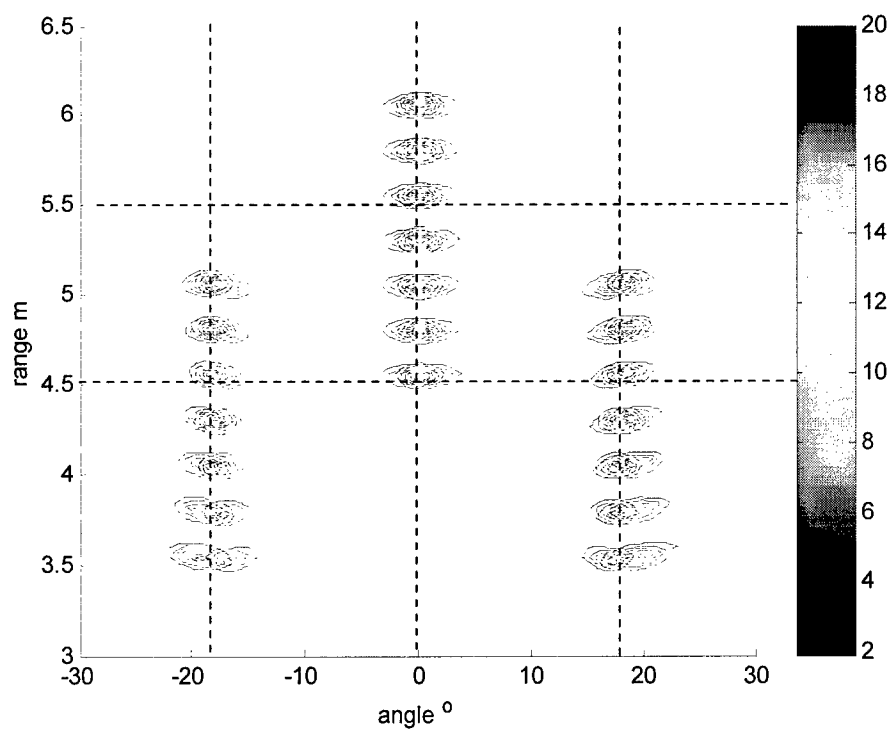
Figure 9 . Images with $\varepsilon_e = 12.25$ from standoff at (0,-3)m and (0,0)m
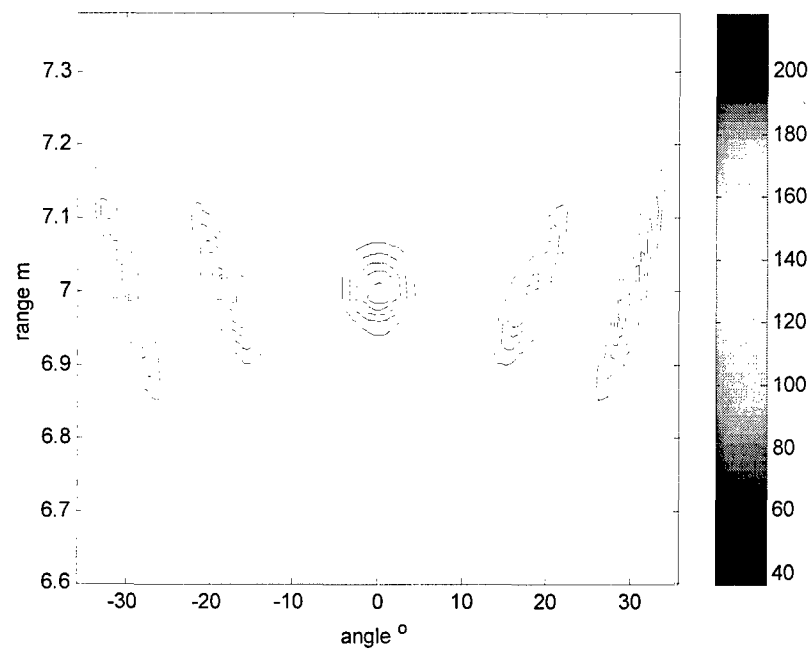
Figure 10 . Image with standoff distance 8m
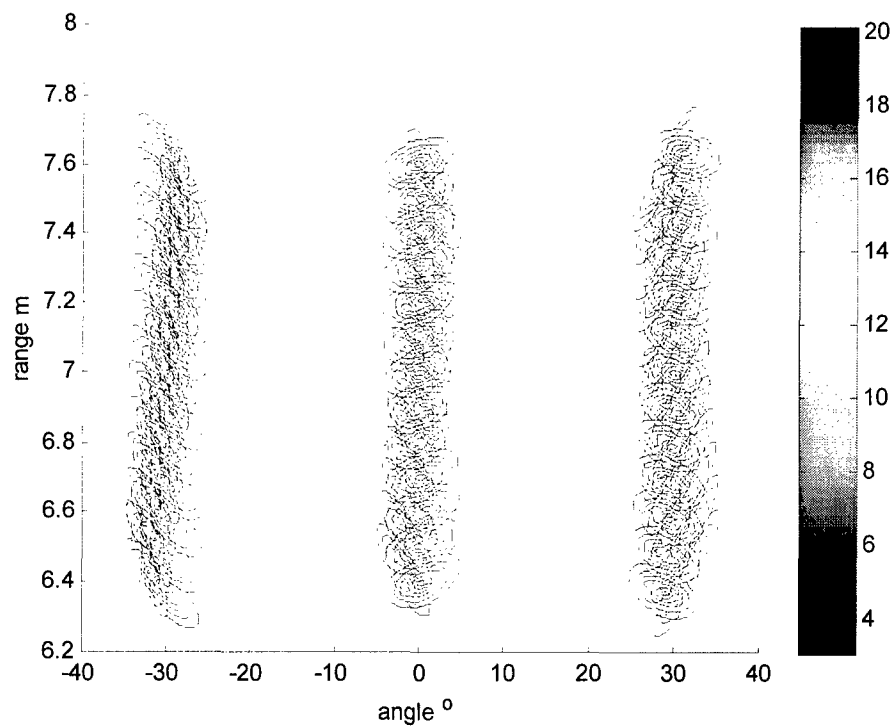
Figure 11 (a). Images with $\varepsilon_e = \varepsilon = 9$ from two standoff distances (-3,-4)m, and (1,-8)m
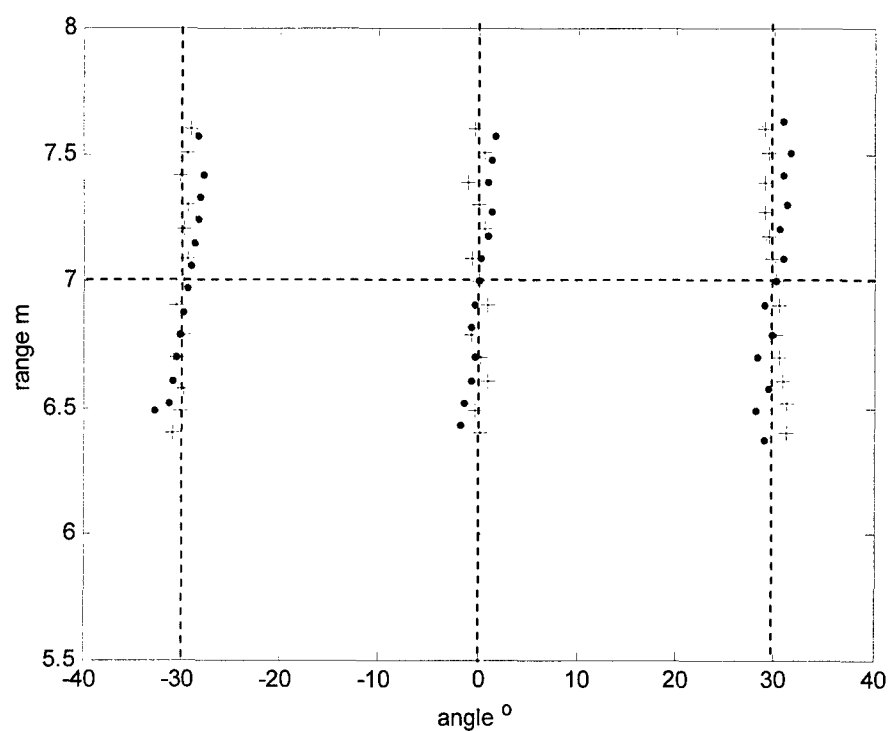
Figure 11 (b). Peaks of the images in Fig. 11 (a)
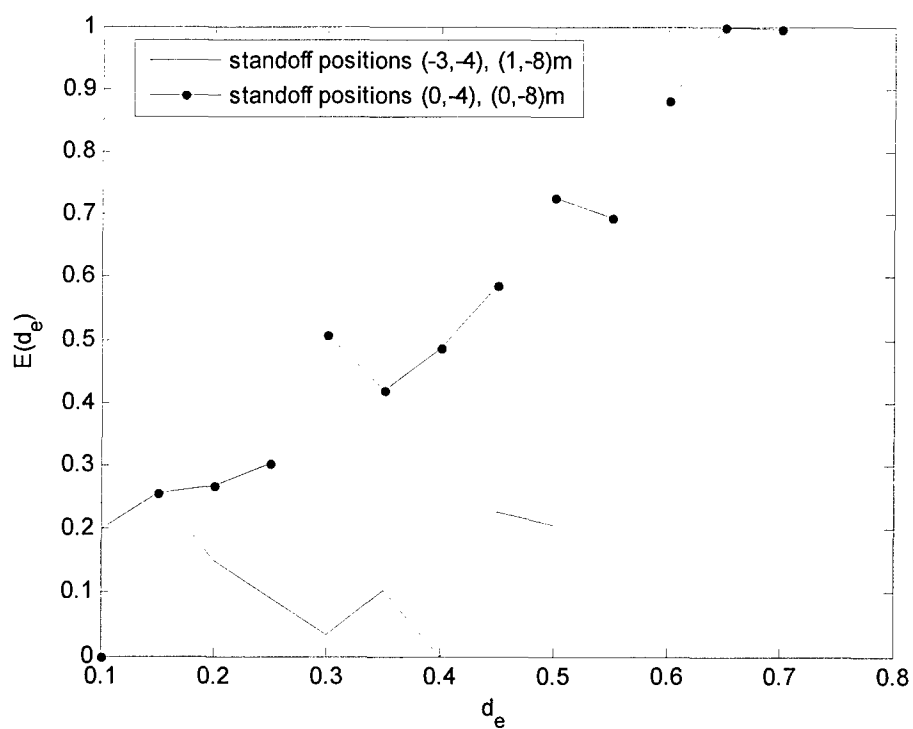
Figure 11 (c). Normalized Entropies of composite images
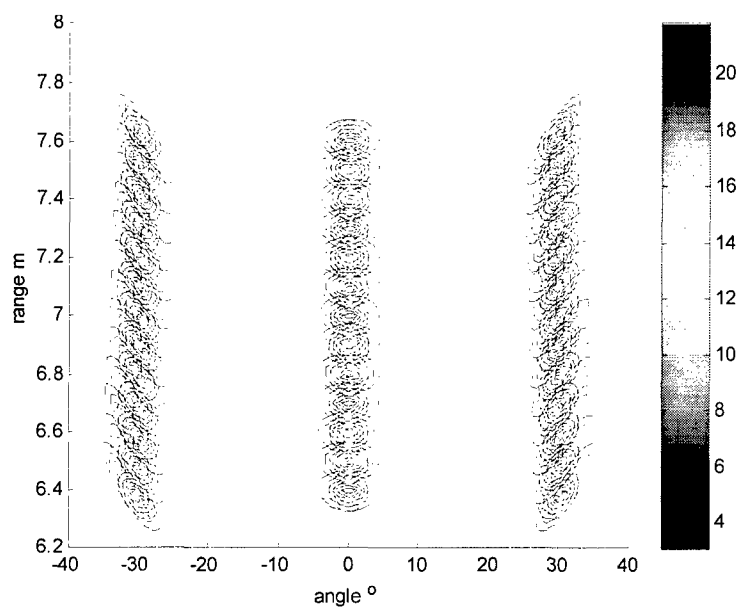
Figure 12. Images with $\varepsilon_e = \varepsilon = 9$ from two standoff distances $(0,-4)m$, and $(0,-8)m$
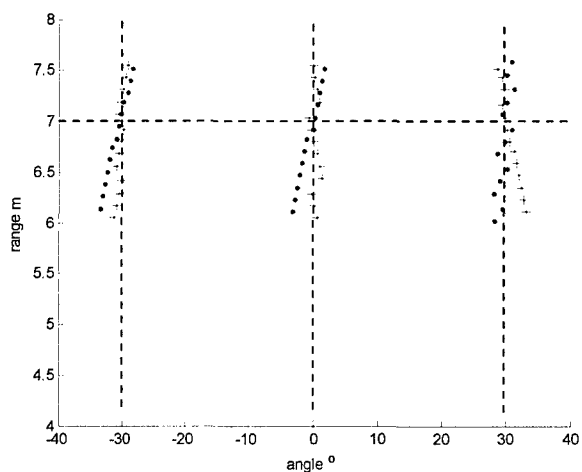
(a)
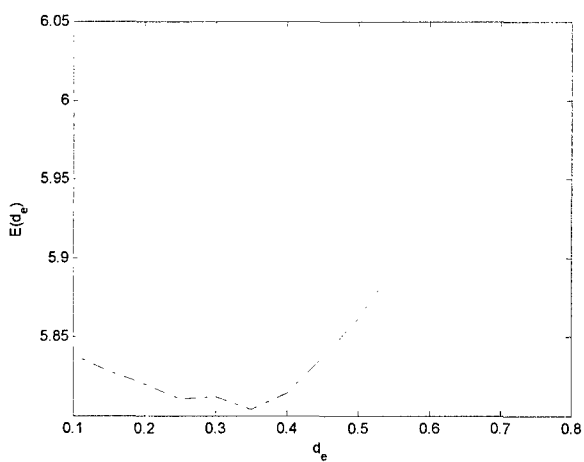
(b)

Figure 13. Peaks and Entropy of the composite image with $\varepsilon_e = \varepsilon = 12.25$ from two standoff distances $(-3,-4)m$, and $(1,-8)m$
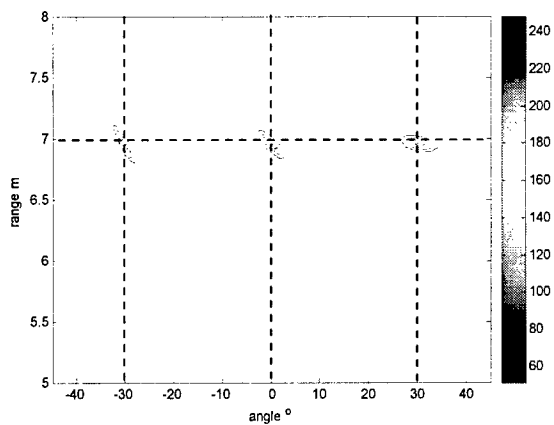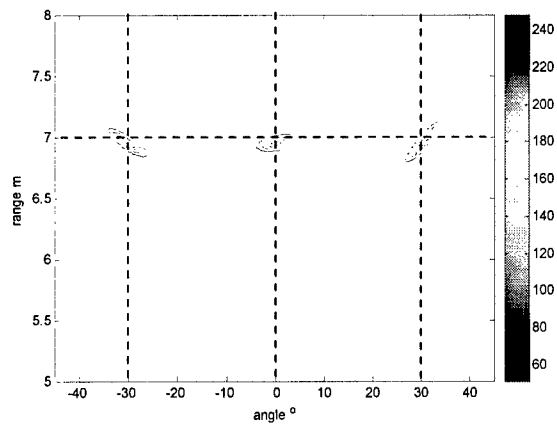
(a) Standoff at (-3,-4)m   (b) Standoff at (1,-8)m

Figure 14 Final image from single standoff with $(d_e, \varepsilon_e) = (0.35, 12.25) \neq (d, \varepsilon)$

Chapter 4

Autofocusing of Through-the-Wall Radar Imagery under Unknown Wall Characteristic

Abstract

The quality and reliability of through-the-wall radar imagery is governed, among other things, by the knowledge of the wall characteristics. Ambiguities in wall characteristics smear and blur the image, and also shift the imaged target positions. An autofocusing technique, based on higher order statistics, is presented which corrects for errors under unknown walls. Simulation results show that the proposed technique provides high-quality focused images with target locations in close proximity to true target positions.

1. INTRODUCTION

Through-the-Wall Radar Imaging (TWRI) is an emerging technology that addresses a number of civilian problems and has a dual-use with obvious military applications. TWRI can be used in rescue missions, behind-the-wall target detection, and surveillance and reconnaissance in urban environments. There are several studies on TWRI to detect the presence of persons behind walls and track their movements with known wall parameters, such as wall thickness and dielectric constant [1-10]. In practical situations, however, the wall characteristics are not known a priori, and need to be estimated. Ambiguities in wall parameters smear and blur the image and cause the imaged targets to shift away from their true positions. These effects increase significantly when multiple walls separate the targets from the radar, which typically is the case in urban sensing applications [11]. If unaccounted for, the image degradations reduce the accuracy and reliability of TWRI and compromise the integrity of the system.

A TWRI technique that provides correct locations of stationary targets without the knowledge of wall parameters was proposed in [12-13]. This technique is based on coherent wideband beamforming, and uses the bias in imaged target location, when incorporating incorrect walls. It requires the use of two or more different array structures, and corrects for wall ambiguities by utilizing the distinctions in the respective location bias trajectories. In this chapter, unlike the work in [12-13], we examine the effect of wall ambiguities on the target spread and intensity profile, aiming to focus the image and correct for shifts in locations of imaged stationary targets. We use a single array structure and assume the transmit and receive arrays are placed against a single uniform wall. We investigate both conventional contrast measures and higher order standardized moments as potential candidates for measuring the degree of smearing and blurriness of through-the-wall images of stationary target distributions. These images are obtained using high-resolution coarray-based subarray aperture synthesis and post-data acquisition wideband near-field beamforming [5, 14]. The coarray formalism allows synthesizing a desired aperture with significant savings in the number of required transmit and receive antennas. The coarray was originally defined for narrowband far-field active imaging [15], and subsequently extended to wideband

imaging in [16]. It is represented by the set of all pair-wise sums of the position vectors of the elements in the transmit and receive apertures.

It is noted that, cost and technology permitting, both hardware wideband beamforming using a full array and post-data acquisition wideband beamforming with aperture synthesis can be used for imaging and are equivalent. However, wideband beamformers are difficult to implement in hardware because time delays, instead of phase shifters, are required to steer the transmit and receive beams [17-19]. Moreover, the beams have to be steered to different pixels both in range and angle over the region of interest. This requires the delays to be flexible and tunable. Therefore, wideband signals are typically processed by splitting the spectrum into subband or narrowband components so that phase steering, instead of time delays, is applicable [17-19]. An alternative is post-data acquisition beamforming which eliminates the need for hardware delay lines. However, in order to retain the ability to form and steer both transmit and receive beams, it requires independent use of each transmit element for data acquisition, thereby allowing aperture synthesis through the use of subarrays. The subarrays consist of a single transmitter and one or more receivers. Two different arrangements can be used for aperture synthesis [14, 20]. Either all the elements of the intended transmit and receive arrays can be physically present and share transmit and receive processing channels via a multiplexer, or a single subarray can be used to realize the full transmit and receive arrays by moving this subarray to different locations forming the array aperture.

The proposed through-the-wall autofocusing system eliminates image distortions caused by errors in wall parameter estimates. The system block diagram is shown in Fig. 1. The system consists of a measuring module that provides a feedback of the image quality, measured using a suitable focusing metric, to an adjustment module in which the wall parameters are tuned to reduce degradation. This feedback scheme relies on an iterative application of the focusing metric. At each iteration, the assumed wall parameters are changed and a subsequent beamformed image is generated based on the updated wall parameters. An image quality optimization scheme may be applied to recursively autofocus the images. The non-convex multi-modal nature of the associated cost function may occasionally force the algorithm to converge to a small local solution or could prevent it from convergence at all. The viability of the

image quality optimization may be improved by enhancing the optimization algorithm to effectively tackle the multiplicity of local solutions. However, this investigation is beyond the scope of this work. We, therefore, assume that the algorithm initializations lead to a local or global solution or the system operator guides the tuning of the wall parameters to optimize the image quality metric.

For the system of Fig. 1, we analyze the target image intensity under far-field conditions and assume the wall parameter error values to be small. Our analysis shows that exact as well as incorrect assumed wall characteristics, defined by wall thickness and dielectric constant, can lead to focused images with imaged target positions in close proximity to true target locations. It is important to note that the far-field results become even more applicable for longer standoff distances from the wall.

The chapter is organized as follows. We provide in Section 2 the fundamental equations of wideband through-the-wall radar imaging. The effect of wall parameter ambiguities on the image intensity under far-field conditions is discussed in Section 3. In Section 4, we investigate both conventional contrast based metrics and higher order standardized moments as possible candidates for autofocusing of through-the-wall radar imagery. Section 5 contains the concluding remarks.

2. WIDEBAND THROUGH-THE-WALL BEAMFORMING

In order to present the effect of wall errors on target image blurriness as well as demonstrate image refocusing using proposed sharpness measures, we summarize in this section the fundamental equations describing wideband synthetic aperture beamforming in the presence of the wall. It is noted that these equations along with detailed analyses of the known wall-based imagery are given in [5, 12]. Consider a subarray, consisting of a single transmitter and a single receiver, used to synthesize an M-element transmit and an N-element receive line arrays, both located along the x-axis. The region to be imaged is located along the positive y-axis. Let the transmitter, placed at the m-th transmit location $\mathbf{x_{tm}} = (x_{tm}, 0)$, illuminate the scene with a wideband signal $s(t)$. The reflection by any target located in the region being imaged is measured and recorder at the n-th receiver located at $\mathbf{x_{rn}} = (x_{rn}, 0)$. For the case of a single

point target located at $\mathbf{x_p} = (x_p, y_p)$, the output of the n-th receiver is given by $a(\mathbf{x_p})s(t - \tau_{p,mn})$, where $a(\mathbf{x_p})$ is the complex reflectivity of the point target. As shown in Fig. 2, the propagation delay, $\tau_{p,mn}$, encountered by the signal as it travels from the m-th transmitter to the target located at $\mathbf{x_p}$, and back to the n-th receiver, is given by

$$\tau_{p,mn} = \frac{r_{m,p,air} + l_{n,p,air}}{c} + \frac{r_{m,p,wall} + l_{n,p,wall}}{v} \tag{1}$$

where c is the speed of light, and $v = c/\sqrt{\varepsilon}$ is the speed though the wall with a dielectric constant ε. The variables $r_{m,p,air}$ and $r_{m,p,wall}$ represent the traveling distances of the signal in the air and wall, respectively, from the m-th transmitter to the target at $\mathbf{x_p}$, whereas $l_{n,p,air}$ and $l_{n,p,wall}$ are the traveling distances of the wave in the air and wall, respectively, from the target at $\mathbf{x_p}$ to the n-th receiver. The analytical expression for the propagation delay was derived in [5] and is given by

$$\tau_{p,mn} = \frac{1}{v}\frac{d}{\cos\theta_{t_m,p}} + \frac{1}{c}\sqrt{(dist(\mathbf{x_{tm}},\mathbf{x_p}))^2 - \frac{d^2}{\cos^2\theta_{t_m,p}}\sin^2(\theta_{t_m,p} - \varphi_{t_m,p})}$$

$$-\frac{1}{c}\frac{d}{\cos\theta_{t_m,p}}\cos(\theta_{t_m,p} - \varphi_{t_m,p}) + \frac{1}{v}\frac{d}{\cos\theta_{r_n,p}} + \frac{1}{c}\sqrt{(dist(\mathbf{x_{rn}},\mathbf{x_p}))^2 - \frac{d^2}{\cos^2\theta_{r_n,p}}\sin^2(\theta_{r_n,p} - \varphi_{r_n,p})} \tag{2}$$

$$-\frac{1}{c}\frac{d}{\cos\theta_{r_n,p}}\cos(\theta_{r_n,p} - \varphi_{r_n,p})$$

where $dist(\cdot)$ is the Euclidean distance between two position vectors.

This process is repeated with the transmitter at the m-th location until all the N receive locations have been used sequentially. The corresponding N outputs are processed as follows. The region of interest is divided into a finite number of pixels in range and angle. The complex composite signal corresponding to the image of the pixel located at $\mathbf{x_q} = (x_q, y_q)$, is obtained by applying time delays and weights to the N received signals, and summing the results. The output for a single target case is given by

$$z_{mq}(t) = \sum_{n=1}^{N} w_{n} a(\mathbf{x_p})s(t - \tau_{p,mn} + \tau_{q,mn}) \tag{3}$$

88

where w_{rn} is the weight applied to the output of the n-th receiver, and $\tau_{q,mn}$ is the focusing delay applied to the output of the n-th receiver when the transmitter is at the m-th location. This delay, given by (2) with the target pixel subscript p replaced by the focusing pixel subscript q, synchronizes the arrivals at different receive locations for the same focusing pixel, and thus allows near-field imaging of the scene.

The above process is repeated by sequential use of the M transmit locations and produces M complex composite signals, $z_{mq}(t)$, $m=1,2,\ldots,M$, corresponding to the image of the pixel at $\mathbf{x_q}$. The complex signal corresponding to the pixel located at $\mathbf{x_q}$ is obtained by the coherent weighted linear combination

$$z_q(t) = \sum_{m=1}^{M} w_{tm} z_{mq}(t) = \sum_{m=1}^{M} \sum_{n=1}^{N} w_{tm} w_{rn} a(\mathbf{x_p}) s(t - \tau_{p,mn} + \tau_{q,mn}) \tag{4}$$

where w_{tm} is the weight applied to the component signal $z_{mq}(t)$ obtained using the m-th transmitter. The complex amplitude image value for the pixel located at $\mathbf{x_q}$ is obtained by passing the signal $z_q(t)$ through a filter matched to the transmitted pulse and sampling the output of the filter at time $t = 0$,

$$I(\mathbf{x_q}) = (z_q(t) * h(t))\Big|_{t=0} = \sum_{m=1}^{M} \sum_{n=1}^{N} w_{tm} w_{rn} a(\mathbf{x_p}) s(t - \tau_{p,mn} + \tau_{q,mn}) * h(t)\Big|_{t=0} \tag{5}$$

where $h(t)=s^{*}(-t)$ is the impulse response of the matched filter. The process described by (3)-(5), is performed for all pixels in the region of interest to generate the composite image of the scene. The general case of multiple targets can be obtained by superposition.

Note that the focusing delays have taken into account the change in propagation speed and the bending effect of the wave as it propagates through and out of the dielectric wall for reliable and accurate imaging. The focusing delays can be precisely computed, given the exact knowledge of the wall parameters such as its thickness and dielectric constant, and as such cancel the propagation delays when $\mathbf{x_q}=\mathbf{x_p}$. However, in typical through-the-wall imaging scenario, the wall parameters are not known a priori and an estimate of these parameters would have to be used for computing the focusing delays. Ambiguities in wall parameters lead to errors in the focusing delays. As a consequence, the focusing delays do not exactly cancel the propagation delays, even when $\mathbf{x_q}=\mathbf{x_p}$. These errors compromise the beamformer performance and the resultant images are blurred, smeared, and the target location estimates

are biased. This degradation of image quality will be more pronounced in wall materials with high dielectric constants and in the presence of multiple walls separating the targets and the radar.

3. EFFECT OF WALL PARAMETER AMBIGUITIES ON IMAGE INTENSITY

Consider the case when the wall parameters are not exactly known. Let the estimated wall thickness be $d+\delta_w$ and the estimated refractive index be $\sqrt{\varepsilon}+\delta_\varepsilon$. In this case, the complex amplitude image value $\hat{I}(\mathbf{x_q})$ in the presence of wall parameter ambiguities is given by (5) with v, d, and $\sqrt{\varepsilon}$ replaced by $c/\sqrt{\varepsilon}+\delta_\varepsilon$, $d+\delta_w$, and $\sqrt{\varepsilon}+\delta_\varepsilon$, respectively in the expression for the focusing delay $\tau_{q,mn}$. We will now determine the conditions under which the image intensity at pixel $\mathbf{x_q}$, for far-field and small error assumptions, will be equal to the intensity in the absence of wall errors.

Assume that the targets being imaged are located in the far-field of the array and the errors δ_w and δ_ε are relatively small. Then, the complex amplitude image value $\hat{I}(\mathbf{x_q})$ can be simplified as

$$\hat{I}(\mathbf{x_q}) \approx I(\mathbf{x_q}) + \delta_w \frac{2(\sqrt{\varepsilon}-1)}{c} \sum_{l=1}^{N_c} g_l a(\mathbf{x_p}) \frac{d\psi_s(t)}{dt}\bigg|_{t=\tau_{l1}} + \delta_\varepsilon \sum_{l=1}^{N_c} g_l a(\mathbf{x_p}) \left(\frac{2d-z_l\theta_q}{c}\right) \frac{d\psi_s(t)}{dt}\bigg|_{t=\tau_{l1}} \tag{6}$$

where $I(\mathbf{x_q})$ is the pixel value in the absence of wall errors under far-field assumptions, $\psi_s(t)$ is the autocorrelation function of the pulse $s(t)$, N_c is the number of points in the coarray corresponding to the M-element transmit and N-element receive arrays, z_l is the l-th coarray location, g_l is the coarray weighting, which is defined as [15]

$$g_l = \sum_{(a,b)\in C_l} w_{ta} w_{rb}, \qquad C_l = \{(a,b) \mid z_l = x_{ta} + x_{rb}\} \tag{7}$$

and

$$\tau_{l1} = \frac{2(R_q - R_p)}{c} - \frac{\sqrt{\varepsilon} z_l(\theta_q - \theta_p)}{c} \tag{8}$$

In eq. (8), $R_q = \sqrt{x_q{}^2 + y_q{}^2}$, $R_p = \sqrt{x_p{}^2 + y_p{}^2}$, and θ_j is the incident angle related to the path from the origin to the target (for $j=p$) and the focusing pixel for $j=q$, as shown in Fig. 3. The derivation of (6) is given in the Appendix.

The intensity of the image pixel at $\mathbf{x_q}$ can, therefore, be expressed as

$$\left|\hat{I}(\mathbf{x_q})\right|^2 = \left| I(\mathbf{x_q}) + \delta_w \frac{2(\sqrt{\varepsilon}-1)}{c} \sum_{l=1}^{N_c} g_l a(\mathbf{x_p}) \frac{d\psi_s(t)}{dt}\bigg|_{t=\tau_{l1}} + \delta_\varepsilon \sum_{l=1}^{N_c} g_l a(\mathbf{x_p}) \left(\frac{2d - z_l \theta_q}{c}\right) \frac{d\psi_s(t)}{dt}\bigg|_{t=\tau_{l1}} \right|^2 \quad (9)$$

Expanding the right hand side of (9) and retaining only the linear error terms, we obtain

$$\left|\hat{I}(\mathbf{x_q})\right|^2 \approx \left|I(\mathbf{x_q})\right|^2 + 2\delta_w \frac{2(\sqrt{\varepsilon}-1)}{c} \mathrm{Re}\left\{ I^*(\mathbf{x_q}) \sum_{l=1}^{N_c} g_l a(\mathbf{x_p}) \frac{d\psi_s(t)}{dt}\bigg|_{t=\tau_{l1}} \right\}$$
$$+ 2\delta_\varepsilon \mathrm{Re}\left\{ \sum_{l=1}^{N_c} g_l I^*(\mathbf{x_q}) a(\mathbf{x_p}) \left(\frac{2d - z_l \theta_q}{c}\right) \frac{d\psi_s(t)}{dt}\bigg|_{t=\tau_{l1}} \right\} \quad (10)$$

Further simplification of (10) leads to

$$\left|\hat{I}(\mathbf{x_q})\right|^2 \approx \left|I(\mathbf{x_q})\right|^2 + 2\delta_w \frac{2(\sqrt{\varepsilon}-1)}{c} \sum_{l=1}^{N_c} \mathrm{Re}\left\{ g_l a(\mathbf{x_p}) I^*(\mathbf{x_q}) \frac{d\psi_s(t)}{dt}\bigg|_{t=\tau_{l1}} \right\}$$
$$+ 2\delta_\varepsilon \sum_{l=1}^{N_c} \left(\frac{2d - z_l \theta_q}{c}\right) \mathrm{Re}\left\{ g_l a(\mathbf{x_p}) I^*(\mathbf{x_q}) \frac{d\psi_s(t)}{dt}\bigg|_{t=\tau_{l1}} \right\} \quad (11)$$

The following observations from the intensity profile in (11) are in order. For cases when only one of the wall parameters is unknown, either the wall thickness or the dielectric constant, $\left|\hat{I}(\mathbf{x_q})\right|^2$ will be equal to $\left|I(\mathbf{x_q})\right|^2$ only at the true value of the unknown parameter. On the other hand, when both wall parameters are unknown, the condition for $\left|\hat{I}(\mathbf{x_q})\right|^2$ to be equal to $\left|I(\mathbf{x_q})\right|^2$ for all pixels in the image is given by

$$\delta_\varepsilon = -\delta_w \frac{\frac{2(\sqrt{\varepsilon}-1)}{c} \sum_{l=1}^{N_c} \mathrm{Re}\left\{ g_l a(\mathbf{x_p}) I^*(\mathbf{x_q}) \frac{d\psi_s(t)}{dt}\Big|_{t=\tau_{l1}} \right\}}{\sum_{l=1}^{N_c} \left(\frac{2d - z_l \theta_q}{c} \right) \mathrm{Re}\left\{ g_l a(\mathbf{x_p}) I^*(\mathbf{x_q}) \frac{d\psi_s(t)}{dt}\Big|_{t=\tau_{l1}} \right\}} \qquad (12)$$

That is, the image intensity, $\left|\hat{I}(\mathbf{x_q})\right|^2$, at pixel $\mathbf{x_q}$, under far-field and small error assumptions, will be equal to the intensity $\left|I(\mathbf{x_q})\right|^2$ in the absence of wall errors for several other values of the wall parameters in addition to the true values. In these situations, the effects of the errors in both d_w and $\sqrt{\varepsilon}$ tend to cancel out, leading to the correct set of delays required to coherently combine the waveform returns from the target positions. Moreover, it follows from (12) that if $\sqrt{\varepsilon} > 1$ and $2d > |z_l|_{\max} |\theta_q|_{\max}$ for all pixels in the region of interest, the values of δ_ε and δ_w, necessary to correct for wall parameter errors, will be of opposite polarity.

4. FOCUSING METRICS

We employ image quality measures for autofocusing of through-the-wall radar imagery under unknown walls. The image of a point target, located at (6m, 0°), was simulated with exact knowledge of wall parameters and with wall parameters underestimated by 30%. Figure 4 shows the range profile at an angle of 0° for both cases. We observe that, in addition to the incorrect imaged target location, the range profile under wall ambiguities (dashed line) is smeared while the one with known wall (solid line) is sharper (of higher contrast). We will, therefore, consider the use of contrast in the image as an image quality measure.

4.1. Conventional Contrast Measures

Several metrics have been used in the literature in a variety of imaging paradigms to measure image contrast or sharpness [21-26]. After careful screening of the literature, the following contrast measures were selected as potential candidates for through-the-wall imaging applications.

1) Normalized sum of image intensity

$$C_1 = \frac{\sum_{q=1}^{Q} |I(x_q, y_q)|^2}{(\sum_{q=1}^{Q} |I(x_q, y_q)|)^2} \qquad (13)$$

where $I(x_q, y_q)$ represents the q-th image pixel value and Q is the total number of pixels in the image.

2) Normalized sum of squared intensity

$$C_2 = \frac{\sum_{q=1}^{Q} |I(x_q, y_q)|^4}{(\sum_{q=1}^{Q} |I(x_q, y_q)|)^4} \qquad (14)$$

3) Negative of Image Entropy

$$C_3 = \sum_{q=1}^{Q} ss(x_q, y_q) \ln[ss(x_q, y_q)] \qquad (15)$$

where $ss(x_q, y_q) = \dfrac{|I(x_q, y_q)|^2}{\sum_{q=1}^{Q} |I(x_q, y_q)|}$.

4) Ratio of Standard Deviation to mean amplitude

$$C_4 = \frac{\sqrt{\sum_{q=1}^{Q} \left[|I(x_q, y_q)| - \frac{1}{Q} \sum_{q=1}^{Q} |I(x_q, y_q)| \right]^2}}{\sum_{q=1}^{Q} |I(x_q, y_q)|} \qquad (16)$$

A good measure of the contrast should reach the highest or the lowest value only for the undistorted image, corresponding to the correct wall. If the contrast measures defined above tend to change monotonically with increasing magnitudes of the errors in wall parameters, we can reduce focusing errors by varying the estimates in a carefully-designed, controlled way to optimize image contrast.

4.1.1. *Simulation Results for Contrast Measures*

The behavior of the each of the above contrast measures, as a function of errors in wall parameters, was thoroughly investigated and evaluated under both single and two point target distributions, with cases involving individual as well as combined wall thickness and dielectric constant errors. The following parameters were used for simulating the through-the-wall beamformer of (5). An amplitude modulated rectangular pulse of 1 GHz bandwidth centered at 2 GHz is used for imaging. A subarray, consisting of a single transmitter and a single receiver, is used to synthesize a 4-element transmit and an 8-element receive line arrays, both located along the x-axis at positions listed in Table I. Both the transmit and receive antennas were placed against the wall and unit weights were applied to all elements. The wall through which the system is imaging is assumed to be a 0.15m thick concrete wall with dielectric constant $\varepsilon = 9$. The refractive index $\sqrt{\varepsilon}$, therefore, equals 3. These radar system characteristics are maintained throughout the chapter. The error in wall thickness was varied from -0.1m to +0.1m in 1cm increments, whereas the refractive index error was considered to be between -1 and +1 with increments of 0.1. In all of the figures that follow, we plot the percentage error[1] of the various criteria versus the errors in wall parameters, unless specified otherwise.

Figure 5 shows the percentage error variation of the four contrast criteria of (13)-(16) for a single target scene under various error conditions. Although the sum of squared intensity metric performed best in most trials, none of the above four metrics stands out in terms of its sensitivity to errors in wall parameters. This is evident from the insignificant change in percentage error in Figure 5. The results for the two-target case are similar and hence are not provided. Therefore, new image quality criteria, with a high degree of sensitivity to wall thickness and dielectric constant (refractive index) errors, are most desirable for through-the-wall applications.

---

[1] Let the true value (no wall parameter errors) of a metric be z and the measured or inferred value be z_0. Then, the percentage error is defined by $\delta z = \dfrac{z_0 - z}{z} \times 100$.

4.2. Higher-Order Metrics

We now investigate standardized moments as potential alternative measures for autofocusing and deblurring of through-the-wall radar imagery. Let $P(x_q, y_q) = |I(x_q, y_q)|$ be the magnitude of the q-th image pixel. Then, the n-th standardized moment of $P(\cdot)$ is defined as the ratio of the n-th moment-about-the-mean and the n-th power of the standard deviation. For an image consisting of Q pixels, this moment is given by [27]

$$\gamma_n = \frac{\sum_{q=1}^{Q} (P(x_q, y_q) - \hat{\mu})^n}{(Q-1)\hat{\sigma}^n} \tag{17}$$

where $\hat{\mu}$ and $\hat{\sigma}$ denote the sample mean and the sample standard deviation of $P(\cdot)$ and are, respectively, given by

$$\hat{\mu} = \frac{1}{Q} \sum_{q=1}^{Q} P(x_q, y_q) \tag{18}$$

$$\hat{\sigma} = \left[\frac{1}{Q-1} \sum_{q=1}^{Q} (P(x_q, y_q) - \hat{\mu})^2 \right]^{1/2} \tag{19}$$

In particular, we deal with standardized moments for $n \geq 3$. The third and fourth standardized moments are used to define skewness and kurtosis, which are higher order metrics typically used for image enhancement in coherent imaging applications [28-29].

$$Skew[P] = \gamma_3 = \frac{\sum_{q=1}^{Q} (P(x_q, y_q) - \hat{\mu})^3}{(Q-1)\hat{\sigma}^3} \tag{20}$$

$$Kurt[P] = \gamma_4 - 3 = \frac{\sum_{q=1}^{Q} (P(x_q, y_q) - \hat{\mu})^4}{(Q-1)\hat{\sigma}^4} - 3 \tag{21}$$

In order to evaluate the performance of the higher order metrics, we first consider the case when only one of the two wall parameters, i.e., wall thickness or dielectric constant, is known. The simulation parameters are the same as described in Section 4.1. Let the wall dielectric constant be known. By using

several assumed values of the wall thickness, a series of images of both single and two target scenes were generated. Skewness, kurtosis, and several higher standardized moments were then computed for both single and two target scenes. Figure 6(a) shows the percentage error of the various metrics as a function of the wall thickness error for the single target distribution. It is evident that the percentage error for all of the higher order metrics becomes zero only for the correctly focused image i.e. for the correct wall thickness. The results for the two target scene are similar. Compared to Fig. 5(a), Fig. 6(a) clearly depicts the high sensitive behavior of the higher order criteria to wall errors as compared to the conventional contrast-based criteria. In fact, the higher the order of the standardized moment, the more sensitive the criterion becomes to the wall thickness errors; the tradeoff, of course, being the increased computational load. Similar observations can be made for the case when the wall thickness is known and the dielectric constant is unknown, shown, respectively, in Fig. 6(b) and Fig. 8 (solid line) for the single and two target distributions.

Now, we consider the case in which both the wall thickness and the dielectric constant are unknown. Figure 7 shows the percentage error of skewness, the 15-th, and the 25-th standardized moments for the single target scene whereas the performance of the 25-th standardized moment for the two target scene is depicted in Fig. 9(a). For these metrics, although the percentage error peaks at the correctly focused image (zero errors in wall thickness and dielectric constant), the surface is very noisy, and as expected from the analysis in Section 3, has several local maxima as well.

It is not surprising that increasing the order of the standardized moment leads to an increased sensitivity to wall parameter errors. This is because the peaks in the image intensity profile become sharper as the image intensity is raised to a higher power, increasing the overall image contrast.

4.2.1. Gamma Correction

We consider modification of the gamma characteristic of the image as an approach to smooth the error surface. The gamma characteristic of an image controls its overall brightness. If a pixel with value P is gamma corrected by "g", it means the new value of the pixel is P^g [30]. When the value of g is unity, we

obtain the original image without any modifications. For $g<1$, dark regions in the image are increased in brightness with a corresponding overall decrease in contrast between the light and dark areas. For $g>1$, overall contrast is increased by suppressing the dark features. We have examined the effects of gamma correction on the sensitivity of higher order metrics to errors in wall parameters for both single and two target cases. Figure 8 considers the two target scene when the wall thickness is known and the dielectric constant is unknown. It clearly indicates the advantage of using the higher order criteria, coupled with gamma correction of $g>1$. The maxima at the correct value of the unknown wall parameter are further accentuated by gamma correction for all metrics. It is observed that the results for certain combinations of gamma values and order of the standardized moments look similar, however, they are not identical. It can be readily shown that using a gamma value of g with an n-th order moment is not equivalent to using a moment of order $g \times n$ without gamma correction. This is due to the presence of the sample mean and variance of the Q-pixel image in expression (17) for the standardized moments.

For the case of combined wall thickness and dielectric constant errors, we again witness the advantage of using gamma correction in conjunction with higher order metrics. The plots in Fig. 9 show that gamma correction reduces the noise and accentuates the maximum peak corresponding to exact wall parameters for the 25-th order standardized moment. Also, as expected, multiple local maxima still exist. Similar observations were made for the single target case as well under various error conditions.

We estimated the wall parameters for the two target scene by minimizing the negative of the 25-th standardized moment with a gamma of 3. The simplex method of Nelder and Mead, which is a standard multi-variable nonlinear minimization technique, was used [31]. When initialized with values of wall thickness and refractive index, respectively, overestimated by 20% and 10%, the algorithm converged to a dominant local solution corresponding to a wall thickness error of 0.0199 and refractive index error of 0.2049. Note that the true values of the wall parameters are (0.15m, 9). However, when initialized with wall parameter values that lie close to the small local peaks of the metric, the algorithm was unable to

converge to one of the dominant peaks. Improved optimization algorithms may be required to tackle this optimization problem which has a multiplicity of local solutions [32].

In Fig. 9, the error surfaces have a local maximum at a wall thickness error of 0.02m and a refractive index error of 0.2. This corresponds to the estimated wall thickness and dielectric constant pair of (0.17m, 10.24). Another local maximum exists at the pair (0.07m, 13.69), which corresponds to thickness error of -0.08m and refractive index error of 0.7. We used these estimated wall parameter pairs to generate beamformed images, without gamma correction, of the two target scene. Figure 10 shows the range profiles at an angle of -10° corresponding to the estimated parameter pairs (0.17m, 10.24) (dashed line) and (0.07m, 13.69) (dash-dotted line), respectively. For comparison, the range profile for the zero error case (solid line) is also provided. Both of the estimated wall parameter pairs yield good focus and an error in imaged target positions of less than 2% of the true target locations. This is expected because, as proven in Section 3, the image intensity profile for these wall parameter pairs is close to that under exact knowledge of wall parameters, thereby yielding the same focusing performance. Hence, any of the maxima of the error surface of a higher order metric can be used to achieve high level of autofocusing and deblurring of through-the-wall radar imagery, even when residual error in imaged target locations is present. This outcome is acceptable because it leads to localization errors relatively smaller than the case if the wall ambiguities were left unresolved. To highlight this point further, we consider the case when the two target distribution is imaged through two consecutive identical walls, each with a thickness of 0.15m and a dielectric constant of 9. Figure 11 shows the range profiles at an angle of -10° under known walls (solid line) and with wall parameters underestimated by 30% (dash-dotted line). It is evident that the effects of wall ambiguities in the presence of two walls, especially the shift in the imaged target location, have increased compared to imaging through a single wall (see Fig. 4). We then used the wall thickness and dielectric constant pair of (0.17m, 10.24), corresponding to a local maximum in Fig. 9, to generate the range profile at an angle of -10°, shown in Fig. 11 (dashed line). Again, the incorrect wall parameter pair leads to good focus and much improved target localization.

5. CONCLUSIONS

"Seeing" through the wall using radio frequencies is finding increased number of civilian and defense applications. It is an emerging technology that is currently sought out by both the commercial and government sectors. The fact that wall characteristics may be unknown in practice presents a challenge in producing accurate and reliable images. In this chapter, we presented an autofocusing system for through-the-wall applications that focuses the image and corrects for shifts in imaged locations of stationary targets. We analyzed the intensity profile, for this system, under far-field and small error assumptions. We considered point targets and assumed single uniform walls. Our analysis showed that exact as well as incorrect assumed wall thickness and dielectric constant, can lead to similar focused images with satisfactory imaged target positions. We examined potential image quality metrics that allow the system operator to perform imaging under wall parameter ambiguities. It was shown that higher order statistics are more sensitive to errors in wall parameters as compared to conventional contrast measures such as sum of squared intensity. This is because the peaks in the image intensity profile become sharper as the image intensity is raised to a higher power, increasing the overall image contrast. This high sensitivity, combined with gamma correction, which further increases the overall contrast of the image, shows promise for high-quality autofocusing of through-the-wall radar imagery. Several simulation examples were presented which demonstrated the effectiveness of the proposed approach.

APPENDIX

Assume that the targets being imaged are located in the far-field of the array and the errors δ_w and δ_ε are relatively small. Then, the targets and the pixels being imaged will subtend the same angle to all the elements of the transmit and receive arrays. Therefore,

$$\theta_{t_m,q} \approx \theta_q, \quad \theta_{r_n,q} \approx \theta_q, \quad \theta_{t_m,p} \approx \theta_p, \quad \theta_{r_n,p} \approx \theta_p$$
$$\varphi_{t_m,q} \approx \varphi_q, \quad \theta_{r_n,q} \approx \varphi_q, \quad \theta_{t_m,p} \approx \varphi_p, \quad \theta_{r_n,p} \approx \varphi_p$$

(A-1)

for all *m, n*, where θ_j, φ_j, for *j=p,q*, are the angles with respect to the origin, as shown in Fig. 3 (it is not necessary that an antenna element should exist at the origin). Also, under far-field approximation, the following Euclidean distances can be approximated as

$$dist(\mathbf{x_{tm}}, \mathbf{x_q}) \approx R_q - x_{tm} \sin \varphi_q, \qquad dist(\mathbf{x_{rn}}, \mathbf{x_q}) \approx R_q - x_{rn} \sin \varphi_q$$
$$dist(\mathbf{x_{tm}}, \mathbf{x_p}) \approx R_p - x_{tm} \sin \varphi_p, \qquad dist(\mathbf{x_{rn}}, \mathbf{x_p}) \approx R_p - x_{rn} \sin \varphi_p \tag{A-2}$$

where

$$R_q = \sqrt{x_q^2 + y_q^2}, \qquad R_p = \sqrt{x_p^2 + y_p^2} \tag{A-3}$$

In through-the-wall imaging, as the targets are located inside an enclosed area, the region of interest and hence the angles φ_j, for *j=p, q*, in the far-field of the array will be further limited by the side walls. As a result, under far-field conditions, the corresponding angles θ_j, for *j=p, q*, will be concentrated in a narrow region around broadside [5]. This is especially true for wall materials with high dielectric constants such as concrete. In fact, the greater the dielectric constant, the closer the angles θ_j are to zero. Using Snell's Law equations, the following approximations are valid for small angular values,

$$\sin \theta_p \approx \theta_p, \qquad \cos \theta_p \approx 1, \qquad \sin \varphi_p \approx \sqrt{\varepsilon} \theta_p, \qquad \cos \varphi_p \approx 1 - \frac{\varepsilon \theta_p^2}{2}$$
$$\sin \theta_q \approx \theta_q, \qquad \cos \theta_q \approx 1, \qquad \sin \varphi_q \approx (\sqrt{\varepsilon} + \delta_\varepsilon) \theta_q, \qquad \cos \varphi_q \approx 1 - \frac{(\varepsilon + 2\sqrt{\varepsilon}\delta_\varepsilon) \theta_q^2}{2} \tag{A-4}$$

Therefore, the complex amplitude image value, $\hat{I}(\mathbf{x_q})$, under far-field and small error assumptions, is given by (5) (reproduced here for convenience)

$$\hat{I}(\mathbf{x_q}) = \sum_{m=1}^{M} \sum_{n=1}^{N} w_{tm} w_{rn} a(\mathbf{x_p}) s(t - \tau_{p,mn} + \tau_{q,mn}) * h(t) \Big|_{t=0} \tag{A-5}$$

with $t - \tau_{p,mn} + \tau_{q,mn}$ approximated by

$$t - \tau_{p,mn} + \tau_{q,mn} \approx t + \frac{2(R_q - R_p)}{c} - \frac{\sqrt{\varepsilon}(x_{tm} + x_{rn})(\theta_q - \theta_p)}{c} + \frac{2d - (x_{tm} + x_{rn})\theta_q}{c} \delta_\varepsilon$$
$$+ \frac{2(\sqrt{\varepsilon} - 1)}{c} \delta_w + \frac{2}{c} \delta_w \delta_\varepsilon \tag{A-6}$$

Let $S(\omega)$ be the Fourier transform of the wideband signal $s(t)$. The frequency response of the matched filter is $S^*(\omega)$. Then, $\hat{I}(\mathbf{x_q})$ can be rewritten as

$$\hat{I}(\mathbf{x_q}) = \frac{1}{2\pi} \sum_{m=1}^{M} \sum_{n=1}^{N} w_{tm} w_{rn} a(\mathbf{x_p}) \int_{-\infty}^{\infty} |S(\omega)|^2 \exp(j\omega(\tau_{q,mn} - \tau_{p,mn})) d\omega \qquad \text{(A-7)}$$

with $\tau_{q,mn} - \tau_{p,mn}$ given by (A-6) with $t=0$. Using a change of variables, (A-7) can be expressed as

$$\hat{I}(\mathbf{x_q}) = \frac{1}{2\pi} \sum_{l=1}^{N_c} g_l a(\mathbf{x_p}) \int_{-\infty}^{\infty} |S(\omega)|^2 \exp(j\omega\tau_l) d\omega \qquad \text{(A-8)}$$

where $\tau_l = \tau_{q,mn} - \tau_{p,mn}$, which can be rewritten as

$$\tau_l = \frac{2(R_q - R_p)}{c} - \frac{\sqrt{\varepsilon} z_l(\theta_q - \theta_p)}{c} + \frac{2d - z_l\theta_q}{c}\delta_\varepsilon + \frac{2(\sqrt{\varepsilon} - 1)}{c}\delta_w + \frac{2}{c}\delta_w\delta_\varepsilon \qquad \text{(A-9)}$$

and N_c is the number of points in the coarray, z_l is the l-th coarray location, and g_l is the coarray weighting, which is defined as [15]

$$g_l = \sum_{(a,b) \in C_l} w_{ta} w_{rb}, \qquad C_l = \{(a,b) \mid z_l = x_{ta} + x_{rb}\} \qquad \text{(A-10)}$$

Eq. (A-8) is an alternate expression for the complex amplitude of the pixel being imaged in the presence of small errors in wall parameters for far-field scenario in terms of the coarray. The term $\exp(j\omega\tau_l)$ in (A-8) can be expressed as a product of two complex exponentials,

$$\exp(j\omega\tau_l) = \exp(j\omega\tau_{l1})\exp(j\omega\tau_{l2}) \qquad \text{(A-11)}$$

where

$$\tau_{l1} = \frac{2(R_q - R_p)}{c} - \frac{\sqrt{\varepsilon} z_l(\theta_q - \theta_p)}{c}$$
$$\tau_{l2} = \frac{2d - z_l\theta_q}{c}\delta_\varepsilon + \frac{2(\sqrt{\varepsilon} - 1)}{c}\delta_w + \frac{2}{c}\delta_w\delta_\varepsilon \qquad \text{(A-12)}$$

For small errors, we replace $\exp(j\omega\tau_{l2})$ in (A-11) with the first few terms of its series expansion $(1 + j\omega\tau_{l2} - \omega^2\tau_{l2}^2/2 - \cdots)$, substitute the value of τ_{l2} from (A-12), multiply the factors, and retain only the linear error terms. This leads to

$$\exp(j\omega\tau_l) \approx \exp(j\omega\tau_{l1})\left(1 + j\omega\frac{2d - z_l\theta_q}{c}\delta_\varepsilon + j\omega\frac{2(\sqrt{\varepsilon}-1)}{c}\delta_w\right) \tag{A-13}$$

Substituting the value of $\exp(j\omega\tau_l)$ from (A-13) in (A-8), and taking the inverse Fourier transform, we obtain

$$\hat{I}(\mathbf{x_q}) \approx \sum_{l=1}^{N_c} g_l a(\mathbf{x_p})s(t+\tau_{l1})*h(t)\Big|_{t=0} + \delta_w\frac{2(\sqrt{\varepsilon}-1)}{c}\sum_{l=1}^{N_c} g_l a(\mathbf{x_p})\frac{d\psi_s(t)}{dt}\Big|_{t=\tau_{l1}}$$
$$+ \delta_\varepsilon\sum_{l=1}^{N_c} g_l a(\mathbf{x_p})\left(\frac{2d - z_l\theta_q}{c}\right)\frac{d\psi_s(t)}{dt}\Big|_{t=\tau_{l1}} \tag{A-14}$$

where $\psi_s(t)$ is the autocorrelation function of the pulse $s(t)$. We note that the first summation is the far-field equivalent of (5). Therefore, (A-14) takes the form

$$\hat{I}(\mathbf{x_q}) \approx I(\mathbf{x_q}) + \delta_w\frac{2(\sqrt{\varepsilon}-1)}{c}\sum_{l=1}^{N_c} g_l a(\mathbf{x_p})\frac{d\psi_s(t)}{dt}\Big|_{t=\tau_{l1}} + \delta_\varepsilon\sum_{l=1}^{N_c} g_l a(\mathbf{x_p})\left(\frac{2d - z_l\theta_q}{c}\right)\frac{d\psi_s(t)}{dt}\Big|_{t=\tau_{l1}} \tag{A-15}$$

where $I(\mathbf{x_q})$ is the pixel value in the absence of wall errors.

REFERENCES

[1] D. D. Ferris Jr. and N. C. Currie, "A survey of current technologies for through-the-wall surveillance (TWS)," *Proc. SPIE*, vol. 3577, pp. 62-72, 1998.

[2] N. C. Wild, F. Felber, M. Treadaway, F. Doft, D. Breuner, and S. Lutjens, "Ultrasonic through-the wall surveillance system," *Proc. SPIE*, vol. 4232, pp. 167-176, Nov. 2000.

[3] E. F. Greneker, "RADAR flashlight for through-the-wall detection of humans," *Proc. SPIE*, vol. 3375, pp. 280-285, April 1998.

[4] J. D. Black, "Motion and Ranging Sensor through-the-wall surveillance system," *Proc. SPIE*, vol. 4708, pp. 114-121, April 2002.

[5] F. Ahmad, M. G. Amin, and S. A. Kassam, "Synthetic aperture beamformer for imaging through a dielectric wall," *IEEE Trans. Aerosp. Electron. Syst.*, vol. 41, no. 1, pp. 271-283, Jan. 2005.

[6] P. Withington, H. Fluhler, and S. Nag, "Enhancing homeland security with advanced UWB sensors," *IEEE Microw. Mag.*, vol. 4, no.3, pp. 51-58, Sept. 2003.

[7] A. R. Hunt, "Stepped-frequency CW radar for concealed weapon detection and through-the-wall surveillance," *Proc. SPIE*, vol. 4708, pp. 99-105, April 2002.

[8] V. Venkatasubramanian and H. Leung, "A novel chaos based high resolution imaging and its applications to through-the-wall imaging," *IEEE Signal Process. Lett.*, vol. 12, no. 7, pp. 528-531, July 2005.

[9] A. R. Hunt, "Image formation through walls using a distributed radar sensor network," *Proc. IEEE AP-S International Symposium*, June 2004.

[10] F. Ahmad and M. G. Amin, "Noncoherent approach to through-the-wall radar localization", *IEEE Trans. Aerosp. Electron. Syst.*, Vol. 42, No. 4, Oct. 2006.

[11] http://www.schafertmd.com/VisibuildingIndustryDay/documents/VisiBuilding_Proposers_Briefing.pdf

[12] G. Wang, Y. Zhang, and M. G. Amin, "A new approach for target locations in the presence of wall ambiguities", *IEEE Trans. Aerosp. Electron. Syst.*, Vol. 42. No. 1, Jan. 2006.

[13] G. Wang and M. G. Amin, "Imaging through unknown walls using different standoff distances", *IEEE Trans. Signal Process.*, Vol. 54, No. 10, pp. 4015-4025, Oct. 2006.

[14] F. Ahmad, G. J. Frazer, S. A. Kassam and M. G. Amin, "Design and implementation of near-field, wideband synthetic aperture beamformers," *IEEE Trans. Aerosp. Electron. Syst.*, vol. 40, no. 1, pp.206-220, Jan. 2004.

[15] R. T. Hoctor and S. A. Kassam, "The unifying role of the coarray in aperture synthesis for coherent and incoherent imaging," *Proc. IEEE*, vol. 78, no. 4, pp. 735-752, Apr. 1990.

[16] F. Ahmad and S. A. Kassam, "Coarray analysis of the wide-band point spread function for active array imaging," *Signal Processing*, vol. 81, pp. 99-115, Jan 2001.

[17] S. Weiss, C. L. Koh, and W. Liu, "A comparison of adaptive beamforming implementations for wideband scenarios," *Proc. Second IEE/EURASIP Conference on DSP Enabled Radio*, 2005.

[18] A. Hoffman and S. M. Kogon, "Subband STAP in wideband radar systems," *Proc. IEEE Workshop on Sensor Array and Multichannel Signal Processing (SAM2000)*, pp. 256-260, 2000.

[19] P. Saengudomlert and V.W.S. Chan, "Using optical switches and fiber delay lines for wideband beamforming with RF uniform line arrays," *Proc. IEEE Region 10 Conference*, pp. 555-558, 2004.

[20] R. T. Hoctor and S. A. Kassam, "Array redundancy for active line arrays", IEEE Trans. on Image Processing, vol. 5, no. 7, pp. 1179-1183, 1996.

[21] P. T. Gough, M. P. Hayes, and H. J. Callow, "Strip-map path correction using phase matching autofocus," *Proc. Fifth European Conf. on Underwater Acoustics*, vol. 1, July 2000, pp. 413-418.

[22] F. Berizzi and G. Corsini, "Autofocusing of inverse synthetic aperture radar images using contrast optimization," *IEEE Trans. Aerosp. Electron. Syst.*, vol. 32, no. 3, July 1996.

[23] R. A. Muller and A. Buffington, "Real-time correction of atmospherically degraded telescope images through image sharpening," *Journal of Optical Society of America*, vol. 64. no. 9, pp. 1200-1210, Sept. 1974.

[24] J. R. Fienup, "Synthetic-aperture radar autofocus by maximizing sharpness", *Optics Letters*, vol. 25, no. 4, Feb. 2000.

[25] Alparone, L; Argenti, F.; Aiazzi, B.; Baronti, S., "Multiresolution approaches to adaptive speckle reduction in synthetic aperture radar images", *Proc. ICIP 2003*, vol.1, pp. 109-112, 2003.

[26] S. Fortune, M. Hayes and P. Gough "Statistical Autofocus of Synthetic Aperture Sonar Images using Image Contrast Optimization," *OCEANS 2001*, vol.1, 2001, pp. 163-169.

[27] *NIST/SEMATECH e-Handbook of Statistical Methods*, http://www.itl.nist.gov/div898/handbook/.

[28] Gunawan, D., "Microcalcification detection using wavelet transform," *Proc. IEEE Pacific Rim Conf. on Communications, Computers and Signal Processing*, vol. 2, 2001, pp. 694-697.

[29] L. Ta-Hsin and L. Ke-Shin, "Deblurring two-tone images by a joint estimation approach using higher-order statistics" *Proc. IEEE Signal Process. Workshop on Higher-Order Statistics*, 1997, pp. 108-111.

[30] C. Poynton, *A technical introduction to digital video*, John Wiley and sons, 1996.

[31] J. E. Dennis Jr. and D. J. Woods, *New Computing Environments: Microcomputers in Large-Scale Computing*, Edited by A. Wouk, SIAM, pp. 116-122, 1987.

[32] M. A. Luersen and R. Le Riche, "Globalized Nelder-Mead method for engineering optimization," *Proc. Third International Conference on Engineering Computational Technology*, pp. 165-166, 2002.
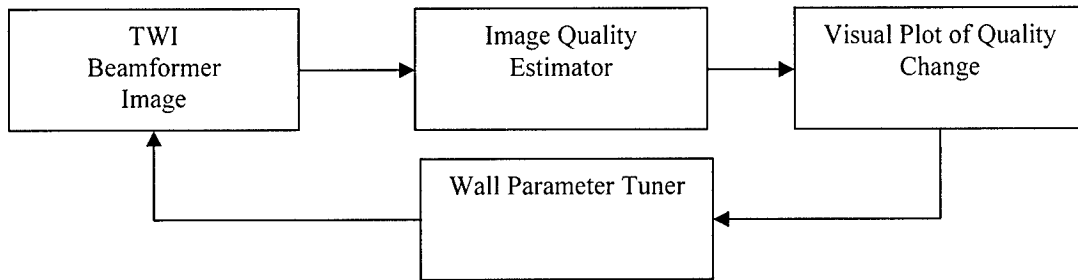
Figure 1. Image Quality Adjustment Feedback Mechanism
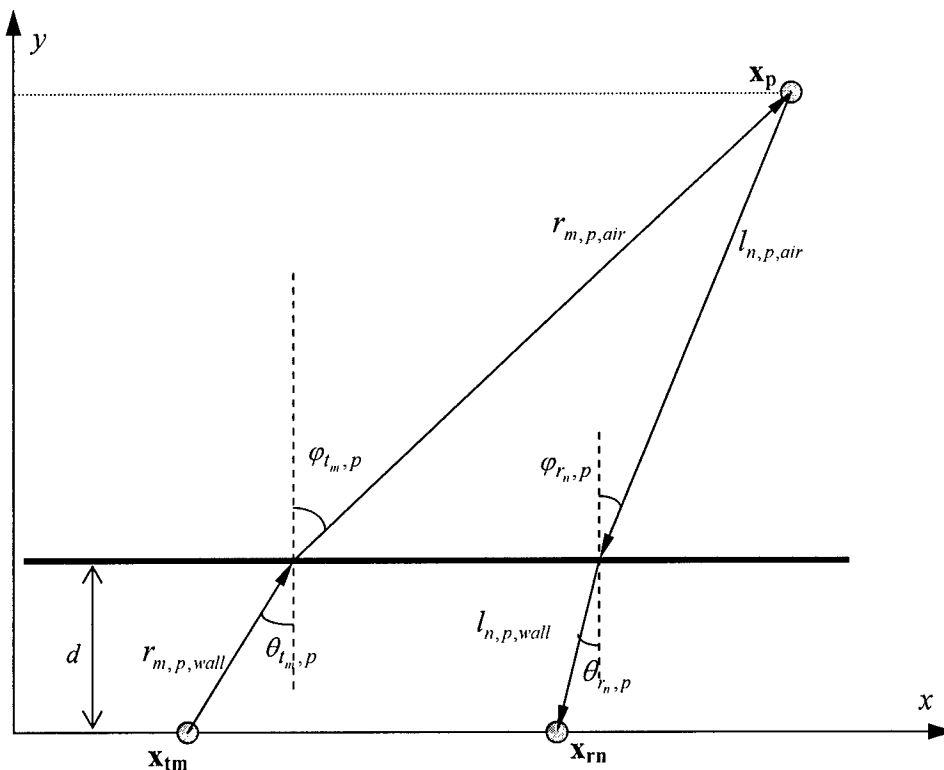
Figure 2. Geometry for computing the distances on transmit and receive. The figure shows the parameters for propagation delay with target at x_p. The same figure is valid for focusing delays for a pixel at x_q by replacing the subscript p with q.

Element #	1	2	3	4	5	6	7	8
Transmit (m)	-0.9	-0.3	0.3	0.9				
Receive (m)	-0.2625	-0.1875	-0.1125	-0.0375	0.0375	0.1125	0.1875	0.2625

Table I. Transmit and Receive Array locations.
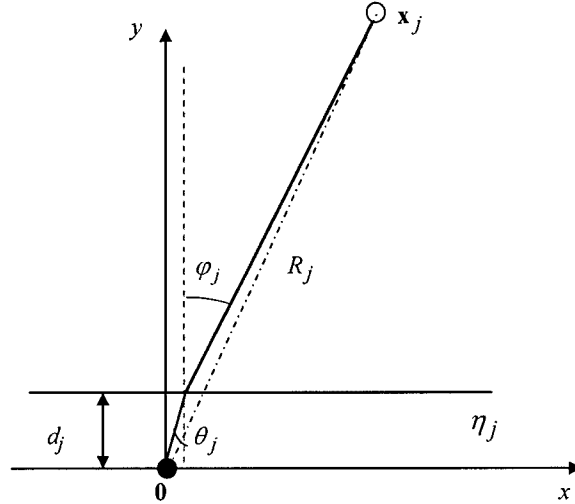
Figure 3. Geometry for propagation ($j=p$) and focusing ($j=q$) under far-field conditions at the origin. The wall thickness and refractive index pair (d_j, η_j) equals $(d, \sqrt{\varepsilon})$ for $j=p$ and $(d + \delta_d, \sqrt{\varepsilon} + \delta_\varepsilon)$ for $j=q$.
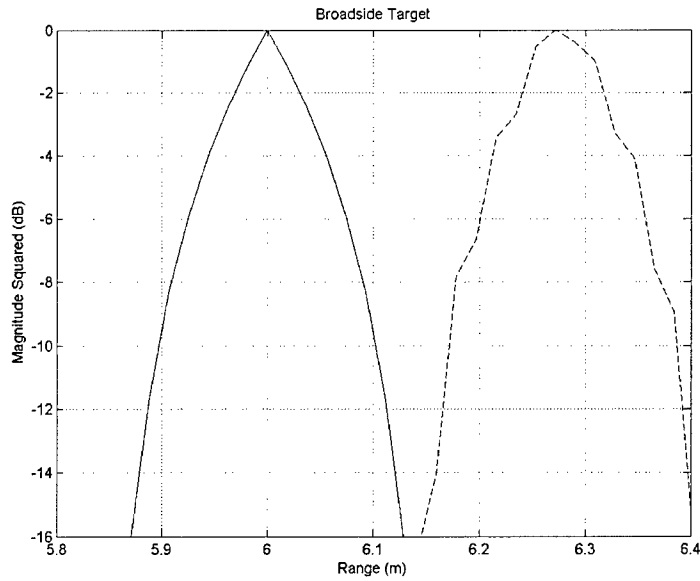
Figure 4. Range profile of a point target, located at (6m, 0°) under known wall (solid line) and with wall parameters underestimated by 30% (dashed line).
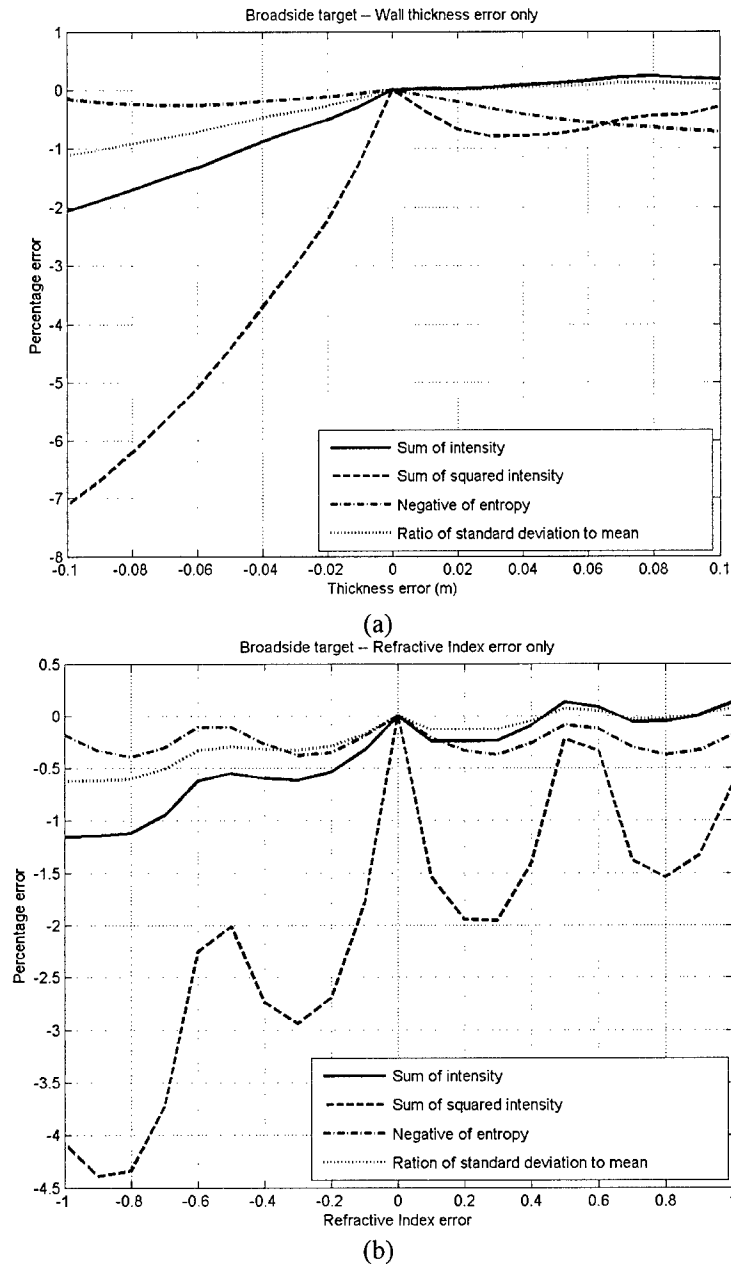
Figure 5. Percentage error of contrast measures (eqs. (13)-(16)) for a scene consisting of a single target located at (6m, 0°); (a) Dielectric constant (refractive index) is known, thickness is unknown, (b) Thickness is known, dielectric constant (refractive index) is unknown.
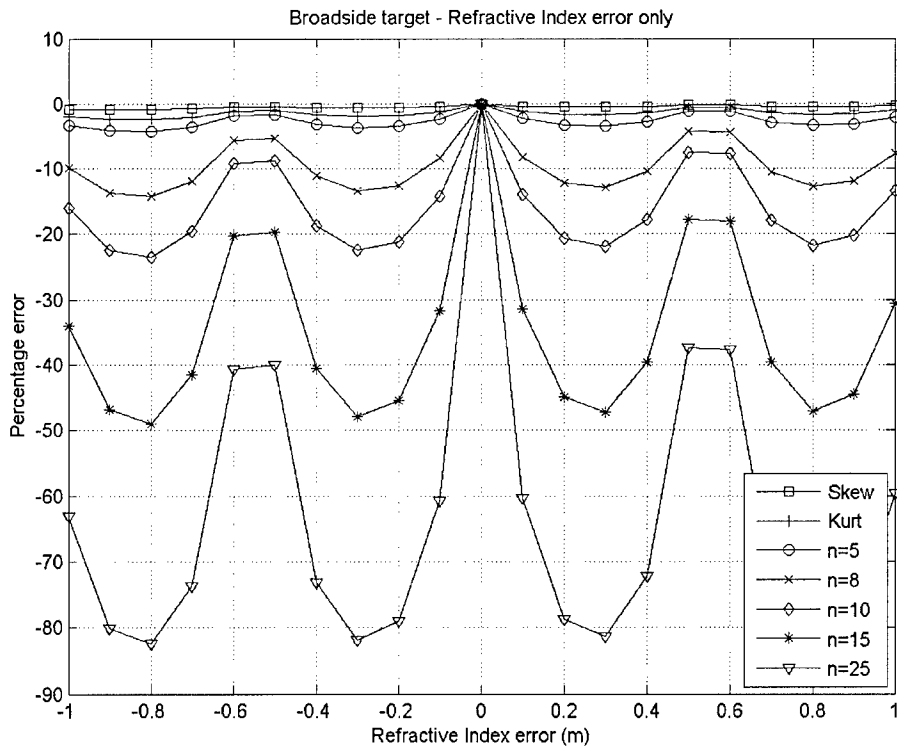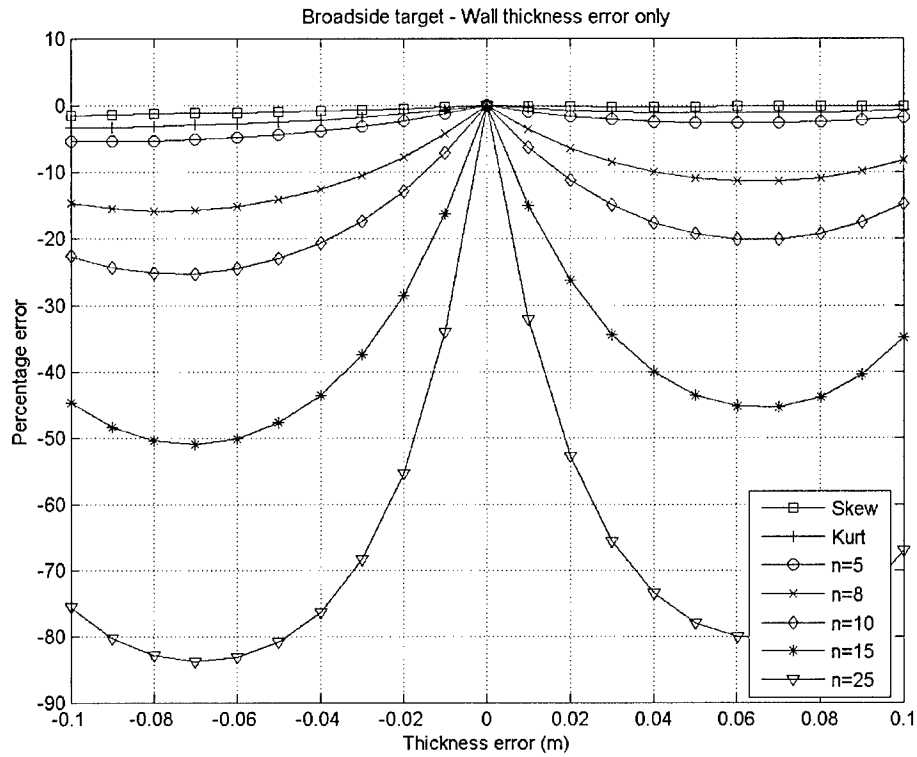
Figure 6. Percentage error of standardized moments for a scene consisting of a single target located at (6m, 0°) (a) The dielectric constant (refractive index) is known, wall thickness is unknown, (b) The dielectric constant (refractive index) is unknown, wall thickness is known.
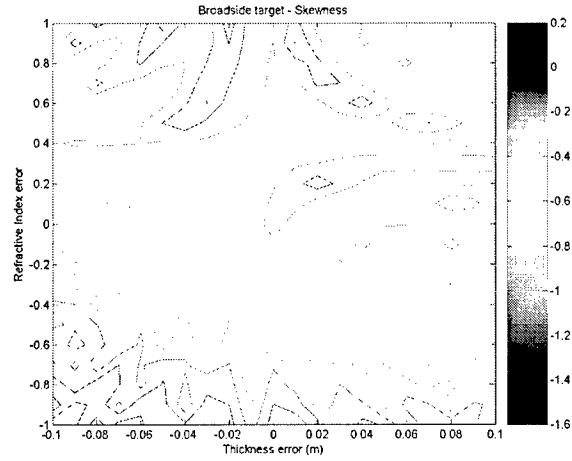
(a)
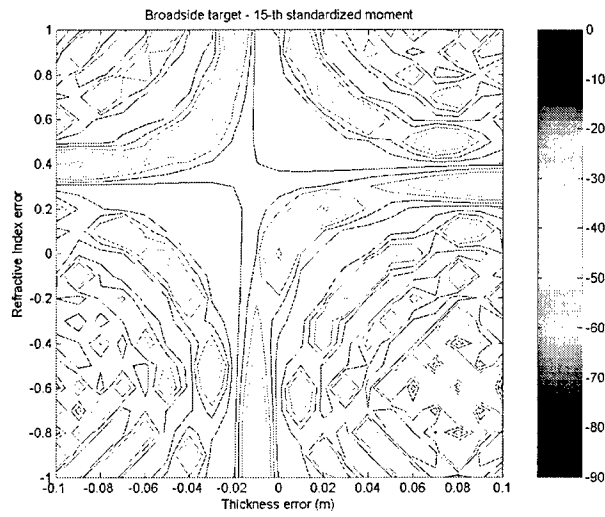
(b)
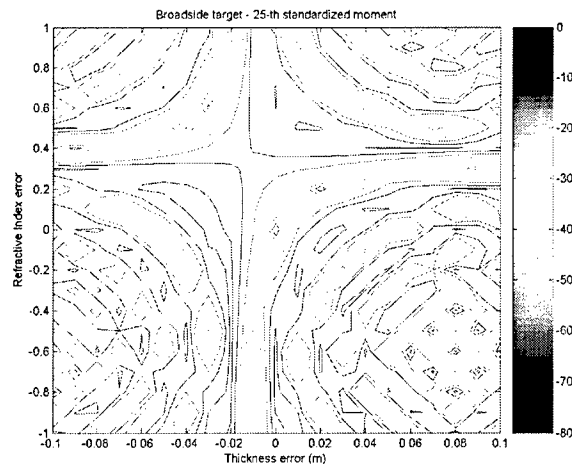
(c)

Figure 7. Percentage error of (a) skewness, (b) 15-th standardized moment, (c) 25-th standardized moment, for a scene consisting of a single target, located at (6m, 0°), when both the dielectric constant (refractive index) and the wall thickness are unknown.

109
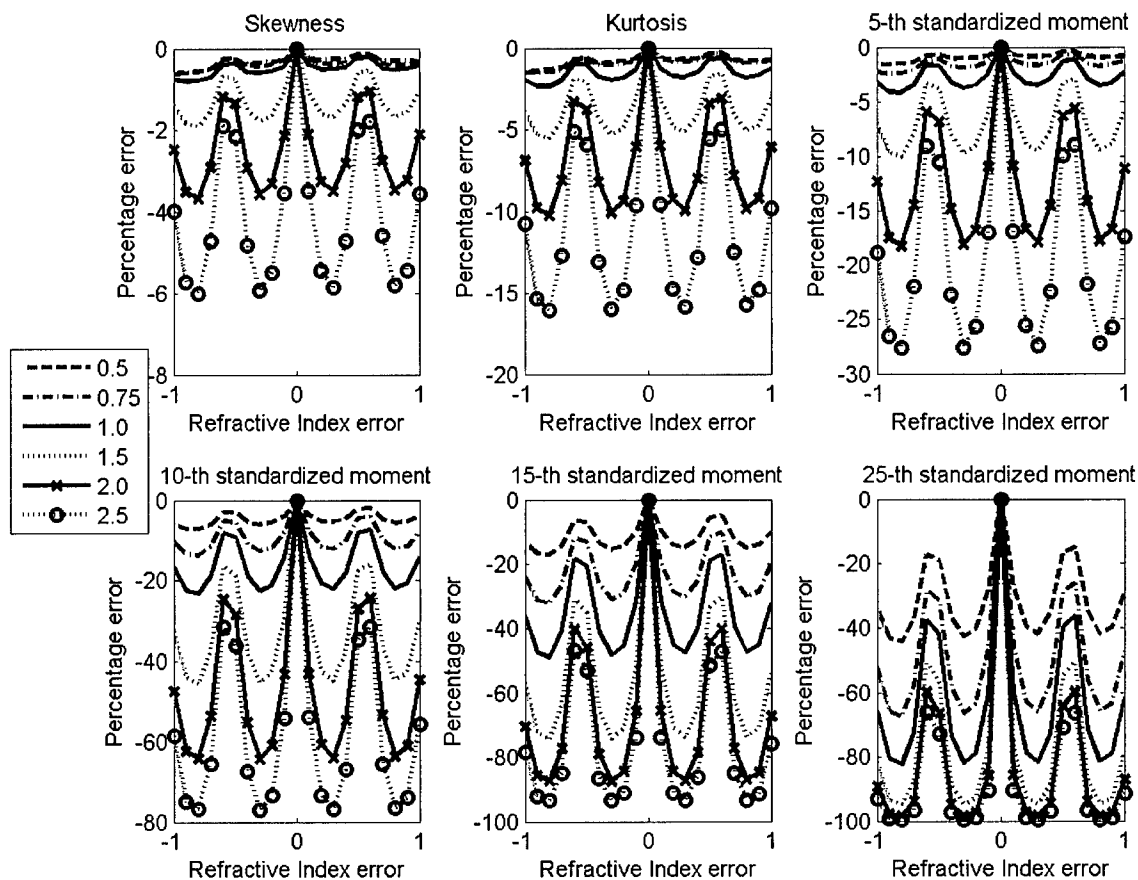
Figure 8. Effect of Gamma correction on higher order metrics for a scene consisting of two targets, located at (6m, -10°) and (6m, 10°). Wall thickness is known, dielectric constant is unknown. Multiple curves on each plot correspond to different values of gamma '*g*'.
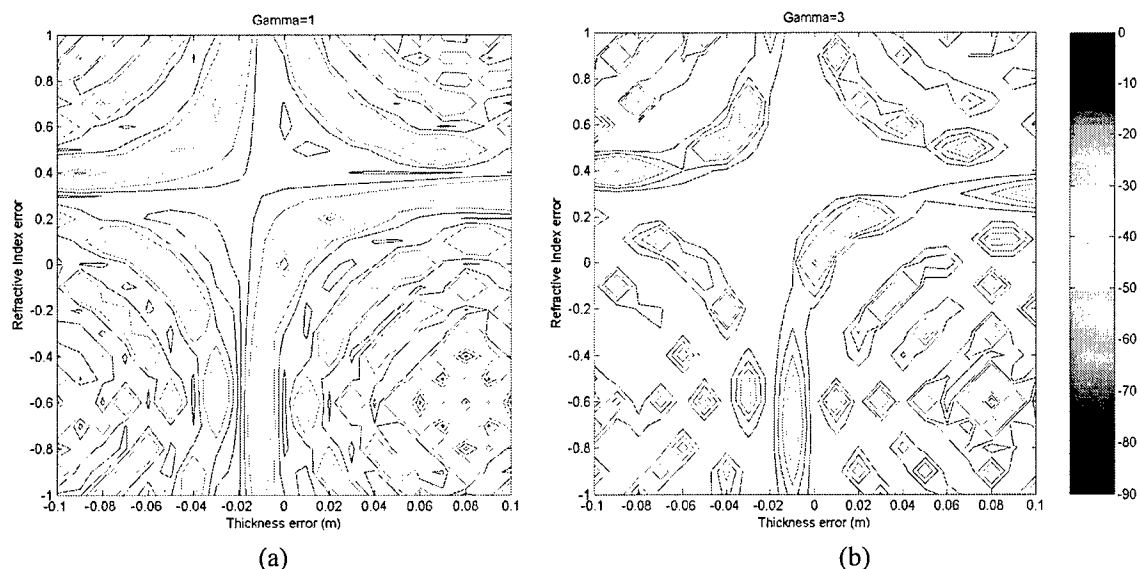
Figure 9. Gamma corrected error surface contour plots of the 25-th standardized moment for the two target scene. (a) n =25, g=1; (b) n =25, g=3.
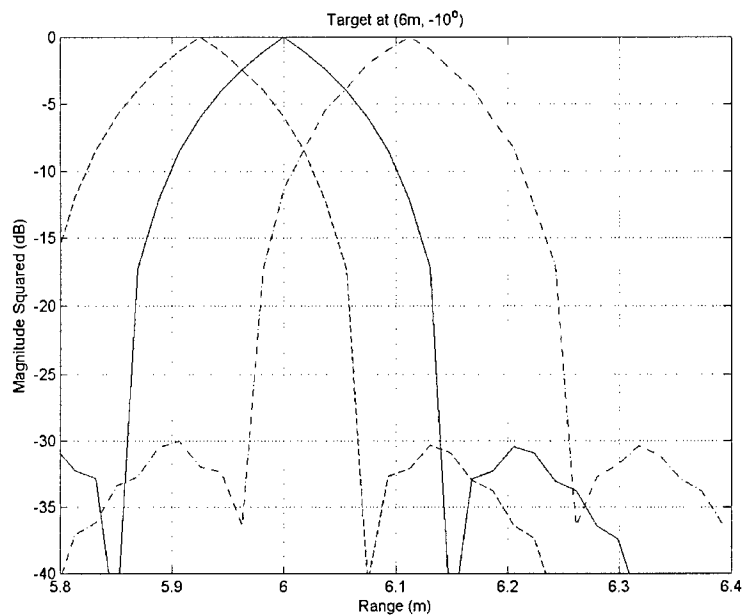
Figure 10. Range profiles of the two target scene at an angle of -10° for various estimated wall parameter pairs ((0.15m, 9) solid line , (0.17m, 10.24) dashed line, (0.07m, 13.69) dash-dotted line.
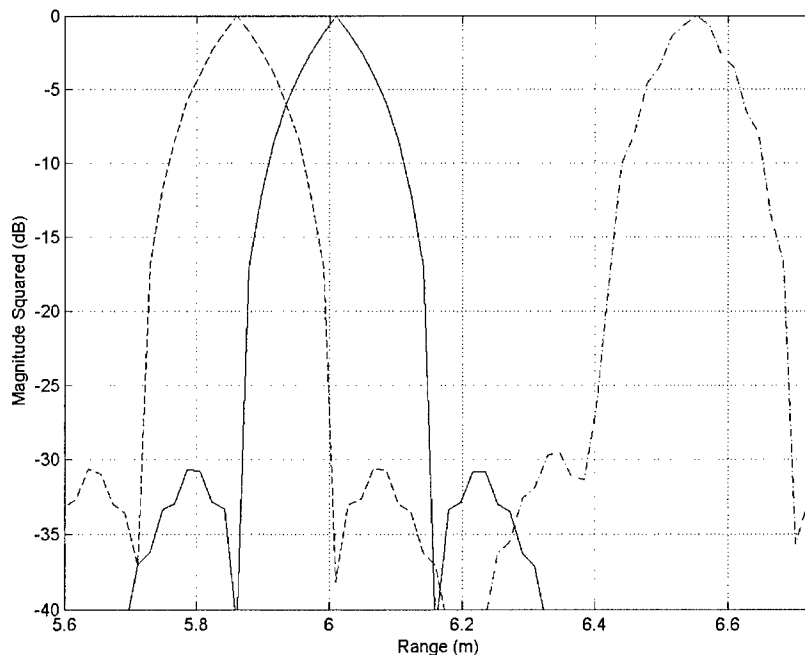
Figure 11. Range profiles of the two target distribution, at an angle of -10°, when imaged through two walls of identical characteristics under three cases: known walls (solid line), wall parameters underestimated by 30% (dash-dotted line), estimated wall parameter pair (0.17m, 10.24) (dashed line).

111

Chapter 5
Blind Source Separation in the Time-Frequency Domain Based on Multiple Hypothesis Testing

Abstract

This chapter considers a time-frequency (t-f) based approach for blind separation of nonstationary signals. In particular, we propose a time-frequency 'point selection' algorithm based on multiple hypothesis testing, which allows automatic selection of auto- or cross-source locations in the time-frequency plane. The selected t-f points are then used via a joint diagonalization and off-diagonalization algorithm to perform source separation. The proposed algorithm is developed assuming deterministic signals with additive white complex Gaussian noise. A performance comparison of the proposed and existing approaches is provided.

I. INTRODUCTION

The problem of blind source separation (BSS) involves recovery of a number of unobserved signals from their observed mixtures. In certain applications, such as radar, sonar and telecommunications, the signals of interest are typically wideband, but instantaneously narrowband in nature. These nonstationary signals, which exhibit a significant variation in spectral content over the observation interval, may be processed using techniques that exploit the nonstationary signal properties, in particular the instantaneous frequency, to obtain improved performance over more general methods.

The use of spatial time-frequency distribution (STFD) matrices has been shown to provide excellent performance for separation of nonstationary sources [3]. This approach requires joint diagonalization (JD) of a set of STFD matrices formed at source auto-term locations in the TF plane. The approach in [3] was then extended in [4] to utilize the cross-terms via joint off-diagonalization (JOD). The combination of JD and JOD (JDOD) was also proposed in [4]. A key issue in applying these methods is 'point selection', i.e. blindly choosing appropriate auto- and cross- source locations on the time-frequency plane which are suitable for applying the JDOD criterion.

A number of approaches to TF point selection have been proposed in the literature. In the initial work [5], a criterion was suggested for discriminating peaks of the sensor STFD as belonging to auto- or cross-source distributions. A shortcoming of this approach is that it requires an *ad hoc* threshold to be chosen when making a decision. The appropriate value of this threshold is heavily signal dependent. An alternative method for choosing single auto-term (SAT) locations was proposed in [6]. The SAT locations are TF points at which the energy of a single source is dominant. This approach provides information for the JD only and does not exploit the source cross-terms in the separation process.

Other methods for point selection are based on hypothesis testing. For these methods one tries to formulate a test statistic that contains information about the auto- or cross-source terms and set an appropriate threshold based on the probability distribution function of the statistics. Initial work was

based on the criterion of Belouchrani *et al* [5]. Because the distribution of the statistic was difficult to obtain analytically, a resampling scheme was proposed to estimate this distribution [7]. This approach, however, requires a significant computational burden. In later work [1], [8] simpler test statistics were proposed in where the distribution could be well approximated analytically. These studies, however, did not consider the multiplicity of the problem, i.e. that we wish to test many TF locations simultaneously in the search for the desired TF points.

In this paper, we propose a point selection scheme based on multiple hypothesis testing. The proposed approach is used to determine both auto- and cross-terms to be used in JD and/or JOD respectively. Use of a statistical multiple hypothesis testing approach allows one to control the probability of selecting false t-f locations and provides an appropriate framework for testing multiple locations in the t-f plane simultaneously. Suitable statistics are proposed for determining the auto- and cross-source locations, along with second-order analysis needed to define pivotal test statistics. The paper is organized as follows: We define the BSS problem in Section II and briefly review STFD matrices and their application to BSS in Section III. The proposed TF point selection scheme is described in Section IV and compared to other existing approaches, in terms of a source separation performance index, in Section V. Conclusions follow in Section VI.

II. PROBLEM FORMULATION

In the following, $(\cdot)'$ and $(\cdot)^H$ denote matrix transposition and Hermitian transposition respectively. We consider an m-element sensor array observing an instantaneous linear mixture of uncorrelated signals emitted from $d < m$ narrowband sources. When dealing with RF signals, only single-polarized antennas are considered. The baseband array output model is

$$X(t) = AS(t) + V(t) \tag{1}$$

where $X(t) \in \mathbb{C}^{m \times 1}$ is the array output vector at time $t \in \mathbb{R}$ and $S(t) \in \mathbb{C}^{d \times 1}$ is the source signal vector. $V(t) \in \mathbb{C}^{m \times 1}$ is a stationary white noise process satisfying

$$\mathsf{E}\left[V(t+\tau)V^H(t)\right] = \sigma_V^2 I \delta_\tau$$

$$\text{and} \quad \mathsf{E}\left[V(t+\tau)V^T(t)\right] = 0, \tag{2}$$

where δ_τ is Kronecker's delta function; equal to zero when $\tau = 0$ and zero otherwise. I and 0 are identity and zero matrices, respectively.

We assume that the array output is sampled above the Nyquist rate generating N observations, $\{x(n)\}_{n=0}^{N-1}$, of the process $X(t)$. The underlying problem is to estimate the mixing system and/or source signals, up to unknown permutation and complex scaling factors.

III. APPROACH

A. Spatial Time-Frequency Distributions

In this work, we make use of the BSS method based on combined JDOD of STFD matrices, as proposed in [4]. The sensor STFD matrix is defined as

$$D_{XX}(t, \omega) = (2\pi)^{-1} \int \int \varphi(t-u, \tau) e^{-j\omega\tau} \mathsf{E}\left[X(u+\tau/2)X^H(u-\tau/2)\right] du \, d\tau \tag{3}$$

where φ is the kernel function defining a distribution from Cohen's class of TFDs [9]. In the following, we use the symbol ζ to represent a point (t, ω) in the t-f plane. Substituting the signal model of Equation (1) into Equation (3) we obtain

$$D_{XX}(\zeta) = AD_{SS}(\zeta)A^H + \sigma^2 I, \tag{4}$$

where σ^2 depends on the noise power and the kernel function according to $\sigma^2 = \sigma_V^2 (2\pi)^{-1} \int \varphi(u, 0) du$. From Equation (4), it is clear that the sensor STFD matrix exhibits the same eigen-structure as the data covariance matrix commonly used in array processing. The source signals' covariance matrix is replaced by a source STFD matrix composed of the auto- and cross-source TFDs on the diagonal and off-diagonal entries, respectively. Provided there are peaks of $|D_{S_i S_i}(\zeta)|$; $i \in [1, d]$ and $|D_{S_i S_j}(\zeta)|$, $i \neq j \in [1, d]$,

115

which occur at mutually exclusive locations in the t-f plane, we can obtain a strong diagonal or off-diagonal structure in the matrix $D_{SS}(\zeta)$. This structure may then be exploited via joint diagonalization and off-diagonalization algorithms for separation of the source signals.

Let us assume that the STFD matrix is evaluated for a set $\mathcal{S} = \{\zeta_i; i \in [1, p]\}$ of points in the t-f plane. We define the set $\mathcal{S}_A \subseteq \mathcal{S}$ of auto-source points as

$$\mathcal{S}_A \triangleq \left\{ \zeta_k; \ \forall k \in [1, p] \text{ where } \sum_{i=1}^{d} |D_{s_i s_i}(\zeta_k)| > 0 \right\}$$

and the set $\mathcal{S}_C \subseteq \mathcal{S}$ of cross-source points as

$$\mathcal{S}_C \triangleq \left\{ \zeta_k; \ \forall k \in [1, p] \text{ where } \sum_{i=1}^{d-1} \sum_{j=i+1}^{d} |D_{s_i s_i}(\zeta_k)| > 0 \right\}.$$

In practice, $\mathcal{S}_A$ and $\mathcal{S}_C$ are not necessarily mutually exclusive, as the main- and sidelobes of the auto- and cross-distributions may significantly overlap. This problem is accentuated by short observation intervals which result in poor t-f resolution when estimating (3).

In order to ensure the desired diagonal or off-diagonal structure of $D_{SS}(\zeta)$ we consider the *dominant* auto- and cross-source points given respectively by

$$\mathcal{S}_{\tilde{A}} \ = \ \mathcal{S}_A \bigcap \overline{\mathcal{S}_A \bigcap \mathcal{S}_C} \tag{5}$$

$$\text{and} \ \mathcal{S}_{\tilde{C}} \ = \ \mathcal{S}_C \bigcap \overline{\mathcal{S}_A \bigcap \mathcal{S}_C}. \tag{6}$$

To maximize the number of points in $\mathcal{S}_{\tilde{A}}$ and $\mathcal{S}_{\tilde{C}}$, we choose a distribution characterized by φ such that the auto- and cross-term points for the signals interest are both well separated and highly localized in the t-f plane. An example of such a kernel when dealing with chirp signals is the Wigner-Ville distribution (WVD). It is noted that the Spectrogram is a TFD which results in cross-terms that lie under the auto-terms and thus resulting in empty sets $\mathcal{S}_{\tilde{A}}$ and $\mathcal{S}_{\tilde{C}}$. In this work, we shall make use of the pseudo Wigner-Ville distribution (PWVD), since other distributions diminish the amplitude and localization of the cross-terms which in turn degrades the performance of the JDOD algorithm. In the following section,

we propose a statistical test for estimating the sets $\mathcal{S}_A$ and $\mathcal{S}_C$. The dominant auto- and cross-source points may then be estimated based on the relationship in Equations (5) and (6).

B. Blind Source Separation Procedure

The BSS procedure contains two main steps, described as follows:

1. Spatial whitening:

Let W define a whitening matrix such that $U = WA$ is unitary, i.e. W whitens the signal part of the observations. A whitened and noise compensated STFD matrix is defined as

$$
\begin{aligned}
\underline{D}_{XX}(\zeta) &= W\big(D_{XX}(\zeta) - \sigma^2 I\big)W^H \\
&= U D_{SS}(\zeta) U^H.
\end{aligned}
\tag{7}
$$

In practice, W and σ^2 may be estimated from the sample covariance matrix as discussed in [3], while $D_{XX}(\zeta)$ is estimated based on a discrete-time formulation of the TFDs as discussed in the appendix.

2. Signal Estimation:

From Equation (7), we note that $\underline{D}_{XX}(\zeta)$ is a unitary transformation of a diagonal matrix for $\zeta \in \mathcal{S}_{\tilde{A}}$ and an off-diagonal matrix for $\zeta \in \mathcal{S}_{\tilde{C}}$. Therefore, by estimation of the matrix Equation (7) at appropriate TF points, one may estimate the unitary transformation, U, via optimization of a JDOD criterion, as detailed in [4]. Based on the estimate $\hat{U}$, of the unitary transform, the source signals are recovered (up to an unknown permutation and complex scalar), according to:

$$
\hat{s}(n) = \hat{U}^H \hat{W} x(n); \quad n = 0, \ldots, N-1.
$$

As we shall illustrate in Section V, accurate estimation of $\mathcal{S}_{\tilde{A}}$ and $\mathcal{S}_{\tilde{C}}$ is crucial for good source separation performance.

IV. POINT SELECTION

In the following we shall denote an estimator of $D_{XX}(\zeta)$ as $\hat{D}_{XX}(\zeta)$ and a particular estimate, obtained from the observations, as $\hat{D}_{xx}(\zeta)$. We will deal here with purely deterministic signals so the stochastic nature of $\hat{D}_{XX}(\zeta)$ arises solely due to the noise influence. In this case the 'uncorrelated' sources assumption implies

$$\lim_{N \to \infty} \frac{1}{N} \sum_{n=0}^{N-1} s(n) s^H(n) = I.$$

A. Testing in the time-frequency plane

We tackle the problem of point selection, i.e. estimating $\mathcal{S}_A$ and $\mathcal{S}_C$, using a hypothesis testing framework. For a single point, ζ, in the t-f plane, we may wish to test the null hypothesis H against the alternative K, defined respectively by

$$\begin{aligned} \mathsf{H} &: \quad g\left(D_{ss}(\zeta)\right) = 0, \\ \mathsf{K} &: \quad g\left(D_{ss}(\zeta)\right) \neq 0, \end{aligned} \tag{8}$$

where $g(\cdot)$ yields some combination of the source signal auto- and/or cross-TFDs at the t-f point ζ. The hypothesis test is evaluated such that the probability of rejecting H when H is true (analogous to false alarm) is kept below a certain nominal value, termed the level of significance (LOS), while the power of the test to reject H when K is true (analogous to detection), is maximized [10].

In the more general case, we wish to test a set, $\mathcal{S} = \{\zeta_i; i \in [1, p]\}$, where p is the total number of considered t-f locations. The ith null and alternative hypothesis for each $\zeta_i \in \mathcal{S}$ given respectively by

$$\begin{aligned} \mathsf{H}_i &: \quad g\left(D_{ss}(\zeta_i)\right) = 0 \\ \mathsf{K}_i &: \quad g\left(D_{ss}(\zeta_i)\right) \neq 0, \end{aligned} \tag{9}$$

for $i = 1, \ldots, p$. In this case, evaluation of the multiple hypothesis test (MHT) will result in r rejected null hypothesis, of which r_{H} were true (erroneously rejected) and r_{K} were false (correctly rejected). Various approaches exist for evaluating an MHT which aim to control a global LOS, while achieving a

high power [11]. In the problem at hand, it is expected that the test statistics may be correlated due to the effect of a sliding window used in the computation of the TFDs. This property calls for the application of test procedures which do not assume independence of the test statistics. This assumption is not made by the multiple hypothesis testing methods discussed below.

Often in multiple hypothesis tests, the global level of significance, denoted α, is defined as the family wise error rate (FWE) which is the probability of rejecting at least one null hypothesis when all are true:

$$\alpha = \Pr\left[\text{reject at least one } H_i | \text{all } H_i \text{ are true}\right]. \tag{10}$$

Strong control of the FWE implies that Equation (10) is satisfied for all subsets of hypotheses including the global null and therefore $\alpha \equiv \Pr\left[r_H \geq 1\right]$. Testing procedures which strongly control the FWE include the sequentially rejective Bonferroni (SRB) tests of Holm [12] and Hochberg [13], and the closed test procedure of Hommel [14]. Although it can be shown that Hommel's test is the most powerful among these methods [15], all tests tend to give similar performance as the number of hypotheses increases. However, the complexity of Hommel's test is also the greatest. Among the relatively simple SRB procedures, Hochberg's approach is most powerful and will be used herein.

Strong control of the FWE tends to be conservative as the number of hypotheses increases. More recently, Benjamini and Hochberg have proposed controlling the expected proportion of falsely rejected null hypotheses [16]. In this case, the global level of significance, α, is termed the false discovery rate (FDR):

$$\alpha = \mathsf{E}\left[r_H / r\right] \text{ for } r \neq 0 \text{ and } \alpha = 0 \text{ for } r = 0. \tag{11}$$

The FDR is equivalent to the FWE when all null hypotheses are true, otherwise it is smaller. Therefore when control of the FDR is appropriate, there is a potential for a gain in power over methods strongly controlling the FWE.

In the following we describe suitable test statistics for detecting auto- and cross-source locations and

discuss how the FWE and FDR controlling procedures apply to the problem at hand.

B. Auto-Source Test Statistic

In constructing a test for the auto-source points, the function g of Equation (8) is chosen to be the matrix trace operation, denoted $\text{Tr}[\cdot]$,

$$g(\boldsymbol{D_{ss}}(\zeta)) = \text{Tr}[\boldsymbol{D_{ss}}(\zeta)] = \sum_i D_{s_i s_i}(\zeta).$$

The test is therefore to determine if the sum of auto-source terms is nonzero. If we choose a TFD kernel which always yields positive peaks at the signal auto-terms, then we have a one-sided test with the ith alternate hypothesis stated as $\text{K}_i > 0$, $i = 1, \ldots, p$, in (9). Since the matrix trace operation is invariant under a unitary transformation, then $\text{Tr}[\underline{D}_{XX}(\zeta)] = \text{Tr}[D_{SS}(\zeta)]$. We therefore propose a test statistic as follows:

$$T_A(\zeta) = \frac{\text{Tr}[\boldsymbol{W}(\hat{\boldsymbol{D}}_{XX}(\zeta) - \sigma^2 \boldsymbol{I})\boldsymbol{W}^H]}{\sigma_A(\zeta)}, \tag{12}$$

where $\sigma_A(\zeta)$ is chosen such that $T_A(\zeta)$ has unit variance under the null hypothesis.

A derivation of the variance, $\sigma_A(\zeta)$, for a general class of discrete-time TFDs can be found in the appendix. In the case of the PWVD, we show that

$$\sigma_A^2(\zeta) \approx E_w \sigma_v^2 \left(2\|\boldsymbol{W}\|^2 + \|\boldsymbol{W}\boldsymbol{W}^H\|^2 \sigma_V^2 \right), \tag{13}$$

where E_w denotes the energy of the PWVD window function. We note that the variance is uniform across the TF plane for the PWVD, which has also been shown for the single sensor case by Stankovic [17].

C. Cross-Source Test Statistic

In the case of cross-source points, it is intuitive to define the function g of Equation (9), as the sum of of the magnitude of off-diagonal elements, denoted $\text{Off}[\cdot]$;

$$g(\boldsymbol{D_{ss}}(\zeta)) = \text{Off}[\boldsymbol{D_{ss}}(\zeta)] = \sum_{i \neq j} |D_{s_i s_j}(\zeta)|. \tag{14}$$

120

Typically the cross-terms peaks are highly oscillatory in nature and take on both positive and negative values. By considering the magnitude of components in $D_{ss}(\zeta)$, we ensure that terms in the summation of Equation (14) do not add destructively.

Unfortunately, the quantity Off$[D_{ss}(\zeta)]$ is not easily estimated from $D_{XX}(\zeta)$. It is possible, however, to determine a statistic which is zero when Equation (14) is zero, and greater than or equal to zero when Equation (14) is greater than zero. Consider in the noise-free case, the quantity

$$
\begin{aligned}
B_k(\zeta) &= D_{X_k X_k}(\zeta) - m^{-1} \sum_{i=1}^{m} D_{X_i X_i}(\zeta) \\
&= \sum_{u=1}^{d} \sum_{v=1}^{d} \left(a_{ku} a_{kv}^* - m^{-1} \sum_{l=1}^{m} a_{lu} a_{lv}^* \right) D_{s_u s_v}(\zeta),
\end{aligned}
\tag{15}
$$

for $k = 1, \ldots, m$. The auto-source contribution in the above expression occurs when $u = v$ in the double summation, which is given by

$$
\begin{aligned}
B_{k|\text{auto-source}}(\zeta) &= \sum_{u=1}^{d} \left(|a_{ku}|^2 - m^{-1} \sum_{l=1}^{m} |a_{lu}|^2 \right) D_{s_u s_u}(\zeta) \\
&= 0 \text{ when } |a_{ij}|^2 = P_j \ \forall \ i \in [1.m],
\end{aligned}
$$

where P_j is the received power of source j at the array. The difference of a sensor TFD and the average of sensor TFDs therefore results in complete cancellation of the auto-source terms, independent of the array geometry, provided the received power for each source is the same at each sensor. This condition is met when each sensor has the same magnitude gain response, and the sources are in the far-field of the array. It is noted that the above criterion is robust to variations in the antenna phase responses across the array.

Based on the Equation (15), we propose a cross-source test statistic as follows:

$$
T_C(\zeta) = \sum_{i=1}^{m} \frac{1}{\sigma_{Ci}^2} \left(\hat{D}_{X_i X_i}(\zeta) - m^{-1} \text{Tr}[\hat{D}_{XX}(\zeta)] \right)^2,
\tag{16}
$$

where σ_{Ci}^2 is the variance of $\hat{D}_{X_i X_i}(\zeta)$, for $i = 1, \ldots, m$. The variance $\sigma_{Ci}^2(\zeta)$ is derived for a general

121

class of discrete-time TFDs in the appendix. In the case of the PWVD, we show that

$$\sigma_{Ci}^2 \approx E_w \sigma_V^2 \left(2\mathrm{Tr}[\boldsymbol{R_{XX}}]/m - \sigma_V^2 \right); \quad i = 1, \ldots, m, \tag{17}$$

where $\boldsymbol{R_{XX}}$ is the data covariance matrix and E_w denotes the energy of the PWVD window function.

From (15) we can see that the scaling of cross-source terms depends on the array response. In the typical example of a uniform linear array (ULA) of m sensors, the response at sensor k to source l is given by

$$a_{kl} = \sqrt{P_l} \exp\left\{ \mathrm{j}\Delta(k-1)\sin\theta_l \right\} \tag{18}$$

where source l has direction of arrival (DOA) θ_l relative to the array broadside and Δ is a constant depending on the inter-sensor spacing and carrier wavelength [18]. Substituting (18) into (15) yields

$$B_k(\varsigma) = \sum_{u=1}^{d} \sum_{v=1}^{d} \sqrt{P_u}\sqrt{P_v} b'(k, \phi_{uv}, m) D_{s_u s_v}(\varsigma)$$

where

$$b'(k, \phi_{uv}, m) \triangleq \exp\{\mathrm{j}\Delta(k-1)\phi_{uv}\} - \frac{1 - \exp\mathrm{j}\Delta\phi_{uv}m}{1 - \exp\mathrm{j}\Delta\phi_{uv}} \tag{19}$$

for $k = 1, \ldots, m$ and $\phi_{uv} = \sin\theta_u - \sin\theta_v$. We note that at each sensor k, Equation (19) depends on the difference between the source electrical angles, ϕ_{uv}, and the total number of sensors m. To have an idea about how cross-source terms are scaled in (16) for a ULA, we plot the function $\sum_{k=1}^{m} [b'(k, \phi_{uv}, m)]^2$ for various values of ϕ_{uv} and m in Figure 1. The surface is generated assuming the two sources have directions of arrival $(-\delta\theta/2, \delta\theta/2)$ and varying $\delta\theta$ from 0 to 180 degrees. We note that for $\delta\theta \to 0°$ and $\delta\theta \to 180°$, the cross-terms are scaled to zero, though for other values of $\delta\theta$ the cross-terms are increasingly amplified as the number of sensors increases.

D. Evaluation of the test

To evaluate the test given in Equation (9), for either auto- or cross-source terms, one must know or estimate the probability distribution of the test statistic under the null hypothesis. Empirical investigation

122

have revealed that for a PWVD window length of greater than 30 samples, the distribution of elements of $\hat{D}_{XX}(\zeta)$ is well approximated as multivariate Gaussian, for a range of finite variance distribution models of $V(t)$. This result is upheld by the Central Limit Theorem, given the finite variance of $\hat{D}_{XX}(\zeta)$. Under this approximation, the null distributions of $T_A(\zeta)$ and $T_C(\zeta)$ are standard normal and Chi-Squared with $m - 1$ degrees of freedom (χ^2_{m-1}), respectively. Also, the use of consistent estimators of W, σ^2_V and R_{XX} instead of the true values, does not change the asymptotic distribution of the test statistics.

We will define the MHT procedures used in terms of p-values; $P_1, \ldots, P_p$, corresponding to hypotheses $H_1, \ldots, H_p$, where P_i is the lowest LOS for which H_i would be rejected based on the observed data. Let $P_{(1)} \leq P_{(2)} \leq \cdots \leq P_{(p)}$ be the ordered p-values with corresponding null hypotheses $H_{(1)}, H_{(2)}, \ldots, H_{(p)}$. Hochberg's SRB procedure for strongly controlling the FWE is defined as [13]:

$$\text{Let } k \text{ be the largest } i \text{ for which } P_{(i)} \leq \frac{1}{p - i + 1}\alpha$$
$$\text{then reject all } H_{(i)} \text{ for } i = 1, 2, \ldots, k.$$

Benjamini and Hochberg's SRB procedure of controlling the FDR is given by [16]:

$$\text{Let } k \text{ be the largest } i \text{ for which } P_{(i)} \leq \frac{i}{p}\alpha$$
$$\text{then reject all } H_{(i)} \text{ for } i = 1, 2, \ldots, k.$$

In the case of auto-terms, we evaluate the p-values based on Equation (12) and define

$$\hat{S}_A = \{\zeta_k; \ \forall k \in [1, p] \text{ where } H_k \text{ is rejected}\}. \tag{20}$$

We shall denote the estimate from Equation (20) obtained using the FWE based procedure as $\hat{S}_{A1}$ and using the FDR based procedure as $\hat{S}_{A2}$. In the same way, calculating p-values based on Equation (16), we obtain estimates of the cross-term locations; $\hat{S}_{C1}$ and $\hat{S}_{C2}$. To illustrate the difference between controlling the FWE and FDR in TF point selection, we provide an example in Figure 2, for selection of auto-source locations. The true peaks of the auto-source distributions lie along the dotted lines. It is clear in comparing

123

Figure 2 (a) and (b) that the FWE procedure has a lower number of correct detections, whereas the FDR procedure results in a number of false detections. Strong control of the FWE is a stricter condition than control of the FDR and therefore results in selection of only the stronger auto- or cross-source points. In the use of JD for BSS, we only need to find a few TF locations where the source STFD has strong diagonal structure (large auto-source terms). However, even the presence of weak off-diagonal terms in the source STFD can destroy the desired structure for JD. This concept holds in reverse for JOD. We therefore propose estimation of the desired TF points for BSS according to:

$$\hat{\mathcal{S}}_{\tilde{A}} = \hat{\mathcal{S}}_{A1} \cap \overline{\hat{\mathcal{S}}_{C2}} \quad \text{and} \quad \hat{\mathcal{S}}_{\tilde{C}} = \hat{\mathcal{S}}_{C1} \cap \overline{\hat{\mathcal{S}}_{A2}}, \tag{21}$$

such that the strongest auto-source (resp. cross-source) terms are chosen for JD (resp. JOD) and locations with any detectable cross-source (resp. auto-source) contribution are omitted.

V. RESULTS

To evaluate the performance of the point selection scheme, in the application to BSS, we use a variation of the performance index proposed in [19]. The power of interference source q in the pth separated source, may be expressed as $I_{pq} = \mathsf{E}|[\hat{U}^H \hat{W} A]_{pq}|^2$. Overall performance is evaluated via the mean rejection level;

$$I_{perf} = (d^2 - d)^{-1} \sum_{p \neq q = 1}^{d} I_{pq}, \tag{22}$$

which gives the average power of an unwanted source component in a separated source. We assess the performance in terms of the SNR and the number, K, of t-f points selected. For the proposed scheme, the LOS is set to $\alpha = 0.01$ for both the FWE and FDR controlling procedures. We then choose the $K/2$ points each from $\hat{\mathcal{S}}_{\tilde{C}}$ and $\hat{\mathcal{S}}_{\tilde{C}}$ having the largest values of T_A and T_C respectively.

We also compare the performance of two other existing approaches. The first is by Belouchrani *et al*

in which the peaks of the sensor TFDs as auto- or cross-terms are classified based on the criterion[1] [4]:

$$C_1(\zeta) = \frac{\text{Tr}[\hat{\underline{D}}_{xx}(\zeta)]}{\left\|\hat{\underline{D}}_{xx}(\zeta)\right\|}. \tag{23}$$

Large (resp. small) values of $C_1(\zeta)$ indicate diagonal (resp. off-diagonal) structure. However, one must set an arbitrary threshold for point selection using Equation (23). In this experiment, we decide a point, ζ, belongs to $\mathcal{S}_{\tilde{A}}$ or $\mathcal{S}_{\tilde{C}}$ if $C_1(\zeta) > 0.8$ or $|C_1(\zeta)| < 0.2$ respectively. These values were found to yield the best results when using Equation (23). We then take $K/2$ points from each set, corresponding to the largest values of $\left\|\hat{\underline{D}}_{xx}(\zeta)\right\|$, for use in the JDOD criterion.

A second approach, proposed by Févotte *et al* in [6], is to choose the t-f locations where only a single diagonal entry of $D_{ss}(\zeta)$ is significant (termed SAT locations). Denoting the sample eigenvalues of $\hat{\underline{D}}_{xx}(\zeta)$ by $\{\lambda_k^\zeta;\ k = 1, \ldots, d\}$, the SAT criterion is defined as

$$C_2(\zeta) = \frac{\max_k \left|\lambda_k^\zeta\right|}{\sum_{k=1}^d \left|\lambda_k^\zeta\right|}, \tag{24}$$

which should be close to one at true SAT locations and smaller otherwise. We note that computation of $C_2(\zeta)$ requires an eigen-decomposition at many points in the t-f plane which implies a high computational load, whereas the p-values required for the proposed scheme can be computed using lookup tables. It was suggested to choose t-f points corresponding to local maxima [6], or simply the largest values [20] of the criterion in Equation (24). However, we obtained the best results with this technique by selecting K points from $\hat{\mathcal{S}}_{A2}$ corresponding to the largest values of Equation (24). This approach uses only JD to estimate the unitary transform of Equation (7).

The following test sources are used in the simulation experiments, consisting of one linear FM and

---

[1]Herein $\|\cdot\|$ denotes the Frobenius norm of a matrix.

two quadratic FM signals:

$$s_1(t) \; = \; e^{j2\pi(0.05t + 7.8125 \times 10^{-4}t^2)},$$

$$s_2(t) \; = \; e^{j2\pi(0.15t + 7.8125 \times 10^{-4}t^2)},$$

$$s_3(t) \; = \; e^{j2\pi(0.25t + 1.2500 \times 10^{-3}t^2 - 6.5104 \times 10^{-6}t^3)}.$$

The mixing system used corresponds to a ULA of $m = 8$ sensors and the sources have direction with respect to the array broadside of $(-15°, 10°, -5°)$. $N = 128$ observations are generated with unit sampling period and white complex Gaussian noise is added. In calculation of the STFD matrices, we used the PWVD with a Hamming window of length 31 samples.

The different point selection procedures are illustrated in Figure 3, where the t-f points selected by each scheme for $K = 40$ and an SNR of 10 dB (with respect to each source) are shown. We see that the scheme of Belouchrani *et al* chooses points for JD where both the auto- and cross-source signatures overlap. Since such points contain contributions from both auto- and cross-source TFDs, the performance of the JDOD algorithm is significantly degraded. This algorithm tends to work better for non-overlapping t-f signatures. Févotte *et al*'s method chooses only auto-source terms, though very few points corresponding to source 2 are chosen due to the overlapping cross-source signature. This can degrade the quality of the source 2 waveform estimate. The proposed scheme selects appropriate auto- and cross-source locations, though no auto-source points are chosen from source two. However, the selection of cross-source locations involving source two means that separation is still successful.

The overall performance of the point selection schemes, across a range of $K = 4$ to $K = 100$, and SNR=0 dB to SNR=20 dB, is shown Figure 4, where the mean rejection level has been estimated using 1000 Monte Carlo runs. Clearly the proposed method achieves the best BSS performance with respect to both SNR and number of t-f points chosen. We note that the performance using $C_1(\zeta)$ is especially poor, due to the selection of points for JD at the intersection of the overlapping t-f signatures. The method

of Févotte *et al* is successful, though the best performance is reached at much higher SNR and number of t-f points as compared to the proposed scheme. Though the total number of points chosen with each method was the same, the selection of some strong cross-source terms for use with JDOD provides better performance than JD alone.

In a second example, we have sources $(s_2(t), s_3(t))$ with DOAs $(-5°, 5°)$ present. An example of each point selection procedure is shown in Figure 5 computed for $K = 40$ and an SNR of 10 dB. In this example we note that the method based on $C_2(\zeta)$ chooses points much farther from the TFD peaks than that of the proposed method. This is because the eigen-value based criterion may have a high value, even at noise locations on the TF plane. The BSS performance index is evaluated across the same range of K and SNR as in the previous example, and the results are shown in Figure 6. We note that, while both the proposed scheme and that of Févotte *et al* are able to choose appropriate points for separation, the energy criterion fails. This is because there are no non-overlapping t-f signatures, as in the previous example, from which correct points for JD would be chosen. In the results shown, the proposed method is seen to achieve good performance with fewer TF points than the method of Févotte *et al*, due both to selection of points closer to the TFD peaks and inclusion of cross-source locations as mentioned previously.

A third example uses two quadratic FM sources defined below, with DOAs $(-5°, -1°)$:

$$s_4(t) = e^{j2\pi(0.4t - 3.3594 \times 10^{-3}t^2 + 1.1393 \times 10^{-5}t^3)},$$

$$s_5(t) = e^{j2\pi(0.3t - 2.2396 \times 10^{-3}t^2 + 7.5955 \times 10^{-6}t^3)}.$$

In this case, the sources have very close t-f signatures and close DOAs. An example of the point selection results from each scheme is shown in Figure 7. We note that here even the criterion $C_2(\zeta)$ chooses many points near the intersection of the TF signatures. This results because the DOAs are very close, so the eigen-values of the STFD matrices are not so well separated, and the use of $C_2(\zeta)$ is therefore not as effective in discriminating SAT locations, especially in the presence of noise. The proposed method,

however, is based on selecting peaks of the auto- or cross-source TFDs and therefore less effected by closely spaced sources. The BSS performance of all three point selection schemes is evaluated as previously and the results plotted in Figure 8. We see that only the proposed method achieves reasonable separation of the sources. Both the energy based criterion and that of Févotte *et al* fail to determine correct t-f point for separation due to the closely spaced t-f and spatial signatures of the sources.

VI. Conclusions

A 'point selection' scheme for selecting STFD matrices with underlying diagonal or off-diagonal structure has been proposed based on multiple hypothesis testing. The proposed method allows blind application of BSS based on JDOD of the STFD matrices. In contrast to other proposed point selection schemes, there is no *ad hoc*, signal dependent threshold value to be chosen, rather, one decides on an acceptable probability of falsely selecting TF points. The simulation examples given here highlight a number of advantages of the proposed scheme:

- Selection of points when overlapping TF signatures are present is handled properly, even with closely spaced sources.

- By selection of both auto- and cross-source locations one can achieve better performance via JDOD than with JD alone.

- The proposed selection scheme results in good BSS performance with fewer chosen TF points and at lower SNR than other methods.

To elaborate upon the last point: as BSS performance is achieved for a smaller number of selected points with the proposed method, fewer STFD matrices must be evaluated and the time required for optimizing the JDOD criterion is reduced. Also, as pivotal test statistics are used, the thresholds for the MHT procedure may be pre-computed and called from a table. The computational complexity of the proposed method is therefore relatively low, compared with that of Févotte *et al*, which requires the

128

eigen-decomposition of many STFD matrices to compute the SAT criterion.

Appendix

In the following we derive the variances required for forming the auto- and cross-source statistics given in Equation (12) and (16) respectively. We consider the following discrete-time estimator of the STFD matrix in bilinear form:

$$\hat{D}_{XX}(n, \omega, \varphi) = \sum_{m} \sum_{l} \varphi(m, l) X(n + m + l) X^*(n + m - l) e^{-j2\omega l} \tag{25}$$

where $\varphi(m, l)$ is the kernel defining the distribution. We also express the corresponding STFD in the inner product form:

$$\hat{Z}_{XX}(n, \omega, \psi) = \sum_{m} \sum_{k} \psi(m, k) [X(n + m) e^{-j\omega m}] \, [X(n + k) e^{-j\omega k}]^H \tag{26}$$

where $\psi(m, k) = \varphi((m + k)/2, (m - k)/2)$. We define the signal part of the observations as $y(n) = As(n)$. The STFD matrix estimator has the form

$$\hat{D}_{XX}(n, \omega, \varphi) = A + B + C$$

where the matrices A, B and C are defined as

$$A = \hat{D}_{yy}(n, \omega, \varphi)$$

$$B = \hat{D}_{yV}(n, \omega, \varphi) + \hat{D}_{Vy}(n, \omega, \varphi)$$

$$C = \hat{D}_{VV}(n, \omega, \varphi)$$

and the dependence on n, ω and φ is omitted from the notation for convenience. The matrices A, B and C shall be referred to as the *signal, signal-noise* and *noise* STFDs respectively. We not that only matrices B and C are comprised of random entries due to the noise.

Lemma 1 (Signal-noise STFD):

1) The expected value is given by $\mathsf{E}\,[B] = 0$ and the covariance of two elements of B is given by

$$\mathsf{Cov}\,[B_{ij}, B_{kl}] = \sigma_V^2 \left[\hat{Z}_{y_i y_k}(n, \omega, \phi)\delta_{j-l} + \hat{Z}_{y_l y_j}(n, \omega, \phi)\delta_{k-i} \right] \tag{27}$$

where the kernel ϕ is related to φ according to

$$\phi(m_1, m_2) = \sum_k \varphi\left(\frac{m_1 + k}{2}, \frac{m_1 - k}{2}\right)\varphi\left(\frac{m_2 + k}{2}, \frac{m_2 - k}{2}\right). \tag{28}$$

This means that two elements on the same row or column of B are correlated.

2) The expected value of the trace of the whitened STFD is $\mathsf{E}\left[\mathsf{Tr}[WBW^{\mathrm{H}}]\right] = 0$ and the variance of the trace of the whitened STFD is given by

$$\mathsf{Var}\,[\mathsf{Tr}[WBW^{\mathrm{H}}]] = 2\sigma_v^2 \sum_{j=1}^{d} \sum_{i=1}^{d} \mathrm{Re}\left\{ \left[(WW^{\mathrm{H}}) \odot \left(W\hat{Z}_{yy}(n, \omega, \phi)W^{\mathrm{H}} \right) \right]_{ij} \right\} \tag{29}$$

where $\odot$ denotes the Hadamard or element-wise matrix product.

Proof:

1) We note that $\mathsf{E}\,[B] = 0$ since $\mathsf{E}\,[V(n)] = 0$ and the covariance between two elements of B is given by

$$
\begin{aligned}
\mathsf{Cov}\,[B_{ij}, B_{kl}] &= \mathsf{E}\left[(\hat{D}_{y_i V_j}(n, \omega, \phi) + \hat{D}^*_{y_j V_i}(n, \omega, \phi))(\hat{D}^*_{y_k V_l}(n, \omega, \phi) + \hat{D}_{y_l V_k}(n, \omega, \phi)) \right] \\
&= \mathsf{E}\left[\hat{D}_{y_i V_j}(n, \omega, \phi)\hat{D}^*_{y_k V_l}(n, \omega, \phi) \right] + \mathsf{E}\left[\hat{D}_{y_l V_k}(n, \omega, \phi)\hat{D}^*_{y_j V_i}(n, \omega, \phi) \right] \\
&= \sigma_V^2 (\hat{Z}_{y_i y_k}(n, \omega, \phi)\delta_{j-l} + \hat{Z}_{y_l y_j}(n, \omega, \phi)\delta_{k-i}),
\end{aligned}
$$

where the last step follows from the results of Stankovic [17] and the noise properties [21].

2) Let $K = \text{Tr}[\boldsymbol{W}\boldsymbol{B}\boldsymbol{W}^{\text{H}}]$. Clearly $\text{E}[K] = 0$ since $\text{E}[\boldsymbol{B}] = 0$. The variance of K is therefore

$$
\begin{aligned}
\text{Var}[K] &= \text{E}[KK^*] \\
&= \sum_{i_1=1}^{d}\sum_{i_2=1}^{d}\sum_{k_1=1}^{m}\sum_{k_2=1}^{m}\sum_{l_1=1}^{m}\sum_{l_2=1}^{m} W_{i_1 k_1} W_{i_1 l_1}^* W_{i_2 k_2}^* W_{i_2 l_2} \text{Cov}\left[B_{k_1 l_1}, B_{k_2 l_2}^*\right] \\
&= \sigma_V^2 \sum_{i_1=1}^{d}\sum_{i_2=1}^{d}\sum_{k_1=1}^{m}\sum_{k_2=1}^{m}\sum_{l_1=1}^{m}\sum_{l_2=1}^{m} W_{i_1 k_1} W_{i_1 l_1}^* W_{i_2 k_2}^* W_{i_2 l_2} \\
&\quad \times (\hat{Z}_{y_{k_1} y_{k_2}}(n,\omega,\phi)\delta_{l_1 - l_2} + \hat{Z}_{y_{l_2} y_{l_1}}(n,\omega,\phi)\delta_{k_1 - k_2}) \\
&= \sigma_V^2 \sum_{i_1=1}^{d}\sum_{i_2=1}^{d}\Bigg\{ \sum_{l=1}^{m} W_{i_2 l} W_{i_1 l}^* \sum_{k_1=1}^{m}\sum_{k_2=1}^{m} W_{i_1 k_1} \hat{Z}_{y_{k_1} y_{k_2}}(n,\omega,\phi) W_{i_1 k_2}^* \\
&\quad + \sum_{k=1}^{m} W_{i_1 k} W_{i_2 k}^* \sum_{l_1}^{m}\sum_{l_2=1}^{m} W_{i_1 l_1}^* \hat{Z}_{y_{l_2} y_{l_1}}(n,\omega,\phi) W_{i_2 l_2} \Bigg\} \\
&= \sigma_V^2 \sum_{i_1}^{d}\sum_{i_2=1}^{d}\Big\{ [(\boldsymbol{W}\boldsymbol{W}^{\text{H}}]_{i_2 i_1}[\boldsymbol{W}\hat{\boldsymbol{Z}}_{\boldsymbol{yy}}(n,\omega,\phi)\boldsymbol{W}^{\text{H}}]_{i_1 i_2} \\
&\quad + [\boldsymbol{W}\boldsymbol{W}^{\text{H}}]_{i_2 i_1}^*[\boldsymbol{W}\hat{\boldsymbol{Z}}_{\boldsymbol{yy}}(n,\omega,\phi)\boldsymbol{W}^{\text{H}}]_{i_1 i_2}^* \Big\} \\
&= 2\sigma_V^2 \sum_{i_1}^{d}\sum_{i_2=1}^{d}\text{Re}\left\{ \left[(\boldsymbol{W}\boldsymbol{W}^{\text{H}}) \odot \left(\boldsymbol{W}\hat{\boldsymbol{Z}}_{\boldsymbol{yy}}(n,\omega,\phi)\boldsymbol{W}^{\text{H}}\right)\right]_{i_1 i_2} \right\}
\end{aligned}
$$

$\blacksquare$

Lemma 2 (Noise STFD):

1) The expected value of the noise STFD and the covariance of two elements of C are given respectively by

$$
\text{E}[C] = \sigma_V^2 \sum_m \varphi(m,0)\boldsymbol{I}, \tag{30}
$$

$$
\text{Cov}[C_{ij}, C_{kl}] = \sigma_V^4 \sum_m \sum_l |\varphi(m,l)|^2 \delta_{k-i}\delta_{l-j}. \tag{31}
$$

This results implies that any two different elements of C are uncorrelated.

2) The expected value and the variance of the trace of the whitened noise STFD are given respectively

by

$$E\left[\text{Tr}[\boldsymbol{W}C\boldsymbol{W}^{\text{H}}]\right] = \|\boldsymbol{W}\|^2\sigma_V^2\sum_m\varphi(m,0), \tag{32}$$

$$\text{Var}\left[\text{Tr}[\boldsymbol{W}C\boldsymbol{W}^{\text{H}}]\right] = \|\boldsymbol{W}\boldsymbol{W}^{\text{H}}\|^2\sigma_V^4\sum_m\sum_l|\varphi(m,l)|^2. \tag{33}$$

Proof:

1) The expected value of the noise STFD given in Equation (30) follows directly from the noise properties. The variance of an element C_{ij} is given by, for $i \neq j$,

$$\text{Var}\left[C_{ij}\right] = E\left[C_{ij}C_{ij}^*\right] = \sum_{m_1}\sum_{l_1}\sum_{m_2}\sum_{l_2}\varphi(m_1,l_1)\varphi(m_2,l_2)^*e^{-j2\omega(l_1-l_2)}\cdot K$$

where

$$K = E\left[V_i(n+m_1+l_1)V_i(n+m_2+l_2)\right]E\left[V_j(n+m_1-l_1)^*V_j(n+m_2-l_2)\right].$$

From the noise complex Gaussian zero-mean properties, it can be seen that K is zero unless $m_1+l_1 = m_2+l_2$ and $m_1-l_1 = m_2-l_2$, or equivalently $m_1-m_2 = l_2-l_1$ and $m_1-m_2 = l_1-l_2$. This condition is only met for $m_1 - m_2 = l_1 - l_2 = 0$, which leads to $K = \sigma_V^4\delta_{m_1-m_2}\delta_{l_2-l_1}$ and

$$\text{Var}\left[C_{ij}\right] = \sigma_V^4\sum_m\sum_l|\varphi(m,l)|^2.$$

The variance of a diagonal element is $\text{Var}\left[C_{ii}\right] = \sigma_V^4\sum_m\sum_l|\varphi(m,l)|^2$ which corresponds to the results of Amin [21]. It is also easily verified from the noise properties that

$$\text{Cov}\left[C_{ij},C_{kl}\right] = 0 \ \forall \ (i,j) \neq (k,l).$$

2) Let $K = \text{Tr}[\boldsymbol{W}C\boldsymbol{W}^{\text{H}}]$, with expected value:

$$E\left[K\right] = \sigma_V^2\sum_{m=-\infty}^{\infty}\varphi(m,0)\text{Tr}[\boldsymbol{W}\boldsymbol{W}^{\text{H}}] = \sigma_V^2\sum_{m=-\infty}^{\infty}\varphi(m,0)\|\boldsymbol{W}\|^2.$$

132

The variance of the trace of the whitened noise STFD is given by

$$
\begin{aligned}
\mathsf{Var}\left[K\right] &= \sum_{i_1=1}^{d}\sum_{i_2=1}^{d}\sum_{k_1=1}^{m}\sum_{k_2=1}^{m}\sum_{l_1=1}^{m}\sum_{l_2=1}^{m} W_{i_1k_1}W_{i_1l_1}^{*}W_{i_2k_2}^{*}W_{i_2l_2}\mathsf{Cov}\left[C_{k_1l_1},C_{k_2l_2}^{*}\right] \\
&= \sum_{i_1=1}^{d}\sum_{i_2=1}^{d}\sum_{k=1}^{m}\sum_{l=1}^{m} W_{i_1k}W_{i_1l}^{*}W_{i_2k}^{*}W_{i_2l}\mathsf{Var}\left[C_{kl}\right] \\
&= \sigma_V^4 \sum_{m}\sum_{u}|\varphi(m,u)|^2 \sum_{k=1}^{m}\sum_{l=1}^{m}\left\{[\boldsymbol{W}^{\mathrm{H}}\boldsymbol{W}]_{kl}^{*}\odot[\boldsymbol{W}^{\mathrm{H}}\boldsymbol{W}]_{kl}^{*}\right\} \\
&= \sigma_V^4 \sum_{m}\sum_{u}|\varphi(m,u)|^2\left\|\boldsymbol{W}^{\mathrm{H}}\boldsymbol{W}\right\|^2.
\end{aligned}
$$

∎

We now consider the use of the PWVD which is defined by the kernel

$$
\varphi(m,l) = w(l/L)\delta_m, \tag{34}
$$

where $w(t)$ is a real positive symmetric function which is zero outside the interval $(-0.5, 0.5)$. In Equation (34), L is an odd integer which specifies the windowing length. Substituting Equation (34) into (28) leads to

$$
\phi(m_1, m_2) = w(m_1/L)w(m_2/L)\delta_{m_1-m_2} \tag{35}
$$

and using the above results gives

$$
\hat{Z}_{y_i y_j}(n, \omega, \phi) = \sum_{m=-(L-1)/2}^{(L-1)/2} w^2(m/L)y_i(n+m)y_j^{*}(n+m). \tag{36}
$$

Equation (36) can be interpreted as a correlation between signals $y_i(n)$ and $y_j(n)$ over a window of length L centered at time n. Under the assumption of uncorrelated sources as described in Section III, for a sufficient window length Equation (36) may be approximated as

$$
\hat{Z}_{y_i y_j}(n, \omega, \phi) \approx E_w\left[\boldsymbol{A}\boldsymbol{A}^{\mathrm{H}}\right]_{ij}, \tag{37}
$$

where $E_w = \sum_n w^2(n)$ is the window energy.

- In order for $T_A(\zeta)$ to have unit variance, we must define

$$
\sigma_A^2(\zeta) = \mathsf{Var}\left[\mathsf{Tr}[\boldsymbol{W}\hat{\boldsymbol{D}}_{XX}(\zeta)\boldsymbol{W}^H]\right] = \mathsf{Var}\left[\mathsf{Tr}[\boldsymbol{W}(\boldsymbol{B}+\boldsymbol{C})\boldsymbol{W}^H]\right].
$$

133

Therefore, by substituting Equation (37) into (29) and combining this with (33) we obtain the expression for $\sigma_A^2(\zeta)$ given in Equation (13).

- For the cross-source test statistic, $T_C(\zeta)$, we obtain (using the PWVD):

$$
\begin{aligned}
\sigma_{C_i}^2 &= \mathsf{Var}\left[\hat{D}_{X_i X_i}(\zeta)\right] = \mathsf{Var}\left[B_{ii} + C_{ii}\right] \\
&= 2\sigma_V^2 \hat{Z}_{y_i y_i}(\zeta; \phi) + \sigma_V^4 \sum_m \sum_l |\varphi(m,l)|^2 \\
&= E\sigma_V^2(2[\boldsymbol{A}\boldsymbol{A}^H]_{ii} + \sigma_V^2),
\end{aligned}
$$

for $i = 1, \ldots, m$. Assuming that each sensor has the same gain, then the diagonal elements of $\boldsymbol{A}\boldsymbol{A}^H$ are equal, while under the uncorrelated sources assumption the array covariance matrix is $\boldsymbol{R}_{XX} = \boldsymbol{A}\boldsymbol{A}^H + \sigma_V^2 \boldsymbol{I}$, which leads to the result given in Equation (17).

REFERENCES

[1] L. Cirillo, A. Zoubir, N. Ma, and M. Amin, "Automatic classification of auto- and cross-terms of time-frequency distributions in antenna arrays," in *Proceedings of the 27*[th] *IEEE Int. Conf. on Acoustics, Speech and Sig. Proc. (ICASSP)*, Orlando, FL USA, May 2002.

[2] L. Cirillo and A. Zoubir, "On blind separation of nonstationary signals," in *Proceedings of the 8*[th] *IEEE Int. Symp. on Signal Processing and its Applications (ISSPA)*, Sydney, Australia, August 2005.

[3] A. Belouchrani and M. G. Amin, "Blind source separation based on time-frequency signal representations," *IEEE Trans. Signal Processing*, vol. 46, no. 11, pp. 2888–2897, November 1998.

[4] A. Belouchrani, K. Adeb-Meraim, M. G. Amin, and A. M. Zoubir, "Blind source separation of nonstationary signals," *IEEE Signal Processing Lett.*, vol. 11, no. 7, pp. 605–608, July 2004.

[5] ——, "Joint anti-diagonalization for blind source separation," in *Proceedings of the 26*[th] *IEEE Int. Conf. on Acoustics, Speech and Sig. Proc. (ICASSP)*, Salt Lake City, USA, May 2001.

[6] C. Févotte and C. Doncarli, "Two contributions to blind source separation using time-frequency distributions," *IEEE Signal Processing Lett.*, vol. 11, no. 3, pp. 386–389, March 2004.

[7] L. Cirillo, A. Zoubir, and M. Amin, "Selection of auto- and cross-terms for blind non-stationary source separation," in *Proceedings of the 2*[nd] *IEEE Int. Symp. on Sig. Proc. and Info. Tech. (ISSPIT)*, Cairo, Egypt, December 2001.

[8] L. Giulieri, N. Thirion-Moreau, and P.-Y. Arques, "Blind sources separation based on bilinear time-frequency representations: A performance analysis," in *Proceedings of the 27th IEEE Int. Conf. on Acoustics, Speech and Sig. Proc. (ICASSP)*, Orlando, FL USA, May 2002.

[9] L. Cohen, *Time-Frequency Analysis*. Prentice Hall, 1995.

[10] E. L. Lehmann, *Testing Statistical Hypotheses*, 2nd ed. John Wiley & Sons, 1986.

[11] Y. Hochberg and A. C. Tamhane, *Multiple Comparison Procedures*. John Wiley & Sons, 1987.

[12] S. Holm, "A simple sequentially rejective multiple test procedure," *Scand J Statist*, vol. 6, pp. 65–70, 1979.

[13] Y. Hochberg, "A sharper Bonferroni procedure for multiple tests of significance," *Biometrika*, vol. 75, no. 4, pp. 800–802, 1988.

[14] G. Hommel, "A stagewise rejective multiple test procedure based on a modified Bonferroni test," *Biometrika*, vol. 75, no. 2, pp. 383–6, 1988.

[15] ——, "A comparison of two modified Bonferroni procedures," *Biometrika*, vol. 76, no. 3, pp. 624–5, 1989.

[16] Y. Benjamini and Y. Hochberg, "Controlling the false discovery rate: a practical and powerful approach to multiple testing," *J. R. Statist. Soc. B*, vol. 57, no. 1, pp. 289–300, 1995.

[17] L. Stankovic, "An analysis of noise in time-frequency distributions," *IEEE Signal Processing Lett.*, pp. 286–289, September 2002.

[18] H. Krim and M. Viberg, "Two decades of array signal processing research," *IEEE Signal Processing Mag.*, pp. 67–94, July 1996.

[19] A. Belouchrani, K. Abed-Meraim, J.-F.Cardoso, and E. Moulines, "A blind source separation technique using second-order statistics," *IEEE Trans. Signal Processing*, vol. 45, no. 2, pp. 434–443, February 1997.

[20] D. Farina, C. Févotte, C. Doncarli, and R. Merletti, "Blind separation of instantaneous mixtures of nonstationary surface myoelectric signals," *IEEE Trans. Biomed. Eng.*, vol. 51, no. 9, pp. 1555–1567, September 2004.

[21] M. G. Amin, "Minimum variance time-frequency distribution kernels for signals in additive noise," *IEEE Trans. Signal Processing*, vol. 44, no. 9, pp. 2352–2356, September 1996.
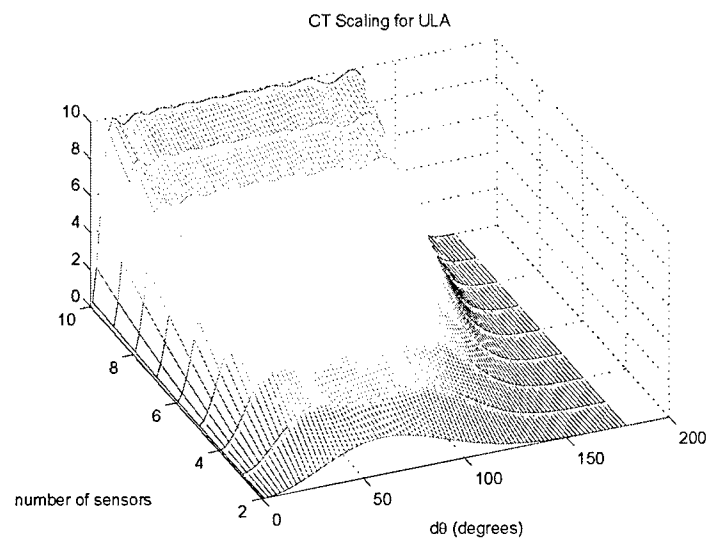
Fig. 1. Scaling of cross-source terms in a ULA when using sensor differenced TFDs, with respect to the spatial separation of the sources and the number of sensors.
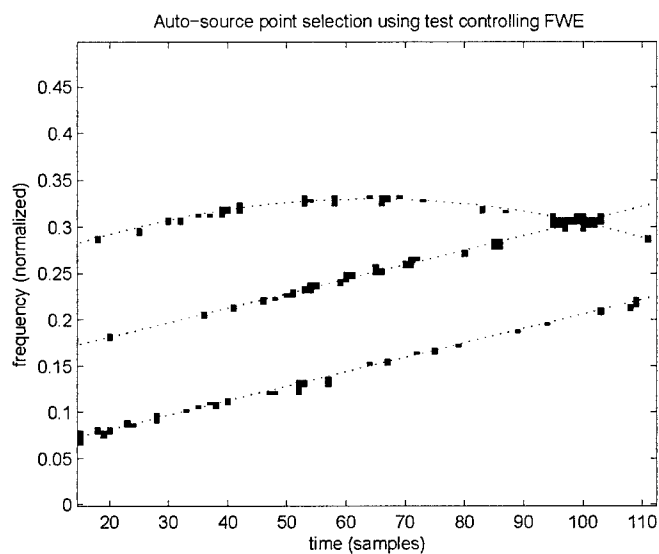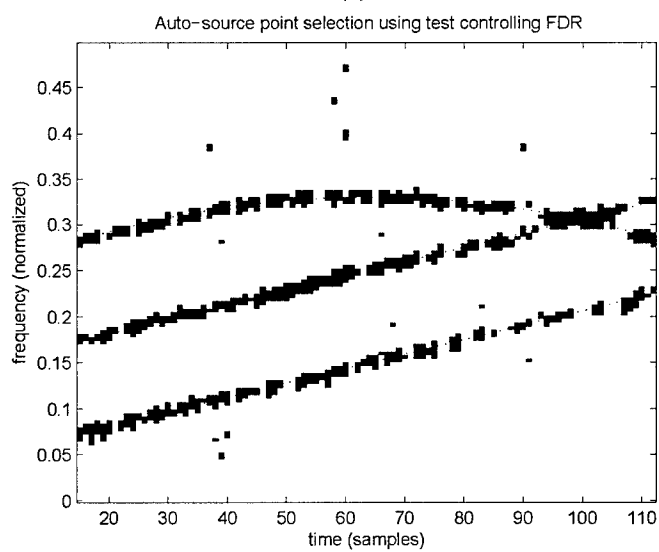
Fig. 2. Example of the MHT procedure for finding auto-term locations, using (a) the FWE and (b) the FDR controlling procedures.
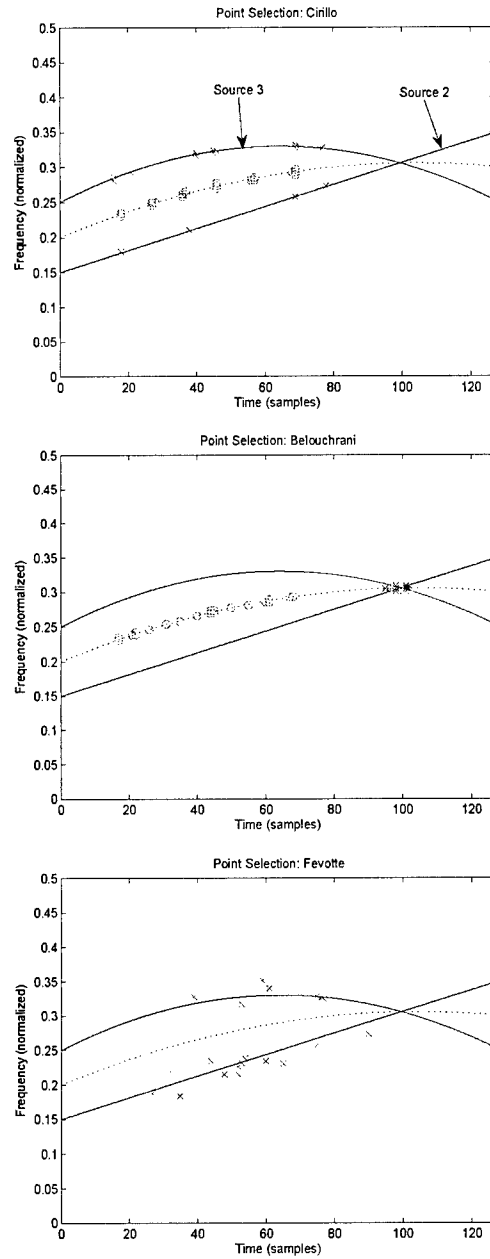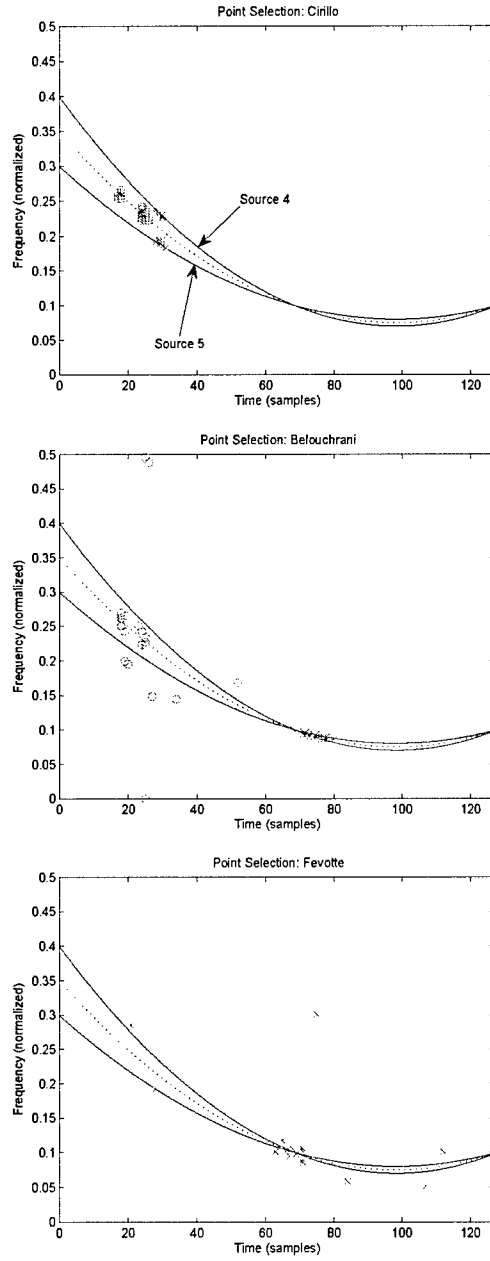
137
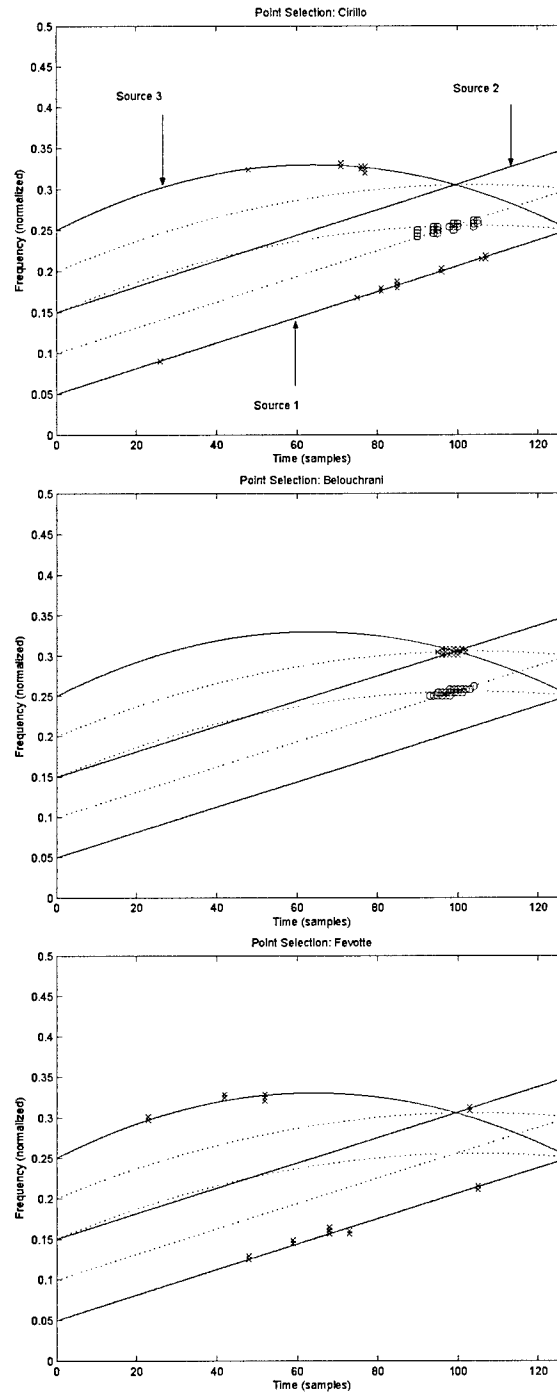
Fig. 3. Example of point selection based on (top) the proposed scheme (center) Belouchrani *et al* (bottom) Fèvotte *et al*. Chosen diagonal and off-diagonal terms are indicated by 'x' and 'o' respectively. The auto- and cross-source signatures are indicated by solid and dashed lines respectively.

138
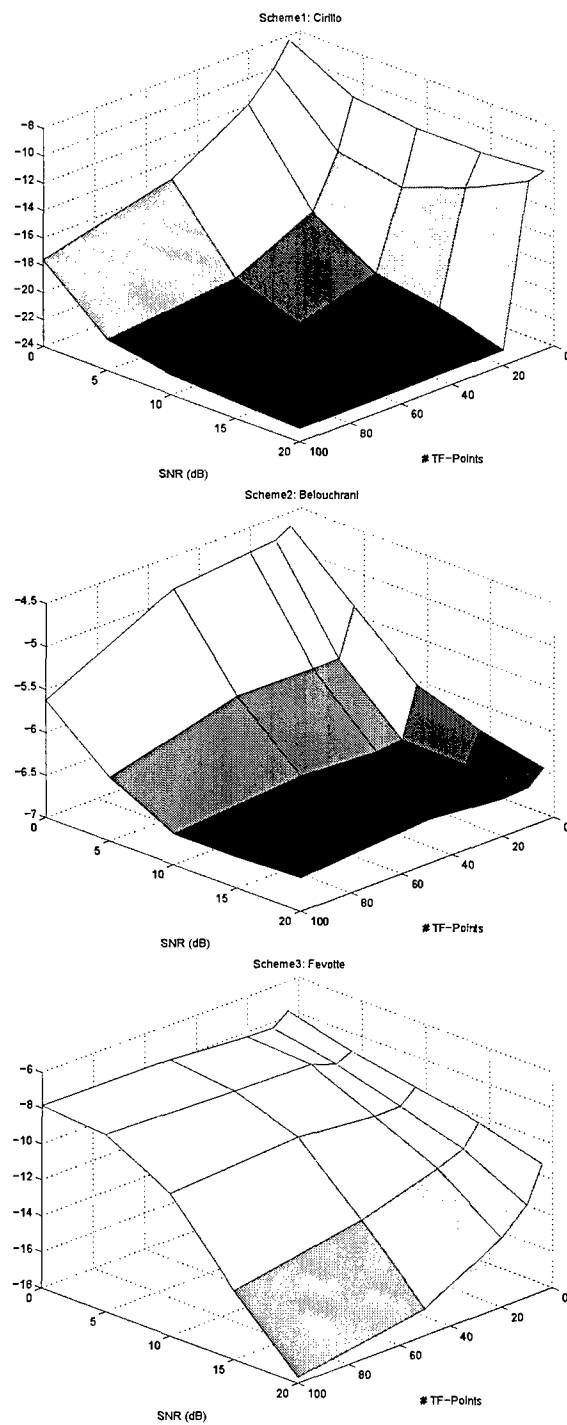
Fig. 4. Mean rejection level versus SNR and number of TF points chosen based on (top) the proposed scheme (center) Belouchrani *et al* (bottom) Fèvotte *et al*.

Fig. 5.   Example of point selection based on (top) the proposed scheme (center) Belouchrani *et al* (bottom) Fèvotte *et al*.

Chosen diagonal and off-diagonal terms are indicated by 'x' and 'o' respectively. The auto- and cross-source signatures are

indicated by solid and dashed lines respectively.
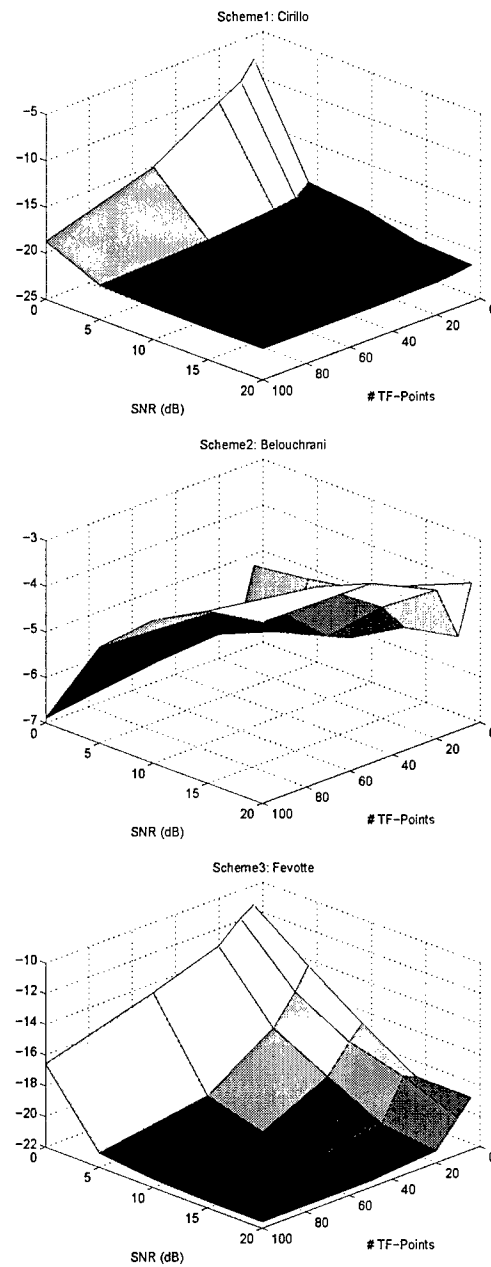
Fig. 6. Mean rejection level versus SNR and number of TF points chosen based on (top) the proposed scheme (center) Belouchrani *et al* (bottom) Fèvotte *et al*.

Fig. 7. Example of point selection based on (top) the proposed scheme (center) Belouchrani *et al* (bottom) Fèvotte *et al.*

Chosen diagonal and off-diagonal terms are indicated by 'x' and 'o' respectively. The auto- and cross-source signatures are indicated by solid and dashed lines respectively.
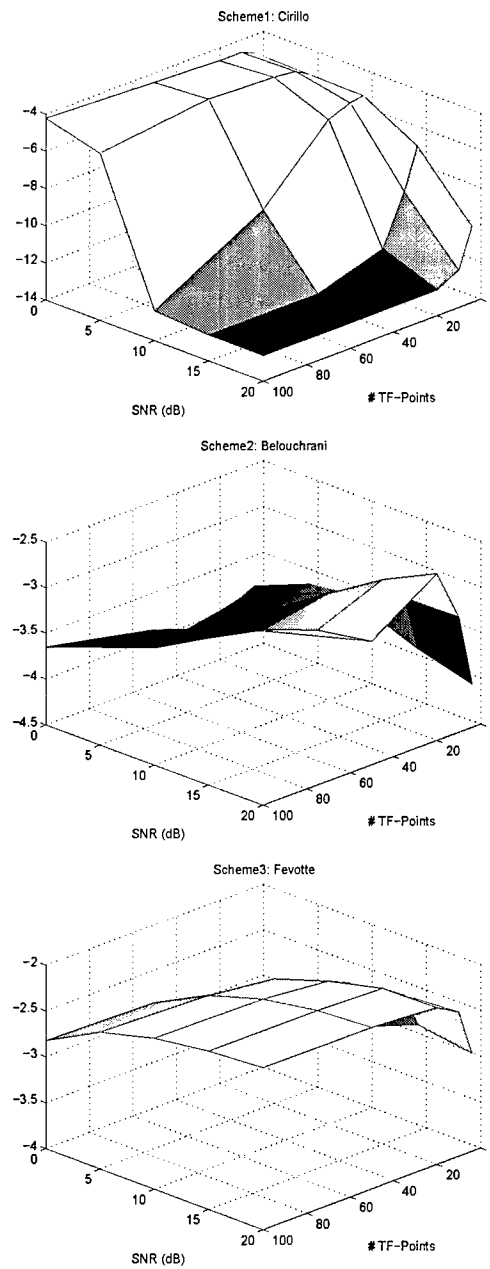
Fig. 8.   Mean rejection level versus SNR and number of TF points chosen based on (top) the proposed scheme (center) Belouchrani *et al* (bottom) Fèvotte *et al.*

143

Chapter 6
Estimation of FM Parameters Using a Time-Frequency Hough Transform

Abstract

An estimator for the phase parameters of mono- and multicomponent FM signals, with both good numerical properties and statistical performance is proposed. The proposed approach is based on the Hough transform of the pseudo Wigner-Ville time-frequency distribution (PWVD). It is shown that the numerical properties of the estimator can be improved by varying the PWVD window length. The effect of the window time extent on the statistical performance of the estimator is delineated. Experimental data is used for validation of the statistical properties.

I. INTRODUCTION

This chapter considers the estimation of the phase parameters of mono- or multicomponent FM signals from noisy observations. The multicomponent signal model is $s(t) = \sum_{k=1}^{K} A_k e^{j\varphi_k(t;\theta_k)}$, where K is the number of components, $\{A_k\}$ are complex-valued amplitudes and $\{\varphi(t;\theta_k)\}$ are the phase functions parameterised by $\{\theta_k\}$ and containing no constant term with respect to time. The instantaneous frequency (IF) of component k is defined as $\omega(t;\theta_k) = d\varphi(t;\theta_k)/dt$. Given N noisy samples of $s(t)$, the problem is to estimate $\{\theta_k\}$. In particular, we focus on the case of a linear FM model, which has importance in many signal processing applications.

A number of approaches exist for estimating $\{\theta_k\}$, given particular phase models such as the polynomial phase transform (PPT) [2], also known as the higher-order ambiguity function (HAF), generalized product and integrated forms of the HAF [3], [4], the Wigner-Hough transform (WHT) [5], [6] and a generalized time-frequency Hough transform [7]. The WHT is of particular interest for linear FM signals, as it offers optimal detection and asymptotically efficient estimation, with an improved SNR performance threshold over other methods such as the PPT. It also provides significant suppression of cross-terms in the multicomponent case.

Statistical analysis of the WHT method was presented in [6], where the output SNR and the estimated parameter variance were derived. It was shown that the method exhibits a performance "threshold effect" in additive white Gaussian noise such that the performance degrades rapidly for SNR below $1/N$. The method was also shown to be asymptotically efficient. However, the phase parameter estimation using the WHT requires optimization of a function with many local minima and operating in a very narrow region of attraction about the global maximum. It was suggested in [6] that this problem may be approached by first decimating and lowpass filtering the Wigner-Ville distribution (WVD) before applying the Hough transform, in order to broaden the peak centered about the true parameter values. While this approach may reduce the total number of Hough transform trajectories needed to find the global maximum, each

145

trajectory implies a computational cost higher than that of the unfiltered WHT, which is already of order N^2.

In the following we investigate an approach based on the Hough transform of the pseudo Wigner-Ville distribution (PWVD) and demonstrate improved numerical properties with respect to the WHT based estimator. The PWVD is computed by first windowing the local auto-correlation function in the lag domain, which serves to both reduce the computational cost, and broaden the peaks of interest in the subsequent Hough transform domain, and as such, improving the numerical properties of the estimator. The price is paid in terms of a reduced SNR performance threshold and statistical efficiency with respect to the WHT. However, using the pseudo Wigner-Hough transform (PWHT) as an initialization step for the WHT provides a computationally efficient means of achieving optimal estimation, in much the same manner that nonlinear instantaneous least-squares (NLIS) improves over a direct nonlinear least-squares (NLLS) approach [8].

In the following we outline an estimation method for linear FM signals based on the PWHT. A region of attraction (RoA) for the estimator is derived which defines the required accuracy of an initial estimate or grid search, such that an efficient gradient-based optimization algorithm will converge to the true global maximum. Statistical analysis in terms of the output SNR and estimation variance is provided and compared to the corresponding results for the WHT method. In addition, we investigate the application of the PWHT to estimation of multicomponent and nonlinear FM signals.

II. THE WIGNER-HOUGH TRANSFORM

The Wigner-Hough transform (WHT) of a signal $s(t)$ is defined as the line integral through the WVD of $s(t)$, along the IF model; $\omega(t; \boldsymbol{\theta})$. The WHT is therefore a mapping from the time domain to the parameter domain of $\boldsymbol{\theta}$. The discrete-time WHT, formed from N samples, $\{s(n)\}_{n=0}^{N}$, of a signal $s(t)$,

is given by

$$W_s(\boldsymbol{\theta}) = \left[\sum_{n=0}^{N/2-1} \sum_{l=-n}^{n} + \sum_{n=N/2}^{N-1} \sum_{l=-(N-1-n)}^{N-1-n} \right] s(n+l)s^*(n-l)e^{-j2\omega(n;\boldsymbol{\theta})l}, \qquad (1)$$

where N is assumed to be even. The WVD is known to be an unbiased estimator of the IF for linear FM signals [9]. However, as the IF becomes nonlinear in nature, the WHT becomes increasingly biased and in most cases, not useful. We therefore restrict our attention to a linear FM signal of the form $s(n) = Ae^{j(a_0 n + b_0/2n^2)}$, where A is a complex valued amplitude, and a_0 and b_0 correspond to the mean frequency and sweep rate respectively.

In the following, we derive expressions for the RoA of the WHT in the case of linear FM signals. Given the point (a_0, b_0) lies somewhere within the space $\Omega \subset \mathbb{R}^2$, the aim is to find a region $\Omega_c \subset \Omega$ such that a gradient-based optimization procedure initialized within Ω_c will converge to the maximum at (a_0, b_0). We derive a conservative RoA as the diamond shaped area centered at (a_0, b_0) with width and height given by the peak width in the a and b directions respectively, as illustrated in Figure 1. The width of the RoA in a and b will be denoted by Δ_a and Δ_b respectively.

When additive noise is present, the observations can be modelled as $x(n) = s(n) + v(n)$, $n = 0, \ldots, N-1$; where $s(n)$ is as defined previously and $v(n)$ is a complex random process. In this case, one may express the WHT of $\{x(n)\}$ as $W_x(a,b) = W_s(a,b) + \delta W_x(a,b)$. In [6], Barbarossa conducted a statistical analysis of $W_x(a,b)$ in the case of additive white Gaussian noise (AWGN) of variance σ_v^2. At the true parameter location (a_0, b_0), the variance of the perturbation term, $\delta W_x(a,b)$, was found to be

$$\text{Var}\left[\delta W_x(a_0, b_0)\right] = \frac{1}{2}[N^3 |A|^2 \sigma_v^2 + N^2 \sigma_v^4]. \qquad (2)$$

In a close neighborhood of (a_0, b_0), we may therefore express the WHT as

$$W_x(a,b) = N^2[\frac{1}{N^2} W_s(a,b) + O(1/\sqrt{N})]. \qquad (3)$$

We note that $W_s(a,b)$ takes its maximum value at (a_0, b_0) of $N^2 |A|^2/2$, which is $O(N^2)$. Thus, from Equation (3) we observe that, to within $O(1/\sqrt{N})$, the shape of $W_x(a,b)$ is determined by the function

147

$W_s(a, b)$, in a close neighborhood of the true parameter values. We therefore determine an approximate

RoA for the WHT estimator based on the shape of $W_s(a, b)$.

It can be readily show by direct substitution into Equation (1) that

$$W_s(a, b_0) = 2 \left[\frac{\sin(\bar{a}N/2)}{\sin(\bar{a})} \right]^2 \tag{4}$$

$$W_s(a_0, b) = \left[\sum_{n=0}^{(N/2-1)} - \sum_{n=N/2}^{(N-1)} \right] \frac{\sin(\bar{b}n(1 + 2n - 2N))}{\sin(\bar{b}n)} \tag{5}$$

where $\bar{a} = a_0 - a$ and $\bar{b} = b_0 - b$. From Equation (4) it is clear that the main peak width is $\Delta_a = 2\pi/N$.

However, it is not easy to analytically solve for the peak width of Equation (5) due to the nonlinear

nature of the expression. We have numerically solved [1] for the main peak width of (5) across a range

of values of N, as the distance between the first local minima either side of the origin ($\bar{b} = 0$). The

useful approximation; $\Delta_b \approx 8\pi/[N(\frac{10}{9}N - 1)]$, was found to deviate from the numerical solution by a

maximum of 1.769%, across the range of values $N = 2^3$ to $N = 2^{14}$.

Restricting attention to the case of non-aliased[2] linear FM signals, we note that $a \in [0, \pi)$ and $b \in$

$[-a/N, (\pi - a)/N]$, i.e. we must search for the true value of a and b over intervals of π rad/s and π/N

rad/s², respectively. From the previous discussion, we conclude that the RoA for the WHT is $O(1/N)$

in a and $O(1/N^2)$ in b, though we may say the RoA is $O(1/N)$ for both a and b with respect to the

non-aliased parameter range. The problem of estimating a and b using the WHT is therefore evident; the

desired peaks of the WHT become narrower as the number of observations increases, making the peak

finding problem increasingly difficult.

---

[1] Optimization routines available within the software package MATLAB® were successfully employed to this end.

[2] Due to the inherent frequency axis scaling of the discrete-time WVD, non-aliased signals are those whose IF lies within

$[0, \pi)$ rad/s within the observation interval.

III. The Pseudo Wigner-Hough Transform

In the discrete-time case, the pseudo Wigner-Hough transform (PWHT) is calculated from N samples $\{s(n)\}_{n=0}^{N}$ of $s(t)$ as,

$$P_s(\theta) = \sum_{n=M}^{(N-M-1)} \sum_{l=-M}^{M} s(n+l)s^*(n-l)e^{j2\omega(n;\theta)l} \tag{6}$$

where M is a parameter defining the odd PWVD window length; $L = 2M + 1$. We have defined the PWHT as the summation over the $N - L + 1$ points in the center of the PWVD, leaving out the rising and falling edges of the distribution, assuming that $L << N$. Defining $R_s(n,l) = s(n+l)s^*(n-l)$ as the local auto-correlation function, we observe that the PWHT is a weighted sum over the center rectangle of the support of $R_s(n,l)$, whereas the WHT sums over the full diamond-shaped support. The computation time of the PWHT is therefore less than that of the WHT. The number of complex multiplications and additions required is summarised in Table I (for N even), which shows that the PWHT has reduced computational cost by a factor of approximately $2L/N$ for $L << N$.

Method	# Complex Mult's	# Complex Add's
WHT	N^2	$N^2/2 - 1$
PWHT	$2L(N - L + 1)$	$L(N - L + 1) - 1$

TABLE I

Comparison of the computational complexity of the PWHT and the WHT.

Apart from reducing the computational complexity, the PWHT has another important and fundamental advantage over the WHT. The PWVD may be seen as the WVD convolved with a sinc function in the frequency domain, which results in a widening of the main lobe of any signal components. Figure 2 depicts the PWHT and WHT functions for a two linear FM component signal observed in AWGN at an SNR of 0dB, with $N = 128$ and $M = 5$. Clearly the peak width in the parameter space is much larger

for the PWHT than for the WHT. This implies improved numerical properties with respect to the WHT, when performing optimization, i.e. a larger RoA. Of course, there is also a disadvantage in the windowing used in the PWHT, which is also evident in Figure 2. Namely, the noise floor has increased due to the shorter summation interval used. This implies that the SNR performance threshold and estimator variance of the PWHT is worse than that of the WHT. In order to clarify these points, we derive in the following sections expressions for the RoA of the PWHT, the output SNR, and the statistical accuracy.

A. Region of Attraction

Herein, we determine an approximate expression for the RoA of the PWHT estimator of linear FM signals. The same notation is used as previously in Section II. In the case of noisy observations, the PWHT may be expressed as $P_x(a, b) = P_s(a, b) + \delta P_x(a, b)$. As shown in Appendix I, the variance of the perturbation term $\delta P_x(a, b)$ at the true parameter location (a_0, b_0) is given by

$$\text{Var}\left[\delta P_x(a_0, b_0)\right] = \frac{2}{3}\sigma_v^2 |A|^2 L(3NL - (L-1)(4L+1)) + \sigma_v^4(N-L+1)L, \tag{7}$$

which is $O(NL^2)$. In a close neighborhood of (a_0, b_0), we may therefore express the PWHT as

$$P_x(a, b) = NL[\frac{1}{NL}P_s(a, b) + O(1/\sqrt{N})]. \tag{8}$$

We note that $P_s(a, b)$ takes its maximum value at (a_0, b_0) of $(N - L + 1)L|A|^2$, which is $O(NL)$. Accordingly, to within $O(1/\sqrt{N})$, the shape of $P_x(a, b)$ is determined by the function $P_s(a, b)$, in a close neighborhood of the true parameter values. We therefore determine an approximate RoA for the PWHT estimator based on the shape of $P_s(a, b)$.

To determine Δ_a and Δ_b, we first compute[3] the derivatives of $P_s(a, b)$ with respect to $\bar{a} = a_0 - a$ and

[3]We work with the window parameter $M = (L - 1)/2$, as it leads to more compact expressions.

150

$\bar{b} = b_0 - b$. Substituting the linear FM signal into Equation (6) and taking $b = b_0$ we obtain:

$$P_s(a, b_0) = (N - 2M) \frac{\sin(\bar{a}(2M + 1))}{\sin(\bar{a})}$$

$$\frac{\partial P_s(a, b_0)}{\partial \bar{a}} = (N - 2M) \frac{[M \sin(2\bar{a}(M + 1)) - (M + 1) \sin(2\bar{a}M)]}{\sin^2(\bar{a})}. \tag{9}$$

Substituting the linear FM signal into Equation (6) and taking $a = a_0$ we obtain:

$$P_s(a_0, b) = \sum_{n=M}^{N-M-1} \frac{\sin(\bar{b}(2M + 1)n)}{\sin(\bar{b}n)}$$

$$\frac{\partial P_s(a_0, b)}{\partial \bar{b}} = \sum_{n=M}^{N-M-1} \frac{n[(M + 1) \sin(2\bar{b}Mn) - M \sin(2\bar{b}(M + 1)n)]}{\sin^2(\bar{b}n)}. \tag{10}$$

To determine the peak width in a, one may solve Equation (9) for the location of the first zeros occurring either side of $\bar{a} = 0$. However, for Equation (10) this approach is not always valid. Depending on the value of M and N, the peak in $\bar{b}$ may not have local minima at the edges, as illustrated in Figure 3, where $P_s(a, b)$ and its derivative are plotted for $M = 10$ and $N = 128$. In this case we define the peak edges as the midpoint between the first and second points of inflection. Determining Δ_a and Δ_b, therefore, requires solving for the zeros of $\partial P_s(a, b_0)/\partial \bar{a}$ and $\partial^2 P_s(a_0, b)/(\partial \bar{b})^2$ respectively, where

$$\frac{\partial^2 P_s(a_0, b)}{(\partial \bar{b})^2} = \sum_{n=M}^{N-M-1} 2n^2 \csc^2(2\bar{b}n) \left[M(M + 1) \cos(2\bar{b}Mn) - M(M + 1) \cos(2\bar{b}(M + 1)n) \right.$$

$$\left. - 2 \cot(2\bar{b}n)[(M + 1) \sin(2\bar{b}Mn) - M \sin(2\bar{b}(M + 1)n)] \right]. \tag{11}$$

For a particular value of M and N, one may numerically solve for the zeros of the nonlinear equations (9) and (11) to determine Δ_a and Δ_b. We have performed the numerical analysis across a wide range of values of M and N and found the following useful empirical approximations:

$$\Delta_a \approx \frac{2\pi}{1.4(2M + 1)} = \frac{2\pi}{1.4L}, \tag{12}$$

$$\Delta_b \approx \frac{2\pi}{(-1.19M^2 + 1.2MN - 3M + 0.4N + 17.5)}$$

$$= \frac{2\pi}{18.7025 - 0.2975L^2 + L(-0.905 + 0.6N) - 0.2N}. \tag{13}$$

The expressions (12) and (13) demonstrate that the RoA in both a and b increases with reduced window length, in the computation of the PWHT. In comparison to the ROA of the WHT, the ROA of the PWHT increases in a from $O(1/N)$ to $O(1/L)$ and in b from $O(1/N^2)$ to $O(1/(LN))$. Again, considering only the non-aliased parameter ranges, the RoA for both a and b is $O(1/L)$. This results is particularly interesting, because the RoA is now *independent of the number of samples*, and as such we may *control the RoA using the window parameter.* Further, the Equations (12) and (13) can be used to determine the appropriate grid sampling density for performing a grid search of the parameter space using the PWHT. By sampling along the a and b parameter directions with spacing $\Delta_a/2$ and $\Delta_b/2$ respectively, we can ensure that one of the trajectories evaluated will lie within the RoA of the PWHT, yielding a suitable initialization for optimization routines. The implementation of the PWHT is further elaborated in the final part of this section.

To illustrate the results derived above, the PWHT and the approximate RoA specified by Equations (12) and (13) are plotted in Figure 4, over the range of non-aliased parameter values. In this example, we show the PWHT function simulated at an SNR of 0 dB, for various values of N and M. The black diamond and cross in each sub-figure show the approximate RoA and true parameter locations respectively. In all sub-figures, the approximate RoA regions lie over the main peak contour as expected. Comparing Figure 4 (a) and (c) we observe that although the sample lengths are different ($N = 64$ and $N = 128$ respectively), using the same PWVD window length ($L = 13$) yields the same RoA. This illustrates how the RoA is independent of the sample length, with respect to the range of non-aliased parameter values. Comparing Figure 4 (b)-(d) we observe how increasing the PWVD window length decreases the RoA, for $L = 7$, 13 and 27 respectively.

B. Output SNR

In the following, we perform a statistical analysis of the PWHT based estimate, in terms of the output SNR. In the case of nonlinear FM signals, the analysis holds based on the assumption:

A1) $\exists M \in \mathbb{Z}^+$ and an interval $\mathcal{I}_n = \{n - M, \ldots, n + M\}\}$ such that:

$$\omega(k; \boldsymbol{\theta}) \approx a_n + b_n k \quad \forall k \in \mathcal{I}_n; \text{ and } \forall n \in \{M, \ldots, N - M - 1\},$$

i.e. the signal IF is approximately linear within all time intervals of length L, over the entire observation period.

We also assume that the noise $v(n)$ is a complex white Gaussian process of variance σ_v^2.

Given observations $\{x(n) = s(n) + v(n)\}_{n=0}^{N-1}$ where $s(n) = Ae^{j\varphi(n; \theta_0)}$, the output SNR is defined as

$$SNR_{out} = \frac{|P_s(\boldsymbol{\theta}_0)|^2}{\mathsf{Var}\left[P_x(\boldsymbol{\theta}_0)\right]}. \tag{14}$$

Assuming the value of M is chosen such that Assumption A1 is satisfied for the given signal and using Equation (6), we obtain the following expression for the output SNR in terms of the input SNR; $SNR_{in} = |A|^2/\sigma_v^2$:

$$SNR_{out} \approx \frac{(N - L + 1)LSNR_{in}^2}{\left(\frac{2}{3}\frac{3NL-(L-1)(4L+1)}{N-L+1}\right)SNR_{in} + 1}, \tag{15}$$

where the above expression becomes exact in the case of linear FM signals. The derivation of Equation (15) is included as Appendix I. Assuming $L << N$, then the denominator of Equation (15) is approximately equal to $(2L)SNR_{in} + 1$. We therefore see a thresholding effect versus the input SNR; for $SNR_{in} >> 1/(2L)$, the output SNR is approximated as $SNR_{out} \approx N(SNR_{in}/2)$. For $SNR_{in} << 1/(2L)$ the output SNR degrades rapidly according to $SNR_{out} \approx (NL)SNR_{in}^2$. The SNR performance threshold of the method is therefore said to occur at the interception point of these two limiting behaviors, i.e. at $SNR_{in} = 1/(2L)$. In comparison with the WHT (suitable only for linear FM signals) which has an SNR performance threshold at $1/N$, the threshold of the PWHT is higher (worse), however the output SNR performance above the input SNR threshold is the same.

C. Estimation accuracy

The mean and variance of the PWHT estimator are derived below via a generalization of the perturbation approach taken in [6], for analysis of the WHT. Assuming the same signal model as in the previous section, we may express the PWHT of the observations as the sum of $P_s(\theta)$ being the PWHT of the noise-free signal and a perturbation $\delta P(\theta)$ composed of cross signal-noise and noise only terms. Under Assumption A1, the maximum of $P_s(\theta)$ occurs at θ_0, but in the presence of noise, the maximum of the PWHT shifts to a location $\theta_0 + \delta\theta$ due to the influence of $\delta P(\theta)$. The bias and variance of the estimator are therefore determined by the mean and covariance matrix of $\delta\theta$. As a first order approximation, the bias $\mathsf{E}[\delta\theta] = 0$ and the covariance matrix $\Gamma_{\delta\theta} = \mathsf{E}[\delta\theta\delta\theta^T] = C^{-1}BC^{-T}$, where

$$C = |A|^2 \sum_{n=M}^{N-M-1} \sum_{l=-M}^{M} \left[-j2l \left. \frac{\partial^2 \omega(n;\theta)}{\partial\theta\partial\theta^T} \right|_{\theta=\theta_0} + 4l^2 \left[\frac{\partial\omega(n;\theta)}{\partial\theta} \frac{\partial\omega(n;\theta)}{\partial\theta^T} \right] \Big|_{\theta=\theta_0} \right], \quad (16)$$

$$B = 8|A|^2\sigma_v^2 \sum_{n=M}^{N-M-1} \sum_{m=M}^{N-M-1} \left[\frac{\partial\omega(n;\theta)}{\partial\theta} \frac{\partial\omega(m;\theta)}{\partial\theta^T} \right] \Big|_{\theta=\theta_0} \sum_{l=-M}^{M} \sum_{k=-M}^{M} l\, k\, \delta(n-m+l-k)$$

$$+ \frac{4}{3}\sigma_v^4 M(M+1)(2M+1) \sum_{n=M}^{N-M-1} \left[\frac{\partial\omega(n;\theta)}{\partial\theta} \frac{\partial\omega(n;\theta)}{\partial\theta^T} \right] \Big|_{\theta=\theta_0}. \quad (17)$$

The derivation of the above formulae is included in Appendix II. From (16) and (17) one can easily show that

$$\Gamma_{\delta\theta} = \frac{1}{SNR_{in}} D + \frac{1}{SNR_{in}^2} E,$$

where the matrices D and E depend on M, N and the first and second order derivatives of the IF model at θ_0. We note that the above expression for $\Gamma_{\delta\theta}$ has the same form as the variance of the WHT estimator given in [6], for linear FM signals. Further, for particular IF models such as PPS, it is evident from (16) and (17) that the variance is independent of the true signal parameter value θ_0.

A Monte Carlo simulation was conducted to verify theoretical results for a number of signal models. In Figures 5, 6 and 7 we show the simulated variance and root mean-squared error (RMSE) for linear FM (LFM), quadratic FM (QFM) and sinusoidal FM (SFM) signal models respectively. The phase function

for each case is defined as

$$\varphi_{LFM}(n;\boldsymbol{\theta}) = an + b/2n^2; \qquad \boldsymbol{\theta} = (a,b)^T$$

$$\varphi_{QFM}(n;\boldsymbol{\theta}) = an + b/2n^2 + c/3n^3; \quad \boldsymbol{\theta} = (a,b,c)^T$$

$$\varphi_{SFM}(n;\boldsymbol{\theta}) = B\sin(\omega_0 n + \phi); \qquad \boldsymbol{\theta} = (B,\omega_0,\phi)^T.$$

All simulations were conducted with 500 Monte Carlo runs, $N = 128$ samples and PWVD window

lengths 27, 21 and 11 respectively. The model parameters used were $\boldsymbol{\theta}_{LFM} = 2\pi(0.025, 6.378 \times 10^{-3})$,

$\boldsymbol{\theta}_{QFM} = 2\pi(0.2, 5.197^{-3}, -3.224 \times 10^{-5})$ and $\boldsymbol{\theta}_{SFM} = 2\pi(0.102, 1.953 \times 10^{-2}, 0.23)$. The Cramér-Rao

Bound (CRB) for each case is also shown as a reference[4]. We note that the simulated variance coincides

with the theoretical expression in all cases. However, the MSE for the amplitude parameter, B, of the

sinusoidal FM model and the first-order phase parameter, a, of the quadratic FM model, differ from the

variance at higher SNR. This bias results from the nonlinearity of the IF and can be reduced by using a

smaller window length, at the expense of increased variance.

For the particular case of linear FM signals, we have also obtained closed form expressions for the

estimator variance. The signal parameters of interest are denoted a_0 and b_0, corresponding to mean

---

[4]A general form of the CRB for the signal model considered here is derived in Appendix III.

frequency and sweep rate. The respective estimators based on the PWHT are denoted $\hat{a}$ and $\hat{b}$, where:

$$
\begin{aligned}
\text{Var}\left[\hat{a}\right] = & \left\{ \frac{12}{SNR_{in}} \left[112(M^6 - M^5(2N-1)) + (N-1)^2(35N^2 + 7N - 1) \right. \right. \\
& \left. -4M^3(77N^3 - 177N^2 + 95N + 5) + 7M^2(10N^4 - 62N^3 + 91N^2 - 28N - 3) \right. \\
& \left. + M(70N^4 - 280N^3 + 283N^2 - 62N - 11) + 8M^4(39N^2 - 64N + 18) \right] \\
& - \frac{105}{SNR_{in}^2} \left[+4M^3(13N^2 - 6N + 1) + 2M(7N^4 - 9N^3 + 3N - 1) \right. \\
& \left. (16M^5 - 40M^4N - (N-1)^2N(2N^2 + N - 1) - 2M^2N(19N^2 - 18N + 3) \right] \right\} \\
& \times \left\{ 70M(M+1)(2M+1)(N-2M)^3(N^2 - 4MN + 4M^2 - 1)^2 \right\}^{-1}
\end{aligned}
\tag{18}
$$

$$
\begin{aligned}
\text{Var}\left[\hat{b}\right] = & \left\{ \frac{108}{SNR_{in}} \left[12(-1 + 32M^4 + M^3(8 - 56N) + 14M^2(N-4)N + 7N^2 + \right. \right. \\
& \left. 2M(-2 - 14N + 7N^2)) \right] - \frac{315}{SNR_{in}^2} \left[8M^3 + N - 12M^2N - N^3 + M(-2 + 6N^2) \right] \right\} \\
& \times \left\{ 35M(1 + 3M + 2M^2)(8M^3 + N - 12M^2N - N^3 + M(-2 + 6N^2))^2 \right\}^{-1}
\end{aligned}
\tag{19}
$$

While the above expressions are somewhat complicated, it can be shown that the estimator is not asymptotically efficient. To illustrate this we have plotted the variance of $\hat{b}$ divided by the CRB, in Figure 8. We note that although the estimation is not efficient, there is clearly an optimal value of M for which the variance is minimized, which occurs[5] at approximately $M = 0.1N$.

The optimal value of M which gives the lowest variance may be obtained by differentiating (18) and (19) with respect to M and solving for the location of the minimum variance in terms of N. However, a direct algebraic solution of the above equations is somewhat difficult due to the high order terms present. Since the minimum is known to occur close to $M = 0.1N$, we have taken a first order Taylor series expansion of the derivatives of (18) and (19) about this location, and solved for M. The approximate

[5]The minimum variance of $\hat{a}$ was found to occur at the same value of M.

expression of the optimal value of M for a and b respectively, were found to be

$$M_{opt,a} = -0.311009 + \frac{1}{SNR_{in}} 2.69542 + 0.103864N + O(1/N),$$

$$M_{opt,b} = -0.344559 + \frac{1}{SNR_{in}} 2.64928 + 0.106091N + O(1/N).$$

In many practical cases of interest, e.g. for $SNR_{in} > 1$ and $N >> 27$, the optimal value of M is close to $0.1N$ for estimation of both a and b and one may use this value as a rule of thumb.

D. Implementation

The proposed estimation algorithm is summarised in Table II and described as follows: Firstly, one chooses a set of window lengths $M_1 < M_2 < \cdots < M_p$ and an initial estimate of the strongest signal component is obtained. This may be done, e.g, via a grid search of the PWHT with $M = M_1$. The appropriate grid spacing in the case of linear FM signals is determined from the RoA expressions given in Section III-A. The estimate is then refined in steps via optimization of the PWHT using $M_1, \ldots, M_q$ successively, where the estimate obtained using $M = M_i$ serves to initialize the optimization with $M = M_{i+1}$. In the case of linear FM signals, one may use the final estimate ($M = M_q$) to initialize optimization of the WHT function.

---

1) Define $M_1 < M_2 < \cdots < M_p$.

2) Perform grid search of using $M = M_1$ to obtain $\hat{\theta}_0$. Set $i \leftarrow 1$.

3) Obtain $\hat{\theta}_i$, via gradient-based optimization of (6), with initial location $\hat{\theta}_{i-1}$.

4) Set $i \leftarrow i + 1$. While $i <= p$ repeat from 3.

5) If a linear FM model is applies, use $\hat{\theta}_p$ to initialize optimization of the WHT, otherwise $\hat{\theta} = \hat{\theta}_p$.

TABLE II

ESTIMATION ALGORITHM BASED ON THE PWHT.

For optimization of the PWHT using efficient gradient based schemes, one may require both the first

157

and second order derivatives with respect to the parameters. We first reformulate the PWHT given in Equation (6), in a more compact matrix equation:

$$P_{xx}(\boldsymbol{\theta}) = \mathbf{1}'(\boldsymbol{R}_{xx} \odot \boldsymbol{W}(\boldsymbol{\theta}))\mathbf{1} \tag{20}$$

where $\mathbf{1}$ is a length L vector of ones and $\boldsymbol{R}_{xx}$ and $\boldsymbol{W}(\boldsymbol{\theta})$ are $L \times N - L + 1$ complex-valued matrices given by

$$[\boldsymbol{R}_{xx}]_{pq} = x(q + p - 2)x^*(q - p + L - 1)$$

$$[\boldsymbol{W}(\boldsymbol{\theta})]_{pq} = \exp[-j2\omega(q + M - 1; \boldsymbol{\theta})(p - M - 1)]$$

for $p = 1, \ldots, L$ and $q = 1, \ldots, N - L + 1$. The first and second order derivatives of $P(\boldsymbol{\theta})$ with respect to the parameters are then given by

$$\frac{\partial P(\boldsymbol{\theta})}{\partial \theta_i} = \mathbf{1}'(\boldsymbol{R}_{xx} \odot \boldsymbol{W}(\boldsymbol{\theta}) \odot \boldsymbol{G}_i(\boldsymbol{\theta}))\mathbf{1} \tag{21}$$

$$\frac{\partial^2 P(\boldsymbol{\theta})}{\partial \theta_i \partial \theta_k} = \mathbf{1}'(\boldsymbol{R}_{xx} \odot (\boldsymbol{G}_i(\boldsymbol{\theta}) \odot \boldsymbol{G}_k(\boldsymbol{\theta}) + \boldsymbol{W}(\boldsymbol{\theta}) \odot \boldsymbol{K}_{ik}(\boldsymbol{\theta})))\mathbf{1} \tag{22}$$

where

$$[\boldsymbol{G}_i(\boldsymbol{\theta})]_{pq} = -j2\frac{\partial \omega(q + M - 1; \boldsymbol{\theta})}{\partial \theta_i}(p - M - 1)$$

$$[\boldsymbol{K}_{ik}(\boldsymbol{\theta})]_{pq} = -j2\frac{\partial^2 \omega(q + M - 1; \boldsymbol{\theta})}{\partial \theta_i \partial \theta_k}(p - M - 1)$$

We can see that to compute the gradient vector and Hessian matrix, we require the first and second order derivatives of the IF model. We also notice from Equation (21) and Equation (22) that the data matrix $\boldsymbol{R}_{xx}$ and the weighting matrix $\boldsymbol{W}(\boldsymbol{\theta})$ need only be computed once. From the matrix formulation in Equation (20) it is clear that there is a separation between the data and model based calculations. For example, one must only calculate the data matrix $\boldsymbol{R}_{xx}$ once for a given set of observations. A set of trajectories $\{\boldsymbol{\theta}_k\}$ through the TF plane corresponding to a rough grid search of the parameter space may be pre-computed and the weighting matrices $\{\boldsymbol{W}(\boldsymbol{\theta}_k)\}$ stored in memory.

To illustrate the performance of the PWHT estimator with the implementation strategy given in Table II, we take the example of an LFM signal with mean frequency $a_0 = 0.12/T_s$ and chirp rate $b_0 = 0.23/(NT_s)$, where T_s denotes the sample period. The root mean square error (RMSE) of the estimator for a and b is simulated and compared with theoretical variance expressions and the CRB, as shown in Figure 9, with $N = 128$. The algorithm of Table II is applied, with the window parameter M values $(3, 6, 9, 13)$. The initial estimate is computed by a grid search of the PWHT with $M = 3$. The parameter space is sampled in the range $a \in [0, \pi)$ and $b \in [-a/N, (\pi - a)/n]$ with spacing $\Delta_a/2$ and $\Delta_b/2$ along a and b direction respectively, where Δ_a and Δ_b are given by (12) and (13), respectively. This sampling scheme requires pre-calculation of a total of 50 PWHT trajectories. We note that a grid search using the same sampling scheme for the WHT (using Δ_a and Δ_b as given in Section II) would require 4736 trajectories. In optimization of the PWHT we have used an efficient gradient based technique proposed by Fletcher and Powell (FP) [10] for an SNR of 0 dB and above. It was found that for an SNR below 0 dB, the FP algorithm did not always converge and in these cases we have used a more robust, albeit more complex, algorithm proposed by Nelder and Mead (NM) [11], known as the simplex algorithm, which was found to produce good results down to about -5 dB SNR. The simulation results have been obtained by averaging 500 Monte Carlo runs.

In order to illustrate the effect of increasing the window length, in the procedure of Table II, the RMSE for each value of M is plotted in Figure 9. While the initial accuracy of the grid search (with $M = 3$) is very poor, it is sufficient for initialization of the optimization routine, which provides increasing accuracy as the value of M is increased. We note that the simulated accuracy shown in Figure 9 is consistent with theoretical analysis (for $M = 13$), down to about -3 dB SNR. The discrepancy at extremely low SNR is expected as assumptions inherent in the derivation of the RoA are no longer valid. As the noise floor increases, the true RoA shrinks, and for SNR $\ll 1$ one needs to use a denser grid search in order to achieve convergence. For higher SNR, although the estimation is not efficient, the performance is still

very close to the CRB and the computation time has been greatly reduced when compared to the WHT based estimator. In this case, the need to use the WHT becomes questionable, since the large increase in computational burden provides only a minor improvement in estimation accuracy. However, statistical efficiency is easily achieved, if desired, by optimising the WHT using the PWHT estimate for initialising the search. The overall approach is still far more computationally efficient than trying to directly optimise the WHT function.

IV. MULTICOMPONENT SIGNAL ESTIMATION

In the case of multicomponent signals, there will be a number of peaks within the parameter space of the PWHT, as illustrated in Figure 2. One approach in this case, is to threshold the (P)WHT function to determine the number and/or rough location of the peaks. However, such a method would require a relatively fine grid search despite the increased peak width of the PWHT, and the issue of how to set an appropriate threshold must be considered. From a statistical point of view, one may formulate the peak search as a detection problem, and set the threshold based on a certain level of significance. This then requires knowledge of the probability distribution of the (P)WHT.

To avoid these issues, we propose sequential estimation of each component. One estimates the 'strongest' component from the largest peak of the PWHT, using the method outlined in Table II. The complex amplitude is then estimated, for example using a simple least-squares approach, and the reconstructed component is then subtracted from the observations. This is repeated until all components have been estimated. If the number of components is unknown, one may construct a test to determine when the residual term contains no more signal components, though this is not elaborated upon here. The estimation procedure is summarised in Table III.

In contrast to sequential phase-based estimation of multicomponent signals [12], we do not require that the component being estimated is stronger than the other components present. However, the proposed

1) Set $i \leftarrow 1$. Organize the observations into the vector $x = (x(0), \ldots, x(N-1))'$.

2) Estimate θ_i using the procedure of Table II, to obtain $\hat{\theta}_i$.

3) Form the vector $s_i = \left(e^{j\varphi(0;\hat{\theta}_i)}, \ldots, e^{j\varphi(0;\hat{\theta}_i)} \right)'$.

4) Estimate the amplitude according to $\hat{A}_i = s^H x / N$.

5) Remove the estimated component: $x \leftarrow x - \hat{A}_i s_i$.

6) Set $i \leftarrow i + 1$. If $i \leq d$, repeat from Step 2.

TABLE III

MULTICOMPONENT ESTIMATION ALGORITHM BASED ON THE PWHT.

approach suffers from an inherent bias since the multiple peaks disturb one another through main and/or side lobes, resulting in a shift of the peak location from the true parameter values, even if Assumption A1 holds. In order to reduce this bias, one may obtain the initial estimates $\{\hat{\theta}_i\}_{i=1}^q$ using the procedure of Table III, followed by a bias reduction step, in which all estimated components but the desired are subtracted from the observations, and the desired component parameters are then re-estimated using the PWHT. In this bias reduction step, one may use the previous (biased) estimate to initialize optimization of the PWHT with the final value $M = M_q$, i.e. it is not necessary to repeat the full estimation procedure of Table II again.

To demonstrate the multicomponent estimation procedure, we first consider a three-component LFM signal. The parameters of the components used were $\theta_1 = 2\pi(0.025, 3.189 \times 10^{-3})$, $\theta_2 = 2\pi(0.42, -2.362 \times 10^{-3})$ and $\theta_3 = 2\pi(0.26, -1.654 \times 10^{-3})$. In the implementation of the procedure from Table II (in step 2 of Table III), we have used the same grid-search points as in the previous section. We have also applied the WHT after the last PWHT step, with two final iterations to reduce bias. Figure 10 shows the simulated estimation accuracy using $N = 128$ observations. It can be seen from the results that after two bias reduction iterations, the estimation accuracy becomes close to that of the single component case. Of

course, at extremely high SNR when the bias becomes the dominant source of estimation error, more bias reduction iterations are typically required to achieve statistical efficiency.

As a second example we consider the SFM model defined previously. As discussed in Section III-C, the estimation of parameter B is biased. In the multicomponent case, we have found that despite this bias, the sequential estimation procedure of Table III remains successful. We illustrate this in application to experimental data, which has been collected from a 24 GHz radar system, observing a rotating fan. The rotational movement of the scatterer in this experiment results in a sinusoidal Doppler shift with respect to time, termed a micro-Doppler signature. To illustrate the estimation of multicomponent signatures, we apply the PWHT estimator to the data collected only from the in-phase baseband channel of the radar system. This effectively produces two "signatures" each π radians out of phase with the other. The baseband signal was sampled at 1000 Hz and we have used an observation interval of 402 samples ($\sim$0.4 seconds) to estimate the micro-Doppler signatures. The initial grid search is performed for $B \in [0, 250]$ Hz, $\phi \in [0, 2\pi)$ rad and $\omega_0 \in [1, 10]$ Hz, with 12, 10 and 6 samples along each parameter range respectively (720 total trajectories). In the initial search, $M = 15$ was used to calculate the PWHT, and in the final optimization step, $M = 35$.

In Figure 11 we show the PWHT of the experimental data for $B = 16$ Hz. The figure shows both cases of $M = 15$ and $M = 35$, which clearly illustrates the advantage of widening the main peak, achieved with the smaller window length. In Figure 12 we show the estimated micro-Doppler signatures overlaid on the PWVD of the data (for $M = 35$). In this figure we see both the initial grid search estimates and the final estimated signatures. It is observed that both the final estimated signatures overlap the TF signatures as expected, although the initial grid search yielded somewhat inaccurate results.

162

V. Conclusions

This work has examined a computationally attractive implementation of the WHT estimator for linear FM signals. A technique for reducing the number of required trajectories to be computed was proposed based on the PWVD, having window length L, which widens the peak of interest in the parameter space. It was shown that the peak width is increased from $O(1/N)$ for the WHT to $O(1/L)$ for the PWHT, allowing one to effectively control the RoA of the estimator. An estimation scheme for both single and multicomponent signals was proposed based on this result. The application of the PWHT to nonlinear FM signals was also considered, and shown to be effective under the assumption that the signal IF is approximately linear within all intervals of length L. Statistical analysis was performed in the case of additive white Gaussian noise, which showed how the SNR performance threshold is affected, and interestingly, that the output SNR is the same as that of the WHT, despite the reduced computational requirement. A general expression for the estimator variance was provided for nonlinear FM signals, and in closed form for linear FM signals. It was shown that in the case of linear FM signals there is clearly an optimal choice for the PWVD window length which yields a performance level close to that of the CRB. Theoretical results presented were verified with simulations for linear and sinusoidal FM signals, in both the single and multicomponent case. Results with experimental data where the sinusoidal FM model applies were also presented, which illustrate the effectiveness of the proposed scheme in practice.

Appendix I

Derivation of the Output SNR

In order to determine the output SNR as defined in Equation (14) we need to find $|P_s(\theta_0)|^2$ and $\text{Var}\left[P_x(\theta_0)\right]$ where $s(n) = Ae^{j\varphi(n;\theta_0)}$ and $x(n) = s(n) + v(n)$. In the following we assume $v(n)$ is a complex circular white Gaussian process of variance σ_v^2.

Let us express the PWHT of the observations as $P_x(\theta) = P_s(\theta) + P_{sv}(\theta) + P_v(\theta)$ where

$$P_{sv}(\theta) \triangleq \sum_{n=M}^{N-M-1} \sum_{l=-M}^{M} [s(n+l)v^*(n-l) + s^*(n-l)v(n+l)]e^{-j2\omega(n,\theta)l} \tag{23}$$

and the expressions for $P_s(\theta)$ and $P_v(\theta)$ follow the definition given in Equation (6). Since the third order moments of $v(n)$ are zero, then $\text{Var}[P_x(\theta_0)] = \text{Var}[P_{sv}(\theta_0)] + \text{Var}[P_v(\theta_0)]$.

From Equation (23) it is clear that $\text{E}[P_{sv}(\theta)] = 0$. The variance is calculated according to:

$$\text{Var}[P_{sv}(\theta_0)] = \text{E}[|P_{sv}(\theta_0)|^2] = \sum_{n=M}^{N-M-1} \sum_{m=M}^{N-M-1} \sum_{l=-M}^{M} \sum_{k=-M}^{M} e^{-j2(\omega(n,\theta_0)l - \omega(m,\theta_0)k)}$$

$$\times \text{E}[[s(n+l)v^*(n-l) + s^*(n-l)v(n+l)][s^*(m+k)v(m-k) + s(m-k)v^*(m+k)]]$$

$$= \sum_{n=M}^{N-M-1} \sum_{m=M}^{N-M-1} \sum_{l=-M}^{M} \sum_{k=-M}^{M} e^{-j2(\omega(n,\theta_0)l - \omega(m,\theta_0)k)}$$

$$\times [s(n+l)s^*(m+k)\text{E}[v^*(n-l)v(m-k)] + s^*(n-l)s(m-k)\text{E}[v(n+l)v^*(m+k)]].$$

Using the circular property of the noise process and assumption A1, we obtain

$$\text{Var}[P_{sv}(\theta_0)] \approx |A|^2\sigma_v^2 \sum_{n=M}^{N-M-1} \sum_{m=M}^{N-M-1} \sum_{l=-M}^{M} \sum_{k=-M}^{M} e^{-j2(a_n+b_n n)l} e^{j2(a_m+b_m m)k}$$

$$\times [e^{j(a_n n + b_n(n+1)^2/2)}\delta(n-m+k-l) + e^{j(a_m m + b_m(m+1)^2/2)}\delta(n-m+l-k)],$$

where (a_n, b_n) and (a_m, b_m) denote the parameters of the linear IF approximation on the intervals $\mathcal{I}_n$ and $\mathcal{I}_m$ respectively. Since the Kronecker delta functions restrict non-zero terms of the summation to the case $|n - m| < L$, we assume $a_n \approx a_m$ and $b_n \approx b_m$ in the above equation, allowing the simplification:

$$\text{Var}[P_{sv}(\theta_0)] \approx |A|^2\sigma_v^2 \sum_{n=M}^{N-M-1} \sum_{m=M}^{N-M-1} \sum_{l=-M}^{M} \sum_{k=-M}^{M} [e^{j(n-m+k-l)(2a_n+b_n(n+m-l-k))/2}\delta(n-m-l+k) +$$

$$e^{-j(n-m+l-k)(2a_n+b_n(n+m+l+k))/2}\delta(n-m+l-k)]$$

$$= |A|^2\sigma_v^2 \sum_{n=M}^{N-M-1} \sum_{m=M}^{N-M-1} \sum_{l=-M}^{M} \sum_{k=-M}^{M} [\delta(n-m-l+k) + \delta(n-m+l-k)]$$

$$= |A|^2\sigma_v^2\frac{2}{3}(2M+1)(3N(2M+1) - 2M(5+8M))$$

$$= |A|^2\sigma_v^2\frac{2}{3}L(3NL - (L-1)(4L+1)).$$

The closed form expression in second-to-last line above was obtained with the aid of the software package Mathematica, and is valid under the condition that $N > 4M + 1$.

The second order moment of $P_v(\theta)$ is given by

$$
\begin{aligned}
\mathsf{E}\left[|P_v(\theta)|^2\right] &= \sum_{n=M}^{N-M-1}\sum_{m=M}^{N-M-1}\sum_{l=-M}^{M}\sum_{k=-M}^{M} e^{-j2(\omega(n,\theta_0)l - \omega(m,\theta_0)k)} \\
&\quad \times \mathsf{E}\left[v(n+l)v^*(n-l)v^*(m+k)v(m-k)\right] \\
&= \sum_{n=M}^{N-M-1}\sum_{m=M}^{N-M-1}\sum_{l=-M}^{M}\sum_{k=-M}^{M} \left[\mathsf{E}\left[v(n+l)v^*(n-l)\right]\mathsf{E}\left[v^*(m+k)v(m-k)\right]\right. \\
&\quad \left. + \mathsf{E}\left[v(n+l)v^*(m+k)\right]\mathsf{E}\left[v^*(n-l)v(m-k)\right]\right] e^{-j2(\omega(n,\theta_0)l - \omega(m,\theta_0)k)}
\end{aligned}
$$

Using the circular property of the noise process and assumption A1, we obtain

$$
\begin{aligned}
\mathsf{E}\left[|P_v(\theta)|^2\right] &\approx \sigma_v^4 \sum_{n=M}^{N-M-1}\sum_{m=M}^{N-M-1}\sum_{l=-M}^{M}\sum_{k=-M}^{M} e^{-j2[(a_n+b_n n)l - (a_m+b_m m)k]} \\
&\quad \times [\delta(l)\delta(k) + \delta(l-k)\delta(n-m)],
\end{aligned}
$$

where (a_n, b_n) and (a_m, b_m) denote the parameters of the linear IF approximation on the intervals $\mathcal{I}_n$ and $\mathcal{I}_m$ respectively. Given the arguments of the Kronecker delta functions the above expression simplifies to:

$$
\begin{aligned}
\mathsf{E}\left[|P_v(\theta)|^2\right] &= \sigma_v^4 \sum_{n=M}^{N-M-1}\sum_{m=M}^{N-M-1}\sum_{l=-M}^{M}\sum_{k=-M}^{M} [\delta(l)\delta(k) + \delta(l-k)\delta(n-m)] \\
&= \sigma_v^4((N-2M)^2 + (N-2M)(2M+1)) \\
&= \sigma_v^4((N-L+1)^2 + (N-L+1)L).
\end{aligned}
$$

Also, $\mathsf{E}[P_v(\theta)] = \sigma_v^2(N-L+1)$, which leads the overall variance expression

$$
\mathsf{Var}\left[P_x(\theta_0)\right] = |A|^2\sigma_v^2\frac{2}{3}L(3NL - (L-1)(4L+1)) + \sigma_v^4(N-L+1)L. \tag{24}
$$

It is easily verified by direction substitution that, under assumption A1,

$$
P_s(\theta_0) = |A|^2 L(N-L-1). \tag{25}
$$

165

Substitution of Equation (25) and (24) into Equation (14) yields the desired expression for the output SNR given in Equation (15). ■

APPENDIX II

DERIVATION OF THE ESTIMATOR BIAS AND VARIANCE

The maximum of $P_x(\theta) = P_s(\theta) + \delta P(\theta)$ occurs at a location $\theta_0 + \delta\theta$, where θ_0 is the true parameter value and $\delta\theta$ is a perturbation due to noise. The maximum of $P_x(\theta)$ satisfies

$$\left[\frac{\partial}{\partial\theta}(P_x(\theta) + \delta P(\theta))\right]_{\theta_0 + \delta\theta} = 0 \qquad (26)$$

We expand Equation (26) using a first order approximation:

$$\left[\frac{\partial}{\partial\theta}(P_s(\theta) + \delta P(\theta))\right]_{\theta_0} + \left[\frac{\partial^2}{\partial\theta\partial\theta^T}P_s(\theta)\right]_{\theta_0} \delta\theta \cong 0. \qquad (27)$$

Under assumption A1, $[\frac{\partial}{\partial\theta}P_s(\theta)]_{\theta_o} = 0$, therefore

$$\delta\theta = -\left[\frac{\partial^2}{\partial\theta\partial\theta^T}P_s(\theta)\right]_{\theta_0}^{-1} \left[\frac{\partial}{\partial\theta}\delta P(\theta))\right]_{\theta_0}. \qquad (28)$$

Defining $C \triangleq [\frac{\partial^2}{\partial\theta\partial\theta^T}P_s(\theta)]_{\theta_0}$ and $b \triangleq [\frac{\partial}{\partial\theta}\delta P(\theta))]_{\theta_0}$, where b is a random vector, the mean and covariance matrix of $\delta\theta$ are given by $\mu_{\delta\theta} = -C^{-1}\mathsf{E}[b]$ and $\Gamma_{\delta\theta} = C^{-1}(\mathsf{E}[bb^T] - \mathsf{E}[b]\mathsf{E}[b^T])C^{-T}$ respectively. Substituting Equation (6) into the expression for C, we obtain

$$\begin{aligned}
C &= \sum_{n=M}^{N-M-1}\sum_{l=-M}^{M} s(n+l)s^*(n-l)\left[\frac{\partial^2}{\partial\theta\partial\theta^T}e^{-j2\omega(n;\theta)l}\right]_{\theta_0} \\
&= \sum_{n=M}^{N-M-1}\sum_{l=-M}^{M} s(n+l)s^*(n-l)e^{-j2\omega(n;\theta_0)l}\left[-j2l\frac{\partial^2\omega(n;\theta)}{\partial\theta\partial\theta^T} + 4l^2\frac{\partial\omega(n;\theta)}{\partial\theta}\frac{\partial\omega(n;\theta)}{\partial\theta^T}\right]_{\theta_0} \\
&= |A|^2\sum_{n=M}^{N-M-1}\sum_{l=-M}^{M}\left[-j2l\frac{\partial^2\omega(n;\theta)}{\partial\theta\partial\theta^T} + 4l^2\frac{\partial\omega(n;\theta)}{\partial\theta}\frac{\partial\omega(n;\theta)}{\partial\theta^T}\right]_{\theta_0}
\end{aligned}$$

where the final simplification above is made using assumption A1. Expanding the expression for b using Equation (6) we obtain

$$\begin{aligned}
b = &-j2\sum_{n=M}^{N-M-1}\sum_{l=-M}^{M} e^{-j2\omega(n;\theta_0)l}l\left[\frac{\partial\omega(n;\theta)}{\partial\theta}\right]_{\theta_0} \\
&\times [s(n+l)v^*(n-l) + s^*(n-l)v(n+l) + v(n+l)v^*(n-l)].
\end{aligned}$$

166

Using the assumption of AWGN,

$$\mathsf{E}\left[b\right] = -j2\sigma_v^2 \sum_{n=M}^{N-M-1} \sum_{l=-M}^{M} \delta(l) l e^{-j2\omega(n;\theta_0)l} \left[\frac{\partial\omega(n;\theta)}{\partial\theta}\right]_{\theta_0} = 0$$

which means that, to a first order approximation, $\mu_{\delta\theta} = 0$ and the estimator is unbiased. The covariance

matrix of b is given by

$$\begin{aligned}
\mathsf{E}\left[bb^H\right] &= 4 \sum_{n=M}^{N-M-1} \sum_{m=M}^{N-M-1} \sum_{l=-M}^{M} \sum_{k=-M}^{M} \left[\frac{\partial\omega(n;\theta)}{\partial\theta}\frac{\partial\omega(m;\theta)}{\partial\theta^T}\right]_{\theta_0} lk e^{-j2[\omega(n;\theta_0)l-\omega(m;\theta_0)k]} \\
&\quad \times \left[s(n+l)s^*(m+k)\mathsf{E}\left[v^*(n-l)v(m-k)\right]\right. \\
&\quad + s^*(n-l)s(m-k)\mathsf{E}\left[v(n+l)v^*(m+k)\right] \\
&\quad \left. + \mathsf{E}\left[v(n+l)v^*(n-l)v(m-k)v^*(m+k)\right]\right],
\end{aligned}$$

which, using assumption A1 and the noise properties, may be simplified as

$$\begin{aligned}
\mathsf{E}\left[bb^H\right] &= 4 \sum_{n=M}^{N-M-1} \sum_{m=M}^{N-M-1} \sum_{l=-M}^{M} \sum_{k=-M}^{M} \left[\frac{\partial\omega(n;\theta)}{\partial\theta}\frac{\partial\omega(m;\theta)}{\partial\theta^T}\right]_{\theta_0} lk \\
&\quad \times \left[|A|^2\sigma_v^2[\delta(n-m-l+k)+\delta(n-m+l-k)]\right. \\
&\quad \left. + \sigma_v^4[\delta(l)\delta(k)+\delta(n-m+l-k)\delta(n-m-l+k)]\right].
\end{aligned}$$

Exploiting symmetry in the summations, and the fact that $\sum_{l=-M}^{M} l^2 = \frac{1}{3}M(M+1)(2M+1)$, we obtain

the final simplification given in Equation (17), where $B \triangleq \mathsf{E}\left[bb^H\right]$ ∎

APPENDIX III

DERIVATION OF THE CRAMÉR-RAO BOUND

In this section we derive a general form of the Cramér-Rao Bound (CRB) for estimating the parameter vector $\theta \in \mathbb{R}^{p\times 1}$ from observations $\{x(n) = s(n) + v(n)\}_{n=0}^{N-1}$ where $s(n) = Ae^{j\varphi(n;\theta)}$ and $v(n)$ is a complex white Gaussian noise sequence of variance σ_v^2. The full vector of unknown parameters is $\eta = (\theta^T, |A|, \angle A, \sigma_v^2)^T$. We organize the observations and signal samples into vectors $x = (x(0), \ldots, x(N-1))^T$ and $s = (s(0), \ldots, s(N-1))^T$ respectively. The CRB is given by the

167

inverse of the Fisher information matrix (FIM); J. Given a Gaussian distributed random vector x, the FIM can be calculated according to [13]:

$$J_{pq} = \text{Tr}\left[\mathbf{\Gamma}^{-1}\frac{\partial \mathbf{\Gamma}}{\partial \eta_p}\mathbf{\Gamma}^{-1}\frac{\partial \mathbf{\Gamma}}{\partial \eta_q}\right] + 2\text{Re}\left[\frac{\partial \mu^H}{\partial \eta_p}\mathbf{\Gamma}^{-1}\frac{\partial \mu^H}{\partial \eta_p}\right], \tag{29}$$

where $\mathbf{\Gamma}$ and μ correspond to the covariance matrix and mean vector of x respectively. Clearly $\mathbf{\Gamma} = \sigma_v^2 I$ and $\mu = s$ in this case. We first find the partial derivatives of s with respect to η as

$$\frac{\partial s}{\partial \eta^T} = \left[j\frac{\partial \varphi(\theta)}{\partial \theta_p} \odot s, \ |A|^{-1}s, \ js, \ 0_N\right] \tag{30}$$

where 0_N denotes a length N column vector of zeros. In Equation (30) we have used the definition $\varphi(\theta) = (\varphi(0;\theta), \ldots, \varphi(N-1;\theta))^T$. We wish to construct the FIM matrix in block form

$$J = \begin{bmatrix} J_{11} & J_{12} \\ J_{21} & J_{22} \end{bmatrix}$$

such that the entries concerned with θ are contained in J_{11}. Using (29) and the partial derivatives of s from Equation (30), we find

$$J_{11} = 2|A|^2/\sigma_v^2 Q^T Q$$

$$J_{12} = J_{21}^T = [\ 0_p, \ 2|A|^2/\sigma_v^2 Q^T 1_N, \ 0_p]$$

$$J_{22} = \text{diag}\left[\ 2N/\sigma_v^2, \ 2N|A|^2/\sigma_v^2, \ N/\sigma_v^4\ \right]$$

where $Q = \partial \varphi(\theta)/\partial \theta^T$ and 1_N is a length N column vector of ones. By use of the partitioned matrix inversion identity we may find the CRB with respect to θ as

$$C(\theta) = (J_{11} - J_{12}J_{22}^{-1}J_{21})^{-1}$$

$$= \frac{N}{2SNR_{in}}(Q^T(NI - 1_N^T 1_N)Q)^{-1}$$

where $SNR_{in} = |A|^2/\sigma_v^2$. ∎

REFERENCES

[1] L. Cirillo, A. Zoubir, and M. Amin, "Estimation of FM parameters using a time-frequency Hough transform," in *Proc. ICASSP*, Toulouse, France, May 2006.

[2] S. Peleg and B. Porat, "Estimation and classification of signals with polynomial phase," *IEEE Trans. Inform. Theory*, vol. 37, pp. 422–430, 1991.

[3] S. Barbarossa, A. Scaglione, and G. Giannakis, "Product higher-order ambiguity function for multicomponent polynomial-phase signal modeling," *IEEE Trans. Signal Processing*, vol. 46, no. 3, pp. 691–708, Mar 1998.

[4] S. Barbarossa and V. Petrone, "Analysis of polynomial phase signals by the integrated generalized ambiguity function," *IEEE Trans. Signal Processing*, vol. 45, no. 2, pp. 316–327, Feb 1997.

[5] J. C. Wood and D. T. Barry, "Radon transform of time-frequency distributions for analysis of multicomponent signals," *IEEE Trans. Signal Processing*, vol. 42, no. 11, pp. 3166–3177, Nov 1994.

[6] S. Barbarossa, "Analysis of multicomponent LFM signals by a combined Wigner-Hough transform," *IEEE Trans. Signal Processing*, vol. 43, no. 6, pp. 1511–1515, Jun 1995.

[7] S. Barbarossa and O. Lemoine, "Analysis of nonlinear FM signals by pattern recognition of their time-frequency representation," *IEEE Signal Processing Lett.*, vol. 3, no. 4, pp. 112–115, Apr 1996.

[8] J. Ängeby, "Estimating parameters using the nonlinear instantaneous least squares approach," *IEEE Trans. Signal Processing*, vol. 48, no. 10, pp. 2721–2732, Oct 2000.

[9] M. Wong and Q. Jin, "Estimation of the time-varying frequency of a signal: the Cramer-rao bound and the application of Wigner distribution," *IEEE Trans. Acoust., Speech, Signal Processing*, vol. 38, no. 3, pp. 519–536, March 1990.

[10] R. Fletcher and M. Powell, "A rapidly convergent descent method for minimization," *Computer J.*, vol. 6, pp. 163–168, 1963.

[11] J. Nelder and R. Mead, "A simplex method for function minimization," *Computer J.*, vol. 7, pp. 308–313, 1965.

[12] P. Oliveria and V. Barroso, "Sequential extraction of components of multicomponent PPS signals," in *Proc. ICASSP*, Phoenix, USA, Mar 1999.

[13] P. Stoica and A. Nehorai, "Performance study of conditional and unconditional direction-of-arrival estimation," *IEEE Trans. Acoust., Speech, Signal Processing*, no. 10, pp. 1783–95, Oct 1990.
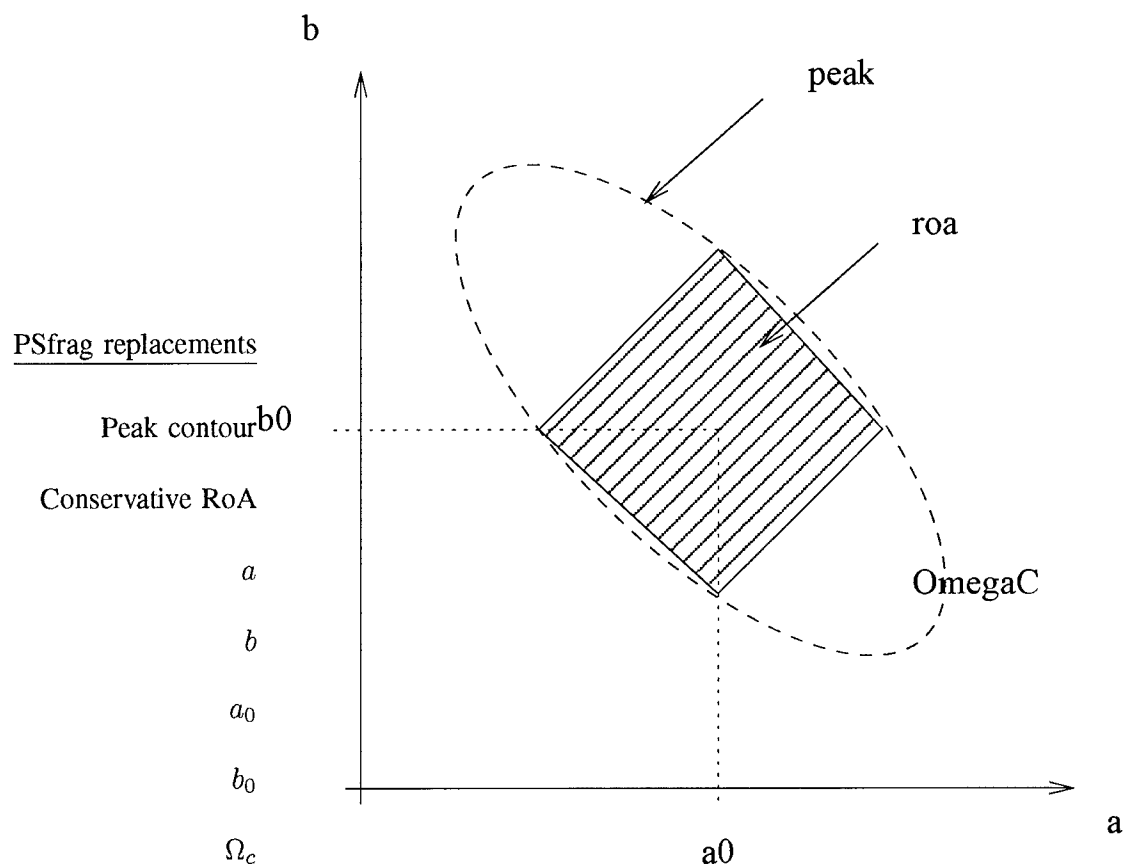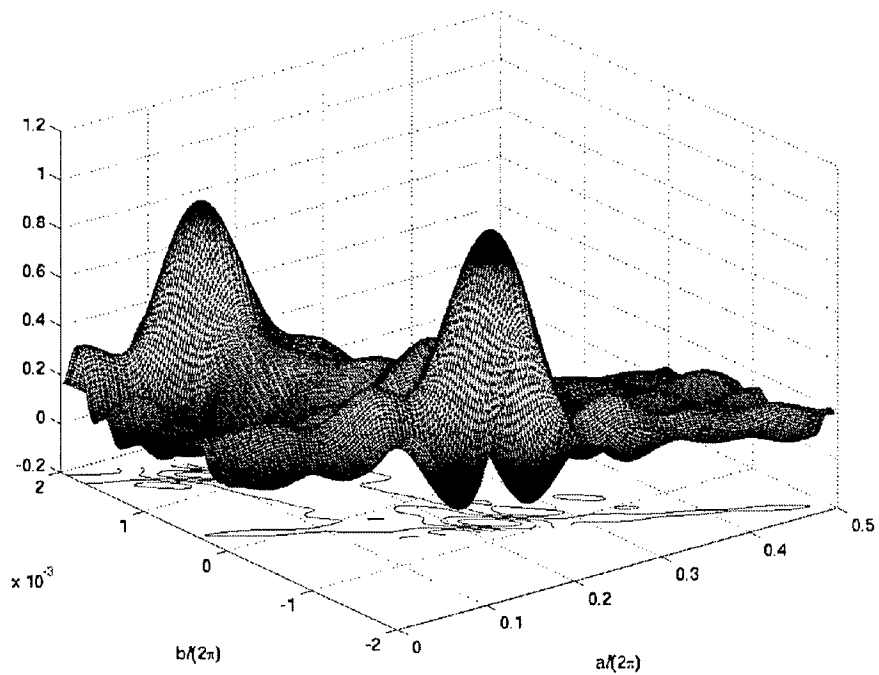
Fig. 1. The RoA is conservatively derived as the diamond shape defined by the peak width in a and b.
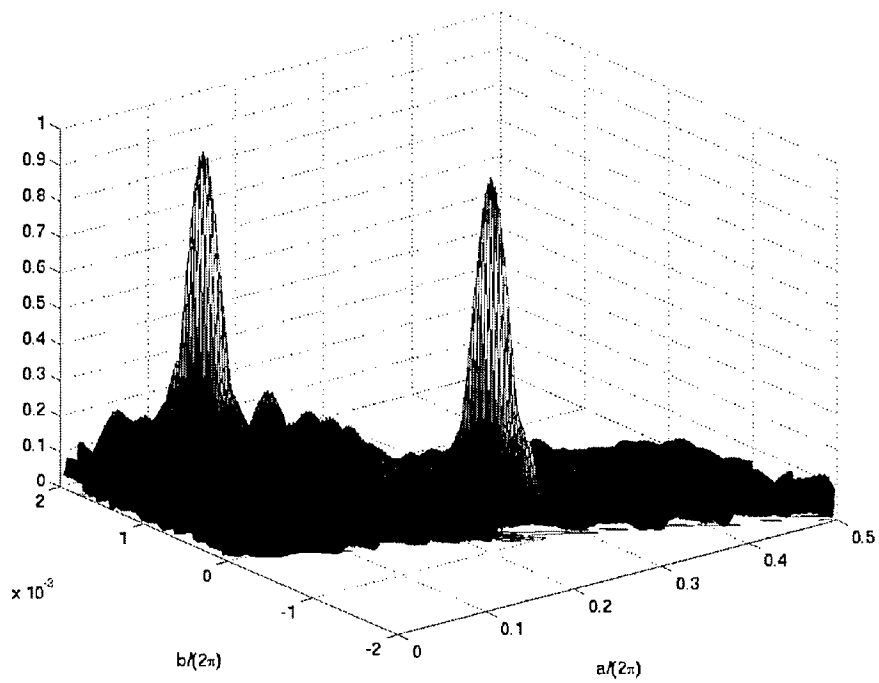
(a)

(b) (a)   (b)

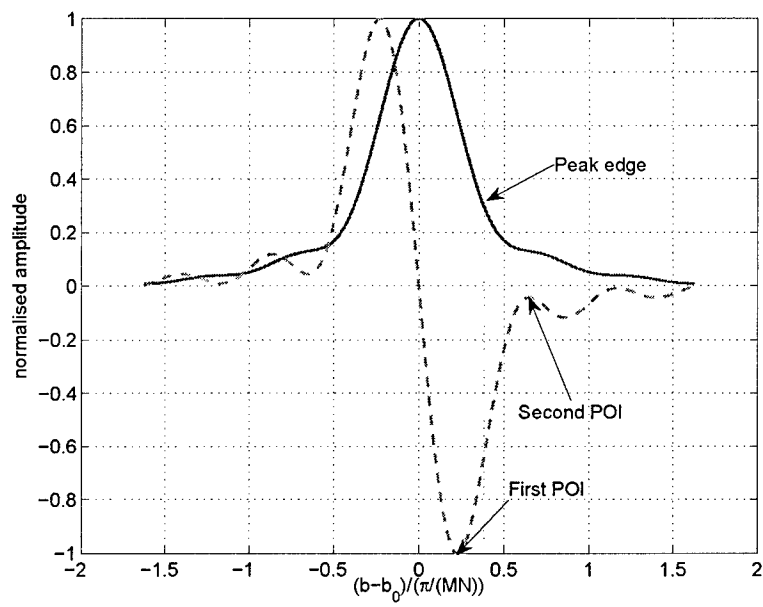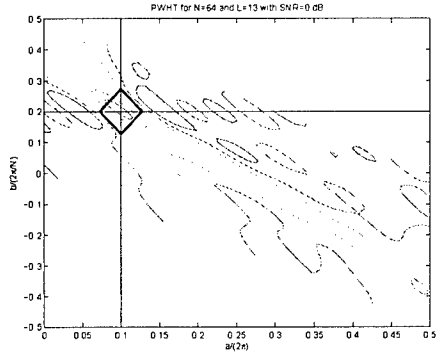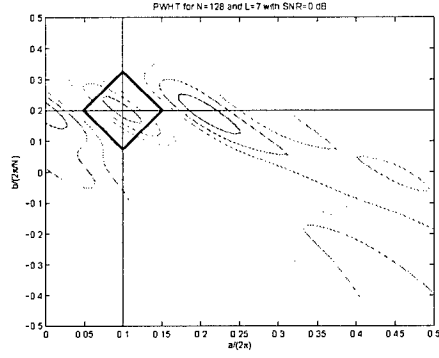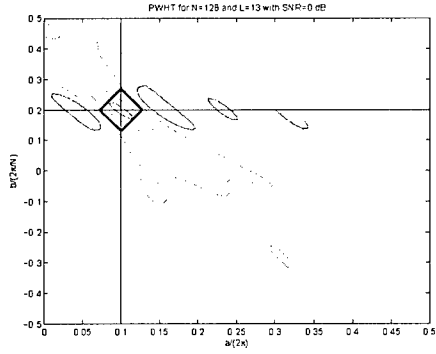Fig. 2.   (a) WHT and (b) PWHT of the sum of two chirp signals.

Fig. 3. Normalized plot of $H_s(a_0, \bar{b})$ versus $\bar{b}$ (solid) and its derivative with respect to $\bar{b}$ (dashed).
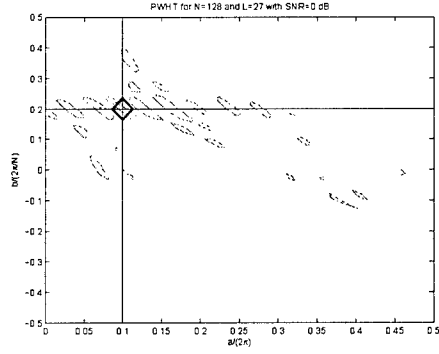
Fig. 4. An example of the PWHT at SNR=0 dB, for (a) $N = 64$ and $L = 13$, (b) $N = 128$ and $L = 7$, (c) $N = 128$ and $L = 13$ and (d) $N = 128$ and $L = 27$. The approximate RoA given by Equations (12) and (13) is shown as a black diamond. The true parameter location at the intersection of the vertical and horizontal black lines.

173
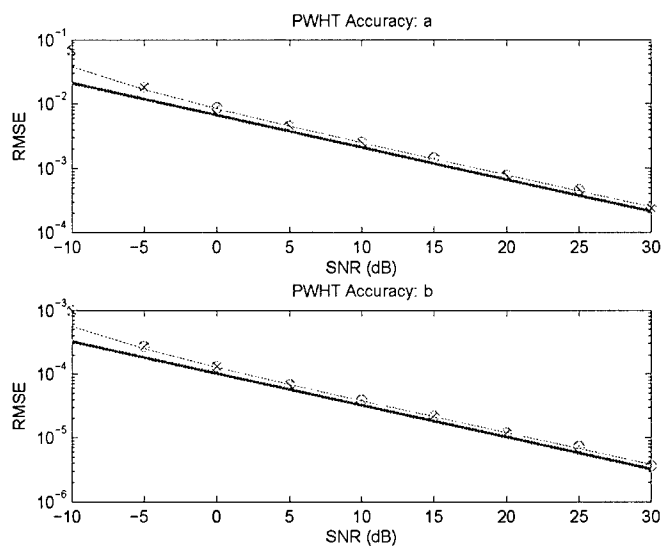
Fig. 5. Theoretical and simulated accuracy of the PWHT estimator for a LFM signal model. Theoretical variance (-) CRB (-) simulated variance (○) simulated RMSE (×).
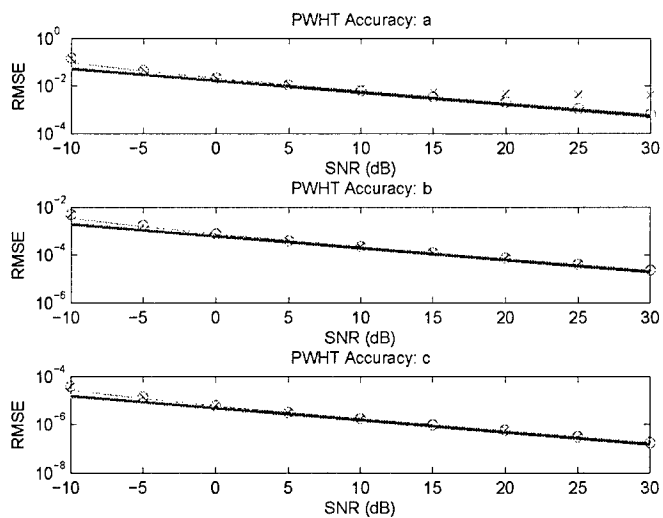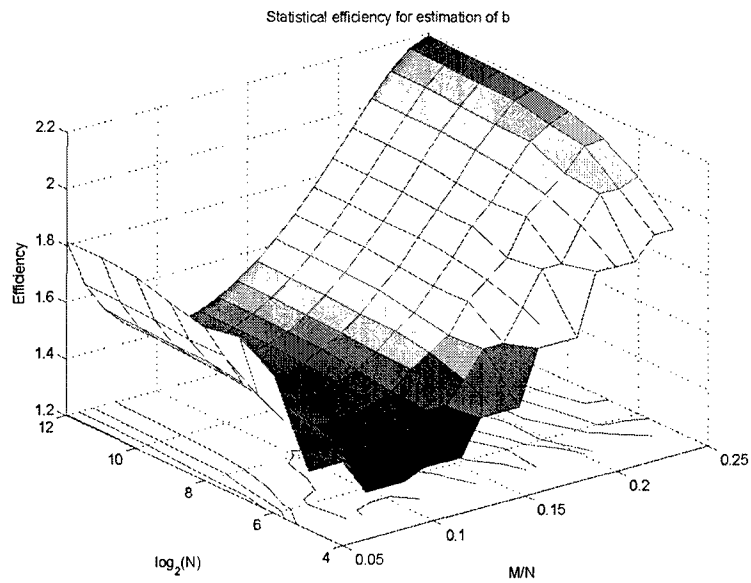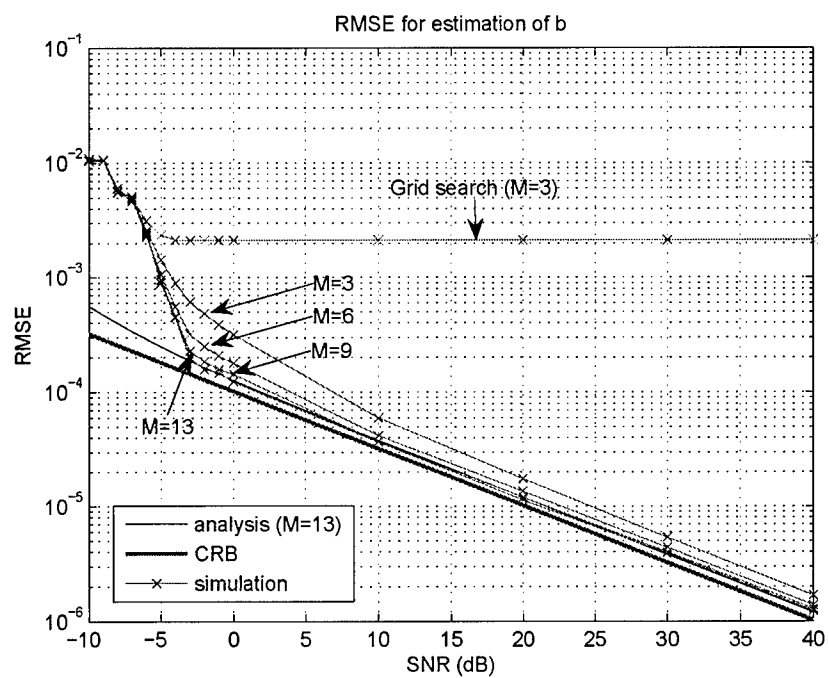

Fig. 6. Theoretical and simulated accuracy of the PWHT estimator for a QFM signal model. Theoretical variance (-) CRB (-) simulated variance (○) simulated RMSE (×).

174
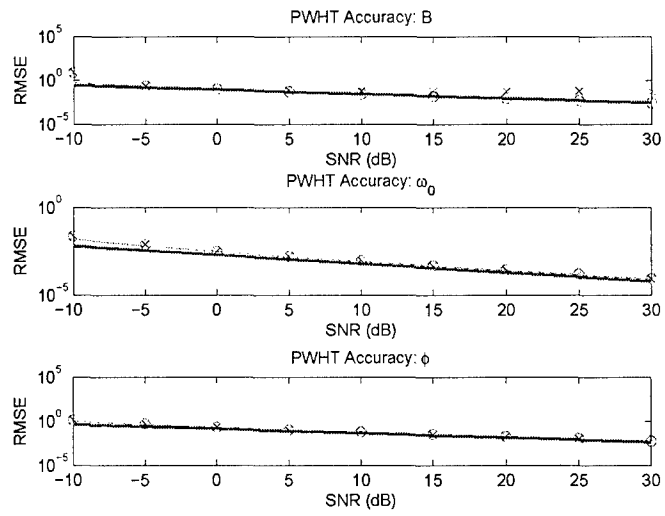
Fig. 7. Theoretical and simulated accuracy of the PWHT estimator for a SFM signal model. theoretical variance (-) CRB (-) simulated variance (o) simulated RMSE (×).

Fig. 8. Efficiency of the PWHT estimator of the chirp-rate.

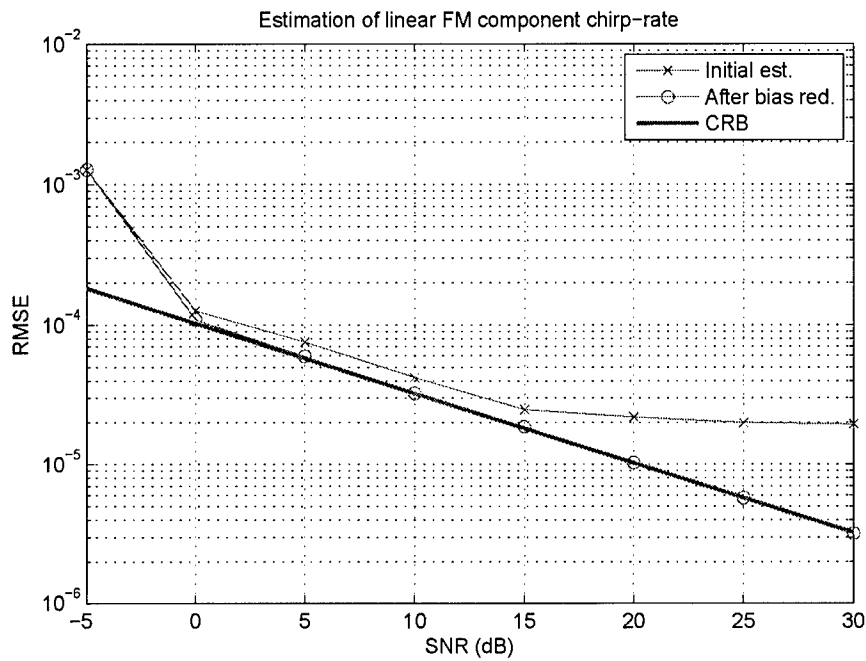Fig. 9. Single-component linear FM example. RMSE for chirp-rate estimation, after each optimization step.

Fig. 10. Multicomponent linear FM example. RMSE for chirp-rate estimation of one of the components, before and after bias reduction.
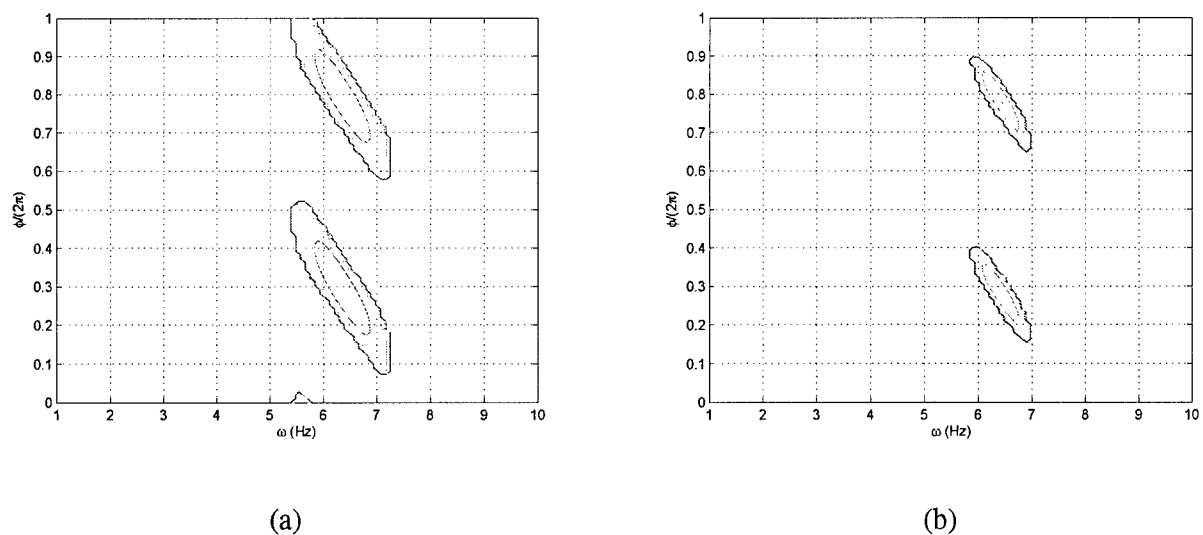

(a)

(b)

Fig. 11. PWHT for $M = 15$ (a) and $M = 35$ (b) of the experimental micro-Doppler data, evaluated for $B = 16$ Hz.
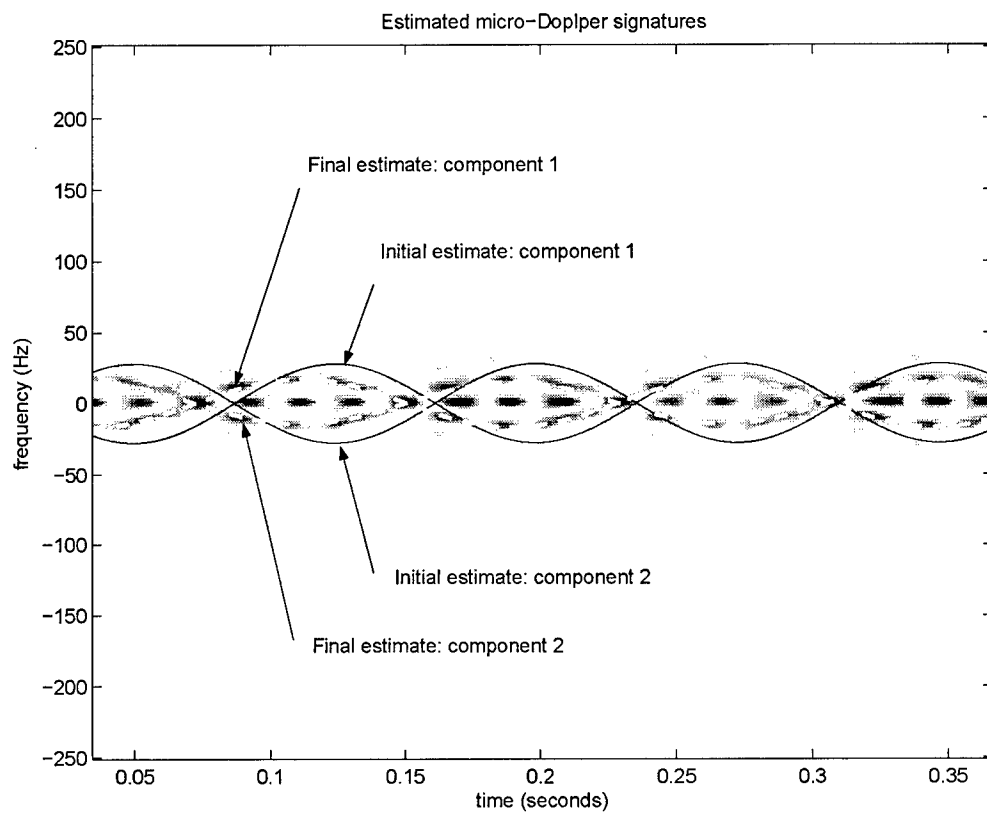
177

Fig. 12. Estimated micro-Doppler signatures from the initial grid search with $M = 15$ (green) and optimization of the PWHT function with $M = 35$ (red), overlaid on the PWVD of the data computed with $M = 35$.

ONR Collection Data

REPORTING PERIOD: 1 October 2001 to 31 March 2007

NAME OF PI: Moeness AMIN

UNIVERSITY/Contractor: Villanova University

TITLE OF PROJECT: Classification and Discrimination of Sources with Time-Varying Frequency and Spatial Spectra

GRANT/CONTRACT/WORK REQUEST NUMBER: N00014-98-1-0176

1. Papers published in referred journals (TITLE; JOURNAL):

W. Mu, M. G. Amin, and Y. Zhang, "Bilinear signal synthesis in array processing," IEEE Transactions on Signal Processing, vol. 51, no. 1, pp. 90-100, January 2003.

Y. Zhang, M. G. Amin, and G. J. Frazer, "High-resolution time-frequency distributions for maneuvering target detection in over-the-horizon radars," IEE Proceedings on Radar, Sonar and Navigation, vol. 150, no.4, pp. 299-304, Aug. 2003.

G. Wang, X.-G. Xia, B. T. Root, V. C. Chen, Y. Zhang, and M. G. Amin, "Maneuvering target detection in over-the-horizon radar by using adaptive clutter rejection and adaptive chirplet transform," IEE Proceedings on Radar, Sonar and Navigation, vol. 150, no. 4, pp. 292-298, Aug. 2003.

F. Ahmad, G. J. Frazer, S. A. Kassam, and M. G. Amin, "Design and implementation of near-field, wideband synthetic aperture beamformers," IEEE Transactions on Aerospace and Electronic Systems, vol. 40, no. 1, pp 206-221, January 2004.

M. G. Amin and Y. Zhang, "Bilinear signal synthesis using polarization diversity," IEEE Signal Processing Letters, vol. 11, no. 3, pp 338-340, March 2004.

A. Belouchrani, K. Abed-Meraim, M. G. Amin, and A.M. Zoubir, "Blind separation of non-stationary sources," IEEE Signal Processing Letters, July 2004.

F. Ahmad, M. G. Amin, S. A. Kassam, "Synthetic aperture beamformer for imaging through a dielectric wall," IEEE Transactions on Aerospace and Electronic Systems, January 2005.

Y. Zhang, K. Yang, and M. G. Amin, "Subband array implementations for space-time adaptive processing," EURASIP Journal on Applied Signal Processing, vol. 2005, no. 1, pp. 99-111, Jan. 2005.

G. Wang, M. G. Amin, and Y. Zhang, "A new approach for target locations in the presence of wall ambiguity," IEEE Transactions on Aerospace and Electronic Systems, January 2006.

Y. Zhang, B. Obeidat, and M. G. Amin, "Spatial polarimetric time-frequency distributions for direction-of-arrival estimations," IEEE Transactions on Signal Processing, April 2006.

Y. Zhang and M. Amin, "Blind separation of nonstationary sources based on spatial time-frequency distributions," EURASIP Journal on Applied Signal Processing, vol. 2006, article ID 64785, 13 pages, 2006.

G. Wang and M. Amin, "Imaging through unknown walls using different standoff distances," IEEE Transactions on Signal Processing, October 2006.

F. Ahmad and M. Amin, "A noncoherent approach to through-the-wall radar imaging," IEEE Transactions on Aerospace and Electronic Systems, October 2006.

Y. Zhang, G. J. Frazer, and M. G. Amin, "Concurrent operation of two over-the-horizon radars," IEEE Journal of Selected Topics in Signal Processing, special issue on Adaptive Waveform Design for Agile Sensing and Communication, in press.

F. Ahmad, M. G. Amin, G. Mandapati, "Autofocusing of through-the-wall radar imagery under unknown wall characteristics," IEEE Transactions on Aerospace Electronics Systems, in press.

L. Cirillo, A. Zoubir and M. Amin, "Blind Source Separation in the Time-Frequency Domain Based on Multiple Hypothesis Testing," submitted to IEEE Transactions on Signal Processing.

L. Cirillo, A. Zoubir and M. Amin, "Estimation of FM Parameters using a Time-Frequency Hough Transform," submitted to IEEE Transactions on Signal Processing.

2. Books or Book chapters published (TITLE; AUTHORS/EDITORS; PUBLISHER):

M. G. Amin and Y. Zhang, "Interference suppression in spread spectrum communication systems," in J. G. Proakis (ed.), The Wiley Encyclopedia of Telecommunications, New York, NY: John Wiley, 2002.

M. G. Amin and Y. Zhang, "Spatial time-frequency distributions and their applications," in B. Boashash (ed.), Time-Frequency Signal Analysis and Processing, Oxford, UK: Elsevier, 2003.

M. G. Amin, Y. Zhang, G. J. Frazer, and A. R. Lindsey, "Spatial time-frequency distributions: Theory and applications," in L. Debnath (ed.), Wavelets and Signal Processing, Boston, MA: Birkhauser, 2003.

Y. Zhang, M. G. Amin, and B. Obeidat, "Polarimetric array processing for nonstationary signals," in S.Chandran (ed.), Adaptive Antenna Arrays: Trends and Applications, Berlin, Germany: Springer-Verlag, 2004.

Y. Zhang, B. Obeidat, and M. G. Amin, "Polorimetric time-frequency MUSIC for direction finding of moving sources with time-varying polarizations," in S. Chandran (ed.), Advances in Direction-of-Arrival Estimation, Boston, MA: Artech House, 2006.

3. Patents (ANNOTATE EACH WITH FILED OR GRANTED):

None

4. Presentations (INVITED):

IEEE Distinguish Lecturer 2003
   Nanyang Technological University (NTU), Singapore
   Defense Science Organization (DSO), Malaysia
  University of Technology of Malaysia (UTM), Kuala Lumpur

Keynote Address, SPIE, Orlando, "Signal Processing and Beamforming Techniques in Wideband Through-the-Wall Radar Imaging," April 2005.

Invited Talks:
   Drexel University – 04/24/06 – "Through-the-Wall Radar Imaging"
   University of Delaware – 05/08/06 – "Through-the-Wall Radar Imaging"
   Michigan State University – 10/19/06 – "Through-the-Wall Radar Imaging"
   IT Institute, Cairo, Egypt – 12/20/2006 – "Through-the-Wall Radar Imaging"

5.   Presentations (CONTRIBUTED):

G. J. Frazer and M. G. Amin, "Characterization of near-field scattering using quadratic sensor-angle distributions," Proceedings of the IEEE International Conference on Acoustics, Speech and Signal Processing, Orlando, FL, May 2002.

G. J. Frazer and M. G. Amin, "Characterization Of Near-Field Scattering Using A Multiple Weighted Summed Beamformer," Proceedings of SPIE 2002, Advanced Signal Processing Algorithms, Architectures and Implementations XII, Seattle, WA, July 2002.

A. Hassanien, A. B. Gershman, and M. G. Amin, "Time-frequency ESPRIT for direction-of arrival estimation of chirp signals," IEEE Sensor Array and Multichannel Signal Processing Workshop, Rosslyn, VA, Aug. 2002.

Y. Zhang, M. G. Amin, and G. J. Frazer, "A new approach to FM jammer suppression for digital communications", Proceedings of the IEEE Sensor Array and Multichannel Signal Processing Workshop, Rosslyn, VA, Aug. 2002.

G. J. Frazer and M. G. Amin, "Near-field scatter measurements using quadratic sensor-angle distributions", in Proceedings of the Second IEEE Sensor and Multichannel Signal Processing Workshop, Washington, DC, Aug. 2002.

Y. Zhang, M. G. Amin, and H. Ge, "Nonstationary interference suppression in DS/SS communications using space-time oblique projection techniques," IEEE International Symposium on Signal Processing and Information Technology, Marrakech, Morocco, December 2002.

Y. Zhang, M. G. Amin, and A. R. Lindsey, "Improved blind separations of nonstationary sources based on spatial time-frequency distributions," Fourth International Symposium on Independent Component Analysis and Blind Signal Processing, Nara, Japan, April 2003.

Y. Zhang, M. Amin, and G. Frazer, "High Resolution Time-Frequency Distribution for Maneuvering Target Detection in Over-The-Horizon Radars," IEEE International Conference on Acoustics, Speech and Signal Processing, Hong Kong, China, April 2003.

L. Cirillo, A. Zoubir, and M. Amin, "Auto-Term Detection Using Time-Frequency Array Processing," IEEE International Conference on Acoustics, Speech and Signal Processing, Hong Kong, China, April 2003.

F. Ahmad, G. Frazer, S. Kassam, and M. Amin, "A New Approach for Near-Field Wideband Synthetic Aperture Beamforming," IEEE International Conference on Acoustics, Speech and Signal Processing, Hong Kong, China, April 2003.

G. Wang, X. Xia, B. Root, V. Chen, M. Amin, and Y. Zhang, "Maneuvering Target Detection In Over-The-Horizon Radar By Using Adaptive Chirplet Transform," IEEE International Conference on Acoustics, Speech and Signal Processing, Hong Kong, China, April 2003.

Y. Zhang, M. G. Amin, and B. Obeidat, "Spatial polarimetric time-frequency distributions and applications to direction-of-arrival estimation," SPIE Annual Meeting, San Diego, CA, Aug. 2003.

Y. Zhang, B. A. Obeidat, and M. G. Amin, "Polarimetric time-frequency MUSIC in coherent signal environment," IEEE Workshop on Statistical Signal Processing, St. Louis, MO, Sept. 2003.

B. A. Obeidat, Y. Zhang, and M. G. Amin, "Polarimetric time-frequency ESPRIT," Proceedings of the 37th Asilomar Conference on Signals, Systems, and Computers, Pacific Grove, CA, Nov., 2003.

Y. Zhang and M. Amin, "Spatial And Polarization Correlations In Nonstationary Array Processing," Proceedings of the IEEE International Conference on Acoustics, Speech, and Signal Processing, Montreal, Canada, May 2004.

B. Obeidat, Y. Zhang, and M. Amin, "Range And Doa Estimation Of Polarized Near-Field Signals Using Fourth-Order Statistics," Proceedings of the IEEE International Conference on Acoustics, Speech, and Signal Processing, Montreal, Canada, May 2004.

Y. Zhang and M. G. Amin, "Spatial and polarization correlations in array processing," Proceedings of the IEEE Sensor Array and Multichannel Signal Processing Workshop, Barcelona, Spain, July 2004.

Y. Zhang, M. G. Amin, and G. J. Frazer, "Simultaneous operation of two over-the-horizon radars," Proceedings of the SPIE Annual Conference, Denver, CO, Aug. 2004.

G. Wang, Y. Zhang, and M. G. Amin, "Cooperation diversity using differential distributed space-time codes," Proceedings of the The Joint Conference of Asia-Pacific Conference on Communications and International Symposium on Multi-Dimensional Mobile Communications, Beijing, China, Aug. 2004.

B. A. Obeidat, Y. Zhang, and M. G. Amin, "DOA and polarization estimation for wideband sources," Proceedings of the Annual Asilomar Conference on Signals, Systems, and Computers, Pacific Grove, CA, Nov. 2004.

Y. Zhang, B. A. Obeidat, and M. G. Amin, "Nonstationary array processing for sources with time-varying polarizations," Proceedings of the Annual Asilomar Conference on Signals, Systems, and Computers, Pacific Grove, CA, Nov. 2004.

M. G. Amin, "A noncoherent radar system approach for through-the-wall imaging," Proceedings of the SPIE Defense & Security Symposium, Conference on Sensors, and Command, Control, Communications, and Intelligence (C3I), Orlando, FL, March 2005.

L. Cirillo, A. Zoubir and M. G. Amin, "Direction finding of nonstationary signals using a time-frequency hough transform," Proceedings of the IEEE International Conference on Acoustics, Speech, and Signal Processing, Philadelphia, PA, March 2005.

B. Obeidat, Y. Zhang, and M. G. Amin, "Nonstationary array processing for tracking moving targets with time-varying polarizations," Proceedings of the IEEE International Conference on Acoustics, Speech, and Signal Processing, Philadelphia, PA, March 2005.

F. Ahmad, M. Amin, and S. Kassam, " A beamforming approach to stepped-frequency synthetic aperture through-wall radar imaging," Proceedings of the IEEE Workshop on Computational Advances in Multi-Sensor Adaptive Processing, Puerto Vallarta , Mexico, December 2005.

F. Ahmad and M. Amin "A Noncoherent Approach to Radar Localization through Unknown Walls" Proceedings of the 2006 IEEE RADAR Conference,Verona, NY, April 2006.

H. Estephan, F. Ahmad, M. Amin, "An Interactive Software for Real-Time Simulation of Through-the-Wall Imaging Radar," Proceedings of the IEEE International Conference on Acoustics, Speech, and Signal Processing, Toulouse, France, May 2006.

L. Cirillo, A. Zoubir, M. Amin, "Estimation of FM Parameters using a Time-Frequency Hough Transform," Proceedings of the IEEE International Conference on Acoustics, Speech, and Signal Processing, Toulouse, France, May 2006

S. Aviyente, F. Ahmad, and M. Amin, "Information theoretic measures for through-the-wall surveillance," Proceedings of the IEEE Workshop on Sensor Array and Multi-channel Processing, Waltham, MA, July 2006.

F. Ahmad, M. Amin, P. Sutler, and P. Zemany, "Moving target localization for indoor imaging using dual frequency cw radars," Proceedings of the IEEE Workshop on Sensor Array and Multi-channel Processing, Waltham, MA, July 2006.

F. Ahmad and M. Amin, "Analyses of autofocusing schemes for indoor imaging with unknown walls," Proceedings of the IEEE Workshop on Sensor Array and Multi-channel Processing, Waltham, MA, July 2006.

F. Ahmad, M.G. Amin, "Through-the-Wall Radar Imaging Experiments," Proceedings of the IEEE Workshop on Signal Processing Applications for Public Security and Forensics, Washington, D.C., April 2007.

S. Aviyente, F. Ahmad, M.G. Amin, "Information theoretic measures for change detection in urban sensing applications, Proceedings of the IEEE Workshop on Signal Processing Applications for Public Security and Forensics, Washington, D.C., April 2007.

F. Ahmad, M. G. Amin, "High-resolution imaging using capon beamformers for urban sensing applications," Proceedings of the IEEE International Conference on Acoustics, Speech, and Signal Processing, Honolulu, HI, April 2007.

P. Setlur, M. G. Amin, F. Ahmad, "Cramer-Rao bounds for range and motion parameter estimations using dual frequency radars," Proceedings of the IEEE International Conference on Acoustics, Speech, and Signal Processing, Honolulu, HI, April 2007.

L. Cirillo, A. Zoubir, and M. Amin, "Estimation of near-field parameters using spatial time-frequency distributions," Proceedings of the IEEE International Conference on Acoustics, Speech, and Signal Processing, Honolulu, HI, April 2007.

P. Setlur, M. G. Amin, F. Ahmad, "A Frequency Diverse Doppler Radar for Range-to-Motion Estimation in Urban Sensing Applications," Proceedings of the 2007 International Waveform Diversity and Design Conference, Pisa, Italy, June 2007.

6. Honors (Presidential YIP, elections to Fellow status in major scientific society; appointed editor of scientific journal, elected NAS/NAE/IOM, awarded medal by scientific society, Chairman of scientific meeting, etc):

SPIE Fellow (2007)

Served on the Franklin Institute Committee on Science and the Arts (on-going)

7. Number of graduate students:

Three graduate student (full-time)

8. Number of Post-doctoral students:

One half-time Postdoctoral Fellow

9. Number of undergraduate students supported:

None

10. Number of under-represented members by group:

None

REPORT DOCUMENTATION PAGE		*Form Approved* *OMB No. 0704-0188*

The public reporting burden for this collection of information is estimated to average 1 hour per response, including the time for reviewing instructions, searching existing data sources, gathering and maintaining the data needed, and completing and reviewing the collection of information. Send comments regarding this burden estimate or any other aspect of this collection of information, including suggestions for reducing the burden, to Department of Defense, Washington Headquarters Services, Directorate for Information Operations and Reports (0704-0188), 1215 Jefferson Davis Highway, Suite 1204, Arlington, VA 22202-4302. Respondents should be aware that notwithstanding any other provision of law, no person shall be subject to any penalty for failing to comply with a collection of information if it does not display a currently valid OMB control number. **PLEASE DO NOT RETURN YOUR FORM TO THE ABOVE ADDRESS.**

1. REPORT DATE *(DD-MM-YYYY)* 04/27/2007	2. REPORT TYPE Final	3. DATES COVERED *(From - To)* October 2001 - March 2007

4. TITLE AND SUBTITLE	5a. CONTRACT NUMBER
Classification and Discrimination of Sources with Time-Varying Frequency and Spatial Spectra	
	5b. GRANT NUMBER N00014-98-1-0176
	5c. PROGRAM ELEMENT NUMBER
6. AUTHOR(S) Amin, Moeness, G. (PI)	5d. PROJECT NUMBER
	5e. TASK NUMBER
	5f. WORK UNIT NUMBER

7. PERFORMING ORGANIZATION NAME(S) AND ADDRESS(ES) Villanova University 800 Lancaster Ave Villanova, PA 19085	8. PERFORMING ORGANIZATION REPORT NUMBER Acct: 527616

9. SPONSORING/MONITORING AGENCY NAME(S) AND ADDRESS(ES) Office of Naval Research Ballston Centre Tower One 800 North Quincy Street Arlington, VA 22217-5660	10. SPONSOR/MONITOR'S ACRONYM(S)
	11. SPONSOR/MONITOR'S REPORT NUMBER(S)

12. DISTRIBUTION/AVAILABILITY STATEMENT

Approved for Public Release; Distribution is Unlimited.

13. SUPPLEMENTARY NOTES

14. ABSTRACT

The research efforts proceeded on different fronts leading to advances in target detection, tracking, and characterization for over the Over-the-Horizon radar applications as well as for urban sensing and through-the-wall radar imaging applications. Improved characterizations of the targets are achieved using multiple OTHRs operating simultaneously as compared to a single OTHR operating alone. We have introduced the spatial polarimetric time-frequency distributions (SPTFDs) as a platform for processing polarized nonstationary signals incident on multiple dual-polarized double-feed antennas. For urban sensing applications, two different techniques to provide high imaging quality of scenes behind walls when wall characteristic are unknown were proposed. When considering chirp radar signals or complex Doppler target signatures, we have improved blind separation of signals with time-varying spectra using Multiple Hypothesis Testing. Further, we have enhanced the estimation of the phase parameters of mono- or multi-component frequency modulated signals from noisy observations using the Time-Frequency Hough Transform.

15. SUBJECT TERMS

Time-frequency distribution, direction-of-arrival (DOA) estimation, polarization, wideband, micro-Doppler

16. SECURITY CLASSIFICATION OF:			17. LIMITATION OF ABSTRACT	18. NUMBER OF PAGES	19a. NAME OF RESPONSIBLE PERSON
a. REPORT U	b. ABSTRACT U	c. THIS PAGE U	UU	183	19b. TELEPHONE NUMBER *(Include area code)*

Standard Form 298 (Rev. 8/98)
Prescribed by ANSI Std. Z39.18